Resonant Readout of a Superconducting Persistent Current Qubit

by

Janice C. Lee

B.Sc., Queen's University (2000)
S.M., Massachusetts Institute of Technology (2002)

Submitted to the Department of Electrical Engineering and Computer Science
in partial fulfillment of the requirements for the degree of

Doctor of Philosophy

at the

MASSACHUSETTS INSTITUTE OF TECHNOLOGY

June 2006

Author .....
Department of Electrical Engineering and Computer Science
May 25, 2006

Certified by .....
Terry P. Orlando
Professor of Electrical Engineering
Thesis Supervisor

Accepted by .....
Arthur C. Smith
Chairman, Department Committee on Graduate Students

Resonant Readout of a Superconducting Persistent Current Qubit

by

Janice C. Lee

Submitted to the Department of Electrical Engineering and Computer Science
on May 25, 2006, in partial fulfillment of the
requirements for the degree of
Doctor of Philosophy

Abstract

Superconducting Josephson junction devices rank among the best candidates for realizing a quantum computer. While the coherent control of quantum dynamics has been demonstrated in these solid-state, macroscopic quantum systems, a major challenge has been to increase the coherence times for these qubits. With an objective to reduce the level of readout-induced decoherence, this thesis work focuses on a resonant readout scheme developed for a niobium persistent-current (PC) qubit. This non-dissipative readout approach detects the flux state of the qubit by sensing a change in the Josephson inductance of a SQUID magnetometer. By incorporating the SQUID inductor in a high-Q resonant circuit, we distinguished the flux states of the qubit as a shift in the resonant frequency at 300 mK. The nonlinearity due to the Josephson inductance has characteristic effects on the resonant behavior of the readout circuit. We observed novel manifestation of this nonlinearity given the high quality factor of the resonance. The readout circuit was characterized in the linear as well as the nonlinear regime for its potential use as a bifurcation amplifier. Numerical simulations based on Josephson-junction circuits were also performed to understand the observed nonlinearity in the resonant behavior.

Thesis Supervisor: Terry P. Orlando
Title: Professor of Electrical Engineering

Acknowledgments

First and foremost, I am most grateful to Professor Terry P. Orlando, who has been a wonderful research advisor to me in the past six years. I benefit tremendously from his technical expertise, guidance, sincere advice, and encouragement. Over the years, as I went through different stages of my graduate development, he has always treated me with patience, kindness, as well as respect. While providing me with general guidance and direction for my research, he also gave me the freedom to try out new things and encouraged me to develop my own research style. He always takes a generous heart to see the goodness in my work. He has given me excellent advice from the beginning of my project, all the way till the end when I had to converge years of research work into this thesis, which he read from word to word to help me make sure it captures and conveys the essence of years of my hard work. For these and many more, I am deeply touched and will forever be grateful.

I would like to acknowledge previous and current members of my research group, a lot of whom have been like family to me in many ways. I want to thank Dr. Ken Segall for his enthusiasm and for giving me advice especially in the beginning of my project. Donald Crankshaw coached me through the cool down of my first sample, and shared with me his knowledge on the experimental aspects in the group. I want to thank Daniel Nakada for being my best friend in the group and for sharing all my ups and downs in research. I could always count on his help and I really appreciate his kind and gentle personality. I enjoyed working with Dr. Yang Yu who taught me a great deal about running experiments in the dilution refrigerator. Over the years I have also become close to his family. I want to thank my buddy Jonathan Habif for always being there when I needed him for technical advice or moral support. I really appreciate his continuing concern for me and the group even after he moved on to his new job. I also want to acknowledge our research scientist Dr. Sergio Valenzuela for teaching me to have faith in my simulations work, for his patience, and for his advice. Thanks also go to Murali Kota for his friendship, and to David Berns and Bill Kaminsky for their help over the years.

My days at Lincoln Lab will always remain a highlight of my graduate experience. It was particularly special to me as it was the time I made my first scientific breakthrough. I am grateful to Dr. William Oliver for providing me the opportunity to do my experiment there, and for coaching and mentoring me during that time. He was always enthusiastic to hear about my work, and shared a lot of my excitements. I hope that he enjoyed working with me as much as I had with him. I had the pleasure to get to meet a lot of fantastic people in group 86, with many of whom I have developed a lasting friendship. I want to acknowledge Dr. Daniel Oates for giving me advice on microwave resonators and microwave measurements. I benefited a great deal from his expertise and always found it stimulating to talk to him. I want to thank Terry Weir for all his technical help, his graciousness whenever

I asked for his help, and for his friendship. He is an amazing character and always kept me great company in the lab. I loved his "daily monologues" when he told me all kinds of cool stories about fishing (especially that time when a whale jumped out of the water near where he fished), his old days as a lobster fisherman, Irish music, and heritage such as Prince Spaghetti night. I want to thank Bobby Konieczka for always brightening my day with his warm personality. He has all the gadgets for making coaxial cables, and I always had a pleasant surprise when I went to him and found the perfect tool for my job. We also have this idea of collecting all our deflated helium balloons and having them all fixed up one day for a balloon party. I also appreciate Rick Slattery for giving me advice when I designed my RF package, and for sharing his life experience with me over dinner. Thanks also go to Mark Gouker, Lenny Johnson, JoAnne Rantz, Vladimir Bolkhovsky, George Fitch, Gerald Dionne, Andrew Messier, Matthew Straayer, and other members of group 86 for their kindness and hospitality.

I would like to thank Professor Mildred Dresselhaus for graciously serving on my thesis committee, and for all her stimulating questions and valuable advice. I also want to express my gratitude to Professor Karl Berggren, who is always approachable for me to talk to, and gives me advice on anything from keeping goldfish to making career choices. I also appreciate him for including me in some of his group social events. I want to thank Professor Jing Kong who has always been very kind and helpful to me. She is very friendly to talk to, and I really appreciate her encouragement and kind thoughts. Thanks also go to Professor Hank Smith, Professor Clifton Fonstad, and Professor Sheila Prasad for their continuing support over the years.

I want to acknowledge my friends in Professor David Cory's group for welcoming me as part of their group, and for all their support. In particular, I want to thank Anatoly Dementyev and Benjamin Levi who are my lunch buddies, Cecilia Lopez, Jamie Yang, and Michael Henry.

I would like to take this opportunity to remember Bhuwan Singh, a very dear friend and colleague of mine. He has touched my heart and many others through his unique character: his great sense of humor, his intelligence and courage, and his devotion to help others so selflessly and lovingly. Bhuwan and I came to MIT and joined the Orlando group around the same time. We went through graduate school together. We fought over silly things, made mistakes together, made fun of each other, and cared a lot about each other. The bonds shared between Daniel, Bhuwan and me were extraordinary. My best memories in the group always had Bhuwan in it, and I think of him a lot. He will be solely missed.

Finally, I would like to express my profound gratitude to my family. My parents always encourage me to reach for my dreams, and have supported me every single day of this journey, with their care, concern, and unconditional love. They are always there to listen,

to understand, and can always find ways to cheer me up and make me laugh. My big brother Jason and my sister-in-law Katy always make sure I don't overwork myself, and send me candies and other goodies every now and then to brighten me up. My graduate experience has pushed me to achieve a level of dedication and perseverance that I did not know exist before. My family is the reason why I could make it through this journey, and more importantly, the reason why it was worth it.

May you enjoy the special pleasures of craft - the private satisfaction of doing a task as well as it can be done.

May you enjoy the special pleasures of profession - the added satisfaction of knowing that your efforts promote a larger public good.

May you be blessed with good luck, and also with the wisdom to appreciate when you have been lucky rather than skillful.

May you find ways to help others under circumstances where they cannot possibly know that you have done so.

May you be patient, and gentle, and tolerant, without becoming smug, self-satisfied, and arrogant.

May you know enough bad weather that you never take today's sunshine for granted, and enough good weather that your faith in the coming of spring is never shaken.

May you always be able to confess ignorance, doubt, vulnerability, and uncertainty.

May the Force be with you.

May you frequently travel beyond the places that are comfortable and familiar, the better to appreciate the miraculous diversity of life.

Jeffrey S. Lehman
11^{th} President of Cornell University
Excerpt from Commencement Address, 2005

Contents

List of Figures

Chapter 1

Introduction

Quantum computing offers great promises in solving classically intractable problems by harnessing the laws of quantum mechanics. While the laboratory realization of a real quantum computer is actively pursued using different physical implementations, macroscopic quantum systems based on superconducting circuits may have the ultimate advantage to be manipulated and controlled in a desired manner for computation. It is truly remarkable that these superconducting circuits of a length scale as large as tens of microns, artificially designed and fabricated using standard integrated-circuit technology, can in fact behave quantum mechanically in many ways similar to microscopic systems involving atoms, electrons or photons.

Superconductors are one of the few examples where the large-scale behavior of the system is described by the collective quantum behavior of the underlying microscopic particles. In a superconductor, pairs of electrons known as Cooper pairs occupy the system's ground state and form a condensate described by a single macroscopic wavefunction. In the 1980's, A.J. Leggett proposed two classes of experiments to demonstrate the evidence of this macroscopic wavefunction: macroscopic quantum tunneling (MQT) and macroscopic quantum coherence (MQC) [1, 2, 3]. MQT phenomena involves the tunneling of the macroscopic wavefunction across a barrier, and have been well observed in superconducting devices comprising thin barriers such as Josephson junctions or SUperconducting Quantum Interference Devices (SQUIDs). On the other hand, MQC phenomena are experimentally harder to observe. They involve the coherent oscillation between two quantum states, and as Leggett put it,

would be more "spectacular evidence" than MQT phenomena which are more "indirect and circumstantial" [3].

Recent interests in quantum computation have lead to a vast amount of exciting achievement in the laboratory realizations of MQC in superconducting circuits. With advances in techniques for fabrication and electronic noise control, macroscopic superposition of quantum states and coherent oscillations have been demonstrated in different superconducting circuit implementations. And just as important, it has also been shown that engineering has a definite role to play in controlling the level of quantum coherence in these circuits.

Due to their macroscopic nature, superconducting circuits are more easily susceptible to environmental noise. The problem of decoherence, where the system loses its quantum information, is more severe for superconducting circuits than other implementations for a quantum computer. However, the ultimate promise of the field is that if successfully implemented, superconducting quantum computation can inherit the wealth of integrated-circuit technology from the semiconducting industry. While the outcome for the race to build a quantum computer remains too early to be foreseen, this "fat Schrödinger's cat" certainly earns a unique place in the race.

1.1 Quantum Computing

Quantum computation was originally proposed by R. P. Feynman in 1982 [4] for performing simulations of quantum behavior. The idea of a quantum computer involves representing bits of information in quantum systems. For instance, the up and down spins of an electron can be used to represent 0 and 1. By maintaining these quantum bits, or qubits, a quantum computer can make use of distinctively quantum mechanical phenomena such as superposition and entanglement of quantum states to operate on the data. Unlike classical bits, an n-qubit register can be in a superposition of all of its 2^n orthogonal eigenstates, and this power of parallel processing offers exponential improvement in computational speed.

The field of quantum computing started to prosper in 1994 when P. Shor developed a quantum algorithm and showed that a quantum computer only takes polynomial time to factor an integer into its primes [5]. The same factoring problem takes exponential time

for a classical computer, and in fact, the infeasibility for an ordinary computer to factor a large number within a reasonable timescale is what modern cryptography techniques are based. So far, the main advantages of quantum computers are known to be solving the factoring problem, a related problem called the discrete-logarithm problem, and performing quantum mechanical simulations. It is by no means intended to replace classical computers, nor does it immediately address the problems related to chip miniaturization faced by the semiconducting industry.

The main requirements for a viable physical implementation for a quantum computer are outlined by DiVincenzo in five criteria [6]. These criteria are concerned with (1) qubit existence: the physical system needs to be scalable with well-defined qubits; (2) qubit reset: the qubit states can be initialized; (3) qubit coherence: qubits have long coherence times compared to the gate time; (4) qubit control: universal gate operations between qubits can be achieved by controllable interactions of the quantum systems; and (5) qubit read-out: an efficient readout procedure exists for the specific qubit implementation. Based on these criteria, there are currently numerous physical systems which are promising candidates for implementing a quantum computer [7, 8]. Some of the examples are NMR, trapped ions/neutral atoms, cavity QED, and superconducting devices.

The major challenge for implementing a quantum computer is to maintain quantum coherence of the qubits long enough to perform useful calculations. The general rule of thumb is that the coherence time should be 10^4 times longer than the gate time to allow the incorporation of a quantum-error-correction algorithm. Decoherence of qubits is due to sources of noise from measurement circuitry or background environment. Most of the physical realizations of qubits are based on microscopic systems, such as spins of nuclei in a liquid, or dipoles of trapped ions/ neutral atoms in vacuum. These qubits are naturally very well isolated from their environment and have long coherence times. For instance, the typical relaxation times for NMR are between 1-30 s, and the dephasing times are between 0.1-10 s [9]. The main challenges for the microscopic implementations are scalability and to enhance inter-qubit coupling to the level required for fast gate operations. The superconducting approach, on the other hand, is scalable to large number of qubits. However, the relaxation times are much shorter and are typically between 0.1 to $1\mu\,s$.

1.1.1 Formulation of the readout problem

We will conclude the general discussion on quantum computing by discussing the challenge of the qubit readout process. The readout circuitry provides a channel for extracting information from the qubit. However, noise and dissipation are also coupled to the qubit through the same channel. The concern is that the readout process causes decoherence of the qubit before its original state can be accurately measured and recorded. The design of a good readout scheme presents us with the usual quantum mechanical dilemma. A readout detector weakly coupled to the qubit has a small effect on decohering the qubit, yet the measured signal can be too weak to be resolved by the measurement apparatus or within a reasonable timescale. On the other hand, a strong coupling between the detector and the qubit yields a strong signal but introduces severe decoherence on the qubit. Ideally, the criteria for choosing and operating a readout detector are [10]:

- An ideal detector should be allowed to switch ON and OFF in a time period that is short compared to the quantum dynamical timescale of the qubit. During the ON stage, the detector should be coupled to the qubit to measure its state. During the OFF stage such as in between measurements, the detector should be completely decoupled from the qubit.

- The strength of the coupling during the ON state between the detector and the qubit can be optimized. One should note that the stronger the coupling strength, the higher the sensitivity of the detector, but at the same time the coupling should be weak enough not to relax the qubit [11].

- The response time (the time needed for the information to be extracted from the qubit) and the reset time (the time needed to prepare the detector before another measurement can be made) should be fast compared to the qubit dynamical timescale.

1.2 Quantum computing with superconductors

Superconducting Josephson junction circuits rank among the best candidates for realizing a quantum computer. Unlike earlier implementations involving liquid-state NMR or ion traps, these superconducting systems are solid-state in nature and utilize familiar electrical devices controlled by voltages and currents. If successfully implemented, superconducting qubits have the advantage of being fabricated using standard integrated-circuit techniques. The integration permits control and readout circuitry to be incorporated on-chip, and provides a manageable option for scaling up to a large number of qubits. However, the solid-state systems are strongly coupled to the outside world. This posts a challenge as qubits must also be sufficiently isolated from the environment so that they can maintain coherence throughout the computation.

Charge qubits versus flux qubits

The types of superconducting qubits are categorized based on the ratio of the Josephson energy E_J to the charging energy E_c of the qubit. The two main types are the charge qubits ($E_J/E_c \sim 0.1$) and the flux qubits $E_J/E_c \sim 100$. A charge qubit, also known as the "Cooper-pair box", is defined by the presence or absence of a Cooper pair on a superconducting island. For a flux qubit, the qubit states correspond to circulating currents in the clockwise and counter-clockwise directions in a superconducting loop interrupted by Josephson junctions. In particular, the 1-junction qubit is realized by the RF SQUID, while the 3-junction qubit is usually referred as the persistent-current qubit (PC qubit). The work presented in this thesis is based on the PC qubit system.

Coherent oscillations has been observed for a single charge qubit in 1999 [12], and with recent improvement the relaxation time is on the order of 100 ns. Since then, coherent oscillations [13], microwave spectroscopy [14] and gate operation [15] have been demonstrated with two coupled charge qubits. For the flux qubit system, superpositions of quantum states have been observed in the PC qubit [16] and the RF-SQUID qubit [18]. Coherent oscillation of a single PC qubit has been observed in [17, 19, 20] with a relaxation time on the order of 100 ns-1 μs. In general, flux qubits have longer coherence times due to their insensitivity to

charge-based fluctuations.

It should be mentioned that quantum coherence has also been demonstrated in two other types of superconducting qubit: the phase qubit ($E_J/E_c \sim 10^4$) based on a single current-biased Josephson junction [21, 22], and the "hybrid" charge-flux qubit ($E_J/E_c \sim 1$) also referred as the "quantronium" [23]. The hybrid qubit was designed so that during the qubit precession, it is insensitive to both charge and flux noise, while at the readout stage it is operated as a flux qubit.

Niobium-based versus aluminum-based qubits

The two common material choices for superconducting qubits are aluminum and niobium, which are both low-temperature superconductors. The critical temperature T_c of niobium is $\sim 9\,\mathrm{K}$, and is higher than the T_c of aluminum which is $\sim 1.5\mathrm{K}$. The superconducting material of choice is based on the following considerations:

1. **Fabrication consideration for junctions:** Devices based on aluminum can be deposited relatively easily using e-beam lithography and shadow evaporation. The minimum feature size for a Josephson junction is typically around 50 nm. Small junction dimensions between 50-100 nm are needed for charge qubits to achieve a small E_J/E_c ratio, and between 200-300 nm for flux qubits to enhance the coupling between the ground and first excited states of the qubit for coherent oscillations to occur. On the other hand, devices based on niobium are defined by optical lithography. The typical feature size of the a junction is larger and on the order of $1\,\mu$m. Recently, MIT Lincoln Laboratory has developed a niobium process which supports a minimum feature size of 150 nm [57]. Calculations have shown that this corresponds to a reasonably large coupling which could be of interests to flux qubit designs.

2. **Fabrication consideration for circuit complexity:** The shadow evaporation technique for fabricating aluminum circuits are impractical to have via structures (hence no inductors) or to support complex circuits. On the other hand, the niobium fabrication technology can easily integrate more complex circuitry on-chip. In particular, it provides the option of incorporating rapid-single flux quantum (RFSQ) electron-

ics for qubit readout and control; RFSQ have been developed based on the niobium fabrication technology.

3. **Quasi-particle consideration:** In general, quasi-particles have a longer relaxation time in niobium than in aluminum. This is undesired as the repetition rate of the readout is limited by the relaxation time of the quasi-particles. In addition, quasi-particles are a source of charge noise, and this poses a problem in particular for charge qubits as they are more sensitive to charge-based fluctuations.

1.2.1 Motivation of this thesis

In the endeavor to increase the coherence times for superconducting qubits, it is generally observed that the measurement results demonstrating the quantum dynamics of the qubit are intervened by noise from the readout process itself. This is especially true for conventional readout methods which are typically *dissipative* in nature and involve high levels of biases. Recently, a considerable amount of effort has been done to develop a so-called *dispersive* readout scheme, where the qubit is coupled to a resonator, and that the qubit state can be detected as a shift in the resonant frequency of the resonator.

The work presented in this thesis focuses on the dispersive readout scheme developed for a niobium persistent-current qubit. The conventional way to measure a PC qubit is by coupling the qubit to a SQUID magnetometer which is operated as a switching current detector. This approach involves high bias current and switches the Josephson junctions from the superconducting state to the voltage stage. The proposed resonant readout detects the qubit state by sensing a change in the Josephson inductance of the SQUID magnetometer, which in turn is detected as a shift in the resonant frequency of a resonator. As a result, the level of readout-induced decoherence on the qubit should be reduced.

Similar approach has also been investigated by [24, 25] for the PC qubit system, by [27] for the hybrid qubit, and by [28] for the charge qubit. Quantum coherence of the qubit has been demonstrated using the dispersive readout in [24, 27, 28], and the visibility of the coherent oscillations as well as the coherence times are shown to be an improvement over previous results based on the conventional readout schemes.

This thesis work differs in a number of ways. First, our qubit and readout circuit were fabricated out of niobium, whereas the implementations mentioned above were aluminum-based. Second, we were able to achieve a high quality factor for the resonator by incorporating RF transformation network on-chip using the planarized niobium process. Third, the nonlinearity due to the Josephson inductance of the SQUID has characteristic effects on the resonant behavior of the readout circuit. We observed novel manifestation of this nonlinearity given the high quality factor of the resonance. Numerical simulations were also performed to understand the observed nonlinearity.

1.3 Overview of thesis

1.3.1 Persistent Current Qubit

The PC Qubit is a superconducting loop interrupted by three Josephson junctions, two of which have the same critical current I_c while the third junction has a critical current scaled down by a factor α [30, 31]. The circuit schematic of the qubit and the picture of an actual device are shown in fig. 1-1. Each Josephson junction in the qubit loop is

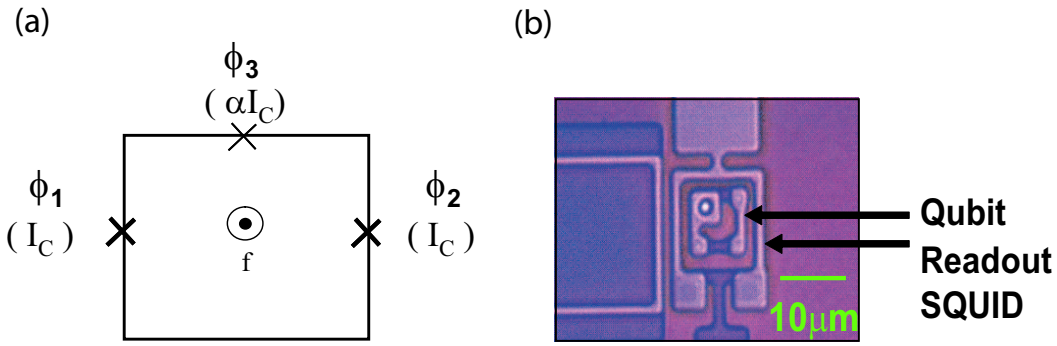

Figure 1-1: (a) Schematic of the persistent current qubit. The symbol 'X' denotes a Josephson junction. Junctions 1 and 2 have the same area while junction 3 is a factor of α smaller. An external magnetic flux f threads the qubit loop and determines its operating point. (b) Optical micrograph of a niobium qubit coupled to a readout SQUID fabricated at MIT Lincoln Laboratory.

characterized by the variable φ, which is the gauge-invariant phase difference between the two superconductors on each side of the tunnel junction. The current-phase relation and the

voltage-phase relation for a Josephson junction are given by:

$$I = I_c \sin \varphi \tag{1.1}$$

$$V = \frac{\Phi_o}{2\pi} \frac{d\varphi}{dt} \tag{1.2}$$

where Φ_o is a flux quantum and has the value of $h/2e = 2.0679 \times 10^{-15}$ Wb. To obtain the Hamiltonian of the PC qubit system, we consider the Josephson energy E_J and the Coulomb energy E_C of the junctions, which are treated as the potential energy and the kinetic energy of the system respectively. The potential landscape of the PC qubit is controlled by the magnetic frustration $f = \Phi_{ext}/\Phi_o$, as well as the fabrication parameter α. It corresponds to a two-dimensional periodic potential for f near 1/2 and is shown in fig. 1-2. We are mostly interested in the double well along the $L_{oo} - R_{oo}$ trajectory, since tunneling between neighboring unit cells is suppressed for the given design parameters. By treating the charging energy of the junctions as the kinetic energy of a particle in this double-well potential, and by considering the circuit quantum mechanically, it has been shown that *the two lowest states of the qubit can be designed to be oppositely circulating currents in the qubit loop.*

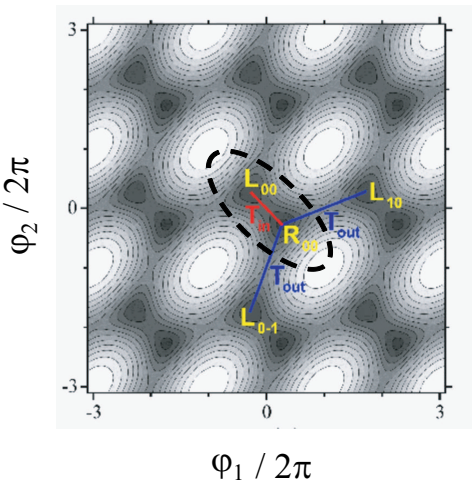

Figure 1-2: Potential landscape U(φ_1, φ_2) of the PC qubit for $f = \frac{1}{2}$ and $\alpha = 0.8$. We are mostly interested in the double-well potential along the $L_{oo} - R_{oo}$ trajectory. Tunneling between neighboring unit cells is suppressed for the given design parameters [30, 31].

1.3.2 Conventional readout of Qubit States: Switching current measurement

From the discussion above, we see that operating the qubit near an external flux bias near $f = \frac{1}{2}$ gives rise to a double well potential along the L_{oo}-R trajectory, and the two lowest energy states correspond to oppositely circulating persistent currents in the qubit loop. To detect the state of the qubit, one notes that the flux of the induced current either adds to or subtracts from the external flux, and thus by detecting the difference in the overall flux sensed by a DC SQUID inductively coupled to the qubit, the states of the qubit can be measured. The size of the flux generated by the persistent current in the qubit depends on the strength of the coupling. The coupling in turn depends on the mutual inductance M between the qubit and the SQUID, and the size of the persistent current I_P within the qubit loop. The range is usually between $0.001\Phi_o$ to $0.01\Phi_o$.

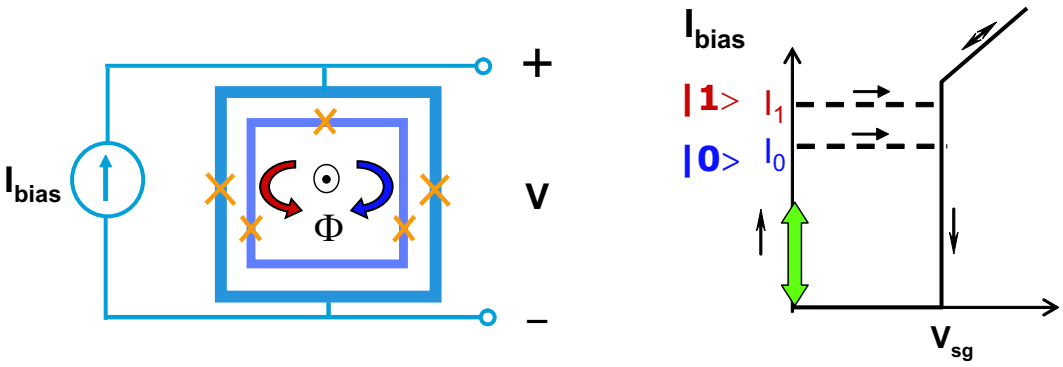

Figure 1-3: Left: The blue and red arrows represent the clockwise and counter-clockwise circulating current states of the qubit. The qubit is inductively coupled to a SQUID magnetometer. Right: The SQUID IV characteristics over a cycle of the switching current readout. The SQUID switches to the voltage state at a different critical current depending on the state of the qubit. The proposed resonant readout approach keeps the bias current well below the critical level (green block arrow).

The conventional scheme to operate the SQUID detector is the so-called switching current readout. This detection scheme employs a non-shunted (underdamped) SQUID and uses the property that its critical current is a function of magnetic flux. Typically, one ramps the current through the SQUID and determines the qubit state either by directly measuring the

switching current, or by detecting the presence or absence of a switching event (fig.1-3). This approach involves high current bias and switches the SQUID from the superconducting state to the voltage state. Calculations based on the spin-boson model have shown that the level of decoherence increases with the amount of bias current that is passed through the SQUID [32]. In addition, the switching action to the finite voltage state also excites a large number of quasi-particles, which must then be allowed to relax to the superconducting state before another measurement can be performed. This relaxation time can be fairly long and may restrict the repetition rate of the measurements [33].

1.3.3 Principles of Resonant Circuit Readout

To reduce these sources of readout-induced decoherence, the research to be presented in this thesis focuses on the implementation of a resonant readout technique for a PC qubit. The main idea is to use the readout SQUID as a flux-sensitive inductor rather than a switching-current detector. It will be shown that the Josephson inductance of a SQUID is a periodic function of the magnetic flux which threads the loop. Thus, by incorporating the readout SQUID in a high-Q resonant circuit, the state of the qubit can be determined from the inductance of the SQUID, which in turn can be measured from the resonant frequency of the readout circuit with high sensitivity. The main advantage of this non-dissipative approach is that it biases the SQUID at low currents and does not require the SQUID to switch to the voltage stage.

Josephson inductance of a SQUID

In section 2.3, we will show that a Josephson junction is inductive in nature, and that the inductance is nonlinear and changes with the current bias through the junction. On the other hand, the Josephson inductance of a SQUID is dependent on both the current bias I_{sq} and the flux bias Φ_{ext}, and in the limit where the SQUID has negligible loop inductance, its Josephson inductance can be expressed as:

$$L_{J,sq} = \frac{\Phi_o}{2\pi I_c(\Phi_{ext})} \frac{\varphi_p}{\sin \varphi_p} \tag{1.3}$$

where $I_c(\Phi_{ext}) = 2I_{co}\cos(\pi\Phi_{ext}/\Phi_o)$ can be considered as the effective critical current of the SQUID, and $\varphi_p = \sin^{-1}(I_{sq}/I_c(\Phi_{ext}))$ is the effective phase. I_{co} is the critical current of a single junction. The current and flux dependence is plotted in fig. 1-4. While the Josephson inductance always increases with the bias current, it can increase or decrease with the flux bias due to the periodic dependence. Therefore, the Josephson inductance of the SQUID is different depending on the flux state of the qubit.

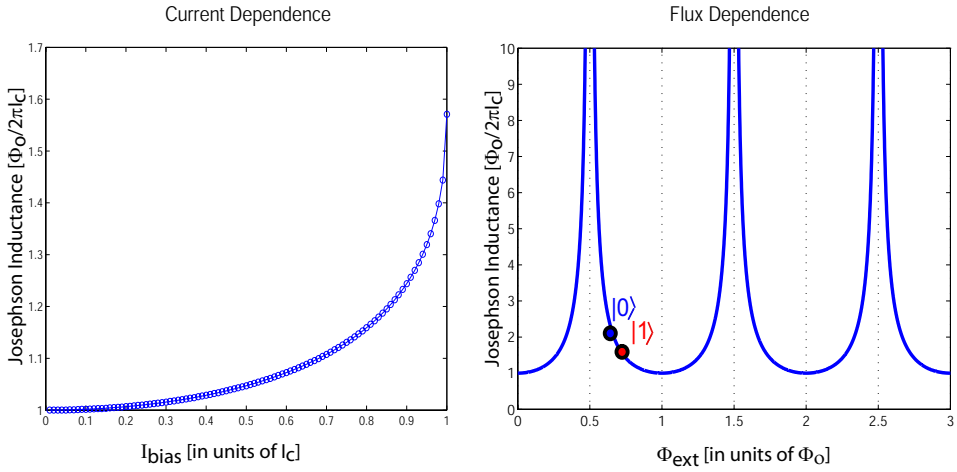

Figure 1-4: The Josephson inductance of a SQUID is nonlinear in the current bias and the flux bias. Depending on the flux states of the qubit, the SQUID will have a different inductance value.

Measurement Scheme for Resonant Circuit Readout

To apply the SQUID inductor as a magnetometer for qubit readout, we need to be able to measure the change in Josephson inductance with high sensitivity. The idea is to incorporate the SQUID inductor in a high-Q resonant circuit, where a change in the inductance corresponding to a transition between qubit states can be detected as a shift in the resonant frequency. For illustrative purposes, we consider a simple parallel RLC resonant circuit. In fig. 1-5, the SQUID is modeled as an ordinary inductor, and the resistance R represents the parallel combination of the source and output impedances. The circuit is driven by an AC source.

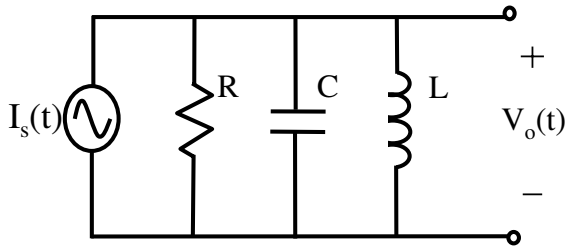

Figure 1-5: A linear RLC resonant circuit in the parallel configuration.

The impedance $Z(\omega)$ of the network is:

$$|Z(\omega)| = \frac{1}{\sqrt{(\frac{1}{R})^2 + (\omega C - \frac{1}{\omega L})^2}} = \frac{R(\frac{\omega\omega_o}{Q})}{\sqrt{(\omega_o{}^2 - \omega^2)^2 + (\frac{\omega\omega_o}{Q})^2}} \tag{1.4}$$

where ω_o is the resonant frequency given by

$$\omega_o = \frac{1}{\sqrt{LC}} \tag{1.5}$$

and Q is the quality factor which characterizes the sharpness of the resonant peak. For a parallel configuraion, Q is given by:

$$Q = \frac{R}{\omega_o L} = \omega_o RC = R\sqrt{\frac{C}{L}} \tag{1.6}$$

Experimentally, the change in the SQUID Josephson inductance can be detected as a shift in the resonant frequency. The resonant frequency can be directly measured with a spectrum/network analyzer. Alternatively, a more rapid readout can be performed by biasing the resonant circuit at a single frequency f_b near the resonant frequency. As illustrated in fig. 1-6, the shift in the resonant frequency is detected as a difference in the output voltage ΔV. Note that ΔV is maximum when f_b is close to f_o, where $V(\omega)$ has the sharpest slope.

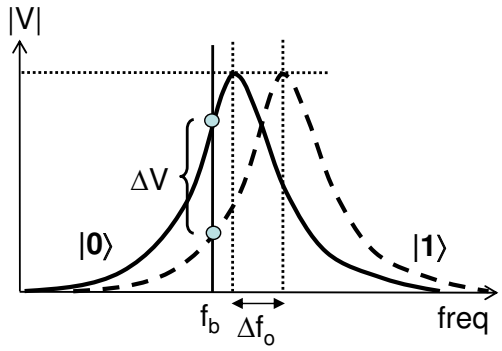

Figure 1-6: Measurement scheme for the resonant readout. The change in resonant frequency can be sensed as a change in the magnitude or phase of the output voltage at a frequency bias f_b. This provides a faster readout then measuring the resonant frequency with a spectrum/network analyzer.

1.3.4 Experimental Realization

The design of the resonant readout circuit shown in fig. 1-7 has employed impedance transformation and impedance matching techniques to achieve a high quality factor [35]. The resonant frequency was designed to be 500 MHz with a Q on the order of 150. The device was fabricated with a planarized Nb trilayer process at MIT Lincoln Laboratory [34]. The inductors and capacitors were also fabricated on the same chip as the junctions. A device micrograph is shown in fig. 1-8.

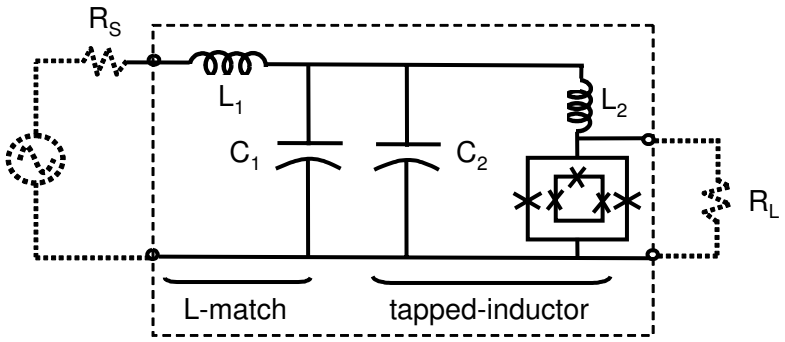

Figure 1-7: Circuit schematic of the resonant readout circuit. Tapped-inductor and L-match impedance transformations were employed to achieve a high quality factor [35]. The components within the dotted box were fabricated on-chip.

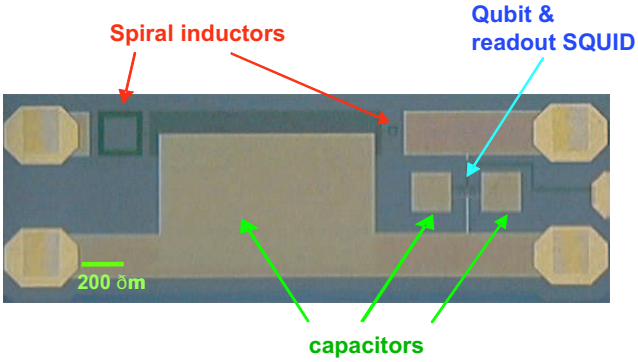

Figure 1-8: Optical micrograph of the actual device fabricated at MIT Lincoln Laboratory.

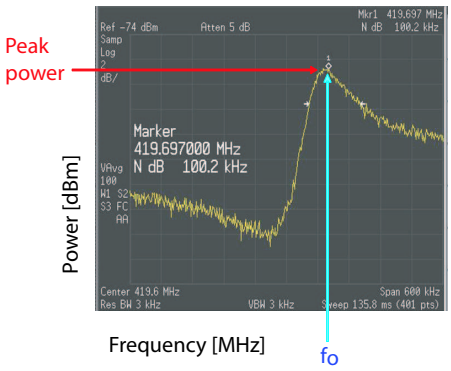

Figure 1-9: A typical resonant spectrum as displayed on a spectrum analyzer. The resonant frequency is around 420 MHz, and Q is on the order of 1000. The data were taken at 300 mK.

The device was measured at 300 mK in a He-3 cryostat. A typical spectrum of the resonant readout circuit is shown in fig. 1-9. The resonant frequency was measured to be about 420 MHz while the quality factor Q was on the order of a 1000. We confirmed the sensitivity of the readout circuit to distinguish the circulating-current states of the qubit. The results are shown in fig. 1-10. When an external DC magnetic field was applied through the SQUID, we observed a modulation of the Josephson inductance, which in turn was manifested as a modulation in the resonant frequency of the readout circuit. At every 1.3 times the SQUID modulation period, a shift in the resonant frequency is observed. These so-called qubit steps represent a qubit transition between oppositely circulating current states. The shift in the resonant frequency is about 40 kHz, corresponding to a change in Josephson inductance of 2 pH. Furthermore, a dip in resonant peak power is observed at the qubit steps. This corresponds to broadening of the resonant spectrum.

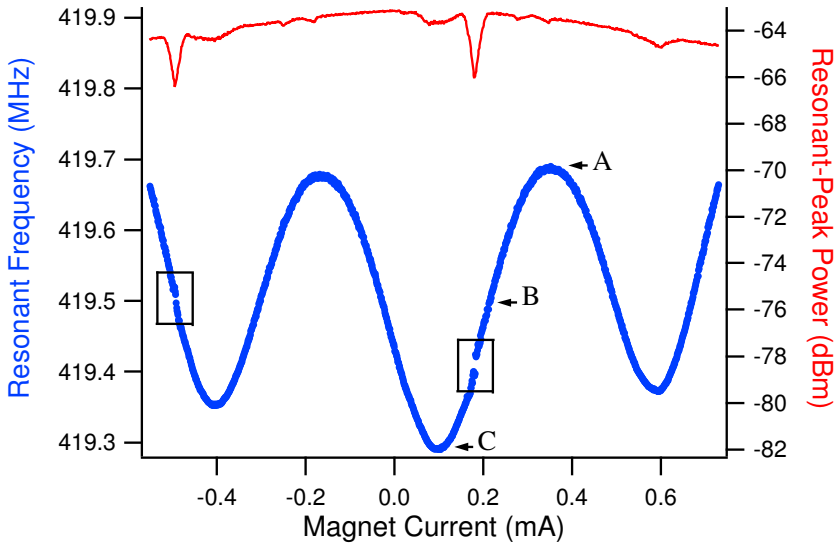

Figure 1-10: The lower plot (left axis) shows the modulation of the resonant frequency with external magnetic field. The upper plot (right axis) shows the corresponding peak amplitude of the resonant spectrum. The dip in peak power coincides with the qubit step. The data were taken at 300 mK.

1.3.5 Resonant Readout in the Nonlinear Regime

As the bias current to the readout SQUID is increased along the supercurrent branch, the SQUID inductance becomes increasingly nonlinear and has observable effects on the resonant spectrum of the readout circuit.

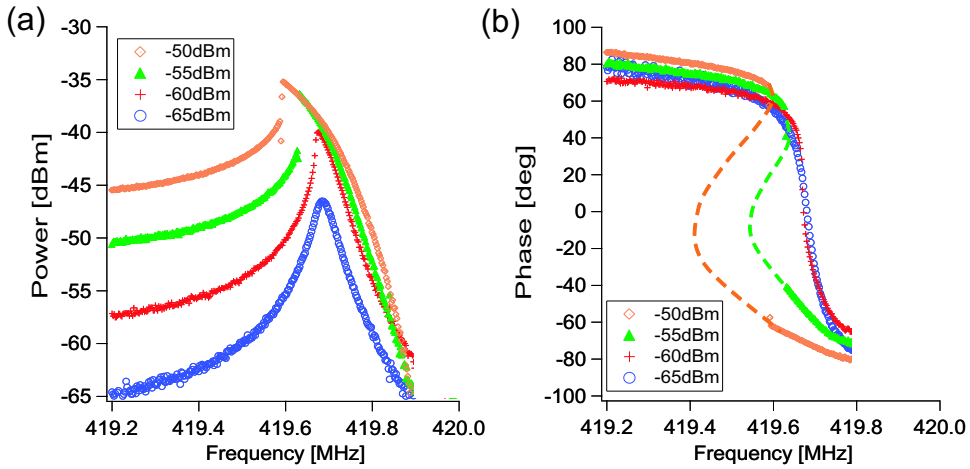

Figure 1-11: (a) Magnitude and (b) phase spectra of the resonant readout circuit as it makes the transition from the linear to the nonlinear regime with increasing source power at $\Phi = 0$.

Fig. 1-11 shows the magnitude and phase spectra of the readout circuit with increasing level of input power at $\Phi = 0$ (position [A], fig. 1-10). At this flux bias, the critical current of the SQUID is maximum, and the SQUID essentially behaves like a single junction. The magnitude spectrum evolves from a symmetric Lorentzian shape to an asymmetric shape with a discontinuity. The asymmetric spectrum leans towards the *lower* frequency side, indicating that *the effective inductance over an oscillation period is higher.* The phase spectrum experiences a 180° shift at the resonant frequency. At low current biases and thus in the linear regime, the phase shift is continuous with frequency and has a finite slope at resonance that is limited by the quality factor. In the nonlinear case, the phase spectrum exhibits a discontinuity similar to the magnitude spectrum.

At different flux biases, the shape of the resonant spectrum evolves from the linear to the nonlinear regime in different ways. Fig. 1-12 compares the results at three different flux biases with increasing input power. At $\Phi = 0.5\,\Phi_o$ (position [C], fig. 1-10), the resonant response

is also linear in the low power limit. As the input power increases, the resonant spectrum becomes increasingly asymmetric. However unlike the case at $\Phi = 0$, the magnitude and phase spectra bend towards the higher frequency side. *The bend of the resonant spectrum towards the higher frequency side suggests that the effective inductance of the SQUID over an oscillation period decreases at this flux bias.* Finally, intermediate behavior is shown for $\Phi = 0.3\,\Phi_o$ (position [B]).

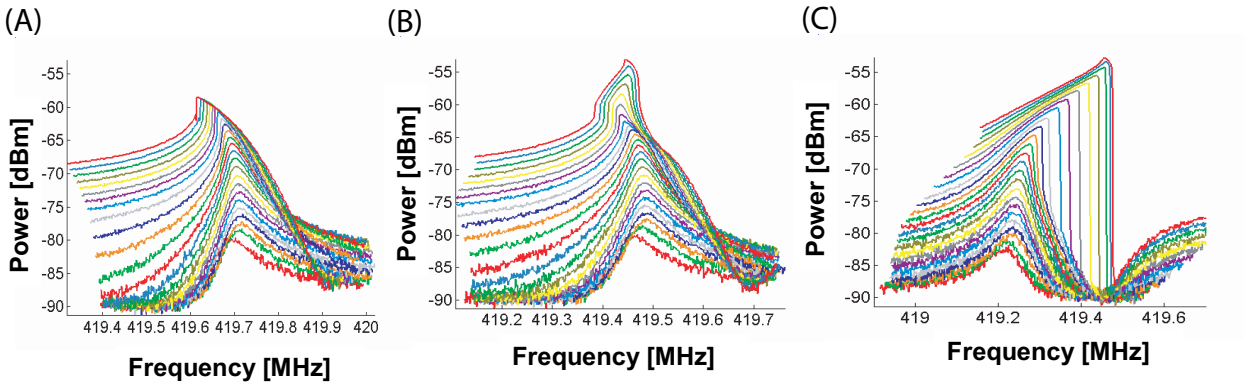

Figure 1-12: Evolution of the magnitude spectrum with increasing input power. The data are shown for three different flux biases: (A) $\Phi = 0$, (B) $\Phi = 0.3\,\Phi_o$, and (C) $\Phi = 0.5\,\Phi_o$

1.3.6 Comparison of simulations with experimental data

One major focus of this thesis is to understand the nonlinear behavior of the resonant circuit due to the SQUID inductor. The magnitude and phase spectra shown in fig. 1-13 were obtained based on the analysis of a single junction. The development of the nonlinear behavior as the drive increases is compared to the experimental data at zero flux bias. The discontinuity observed experimentally in the resonant spectra occurs in the *bifurcation region*, over which the system has multiple solutions.

To analyze the resonant behavior of an AC-driven circuit comprising a SQUID, one needs to numerically solve the differential equations governing the SQUID consistently with the equations governing the rest of the circuit. The numerical simulations can be difficult due to the complexity of the set of coupled differential equations. By developing and analyzing a series of circuit models, we showed that the resultant nonlinear behavior is due to competing

effects from the current bias and the flux bias of the SQUID. We were able to qualitatively reproduce the data when *the nonlinear effect was dominated by the flux bias.* The results shown in fig. 1-14 are based on a circuit model where the SQUID is coupled to an external flux source which will be described in section 5.6.

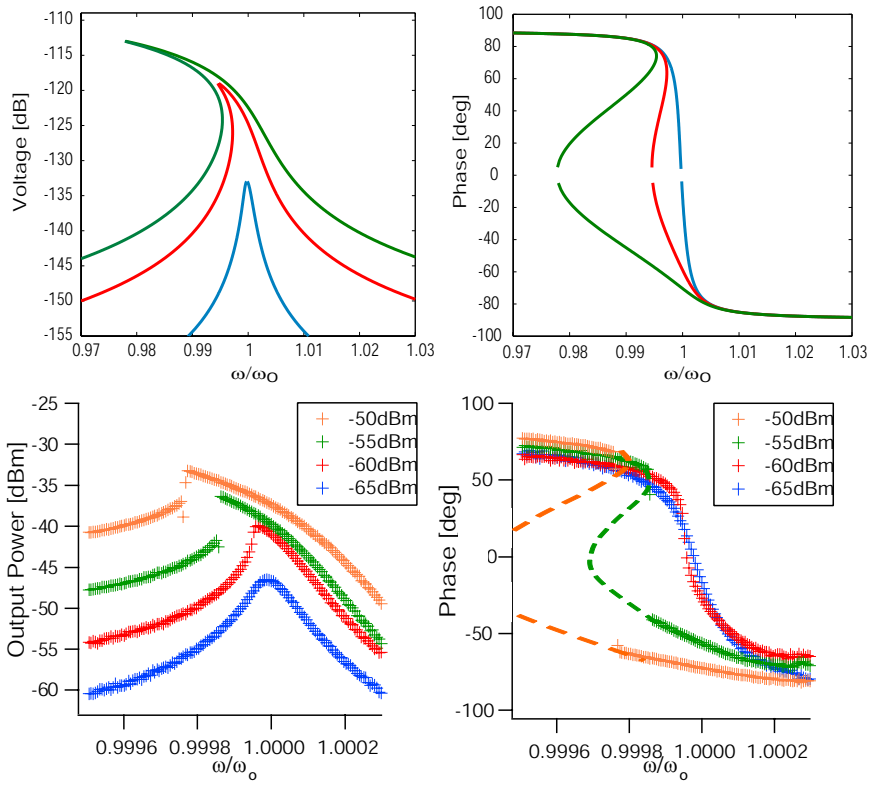

Figure 1-13: Comparison of the magnitude and phase spectra based on the simulations of a single junction (top) with experimental data (bottom) as a function of increasing bias.

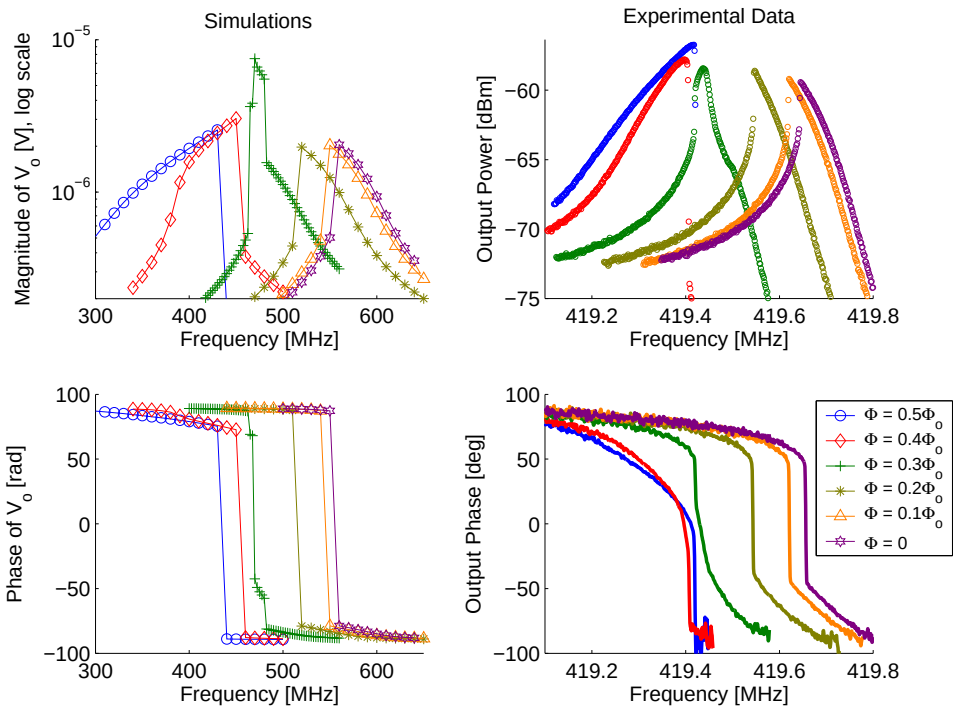

Figure 1-14: Comparison of simulation results with experimental data of the nonlinear spectra at different flux biases. The simulations were based on a circuit model in which the SQUID is coupled to an external flux source. The simulation results qualitatively reproduce the evolution of the peak bending from one frequency side to another.

1.4 Organization of Thesis

This thesis is organized in the following way: the first chapter has provided some background information on quantum computing, with an emphasis on the superconductive approach to implement qubits. An overview of the main results in this thesis work was also presented.

Chapter 2 begins with a discussion of the Persistent Current (PC) Qubit. We will derive the Hamiltonian of the qubit, and show that the two lowest energy states correspond to persistent currents circulating in opposite directions of the qubit loop. We will then switch focus to the readout of the qubit states using a SQUID magnetometer. The conventional readout scheme will first be discussed, followed by some recent experimental results that we obtained based on this readout approach. We then motivate and discuss the principles of the resonant readout scheme, which is the main focus of this work.

Chapters 3 and 4 are the experimental core of this thesis. Chapter 3 describes the

experimental implementation of the resonant readout such as the design of the on-chip resonant circuit, as well as the measurement setup for the electronics and the cryostat. An overview of the niobium fabrication process at MIT Lincoln laboratory will also be discussed. We then present the experimental results of qubit readout using the resonant scheme at 300 mK. Chapter 4 focuses on the characterization of the readout circuit in the nonlinear regime.

Chapter 5 is the simulations chapter which is closely tied to chapter 4. The focus of chapter 5 is to understand the nonlinear resonant behavior of the readout circuit. Results from numerical simulations based on resonant circuits comprising Josephson junctions will be presented.

Finally, we conclude this thesis work in chapter 6 by highlighting some of the main results, and by discussing the future direction of this work.

Chapter 2

Readout Methods for Persistent Current Qubits

Abstract

This chapter begins with a quantum mechanical description of the Persistent Current Qubit (PC Qubit). The logical states of the qubit are represented by oppositely circulating currents in the qubit loop. The focus of the discussion is then switched to the readout of the qubit state using a SQUID magnetometer. We will first discuss a conventional method in which the SQUID is operated as a switching-current detector. Some recent experimental results based on this readout approach will be presented. We then motivate a dispersive resonant readout scheme where we operate the SQUID magnetometer as a flux-sensitive inductor.

2.1 Persistent Current Qubit

The design of the Persistent Current Qubit (PC Qubit) was originally proposed in [30, 31]. It is a superconducting loop interrupted by three Josephson junctions, two of which have the same critical current I_c while the third junction has a critical current scaled down by a factor of $\alpha \simeq 0.8$. The circuit schematic of the qubit and the picture of an actual device are shown in fig. 2-1. The main advantage of the PC qubit over its one-junction or two-junction counterparts is that the loop area can be made small to minimize its coupling to environmentally induced noise. The presence of the third junction contributes to the inductance required to map the qubit energy to a double-well potential, which otherwise needs to be contributed by a large geometric inductance in the qubit loop [18].

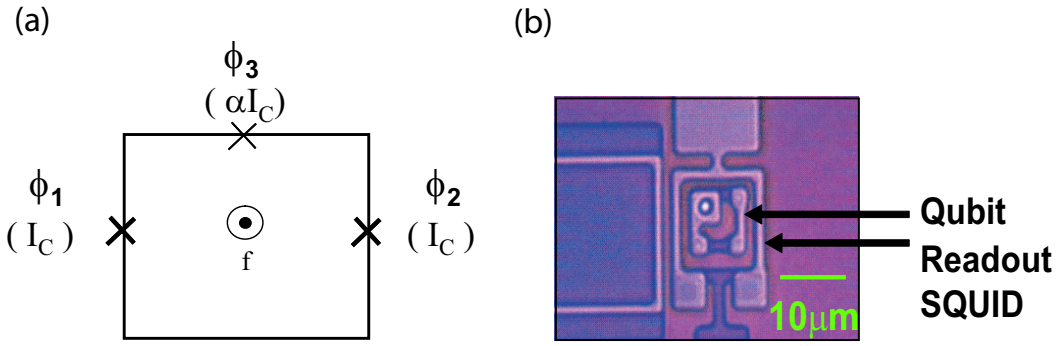

Figure 2-1: (a) Schematics of the persistent current qubit. The symbol 'X' denotes a Josephson junction. Junctions 1 and 2 have the same area while junction 3 is a factor of α smaller. An external magnetic flux f threads the qubit loop and determines its operating point. (b) Optical micrograph of a niobium qubit coupled to a readout SQUID fabricated at MIT Lincoln Laboratory.

Each Josephson junction in the qubit loop is characterized by the variable φ, which is the gauge invariant phase difference between the two superconductors on each side of the tunnel junction. The current-phase relation and the voltage-phase relation for a Josephson junction are given by:

$$I = I_c \sin\varphi \tag{2.1}$$

$$V = \frac{\Phi_o}{2\pi}\frac{d\varphi}{dt} \tag{2.2}$$

where Φ_o is a flux quantum and has the value of $h/2e = 2.0679 \times 10^{-15}$ Wb. It can be derived from this relation that the energy of the junction is given by:

$$E = E_J(1 - \cos\varphi) \tag{2.3}$$

where E_J is the Josephson energy equal to $\Phi_o I_c/2\pi$.

2.1.1 Hamiltonian of PC Qubit

We will now consider the energy of the PC qubit system. We choose the potential energy to be the sum of the Josephson energies of the three junctions in the qubit loop:

$$U(\varphi_1, \varphi_2, \varphi_3) = E_J(1 - \cos\varphi_1) + E_J(1 - \cos\varphi_2) + \alpha E_J(1 - \cos\varphi_3) \tag{2.4}$$

During operations, one applies an external magnetic flux which threads the loop. It is convenient to define a parameter $f = \Phi_{ext}/\Phi_o$, where Φ_o is a flux quantum. It is essentially a normalized flux and is sometimes known as the magnetic frustration. The fluxoid quantization relation is given by:

$$\varphi_1 - \varphi_2 + \varphi_3 = -2\pi f \tag{2.5}$$

The loop inductance of the qubit is assumed to be negligible in the fluxoid relation. Notice that the fluxoid quantization equation relates the phases of the junctions, so the potential energy in eqn. 2.4 is reduced to a function of two variables φ_1 and φ_2:

$$U(\varphi_1, \varphi_2) = E_J(2 + \alpha - \cos\varphi_1 - \cos\varphi_2 - \alpha\cos(2\pi f + \varphi_1 - \varphi_2)) \tag{2.6}$$

The potential landscape is controlled by the magnetic frustration $f = \Phi_{ext}/\Phi_o$, as well as the fabrication parameter α. It corresponds to a two-dimensional periodic potential for f near 1/2 and is shown in fig. 2-2 [31]. We are mostly interested in the double well along the $L_{oo} - R_{oo}$ trajectory. The tilt of the double well is controlled by the flux f, while the classical energy barrier ΔU is controlled by α. The kinetic energy of a particle in this double-well

potential corresponds to the charing energy of the capacitance across the junction:

$$T(\varphi_1, \varphi_2) = \frac{1}{2}CV_1^2 + \frac{1}{2}CV_2^2 + \frac{1}{2}\alpha CV_3^2 \tag{2.7}$$

$$= \frac{1}{2}C\left(\frac{\Phi_o}{2\pi}\right)^2 [\dot{\varphi}_1^2 + \dot{\varphi}_2^2 + \alpha(\dot{\varphi}_2 - \dot{\varphi}_1)^2] \tag{2.8}$$

where we have used the Josephson voltage relation from eqn 2.2. With a change of basis from $\{\varphi_1, \varphi_2\}$ to $\{\varphi_p, \varphi_m\}$, where $\varphi_p = (\varphi_1 + \varphi_2)/2$ and $\varphi_m = (\varphi_1 - \varphi_2)/2$, we can write out the Hamiltonian of the qubit as:

$$H(\varphi_p, \varphi_m) = \frac{P_p^2}{2M_p} + \frac{P_m^2}{2M_m} + E_J[2 + \alpha - 2\cos\varphi_p \cos\varphi_m - \alpha\cos(2\pi f + 2\varphi_m)] \tag{2.9}$$

where the momenta are given by $P_p = M_p\dot{\varphi}_p$ and $P_m = M_m\dot{\varphi}_m$, and the masses by $M_p = (\Phi_o/2\pi)^2 2C$ and $M_m = (\Phi_o/2\pi)^2 2C(1 + 2\alpha)$.

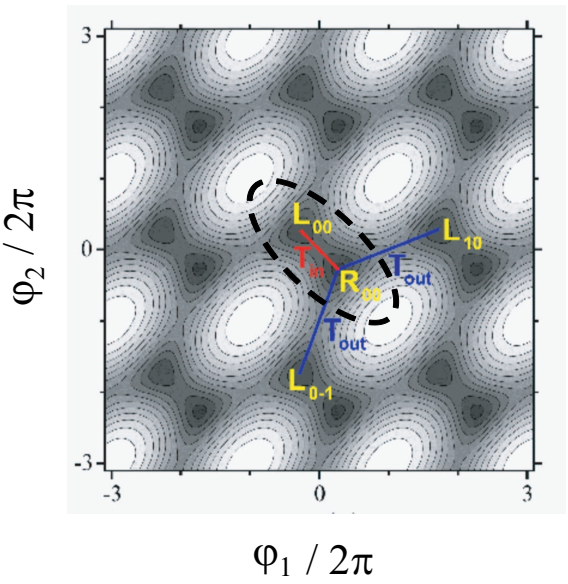

Figure 2-2: Potential landscape U(φ_1, φ_2) of the PC qubit for $f = \frac{1}{2}$ and $\alpha = 0.8$. We are mostly interested in the double-well potential along the $L_{oo} - R_{oo}$ trajectory. Tunneling between neighboring unit cells is suppressed for the given design parameters [30, 31].

The relative size of the potential energy compared to the charging energy of the qubit determines its quantum mechanical behavior. This is usually measured by the ratio E_J/E_c,

where $E_J = \Phi_o I_c/2\pi$ is the Josephson energy and $E_c = e^2/2C$ corresponds to the coulomb energy of a single charge. For the persistent-current qubit, E_J/E_c is about 100, in which case we can say the flux/phase variable is well-defined. For the charge-based qubits, E_J/E_c is usually on the order of 0.1, in which case the charge variable is well-defined.

To treat the PC qubit system quantum mechanically, we define the following operators in phase space:

$$\hat{\varphi} = \varphi \tag{2.10}$$

$$\hat{P_\varphi} = \frac{\hbar}{i}\frac{\partial}{\partial\varphi} \tag{2.11}$$

which are analogous to the position operator $\hat{x} = x$ and momentum operator $\hat{P} = (\hbar/i)\partial/\partial x$ in real space. Thus the Hamiltonian operator for the qubit can be obtained based on eqn. 2.9:

$$\hat{H} = \frac{-\hbar^2}{2M_p}\frac{\partial^2}{\partial\varphi_p^2} - \frac{\hbar^2}{2M_m}\frac{\partial^2}{\partial\varphi_m^2} + E_J[2 + \alpha - 2\cos\varphi_p\cos\varphi_m - \alpha\cos(2\pi f + 2\varphi_m)] \tag{2.12}$$

The 2-d Schrodinger's equation was solved numerically for the eigenenergies and eigenfuctions [31]. The wavefunction can be expressed as a superposition of plane waves, but for the analysis here in phase space, it turns out to be more natural to have the basis functions as impulses:

$$\Psi = \sum_n c_n\phi_n \tag{2.13}$$

$$\phi_n = \delta[\varphi_p - \varphi_{po}]\delta[\varphi_m - \varphi_{mo}] \tag{2.14}$$

The first five energy states and the corresponding eigenfunctions for a qubit with parameters $\alpha = 0.7$, $I_c = 0.5\mu A$ are shown in fig 2-4. The expectation value of the circulating current is given by the slope of the energy levels in flux, $\langle I_p\rangle = \partial E/\partial f$. For values of f near 1/2, the two lowest energy states have opposite slopes, corresponding to persistent currents circulating in opposite directions in the qubit loop. These two persistent current states are chosen as the logical states of the qubit.

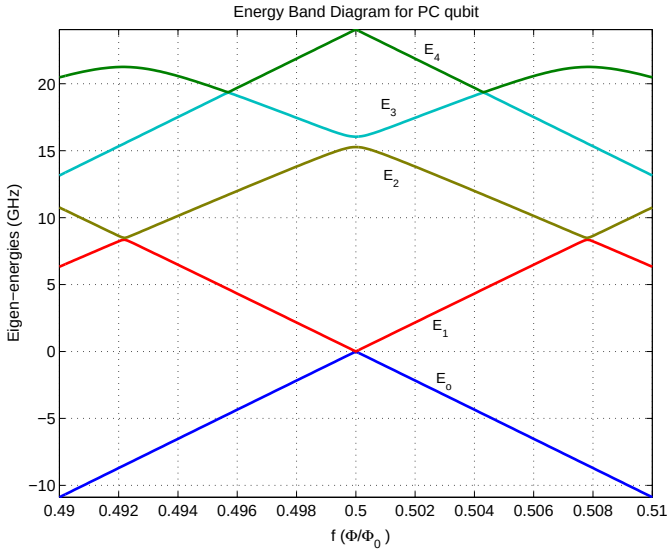

Figure 2-3: The eigen-energies for the five lowest states of a PC qubit near f=1/2. The parameters used were $I_c \approx 0.5\,\mu A$, $\alpha = 0.7$. The energy separation $E_1 - E_o$ at f=1/2 is around 20 MHz.

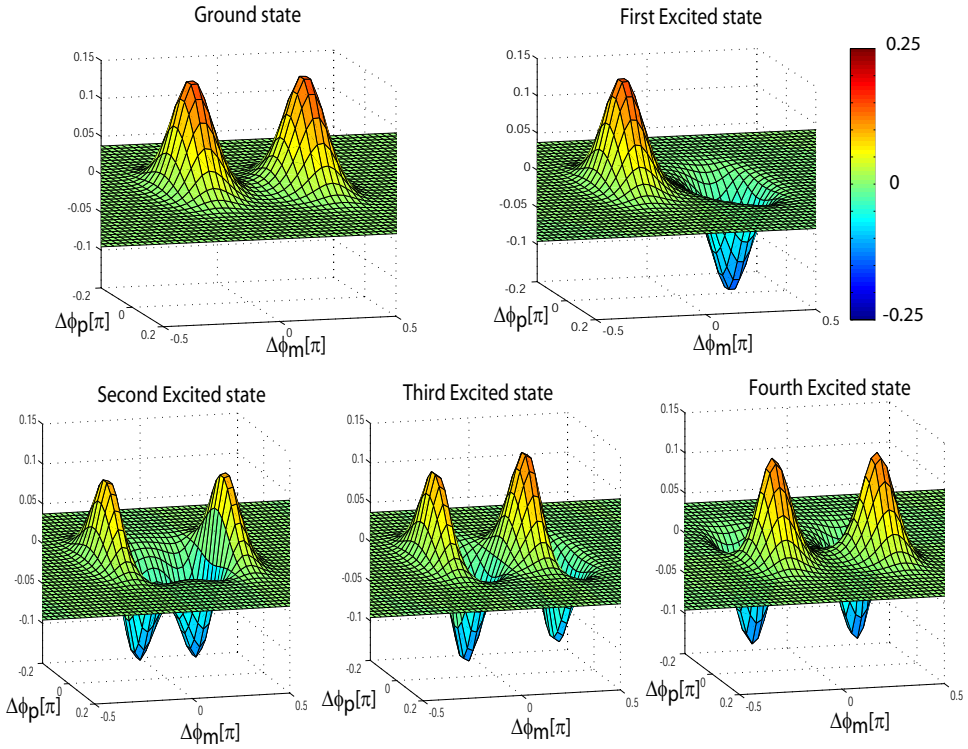

Figure 2-4: Eigenfunctions for the five lowest states at f=1/2 for $I_c \approx 0.5\,\mu A$ and $\alpha = 0.7$. The ground and first excited states are symmetric and anti-symmetric combinations of the basis states that are localized in the left and right potential wells.

2.1.2 Tight-Binding Model

In the tight-binding model, the wavefunction of the qubit is approximated by the first two eigenfunctions in the double-well potential along the $L_{oo} - R_{oo}$ trajectory in fig. 2-2. In the cases for $f < 1/2$ or $f > 1/2$, the double well is tilted such that one well is higher than the other. The first two eigenfunctions in these cases correspond to states localized in the left and right potential wells. At f=1/2, the eigenfunctions are the symmetric and the anti-symmetric combinations of the localized states. This is illustrated in fig. 2-5.

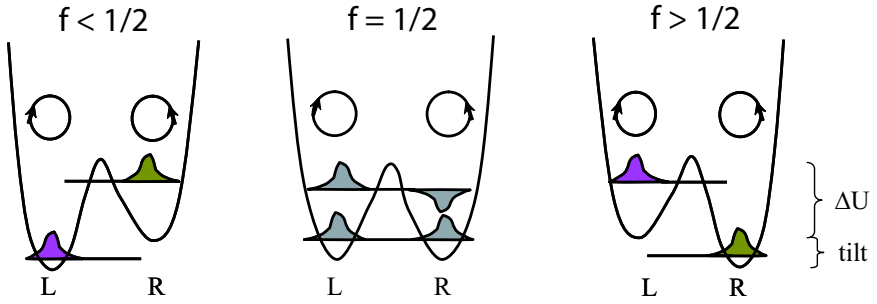

Figure 2-5: Illustration of the double well along the $L_{oo} - R_{oo}$ trajectory. The classical energy barrier ΔU is controlled by α, and the extent of the tilt is controlled by f. The eigenfunctions approximated by the tight-binding model are shown with the vertical shift corresponds to a difference in eigenenergies. The occupancy in the left and right well corresponds to oppositely circulating current states.

If we choose the basis states to be the eigenfunctions localized in the left and right well, the Hamiltonian of the PC qubit can be written as a 2 by 2 matrix:

$$H_{PC} = \begin{bmatrix} \Phi_o I_p (f - \frac{1}{2}) & -\tau \\ -\tau & -\Phi_o I_p (f - \frac{1}{2}) \end{bmatrix} \tag{2.15}$$

where I_p is the classical circulating current of the qubit, and τ is the tunnel splitting determined by the overlap between the eigenfunctions. We recognize that eqn. 2.15 has the same form as the Hamiltonian for any two-level systems. We will therefore continue the discussions below in a more general sense which applies to any two-level system.

2.1.3 Coupling between qubit states

Probability exchange between the eigenstates of a qubit or any two-level system can be induced by energetically coupling the two states. The states can be coupled either statically, e.g., due to overlap of their probability density through a tunnel barrier; or dynamically, e.g., due to a time-dependent sinusoidal drive. In this section, we will discuss both static and dynamical coupling based on the analysis in [38].

Two-level system with static coupling

We assume the wave function of a two-level system with coupling has the general form:

$$\psi = C_1(t)\phi_1 + C_2(t)\phi_2 \tag{2.16}$$

where ϕ_1 and ϕ_2 are the basis states of the problem when there is *no* coupling, in which case the amplitude is simply given by $C_i(t) = C_i e^{-i\frac{E_i}{\hbar}t}$ where $C_i = \langle\phi_i|\psi(0)\rangle$. Note that the probability density $|C_i(t)|^2$ is time-independent. It will be shown that in the presence of coupling, $|C_i(t)|^2$ can be a function of time. First we solve the eigenstates and eigenenergies of the coupled system. This is given by the time-independent Schrodinger's equation:

$$\begin{bmatrix} -\Delta & V \\ V & +\Delta \end{bmatrix} \begin{bmatrix} C_1 \\ C_2 \end{bmatrix} = E \begin{bmatrix} C_1 \\ C_2 \end{bmatrix} \tag{2.17}$$

where we have defined the average energy $\bar{E} = (\langle\phi_1|\hat{H}|\phi_1\rangle + \langle\phi_2|\hat{H}|\phi_2\rangle)/2$ to be zero. In addition, the energy difference is $\Delta = (\langle\phi_1|\hat{H}|\phi_1\rangle - \langle\phi_2|\hat{H}|\phi_2\rangle)/2$, and the static coupling is $V = \langle\phi_1|\hat{H}|\phi_2\rangle = \langle\phi_2|\hat{H}|\phi_1\rangle^*$. The new eigenenergies are given by:

$$E_- = -\sqrt{\Delta^2 + |V|^2} \qquad\qquad E_+ = +\sqrt{\Delta^2 + |V|^2} \tag{2.18}$$

and the corresponding eigenvectors in terms of the original basis set ϕ_1 and ϕ_2 are:

$$\psi_- = \begin{bmatrix} C_1^- \\ C_2^- \end{bmatrix} = \begin{bmatrix} \cos\theta \\ \sin\theta \end{bmatrix} \qquad\qquad \psi_+ = \begin{bmatrix} C_1^+ \\ C_2^+ \end{bmatrix} = \begin{bmatrix} -\sin\theta \\ \cos\theta \end{bmatrix} \tag{2.19}$$

where θ is defined by

$$\sin 2\theta = -\frac{V}{\sqrt{\Delta^2 + V^2}} \qquad \cos 2\theta = \frac{\Delta}{\sqrt{\Delta^2 + V^2}} \tag{2.20}$$

The time evolution of the wave function in the new eigen-basis has the form:

$$\psi(t) = C_-\psi_- e^{-i\frac{E_-}{\hbar}t} + C_+\psi_+ e^{i\frac{E_+}{\hbar}t} \tag{2.21}$$

where $C_- = \langle\psi_-|\psi(0)\rangle$ and $C_+ = \langle\psi_+|\psi(0)\rangle$.

Rabi Oscillation by static coupling

Consider the case when there is finite coupling in the system, and that the wavefunction is initialized in one of the original basis states such that $\psi(0) = \phi_1$. It can be shown that the time evolution of the probability in the original states ϕ_1 and ϕ_2 is given by:

$$P_2(t) = \frac{V^2}{\Delta^2 + V^2}\sin^2\frac{\Omega t}{2} \tag{2.22}$$

$$P_1(t) = 1 - P_2(t) \tag{2.23}$$

which means that the system makes partial oscillation between the two states at a frequency Ω, which is often referred as the *Rabi frequency*:

$$\Omega = \frac{2\sqrt{\Delta^2 + V^2}}{\hbar} \tag{2.24}$$

In the limit that $\Delta = 0$, meaning that ϕ_1 and ϕ_2 were degenerate, then the oscillation becomes a full transition between the two states, where the oscillation frequency $\Omega = 2|V|/\hbar$ is only proportional to the coupling $|V|$. For instance, a π-operation is achieved when $\psi(0) = \phi_1$ is flipped to $\psi(t) = \phi_2$ at $t = \pi/\Omega$.

$$P_2(t) = \sin^2(\frac{\Omega t}{2}) \tag{2.25}$$

$$P_1(t) = \cos^2(\frac{\Omega t}{2}) \tag{2.26}$$

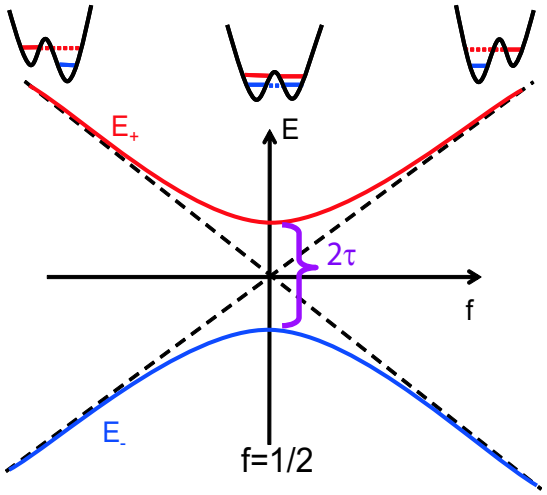

Figure 2-6: The two-level system representation of the PC qubit. The dotted line represents the energy of the uncoupled states. In the PC qubit notation, τ plays the role of coupling V, and f plays the role of the energy difference Δ. The tunnel splitting causes energy repulsion at the anti-crossing at which the uncoupled qubit states would have been degenerate.

Two-level system with dynamical coupling

Oscillation between population of the two basis states can also be caused by time-dependent sinusoidal coupling. Consider the case when the coupling $V_{12} = V_o e^{j\omega t}$ is induced by a sinusoidal source:

$$H = \begin{bmatrix} -\Delta & V_o e^{j\omega t} \\ V_o e^{-j\omega t} & \Delta \end{bmatrix} \tag{2.27}$$

It can be shown that if the system is initialized in the original basis state ϕ_1, then the probability of the system being in ϕ_2 is oscillatory in time and is given by [38]:

$$P_2(t) = \frac{(\frac{2V_o}{\hbar})^2}{(\omega - \omega_o)^2 + (\frac{2V_o}{\hbar})^2} \sin^2 \frac{\Omega t}{2} \tag{2.28}$$

where the Rabi frequency Ω now has the form:

$$\Omega = \sqrt{(\omega - \omega_o)^2 + \left(\frac{2V_o}{\hbar}\right)^2} \tag{2.29}$$

and $\hbar\omega_o = 2\Delta$ corresponds to the energy difference between the uncoupled states. When the driving frequency ω matches the energy difference ω_o, the dynamical coupling is on resonance, and there will be a complete oscillation between the two states. When the driving frequency is detuned from ω_o, then the amplitude of the oscillation falls off according to the Lorentzian lineshape.

Dynamical coupling of Qubit states for PC Qubit

For the PC qubit, population exchange between the two circulating current states can also be induced by a sinusoidal drive. Experimentally, the coupling is provided by an AC flux bias applied perpendicular to the SQUID loop. While some systems such as nuclear spins are described by Hamiltonian given in eqn. 2.27, the dynamical coupling terms for the PC qubit come in the diagonal instead of the off-diagonal terms. Recall from eqn. 2.15 that the Hamiltonian of the PC qubit is given by :

$$H = \begin{bmatrix} \Phi_o I_p(f - \frac{1}{2}) & -\tau \\ -\tau & -\Phi_o I_p(f - \frac{1}{2}) \end{bmatrix} \tag{2.30}$$

where the flux bias f is now assumed to have both DC and AC components:

$$f = f_{dc} + f_{ac}\cos\omega t \tag{2.31}$$

Let

$$F_{dc} = \Phi_o I_p(f_{dc} - \frac{1}{2}) \tag{2.32}$$

$$F_{ac} = \Phi_o I_p f_{ac} \tag{2.33}$$

Then

$$H = \begin{bmatrix} F_{dc} + F_{ac}\cos\omega t & -\tau \\ -\tau & -(F_{dc} + F_{ac}\cos\omega t) \end{bmatrix} \tag{2.34}$$

It can be shown that as long as the static coupling τ is non-zero, the sinusoidal term F_{ac} can have similar effect as an off-diagonal coupling in eqn. 2.27. This involves transforming

the Hamiltonian first from the lab frame to an eigenvalue frame for the undriven qubit, then to a co-rotating frame with angular frequency ω. By further using the rotating wave approximation (RWA) and keeping only the DC terms and neglecting the 2ω components, one can obtain an effective Hamiltonian in the co-rotating frame given by [39, 40]:

$$H_{eff} = \frac{1}{2}\begin{bmatrix} -2\sqrt{F_{dc}^2+\tau^2}-\hbar\omega & F_{ac}\sin\theta \\ F_{ac}\sin\theta & 2\sqrt{F_{dc}^2+\tau^2}+\hbar\omega \end{bmatrix} = \frac{1}{2}\begin{bmatrix} \hbar(\omega_o-\omega) & \hbar\omega_{nut} \\ \hbar\omega_{nut} & -\hbar(\omega_o-\omega) \end{bmatrix} \tag{2.35}$$

where the frequencies are given by:

$$\omega_{nut} = \frac{F_{ac}\sin\theta}{\hbar} \tag{2.36}$$

$$\omega_o = -\frac{2\sqrt{F_{dc}^2+\tau^2}}{\hbar} \tag{2.37}$$

and

$$\theta = \tan^{-1}\left(\frac{\tau}{F_{dc}}\right) \tag{2.38}$$

The nutation frequency ω_{nut} is equivalent to the on-resonance Rabi frequency. Comparing eqn. 2.36 with eqn. 2.24, the AC drive does induce a *static* coupling of size proportional to the amplitude of the drive as well as the angle given by the ratio τ/F_{dc}. If the qubit state is initialized to be [1; 0] which is the lower-energy eigenstate in the co-rotating frame, then the probability of the qubit in the higher energy state in the co-rotating frame is given by

$$P_2(t) = \frac{\omega_{nut}^2}{(\omega-\omega_o)^2+\omega_{nut}^2}\sin^2\frac{\Omega t}{2} \tag{2.39}$$

with the Rabi frequency Ω being:

$$\Omega = \sqrt{(\omega-\omega_o)^2+\omega_{nut}^2} \tag{2.40}$$

Probability between the first and second eigenstates in the co-rotating frame oscillates completely if the drive is on resonance. It can be shown that in the lab frame, the amplitude of the oscillation does not rotate completely even if the drive is on-resonance.

2.2 Readout of Qubit states: Switching Current Measurement

In the previous section, it was shown that when the PC qubit is biased with an external flux near $f = \frac{1}{2}$, the system is analogous to a particle in a two-dimensional double-well potential, and the two lowest energy eigenstates correspond to opposite circulating persistent currents in the qubit loop. These opposite circulating currents are chosen as logical states of the qubit.

To measure the state of the qubit, one recognizes that the induced flux of the persistent current either adds to or subtracts from the external background flux. The difference in the overall flux can be sensed by a SQUID magnetometer. Thus by inductively coupling the qubit to a readout SQUID, the state of the qubit can be detected. The size of the flux signal detected by the SQUID depends on the mutual inductance M between the qubit and the SQUID, and the size of the persistent current I_P within the qubit loop. The range is usually between $0.001\Phi_o$ to $0.01\Phi_o$.

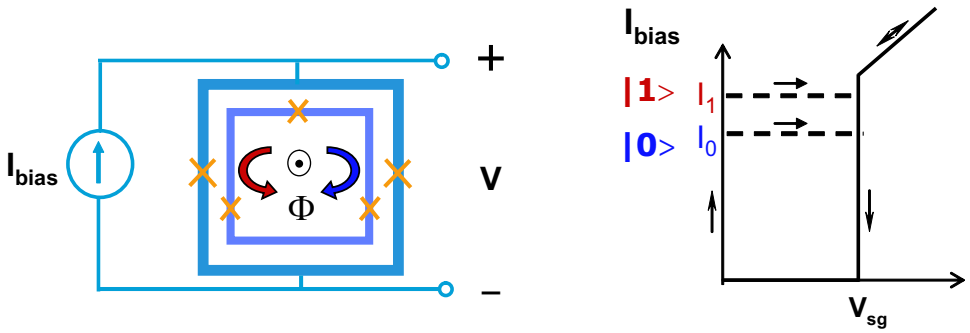

Figure 2-7: Left: The blue and red arrows represent the clockwise and counter-clockwise circulating current states of the qubit. The qubit is inductively coupled to a SQUID magnetometer. The bias current of the SQUID is ramped until the SQUID switches to the voltage state. Right: Typical I-V characteristics for the readout SQUID, which is underdamped and has a hysteretic response. Depending on the state of the qubit, the SQUID has a different switching current.

The conventional method to operate the SQUID magnetometer for qubit state detection is the so-called switching current measurement. So far, this has been the primary readout

approach used to demonstrate quantum coherence of flux qubits [17, 20]. This measurement scheme involves direct measurement of the critical current I_c of the SQUID, which is a periodic function of the external flux. Depending on the qubit state, the readout SQUID senses a difference in magnetic flux which corresponds to a different switching current value.

2.2.1 Switching current of a DC SQUID

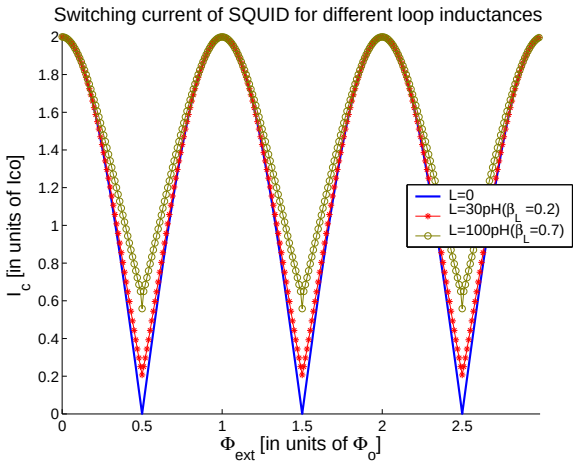

Figure 2-8: Flux dependence of I_c for a SQUID with different loop inductances. I_c is maximum at integrals of Φ_o, and is minimum at half integrals of Φ_o. The amount of modulation of I_c decreases when the SQUID has a larger loop inductance.

For the case when the SQUID has negligible loop inductance, the critical current I_c is given by:

$$I_c(\Phi) = 2I_{co}\left|\cos\left(\frac{\pi\Phi_{ext}}{\Phi_o}\right)\right| \tag{2.41}$$

where I_{co} is the critical current of a single junction, and Φ_{ext} is the external magnetic flux. When the loop inductance of the SQUID has to be taken into consideration, one has to simultaneously solve the current continuity equation (eqn. 2.42) and the fluxoid quantization equation (eqn.2.43):

$$I = I_{co}\sin\varphi_1 + I_{co}\sin\varphi_2 \tag{2.42}$$

$$0 = \varphi_1 - \varphi_2 + \frac{2\pi L I_{co}}{\Phi_o}(\sin\varphi_1 - \sin\varphi_2) + \frac{2\pi\Phi_{ext}}{\Phi_o} \tag{2.43}$$

where φ_1 and φ_2 are the gauge invariant phases of each Josephson junction, and L is the loop inductance of a SQUID arm. I_c can then by obtained numerically by maximizing eqn. 2.42 with respect to one of the phase variables φ_1 or φ_2. The flux dependence of I_c is plotted in fig. 2-8 for a SQUID with different loop inductances. The critical current is suppressed to zero at half integrals of Φ_o only when the loop inductance is zero.

Experimentally, the measured switching current of the SQUID is always less than I_c due to thermal noise fluctuations [41, 42, 43]. By repeating the measurements of the switching current many times, one usually obtains a switching current distribution with a standard deviation that decreases with temperature. A fit to the shape of the switching current distribution can be used to extract the temperature of the device.

2.2.2 Slow measurement of qubit: recording switching current explicitly

We will first describe a *slow* experimental scheme to measure the switching current. At t=0, one linearly ramps the bias current through the SQUID to a value greater than I_c. Then a counter is used to record the time elapse it takes for the SQUID to switch from the zero-voltage state to the finite voltage state [1]. Thus in this measurement scheme, one actually measures a switching time which is then converted to a switching current according to the ramp rate of the bias. This is depicted in fig. 2-9. Depending on the state of the qubit, one measures a switching time of t_o or t_1 which corresponds to a switching current of I_o or I_1. The measurement timescale is on the order of 10 ms.

The switching current measurement is then repeated 1000 times to obtain a probability distribution, from which the average switching current is determined. Fig 2-10 shows the typical results for the average switching current as the magnetic flux is varied. The switching current shows a similar periodic dependence with flux as in fig. 2-8, and the periodicity corresponds to Φ_o for the SQUID. At every period of $1.5\,\Phi_o$, discrete jumps in the switching current were observed, and these corresponded to a small change in flux signal produced

[1] The counter starts timing at t=0, and stops when the SQUID switches and thus has a voltage above the user-defined threshold, which is set slightly below the subgap voltage of the SQUID. The counter essentially acts as a timer and a voltage comparator.

by the qubit. These so-called qubit steps occur near a flux bias of $f \sim 1/2$ for the qubit. Referring to the double-well potential picture in fig 2-5, as f is changed near 1/2, the qubit has to change from one circulating current state to another in order to follow the lowest energy state of the system. This results in an overall change in flux signal detected as a qubit step.

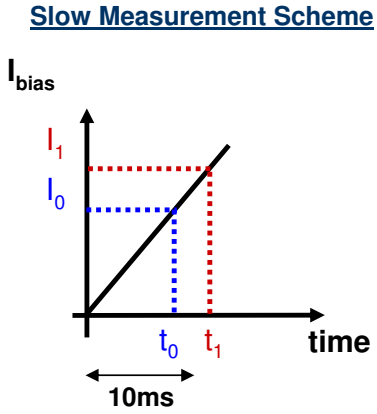

Figure 2-9: Current bias scheme for the SQUID in the slow measurement. The current is linearly ramped to sightly above the switching current level. Experimentally, we measure the switching time which is then converted to a switching current according to the ramp rate. Typical timescale is on the order of 10 ms.

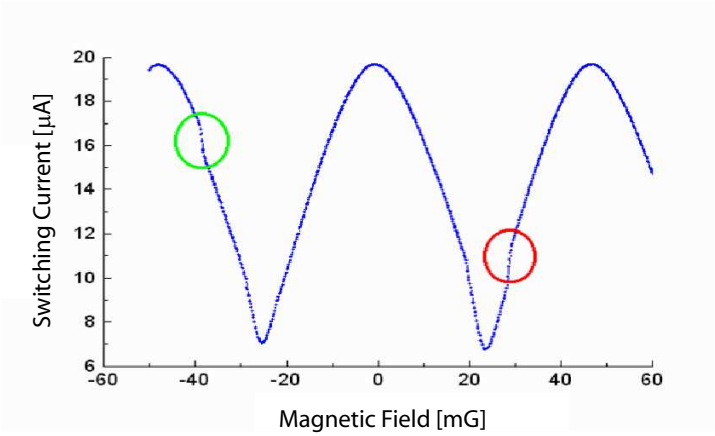

Figure 2-10: Typical results for the mean switching current of a SQUID versus magnetic flux bias. The steps in the plot correspond to when the qubit changes from one classical current state to another. The results were taken at 300 mK. This particular SQUID sample has a relatively large I_c, thus the size of the qubit steps are more easily observed [44].

2.2.3 Fast measurement of qubit: recording the presence or absence of a switching event

In order to follow the quantum dynamics of the qubit, one has to be able to perform qubit readout on a timescale faster than the coherence time of the qubit. We will now describe a *fast* measurement scheme which can be performed on a μs timescale. The bias scheme for the SQUID is depicted in fig. 2-11. The current pulse is first kept at a sample current I_s for 20 ns, then decreased to a hold current I_h for about $20\mu s$. The sample current was chosen to be between the switching currents for the two qubit states I_o and I_1, such that if the qubit is in the $|0\rangle$ state, a zero output voltage or an *absence* of a switching event will be recorded. On the other hand, if the qubit is in the $|1\rangle$ state, a finite output voltage or a *presence* of a switching event will be recorded. Thus the switching current is not measured explicitly at each measurement, but can be obtained after a series of measurements as I_s is gradually increased over the range between I_o and I_1.

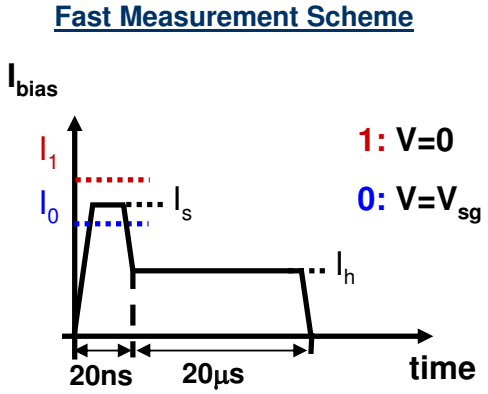

Figure 2-11: Current bias pulse for the SQUID in the fast measurement scheme. The bias level is first held at a high sample current I_s for 20 ns, during which the presence or absence of a switching event is determined. The bias is then held at a lower hold current I_h for 20 μs which allows the voltage signal to be read at a slower rate.

This can be illustrated more clearly by referring to fig. 2-12, which is a zoom-in on the qubit step region obtained from the fast measurement scheme. We will first focus on the qubit step background and will return to the pair of spectroscopy peaks in a subsequent discussion. This 2-d plot shows data taken over the parameter space spanned by the sample

current and the magnetic flux bias. A dark blue data point represents the absence of a switching event ($P_{sw} = 0$), and a dark red data point represents the presence of a switching event ($P_{sw} = 1$). Since the measurements were repeated 1000 times at a given sample current and flux bias, a switching probability P_{sw} can be obtained anywhere between 0 and 1. This is indicated by the color axis. On the left side of the qubit step, the qubit is in the $|1\rangle$ state which corresponds to a high switching current I_1 for the SQUID. As the sample current I_s is gradually increased from below I_1 to above I_1, P_{sw} gradually changes from 0 to 1 (from blue to red). The actual value of I_1 can be extracted from the level where P_{sw} is near 50%. Similarly, on the right side of the qubit step, the qubit is in the $|0\rangle$ state. The probability of switching gradually changes from 0 to 1 as the sample current passes the level of I_0. Note that P_{sw} is the cumulative distribution function, thus the probability of switching in an interval ΔI_s can be obtained from the derivative $\partial P_{sw}/\partial I_s$.

The state of the qubit is measured during the sampling portion of the current pulse. The pulse was then held at I_h for a longer time so that the output voltage can be detected through the slow signal lines. This relies on the fact that after a switching event for an underdamped SQUID, the current bias has to be decreased to zero before the voltage is also returned to zero (see I-V curve in fig. 2-7). Using our experimental setup as an example, the current bias is sent down a coaxial cable with a bandwidth of about 1 GHz, while the output voltage is detected through DC signal lines.

2.2.4 Qubit spectroscopy and coherent dynamics

Spectroscopy of Qubit states

In section 2.1.3, we have discussed that population transition between the 0 and 1 states of the qubit can be induced by an AC flux bias $f_{ac} \cos \omega t$ coupled to the qubit. In particular, when the frequency of the AC drive matches the difference between the eigenenergies of the qubit, population will oscillate coherently between the two qubit states, and this phenomenon is known as Rabi oscillation. Experimentally, the amplitude of the oscillation decays exponentially with the time constant given by the coherence time of the qubit. If the measurement of the qubit is not performed within the coherence time, the transitions become incoherent in phase, and one will observe a population of 50% in both qubit states.

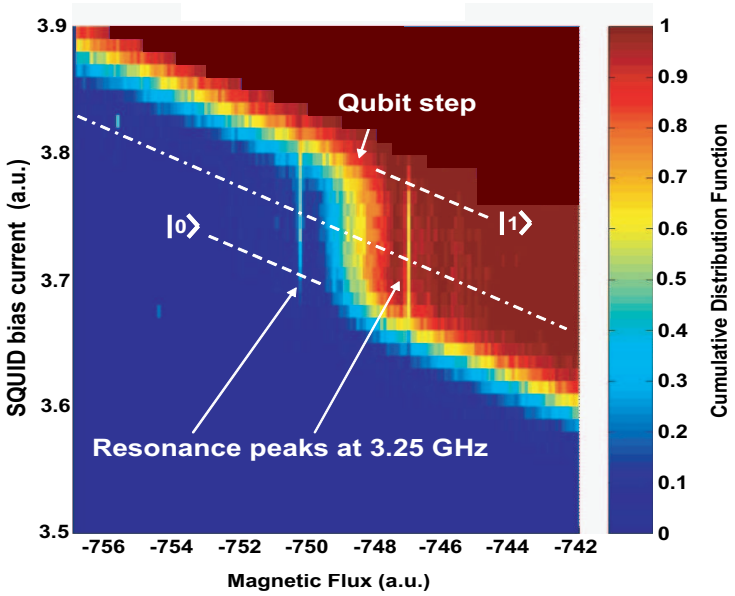

Figure 2-12: Measurement of the qubit step using the fast measurement scheme. Data were taken at dilution refrigerator temperatures $\sim$ 10 mK. The pair of resonance peaks correspond to incoherent excitation from the ground state to the first excited state by microwave radiation at 3.25 GHz. Spectroscopy of the qubit energy band structure was obtained by varying the driving frequency and keeping track of the flux bias at which the resonance peak occurred [45].

Referring back to the qubit step in fig. 2-12, the pair of resonance peaks correspond to incoherent transition between the ground state and the first excited state induced by microwave radiation. The resonance peak occurs when the energy difference between the qubit states is matched by the driving frequency. Note that the population in the driven states is in fact 50% as indicated by the color scale. Spectroscopy of the qubit energy band structure such as that in fig. 2-3 can be obtained by varying the driving frequency and keeping track of the flux bias at which the resonance peak occurs [45]. We observed avoided crossing in the energy band between the third and fourth excited states E_3 and E_4 [2].

[2]The avoided crossing between the ground state and the first excited state cannot be observed, given that the persistent current vanishes at f=1/2.

Quantum coherence of qubit: Landau-Zener transitions

When the qubit is driven by a strong AC flux bias $f_{ac}\cos\omega t$, such that f_{ac} is much larger than the dc flux bias f_{dc}, multiple-photon transitions between the qubit states were observed. Fig. 2-13 shows the multiple resonance peaks where the n-th peak away from the qubit step corresponds to an n-photon transition. In this strongly driven regime, the transition between the qubit states occurs by means of Landau-Zener transition. It can be shown that by transforming the qubit Hamiltonian to a nonuniform rotating frame [3], the effective Hamiltonian has the form [46]:

$$H_{eff} = \begin{bmatrix} -F & -\tau e^{-in\omega t} J_n(\lambda) \\ -\tau e^{-in\omega t} J_n(\lambda) & F \end{bmatrix} \tag{2.44}$$

where $F = \Phi_o I_p (f_{dc} - 1/2)$. Note that the coupling between the qubit states has a Bessel function dependence. As a result, the area under the n-th resonance peak varies with the amplitude of the AC drive according to the Bessel function $J_n(\lambda)$, where λ is the normalized AC amplitude given by $\lambda = \Phi_o I_p f_{ac}/\hbar\omega$, and n corresponds to the number of photons. A fit to the inhomogeneous broadening of the resonance peaks can be used to extract the coherence time of the qubit. The relaxation time T_1 and the dephasing time T_2 based on the single-photon and the 5-th photon transitions are extracted to be on the order of $10\,\mu s$ and $10\,ns$ respectively [46].

Drawbacks of the Switching Current Readout

The switching current readout operates the SQUID magnetometer as a switching detector. By explicitly measuring the switching current of the SQUID (for the slow scheme) or the presence or absence of a switching event (for the fast scheme), the circulating current state of the qubit can be determined. This approach involves high current bias which is on the order of I_c, and it switches the SQUID from the superconducting state to the voltage state. While quantum coherence of superconducting qubits have been demonstrated using the switching current readout, the coherence times remain short and are on the order of 0.1

[3] The nonuniform rotating frame has an oscillating phase of $\lambda\sin\omega t$, where λ is the normalized AC amplitude given by $\lambda = \Phi_o I_p f_{ac}/\hbar\omega$. Conventional rotating frame has a phase of ωt

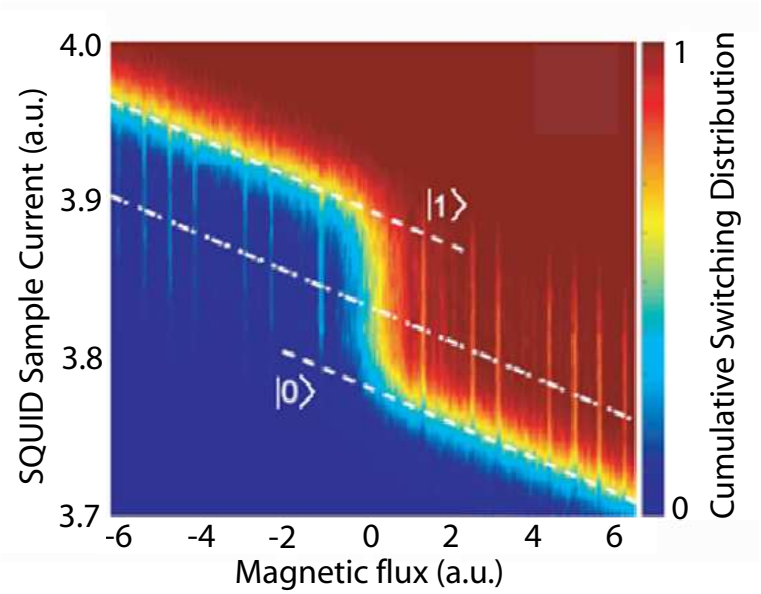

Figure 2-13: Multiple resonances corresponding to multi-photon transitions between the $|0\rangle$ and $1\rangle$ states. The n-th resonant peak away from the qubit step corresponds to an n-photon transition. The area under the n-th peak varies with microwave amplitude according to the Bessel function $J_n(\lambda)$, where λ is the normalized microwave amplitude given by $\Phi_o I_p f_{ac}/\hbar\omega$.

to $1\,\mu s$ [17, 21, 22]. The noise introduced through the readout circuitry is believed to be one of the most dominant sources of decoherence. When evaluating the switching current readout approach, one generally finds the following sources of decoherence to be addressed:

1. High bias currents through the readout SQUID are associated with high level of decoherence. To understand this, we know that the broadband noise from the bias lines is introduced in the current that is symmetrically divided in the two branches of the SQUID. The qubit, on the other hand, is coupled to the circulating current in the SQUID loop. It has been shown that the symmetric current and the circulating current are completely decoupled at zero bias current, and that the coupling strength is directly proportional to the size of the bias current [32]. Since the switching current readout involves high current bias, noise is coupled strongly from the bias lines to the qubit.

2. The switching of the SQUID to the voltage state excites a large number of quasiparticles, which must then be allowed to relax to the superconducting state before

another measurement can be performed. This relaxation time can be fairly long and may restrict the repetition rate of the readout [33].

3. As the current for the SQUID is rapidly ramped to a bias level on the order of I_c during the fast measurement scheme, it introduces higher frequency components which are also coupled to the qubit. This may cause undesirably excitation of the qubit into the higher energy states. For our experiments, the waiting time between subsequent measurements is usually on the order of 1 to 10 ms to ensure the qubit is completely relaxed and initialized in the ground state [47].

2.3 Readout of Qubit States: Resonant Circuit Measurement

The resonant readout was implemented to reduce the sources of readout-induced decoherence for the qubit. The main idea is to operate the SQUID magnetometer as a flux-sensitive inductor, rather than a switching-current detector. It will be shown that the Josephson inductance of a SQUID is a periodic function of the external flux. Thus, by incorporating the readout SQUID in a high-Q resonant circuit, the state of the qubit can be determined from the inductance of the SQUID, which in turn can be measured from the resonant frequency of the readout circuit with high sensitivity. Similar approaches have also been investigated by [24, 25] for the flux qubit, [27] for the hybrid qubit, and [28] for the charge qubit.
This non-dissipative approach biases the SQUID at low currents and does not require the SQUID to switch to the voltage stage. Some of the main advantages are:

1. The low current bias reduces the coupling between the symmetric and the circulating currents of the SQUID, hence minimizes the noise from the bias lines coupled to the qubit and decreases the level of decoherence.

2. Given that the SQUID does not switch to the voltage state, the number of quasiparticles is drastically reduced.

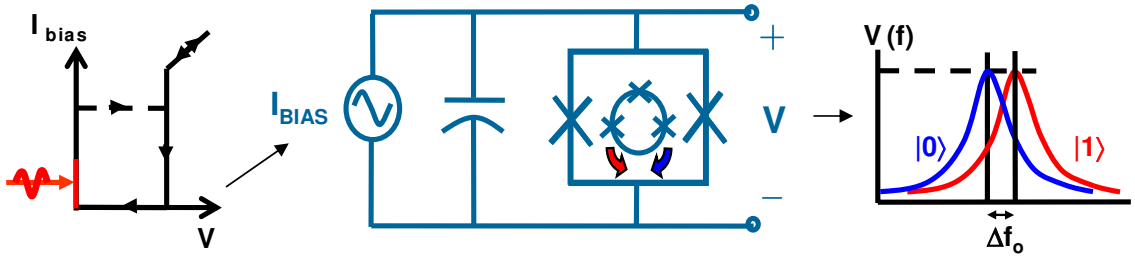

Figure 2-14: In the resonant readout scheme, the SQUID is operated as a flux-sensitive inductor and is incorporated in a high-Q resonant circuit. A change in qubit state is detected as a shift in the resonant frequency of the readout circuit. The advantage of this non-dissipative scheme is that the current bias for the SQUID can be kept significantly below the critical current level.

3. The resonant readout approach naturally provides a narrow-band filtered electrical environment that shields the qubit from broadband noise.

2.3.1 Josephson inductance of a DC SQUID

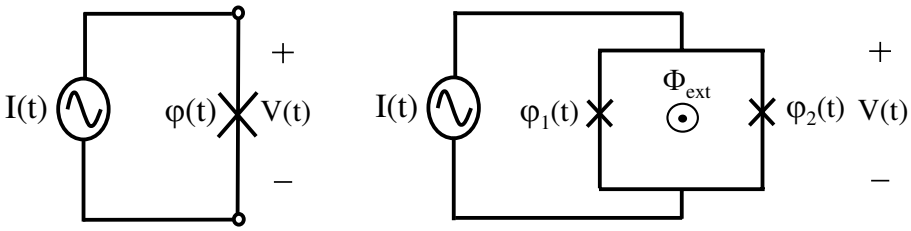

Figure 2-15: Circuit schematics of a single Josephson junction (left) and a SQUID (right).

Recall a Josephson junction is governed by the current-phase relation and the voltage-phase relation:

$$I(t) = I_{co} \sin \varphi(t) \tag{2.45}$$

$$V(t) = \frac{\Phi_o}{2\pi} \frac{d\varphi(t)}{dt} \tag{2.46}$$

where $\varphi(t)$ is the gauge-invariant phase of the junction. The constitutive relation for an

inductor is given by

$$V(t) = \frac{d[L(t)i(t)]}{dt} \tag{2.47}$$

where $L \times i$ corresponds to the flux through the inductor. This definition is applicable for the general case when the inductor is nonlinear [4]. If we substitute in the current and voltage relations from eqns. 2.45 and 2.46 into eqn. 2.47, we obtain

$$\frac{\Phi_o}{2\pi}\frac{d\varphi}{dt} = \frac{d[L_J I_{co} \sin\varphi]}{dt} \tag{2.48}$$

The Josephson inductance L_J of the junction can thus be extracted to be:

$$L_J = \frac{\Phi_o \varphi}{2\pi I_{co} \sin\varphi} \tag{2.49}$$

where φ is given by $\sin^{-1}(I/I_{co})$. The above derivation of the Josephson inductance can be extended to the case of a SQUID. If we assume the SQUID has negligible loop inductance, then it essentially behaves like a single junction with an effective gauge invariant phase φ_p and an effective critical current $I_c = 2I_{co}|\cos(\pi\Phi_{ext}/\Phi_o)|$, where $\varphi_p = (\varphi_1 + \varphi_2)/2$ and Φ_{ext} is the external flux through the SQUID. The Josephson inductance of the SQUID is obtained as follows:

$$L_J = \frac{\Phi_o \varphi_p}{4\pi I_{co} \cos\left(\frac{\pi\Phi_{ext}}{\Phi_o}\right) \sin\varphi_p} \tag{2.50}$$

The current and flux dependence is plotted in fig. 2-16. Note that the current dependence for the SQUID is the same as that for a single junction. While the Josephson inductance always increases with the bias current, it can increase or decrease with the flux bias due to the periodic dependence. A more thorough analysis of Josephson inductive elements will be presented in section 5.1.

[4] Alternatively, the time-varying inductance can be defined using $V(t) = L(t)(dI(t)/dt)$. The Josephson inductance extracted according to this definition is $L_J = \Phi_o/(2\pi I_{co}\cos\varphi)$ which is also commonly used.

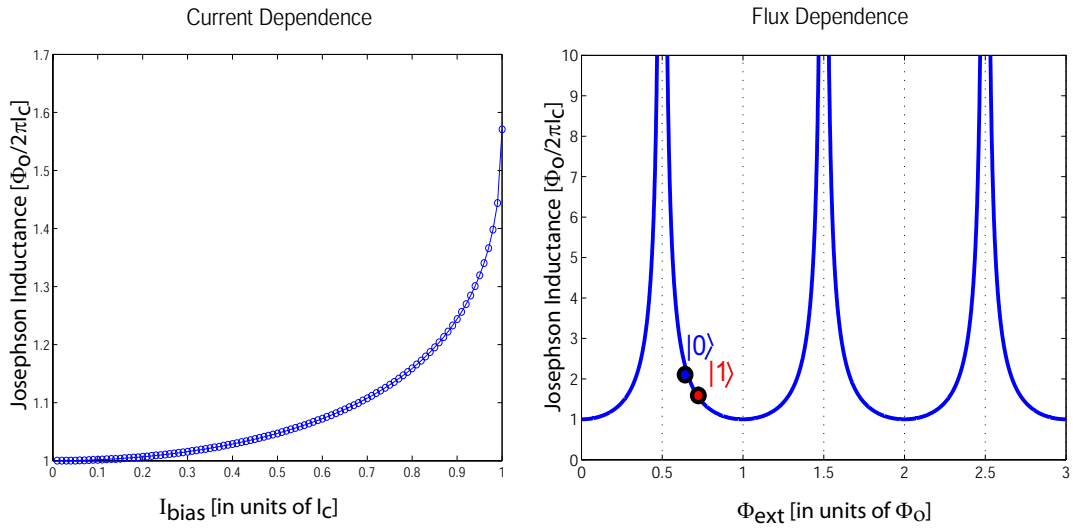

Figure 2-16: The Josephson inductance of a SQUID is nonlinear in the current bias and the flux bias. The inductance is different depending on the flux state of the qubit.

2.3.2 Linear RLC resonant circuit

To operate the SQUID magnetometer as a flux-sensitive inductor for qubit readout, we need to be able to measure the change in Josephson inductance with high sensitivity. This can be achieved by incorporating the SQUID inductor in a high-Q resonant circuit, where a change in inductance corresponding to a transition between qubit states can be detected as a shift in the resonant frequency.

The following analysis reviews some of the basics of a linear resonant circuit [49, 50]. As discussed in the previous section, the SQUID Josephson inductance is in fact nonlinear with the current bias as well as the flux bias. Nevertheless, the analysis here for linear resonant circuits applies to the case when the bias current is low compared to the critical current, and also provides a good starting point to illustrate some general concepts. Analysis of nonlinear resonant circuits comprising a SQUID requires solving the differential equations governing the SQUID as well as the rest of the circuit. This will be the main focus of chapter 5.

In fig. 2-17, the SQUID is shown as a linear inductor in a parallel RLC circuit. The parallel configuration is chosen over its series counterpart, because one can show that the series case is easily overdamped unless the resistance R is very small. The resistance R

represents the parallel combination of the source and output impedances. The circuit is driven by a sinusoidal current source.

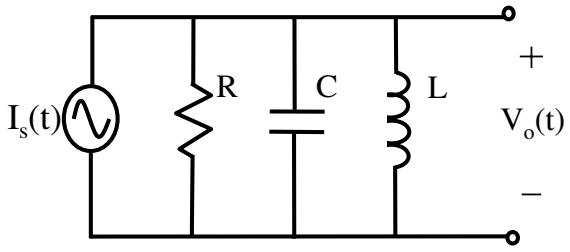

Figure 2-17: A linear RLC resonant circuit in the parallel configuration.

The impedance $Z(\omega)$ of the network is given by:

$$Z(\omega) = \frac{1}{\frac{1}{R} + j\left(\omega C - \frac{1}{\omega L}\right)} \tag{2.51}$$

Let the input current be $I_s = I_m \cos \omega t$ and the output voltage be $V_o = V_m \cos(\omega t + \theta)$. The output voltage is given by $I_s Z$, from which we can see the magnitude and phase are:

$$V_m = \frac{I_s}{\sqrt{(\frac{1}{R})^2 + (\omega C - \frac{1}{\omega L})^2}} \tag{2.52}$$

$$\theta = -\tan^{-1} R\left(\omega C - \frac{1}{\omega L}\right) \tag{2.53}$$

The resonant frequency ω_o of the circuit is defined as the frequency at which the impedance is purely resistive, and is given by:

$$\omega_o = \frac{1}{\sqrt{LC}} \tag{2.54}$$

The quality factor Q characterizes the sharpness of the resonant peak. The following summarizes several equivalent definitions of Q that are often come across:

1. For a parallel configuration, Q is defined as the ratio of the reactive to the resistance at resonance [5]:

$$Q = \frac{R}{\omega_o L} = \omega_o RC = R\sqrt{\frac{C}{L}} \tag{2.55}$$

2. Ratio of the resonant frequency to the bandwidth:

$$Q = \frac{\omega_o}{\beta} \tag{2.56}$$

where the bandwidth β is the frequency range at which the amplitude of the output voltage is $V_m/\sqrt{2}$. For a parallel circuit, β is given by $1/RC$

3. Ratio of the total energy stored in the capacitor and the inductor to the dissipated energy in the resistor over a cycle:

$$Q = 2\pi \left(\frac{CI_m^2 R^2/2}{I_m^2 R/2 f_o} \right) \tag{2.57}$$

4. In the time domain, Q is related to the ringing time required for the circuit to reach steady state. A resonant circuit grows or decays to $1/e \sim 37\%$ of its steady state amplitude in Q/π cycles. For a resonant readout circuit with f_o at 500 MHz and a Q of 1000, the time for it to reach $1/e$ of its steady state amplitude is:

$$\tau = \frac{Q}{\pi} \frac{1}{f_o} = 0.6\mu s \tag{2.58}$$

[5] For a series configuration, Q is defined as the ratio of the resistance to the reactance

Q-enhancement of resonant currents

Consider the current through the inductor and the capacitor at resonance:

$$I_c = \frac{V}{Z_c} = j\omega_o CRI_m = jQI_m \tag{2.59}$$

$$I_L = \frac{V}{Z_L} = \frac{I_m R}{j\omega_o L} = -jQI_m \tag{2.60}$$

Note that the currents through C and L are equal in magnitude and 180^o out of phase. Therefore at resonance, while the current from the source entirely flows through the resistor, there is a large amount of "stored" current which circulates in the resonating loop. The amplitude of this circulating current is Q times the source current.

Effect of Q on the phase spectrum

The quality factor Q defines the sharpness of the magnitude spectrum of the output voltage. We will now comment on the effect of Q on the phase spectrum. First, we can rewrite eqn. 2.53 in terms of Q and ω_o:

$$\theta = -\tan^{-1}\left(\frac{\omega^2 - \omega_o}{\omega\omega_o}\right)Q \tag{2.61}$$

$$\frac{d\theta}{d\omega}\,|_{\omega=\omega_o} = -\frac{2Q}{\omega_o} \tag{2.62}$$

The slope of the phase spectrum at ω_o is thus related to Q. As the Q of the circuit increases, the slope at ω_o becomes sharper. The effect of Q on the magnitude and phase spectra is illustrated in fig. 2-18.

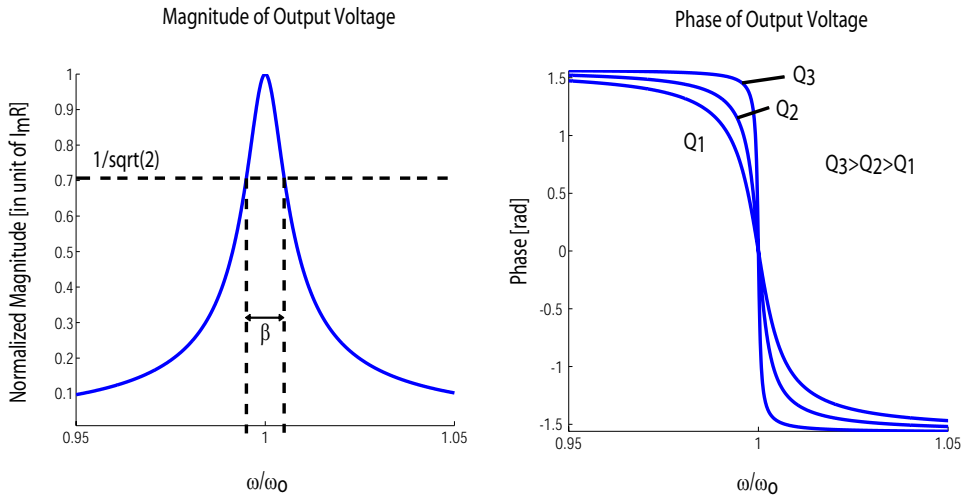

Figure 2-18: Left: The magnitude spectrum of the output voltage. Q is defined as ω_o/β, where the bandwidth β is the frequency range at which the amplitude of the output voltage is dropped by $1/\sqrt{2}$. Right: The effect of Q on the phase spectrum. As Q increases, the slope of the spectrum at ω_o increases. $(Q_3 > Q_2 > Q_1)$

2.3.3 Measurement scheme for Resonant Readout

The resonant readout circuit is essentially a parallel RLC resonant circuit with the inductor replaced by a SQUID magnetometer. The Josephson inductance of the SQUID is nonlinear with the current bias as well as the flux bias. Upon a change in the state of the qubit, the corresponding change of the Josephson inductance causes a shift in the resonant frequency, which can be detected as the qubit signal.

Experimentally, the resonant frequency can be directly measured with a spectrum/network analyzer. This measurement scheme is especially useful in the initial stage when the resonant behavior of the readout circuit is to be characterized. This will be the main focus of chapter 3. An alternative measurement scheme is to bias the readout circuit at a single frequency near the resonant frequency. As illustrated in fig. 2-19, rather than detecting the qubit signal as a shift in the resonant frequency, it is detected as a difference in the magnitude or phase of the output voltage. This measurement scheme allows the readout to be carried out on a faster timescale. The time-resolved scheme will be revisited in chapter 6.

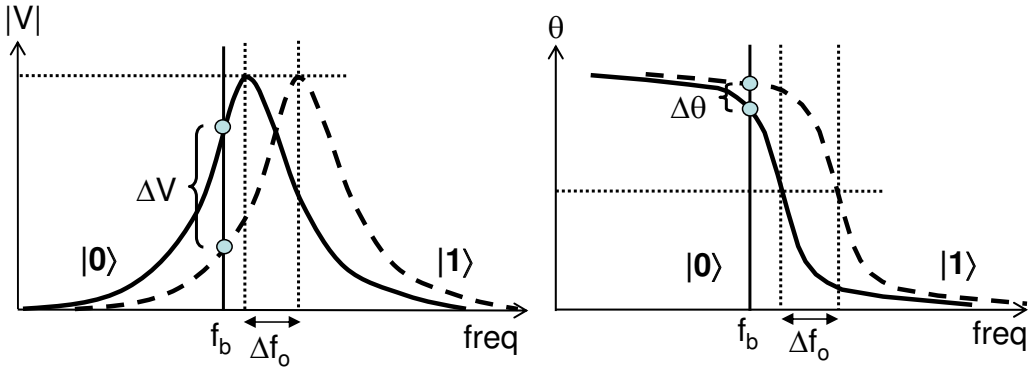

Figure 2-19: Measurement scheme for the resonant readout. The change in resonant frequency can be sensed as a change in the magnitude or phase of the output voltage at a frequency bias f_b. This provides a faster readout then measuring the resonant frequency with a spectrum/network analyzer.

2.4 Summary

In this chapter, we have focused on the two readout methods for the persistent current qubit. The conventional switching current measurement detects the qubit state by directly measuring the switching current, or by detecting the presence or absence of a switching event. The spectroscopy of qubit states as well as Landau-Zener transitions between the qubit states were demonstrated. Yet, the drawbacks of the switching readout scheme motivates the need for a dispersive readout scheme. The proposed resonant readout operates the SQUID as an inductor, and the qubit states are detected as a change in the Josephson inductance, and thus a shift in the resonant frequency of a resonator. We will present the experimental realization of the new resonant readout in the next chapter.

Chapter 3

Experimental Realization of the Resonant Readout

Abstract

In this chapter, we present the experimental realization of the resonant readout for qubit measurements. The resonant circuit was designed to operate at RF frequency. The on-chip fabrication parameters for the circuit elements will also be presented. The sample was measured at 300 mK, and the experimental results confirmed the sensitivity of the resonant readout to distinguish the two classical qubit states as a shift in the resonant frequency.

3.1 Design of Resonant Readout Circuit

3.1.1 Resonant circuit design criteria

In the resonant readout scheme, the SQUID magnetometer is operated as an inductor and is incorporated in a resonant circuit. The qubit states are distinguished as a shift in the resonant frequency of the readout circuit. We will begin this section by discussing the circuit design of the resonant circuit. In particular, the three main considerations for the design are the resonant frequency, the quality factor of the resonance, as well as the size of the Josephson inductance of the SQUID.

Resonant Frequency of the readout circuit

The resonant frequency of the readout circuit should be designed such that it is away from the frequencies which can cause undesired qubit transitions. This is particularly true since the readout circuit will be driven near its resonant frequency. Ideally, the resonant frequency should be lower than the frequency corresponding to the tunnel splitting between the ground and first excited states of the qubit. The tunnel splitting is usually around 1 GHz, which sets the upper bound for the design. At the same time, the frequency cannot be set arbitrarily low, as it would require a large resonating capacitor which could be challenging to implement on-chip. Based on these considerations, the resonant frequency was chosen to be 500 MHz, which is in the radio frequency (RF) regime.

Quality Factor: RF impedance transformation & impedance matching techniques

Considering that the qubit signal is to be detected as a shift in the resonant frequency, the resonant circuit should be designed with a high quality factor to achieve high readout sensitivity. Recall that the quality factor Q for a parallel RLC circuit is given by:

$$Q = R\sqrt{\frac{C}{L}} \tag{3.1}$$

Thus the higher the effective resistance, the higher the quality factor. Our readout circuit design does not require any resistors, thus the effective resistance is simply given by the

parallel combination of the input and the output impedances of the measurement electronics. Given that the typical impedance of RF electronics is $50\,\Omega$, the resulting quality factor could be very low without any transformation network. This is usually referred to as the *loading effect*.

The loaded-Q of the circuit can be increased by employing RF transformation techniques to step up the effective resistance as seen by the resonant circuit [51, 52]. The transformation network is usually designed for a particular frequency of interest, and thus the performance is expected to drop as the operating frequency moves away from the design frequency. For our design, we have employed the *tapped-inductor transformer* on the output side of the circuit. In fig. 3-1, R_L represents the load impedance from the output electronics such as an amplifier. It can be shown that the load resistance R_L is transformed to a higher effective resistance R_T according to the ratio of the inductances:

$$R_T = R_L \left(\frac{L_1 + L_2}{L_2} \right)^2 \tag{3.2}$$

$$L_T = L_1 + L_2 \tag{3.3}$$

The above equations are valid in the limit that the Q of the circuit is much larger than 1. In the general case, the expressions are more complicated, and the full derivation can be found in appendix A.

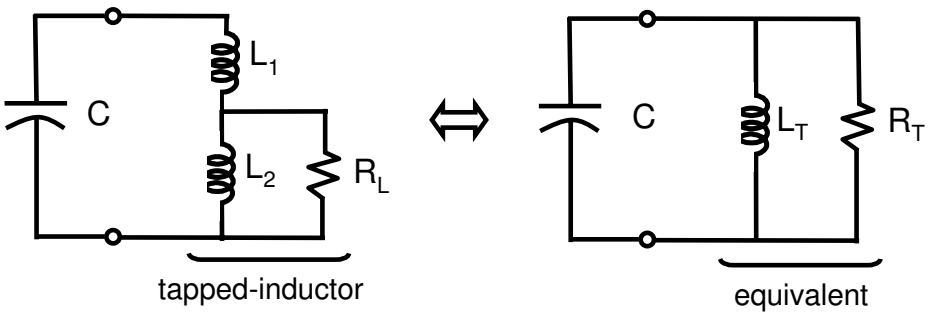

Figure 3-1: Illustration of the tapped-inductor transformer and its equivalent circuit. The load resistance R_L to stepped up to a higher effective resistance R_T according to the ratio of the inductances L_1 and L_2.

While the load impedance is transformed from $50\,\Omega$ to a higher resistance R_T according to the tapped-inductor transformer, the input impedance is yet to be matched for maximum power delivery. Recall that for DC circuits, maximum power is transferred to the load when the source *resistance* is equal to the load *resistance*. For AC circuits, maximum power transfer occurs when the source *impedance* is matched to the complex conjugate of the load *impedance*. Here, the design is simpler since the impedances to be matched are real. We have employed an *L-match impedance network* to match the $50\,\Omega$ source resistance to the transformed output resistance R_T. The name of the network is given for its L-configuration in the circuit schematic. Like the impedance transformer, the matching network is also designed at a particular frequency, which is chosen to be the resonant frequency of the circuit. Fig. 3-2 shows the schematic of the readout circuit with the matching network incorporated. The output side has been replaced by the equivalent circuit for the tapped-transformer.

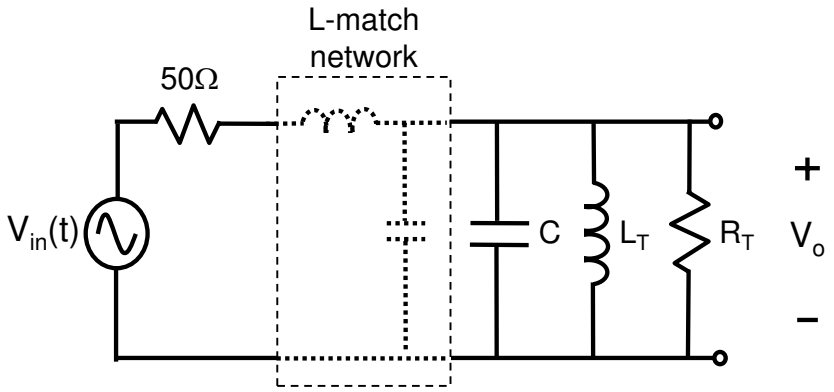

Figure 3-2: Schematic of the readout circuit with the matching network incorporated. The output side has been replaced by the equivalent circuit for the tapped-transformer. An L-match impedance matching network is shown.

In summary, we have employed the impedance transformation and impedance matching networks to increase the effective resistance of the resonant circuit near the resonant frequency, and thereby raising the loaded quality factor. It should also be kept in mind that while a high-Q resonance provides a high readout sensitivity, yet the circuit will require a longer response time to reach steady state. The response time of the readout circuit should be shorter than the coherence time of the qubit.

Typical values for the SQUID Josephson inductance

Recall that the Josephson inductance L_J of a SQUID is nonlinear, and its value changes with the current and flux biases through the SQUID. For circuit design purposes, it is useful to estimate L_J by:

$$L_J = \frac{\Phi_o}{2\pi I_c} \tag{3.4}$$

$$= \frac{\Phi_o}{2\pi(2I_{co})} = \frac{\Phi_o}{4\pi J_c A} \tag{3.5}$$

where I_{co} is the critical current of a single junction and is determined by the fabrication parameters J_c and A, which in turn are the critical current density and the area of the junction, respectively. Note that L_J is inversely proportional to the critical current I_c. For our fabrication parameters, I_c is typically between the range of 1 to 10 μA, which corresponds to L_J between 0.03 nH to 0.3 nH. Since the shift in the resonant frequency corresponding to the qubit signal is proportional to the *absolute* change in the inductance value, one may want to maximize L_J by pushing for the smallest junctions available in a fabrication run. However at the same time, the size of the critical current determines the upper bound of the bias current through the SQUID. Thus one should also be aware that measurements for SQUIDs with small critical currents have a smaller signal to noise ratio.

3.1.2 Actual circuit design for Resonant Readout

One of the actual designs for the resonant readout circuit is shown in fig. 3-3 [35]. The resonant frequency was designed to be 500 MHz with a loaded quality factor of 150. The SQUID was approximated by a linear inductor of $L_J = 0.2$ nH. In this circuit design, the resonating loop is formed by L_J, the bias inductor L_2, and the parallel combination of C_1 and C_2. R_s and R_L represent the 50 Ω input and output impedances from the RF electronics, and no resistors were fabricated on-chip. The tapped-inductor transformer formed by L_2 and L_J steps the output resistance from 50 Ω to 1 $k\Omega$ at the resonant frequency. On the input side, L_1 and C_1 forms an L-match network which matches the 50 Ω source resistance to the transformed output resistance. To reduce the plasma frequency of the SQUID, each junction

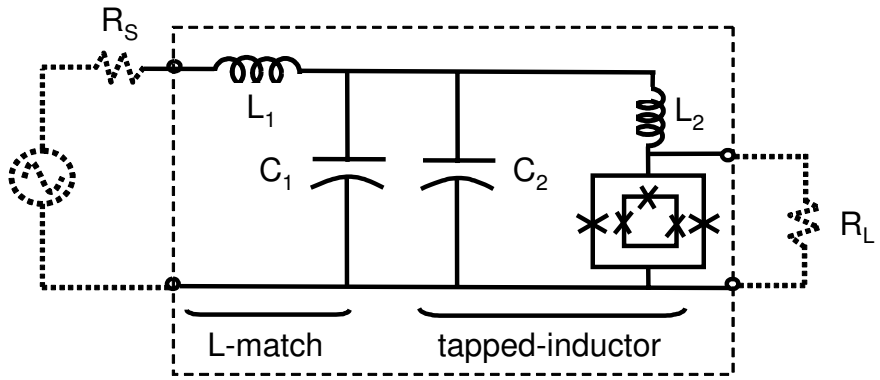

Figure 3-3: Actual circuit design for the resonant readout readout. The SQUID was approximated by a linear inductor L_J. L_1 and C_1 are part of the L-match network, while L_2 and the SQUID L_J form the tapped-transformer. The component values are $L_J = 0.2\,\mathrm{nH}$, $L_1 = 69\,\mathrm{nH}$, $L_2 = 0.78\,\mathrm{nH}$, $C_1 = 1.4\,\mathrm{pF}$, and $C_2 = 100\,\mathrm{pF}$. The junctions of the SQUID are each shunted by a 5 pF capacitor (not shown). The components within the dotted box were fabricated on-chip.

is shunted by a 5 pF capacitor. The simulated circuit response is shown in fig. 3-4. The size of the qubit flux signal is estimated to be $10\,m\Phi_o$, which corresponds to a shift of 1 MHz in the resonant frequency.

It should be mentioned that the bias inductor L_2 was included in the design for two purposes. First, it is part of the tapped-inductor transformer. Second, given the small value of L_J, keeping the resonant frequency near 500 MHz without the bias inductor would have required a large capacitor which could be challenging to implement on-chip. However, the presence of L_2 is expected to reduce the sensitivity of the resonant frequency upon a change in the flux signal. This is because L_J now contributes to only a fraction of the total inductance in the resonating loop, and the change in overall inductance is now given by $\Delta L_J/(L_J + L_2)$, where ΔL_J is the change in the Josephson inductance due to the measured flux change.

On-chip versus Off-chip implementations

There are two approaches to realize the resonant readout circuit. One approach is to have the qubit and SQUID fabricated on-chip, and the rest of the reactive elements implemented

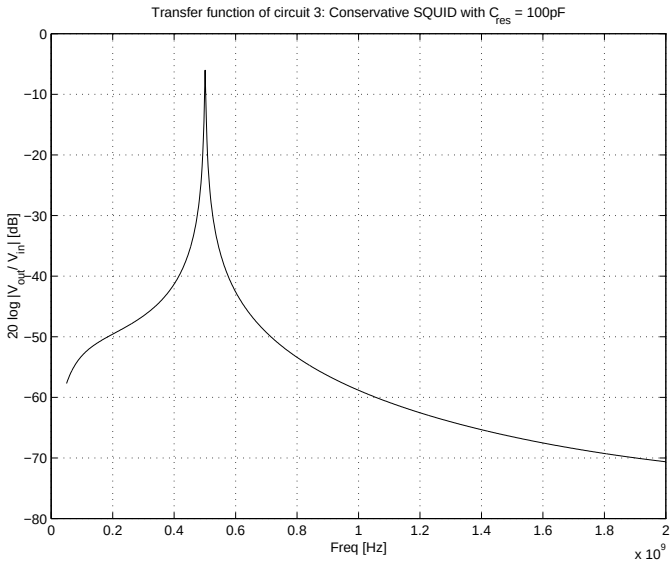

Figure 3-4: Simulated transfer function for the circuit schematic in fig. 3-3. The resonant frequency is designed to be 500 MHz, and the quality factor is 150. The size of the qubit flux signal is estimated to be $10\,m\Phi_o$, which corresponds to a shift of 1 MHz in the resonant frequency [35].

off-chip with surface mount components. The off-chip approach is more conservative as it only requires the SQUID and qubit to yield. However, the RF performance of the resonant circuit is expected to be affected by circuit parasitics from the surface mount components, or wirebond and solder connections between the chip and the off-chip components.

For better RF performance, an alternative approach is to have the complete resonant circuit fabricated on-chip. Not only that circuit parasitics can be drastically reduced, one can also benefit from the high quality factor of the capacitors and inductors fabricated out of superconductors. However, this was a more aggressive approach as it relied on the reactive elements (as well as the Josephson elements) to yield and that their circuit values be reasonably close to the design.

It should be noted that the capability to fabricate capacitors and inductors on the same chip as the Josephson junctions is a major advantage of the niobium fabrication process. On the other hand, aluminum samples are fabricated using the shadow evaporation process which does not support via structures, and thus making it infeasible to implement spiral inductors.

3.1.3 Superconducting Device Fabrication

The superconducting devices measured within the scope of this thesis were fabricated in a planarized niobium trilayer process at MIT Lincoln Laboratory [53]. The particular fabrication run in which the resonant readout samples were fabricated is referred to as QC 4. The following is a brief description of the different layers available in the process for circuit design. The cross section of the chip is shown in fig. 3-5.

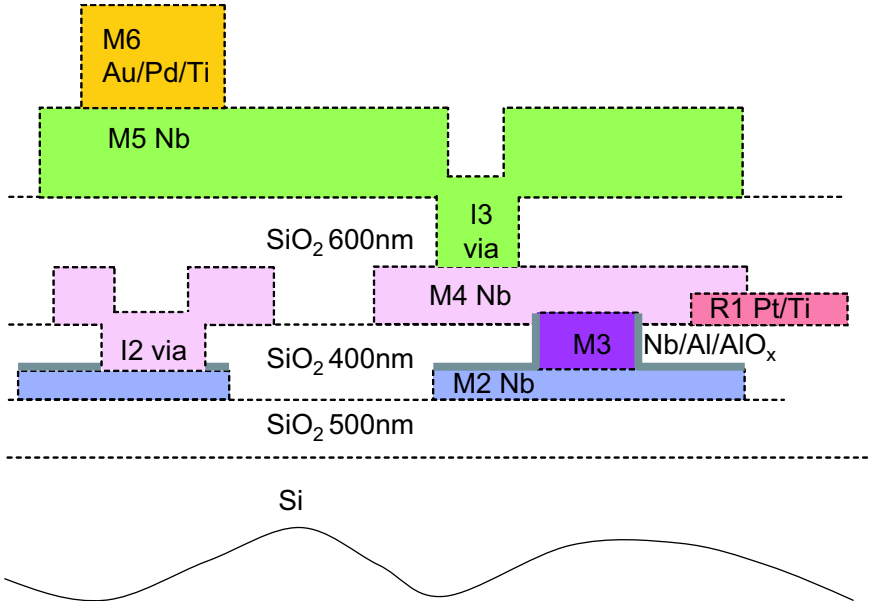

Figure 3-5: Cross section of the finished chip for the QC4 process, showing the deposition of the different layers. The Josephson junctions are defined by M2 and M3; capacitors are defined by M2 and M4, and the spiral inductors are realized in M2 [53].

M2 is a superconducting layer made out of niobium. It generally serves as a lower wiring layer. This layer forms the base electrode of the Josephson junction and the base electrode of a capacitor. The specifications for M2 allows a smaller spacing between adjacent features than other wiring layers, and thus is also a good choice for laying out spiral inductors.

M3 is also a superconducting layer. It defines the area of the junction and serves as its counter electrode. The aluminum oxide layer (AlO_x) which is the tunneling barrier

of the junction is defined between M2 and M3. After M3 is deposited, the junction is anodized and protected by a NbO_x layer. This anodization process improves the uniformity of the current density J_c [34].

M4 is a superconducting layer which serves as the middle wiring layer. It is used to connect the integrated circuit elements to the contact pads. M4 is also used as the upper electrode of a capacitor.

I2 is the first via layer which allows contact between M2 and M4. When defining the wiring for a Josephson junction or a capacitor, a via in I2 is always needed to get contact with the bottom electrode M2.

R1 is the resistor layer made out of 90% platinum and 10% titanium in thickness.

M5 is a superconducting layer generally used as a ground plane. For our designs, ground planes are *not* included such that external magnetic field can be coupled to the samples.

I3 is the second via layer which allows contact between M4 and M5.

M6 defines the gold contact pads

The main descriptions and the thicknesses of the layers are summarized in the following table:

Layer	Thickness [nm]	Description	Minimum feature size [μm]
M2	150 Nb	Base electrode of junction	1.0
M3	250 Nb/2 AlO_x/5 Al	Counter electrode of junction	0.7
M4	250 Nb	Wiring layer	1.0
M5	400 Nb	Wiring layer/ optional ground plane	1.0
M6	50 Au/400 Pd/35 Ti	Gold contact pad	10
R1	90 Pt/10 Ti	Resistor	2.5
I2	–	via between M2 and M4	0.8
I3	–	via between M4 and M5	1.0

3.1.4 Fabrication Parameters for on-chip circuit elements

This section summarizes the fabrication parameters for the circuit elements in fig. 3-3. The parameters were based on a critical current density J_c of $1.5\,\mu A/\mu m^2$ for the QC4 fabrication run[1]. For our designs, we have assumed that the actual dimensions of the Josephson junctions are smaller than the layout dimensions due to an effect called "undercutting". The range of the undercut is expected to be between $0.2 - 0.6\,\mu m$, and we have assumed an undercut of $0.4\,\mu m$ for our designs.

PC Qubit and SQUID Parameters

The fabrication parameters for the PC qubit and the SQUID are summarized in the tables below. The Josephson junctions were defined by the M2 and M3 layers. For the PC qubit, two of the junctions have the same size with layout dimensions of $1.0 \times 1.0\,\mu m^2$. The third junction is smaller with layout dimensions of $0.9 \times 0.9\,\mu m^2$. The junction capacitance is assumed to be $50fF/\mu m^2$. In the summary table, the expected dimensions are based on a $0.4\mu m$ undercut, and the estimation of α, E_J, and E_c are based on the expected dimensions of the small junction and a J_c of $1.5\,\mu A/\mu m^2$. The junctions of the SQUID are laid out to be $1.5 \times 1.5\,\mu m^2$. The linewidths of the qubit and SQUID loops are both $0.8\mu m$. The self and mutual inductances of the qubit and the SQUID are calculated using FASTHENRY which is a three-dimensional inductance extraction program [54].

Qubit Parameters

Large Josephson junction	layout: $1 \times 1\,\mu m^2$ (expected: $0.6 \times 0.6\,\mu m^2$)
Small Josephson junction	layout: $0.9 \times 0.9\,\mu m^2$ (expected: $0.5 \times 0.5\,\mu m^2$)
Loop area	$18.0 \times 18.0\,\mu m^2$
Loop inductance	55 pH
α	0.7
$E_J = \Phi_o I_{co}/2\pi$	$1.2 \times 10^{-22} J$
$E_c = q^2/2C$	$1.0 \times 10^{-24} J$
E_J/E_c	120

[1]The actual critical current density was later measured to be $1.2\,\mu A/\mu m^2$ based on process testing results

SQUID Parameters

Josephson junction	layout: $1.5 \times 1.5\,\mu m^2$ (expected: $1.1 \times 1.1\,\mu m^2$)
Loop area	$20.8 \times 20.8\,\mu m^2$
Loop inductance L_s	65 pH
Josephson inductance $L_J = \Phi_o/(2\pi I_c)$	0.2 nH
$\beta_L = 2\pi L_s I_c/\Phi_o$	0.35
Mutual inductance M to qubit	30 pH
Ratio of SQUID to Qubit loop areas	1.3

Spiral Inductors

The inductors were implemented with square spirals in the M2 layer. The linewidth and the inter-winding spacing of the spirals are $1\,\mu m$. The value of the inductors was estimated using the simulation program FastHenry. The layout of a 69 nH inductor is shown in fig. 3-6. Some useful strategies for designing spiral inductors can be found in [55, 56].

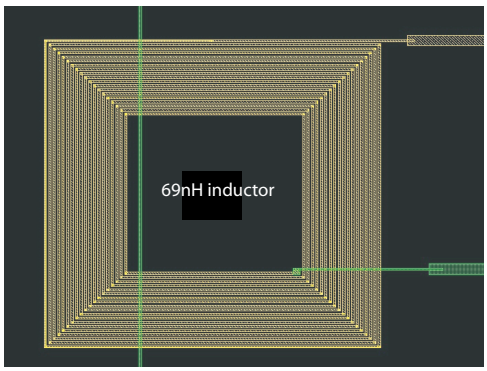

Figure 3-6: Layout of a square spiral with estimated inductance of 69 nH. The linewidth and inter-winding spacing are both $1\mu m$.

Capacitors

The capacitors were made out of Nb electrodes using the M2 and M4 layers. The dielectric consists of 50 nm of Nb_2O_5 and 200 nm of SiO_2 with the layers being on top of each other. We can estimate the overall capacitance by treating the dielectric as two capacitors in parallel. Nb_2O_5 has a dielectric constant of $\epsilon_r = 42$, which is much larger than the dielectric constant

of silicon $\epsilon_r = 3.9$. Thus the capacitance is dominated by the contribution from SiO_2. The estimated capacitance/area is $0.17\,\mathrm{fF}/\mu m^2$.

Overall circuit layout

The layout of the overall resonant circuit is shown in fig. 3-7. The configuration of the layout is very similar to the circuit schematics in fig. 3-3. Each color represents a layer definition. The spiral inductors are shown in yellow (M2) and the capacitors are in yellowish green (M2+M4). We have laid out two SQUIDs next to each other, but only one of the SQUIDs is connected for a given chip by means of two supplementary wiring layers. Waveguide structures were not incorporated on-chip due to limitation in chip space, but were included in the PCB board to which the chip is mounted. For completeness, a optical micrograph of an actual device is also shown.

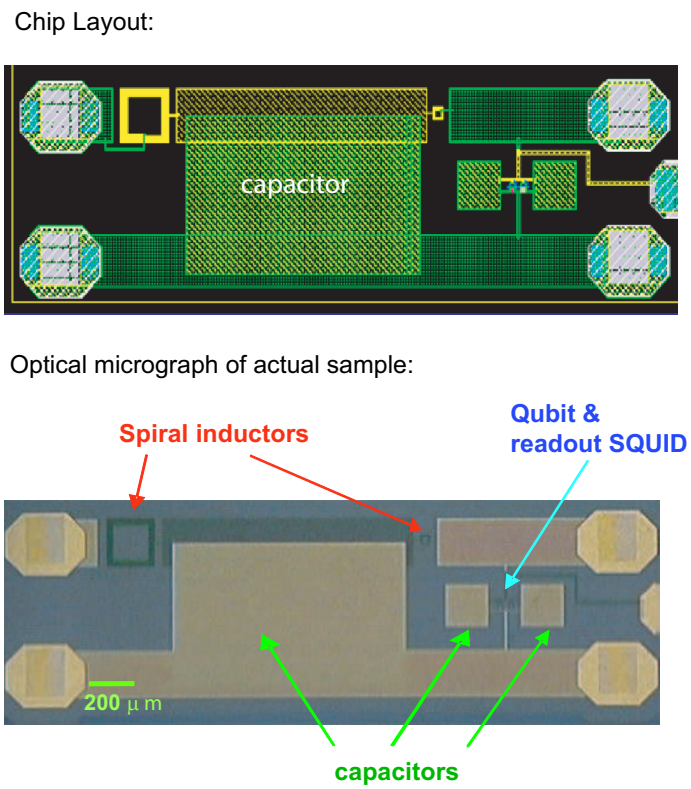

Figure 3-7: Top: Layout of the resonant readout circuit as shown in the XIC design tool. The SQUID and qubit structures are located between the two square capacitors. Bottom: optical micrograph of an actual fabricated device.

Development of the deep sub-micron (DSM) process

Since the QC4 process, Lincoln Laboratory has recently developed a deep sub-micron (DSM) process which supports smaller Josephson junctions with minimum layout dimensions of 200 nm. This corresponds to a minimum electrical feature size of less than 100 nm after process bias. In addition, spiral inductors with 0.5 μm linewidth and inter-winding spacing have also been demonstrated. The process also supports two kinds of capacitors: a low-k dielectric capacitor with SiO_2 ($\epsilon_r \sim 4$) and a high-k dielectric capacitor with NbO_x ($\epsilon_r \sim 40$) [57].

3.2 Measurement Setup

3.2.1 Cryostat

Most of the data presented in this chapter were measured in a sorption pumped helium-3 cryostat (Oxford Heliox) at MIT Lincoln Laboratory. The cryostat has a base temperature of 253 mK. Typically, the temperature rises steadily from 253 mK to 258 mK over the course of 3 days, at which point the cryostat has to be re-condensed in order to reach base temperature. This allows a reasonable time period for systematic measurement scans to be completed within a single cool-down. At temperatures near 300 mK, the thermal energy is large compared to the energy separation of the qubit states under consideration, i.e. $k_B T \gg h\nu$, where k_B is the Boltzmann constant and ν is the frequency of transition between the 0 and 1 states. Thus the energy of the qubit is not expected to be quantized for these measurements, and the two qubit states correspond to classical persistent current states in the qubit loop.

The helium-3 cryostat is equipped with 2 semi-rigid coaxial cables for RF measurements, as well as 4 soft-coax lines for shielded DC measurements. The schematic representation of the signal lines in the cryostat is shown in fig. 3-9.

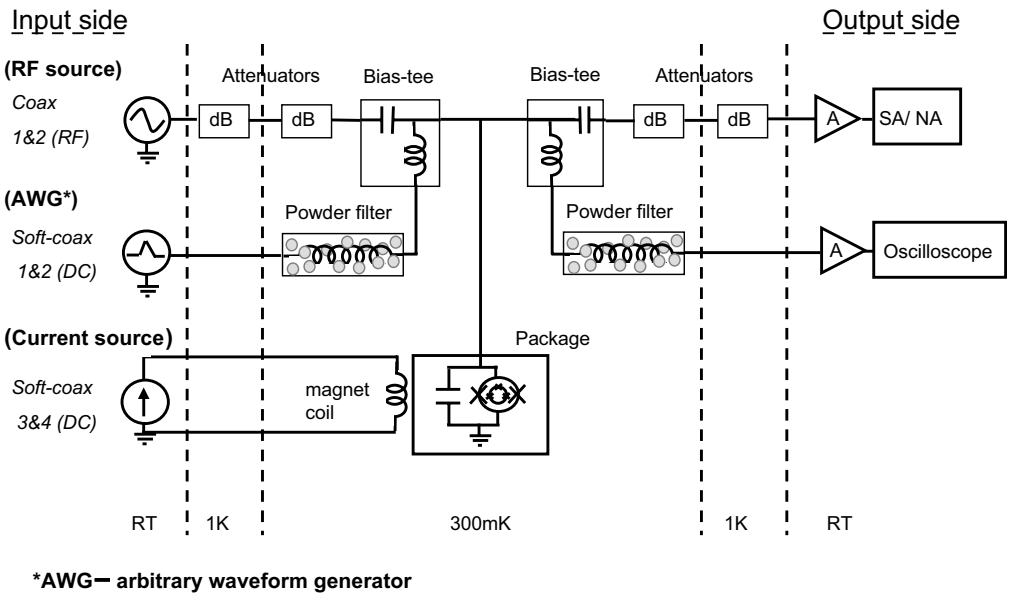

Figure 3-8: Schematic of the electronic setup at the different temperature stages of the Heliox cryostat. The two RF lines are used for the resonant readout, while the four DC lines are for characterization of the sample as well as external magnetic flux bias.

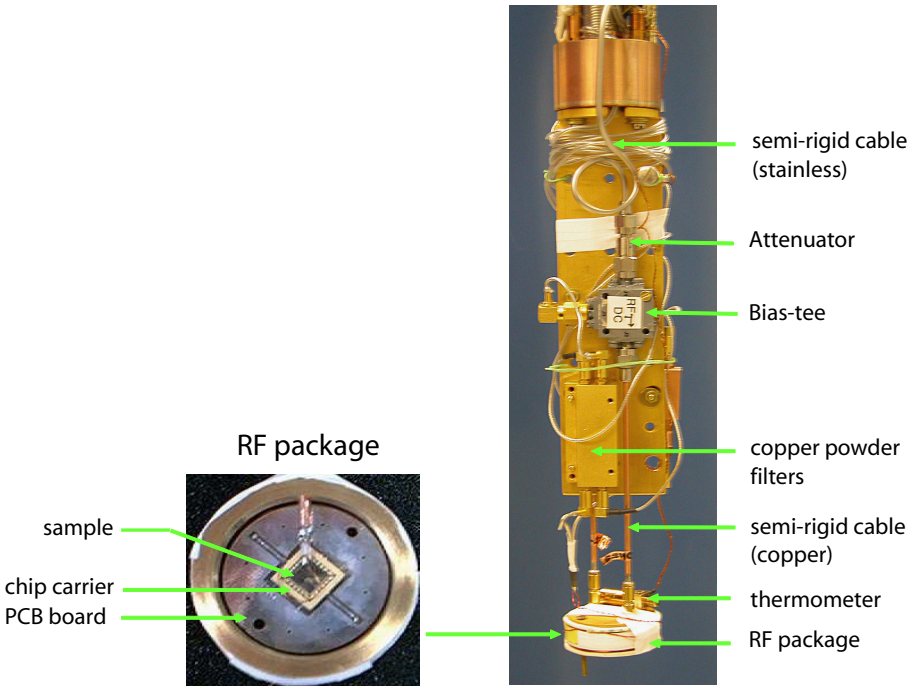

Figure 3-9: Picture of the sample stage of the Heliox. The inset shows the inside of the RF package, where the chip was wirebonded to a chip carrier, which in turn was soldered onto a PCB board with coplanar waveguide structures.

RF coaxial cables: attenuators as thermal anchors and for noise reduction

The RF coaxial cables are equipped with SMA connectors and have a 20 GHz bandwidth. They were installed with attenuators at the 1 K and the 300 mK temperature stages. Installing attenuators on the coax at certain temperature stages of the cryostat is a standard technique to ensure proper thermalization. While the outer conductor of the coax is usually well-anchored and thermalized, the cooling of the inner conductor happens by means of conduction through the dielectric of the coax. Typical dielectric such as teflon tends to contract more than the outer conductor at low temperatures and thus provides poor thermalization for the inner conductor. Attenuators are essentially resistive network which link the inner and outer conductors both electrically as well as thermally.

The second purpose of installing the attenuators at cryogenic temperatures is to reduce Johnson-Nyquist noise (or thermal noise) generated by room-temperature electronics. Recall that the Johnson noise power is given by

$$P_n = 4k_B T \Delta f \tag{3.6}$$

or equivalently the root-mean-square (r.m.s.) voltage/current across a resistor R due to thermal noise are:

$$V_n = \sqrt{4k_B T R \Delta f} \qquad\qquad I_n = \sqrt{\frac{4k_B T \Delta f}{R}} \tag{3.7}$$

where k_B is the Boltzmann constant, and Δf is the bandwidth. While the resistors in the attenuators can also introduce thermal noise, the level of noise is smaller given that the attenuators are at a colder temperature. The amount of attenuation required at a certain temperature stage T_a can be estimated by:

$$dB = 10 \log \frac{T_b}{T_a} \tag{3.8}$$

where T_b is the previous, higher temperature stage. The following table summarizes the attenuation between common temperature stages for a helium-3 cryostat and a dilution refrigerator. One can provide more attenuation to further improve the noise as long as

(1) the cryostat has enough cooling power at that certain temperature stage to handle the dissipation from the attenuator; and (2) if the attenuators are mounted on the output lines, that the output signal is still large enough to be detected after the attenuation.

T_a	T_b	Attenuation
300 K	1 K	-25 dB
1 K	300 mK	-5 dB
1 K	10 mK	-20 dB

The inner and outer conductors of the cables were made out of stainless steel (instead of copper) to reduce thermal conduction between the room temperature and base temperature stages. Stainless steel is a poor conductor, and for our setup, there is in fact an additional 10 dB attenuation distributed along the cable at 500 MHz. Alternatively, one may choose beryllium-copper as the inner conductor for better electrical conduction.

DC signal lines

While the two RF cables were used for the resonant readout, two of the DC lines were used to characterize the I-V properties of the SQUID junctions, and to provide an optional DC bias to the SQUID during the readout. The remaining two DC lines were used for the external magnetic flux bias. The DC lines were filtered with copper powder filters at the 300 mK stage [58, 59]. These are custom-made microwave filters that are used at cryogenic temperatures. A *copper powder filter* is essentially made out of a long wire which is wound in a coil surrounded by stainless steel or copper powder. The oxide on the powder provides the shunting capacitance, while the coil provides the series inductance. The filters have low-pass characteristics, with typical cutoff frequencies between 50 MHz to 1 GHz. The maximum attenuation stays below -100 dB at least up to 20GHz.

A bias-tee was mounted at the He-3 stage to combine the RF and DC signals before sending them to the device. It should be noted that the soft-coaxes were made out of high resistive material, and undesired heating effect was observed in the data when large bias currents were sent down the magnet lines.

RF package for housing sample

The sample was mounted on a chip carrier, which in turn is soldered on a printed-circuit board (PCB). The PCB substrate uses the standard FR-4 as a dielectric with $\varepsilon_r = 4.5$ at 500 MHz. Coplanar-waveguide structures were incorporated on the PCB board. The sample was housed inside a flat cylinder which acts as an RF package. The largest dimension of the package is the diameter of the cylinder which is 3 cm, and this dimension corresponds to a wavelength of 10 GHz. Low frequency noise below half of this wavelength (5 GHz) should be shielded out by the package. Thus the dimension of the package is small enough for our purpose, given that the frequency of interest is around 500MHz.

A superconducting magnet coil was wrapped around the outside of the RF package to provide the external flux bias.

3.2.2 RF Electronics

The RF electronics were set up to measure the *transmission* characteristics of the resonant readout circuit. We used a spectrum analyzer [2] equipped with a tracking generator to measure the magnitude spectrum of the resonant circuit, while the phase spectrum was measured with a network analyzer [3]. We preferred the spectrum analyzer over the network analyzer for magnitude measurements, given that the spectrum analyzer typically has a better noise figure and is more advantageous to detect small signals. The transfer characteristics of the resonant circuit were obtained by sweeping the source frequency over a span of 0.6 MHz around the resonant frequency. To improve the signal to noise ratio, we used a narrow resolution bandwidth (RBW) typically of 3 kHz, and averaged each spectrum 100 times. The signal from the resonant circuit was then amplified at room temperature with a low noise amplifier [4] with a gain of 50 dB and a noise figure (NF) of 1.45 dB at 500 MHz. The external magnetic flux bias was provided by a DC current source [5].

[2] Agilent E4407B ESA series Spectrum Analyzer, 9 kHz to 26.5 GHz
[3] HP 8720B Network Analyzer, 130 MHz to 20 GHz
[4] MITEQ Inc., model no. AM-1309
[5] Yokogawa Corporation of America, DC source model 7651

3.3 Experimental Results

3.3.1 Observation of resonant characteristics

We measured the transmission characteristics of the readout circuit at 300 mK. Typical magnitude and phase spectra are shown in fig 3-10. Based on a Lorentzian fit to the magnitude spectrum near resonance, the resonant frequency for this particular spectrum is extracted to be 419.69 MHz with a quality factor of 7000.

Based on the circuit design, the expected resonant frequency was 500 MHz, and the expected Q was 150. Thus the actual resonant frequency is lower than the expected resonant frequency, while the quality factor is more than 10 times larger. This was likely due to discrepancies between the actual and estimated values for the on-chip reactive elements. In particular, the high quality factor could be resulted if the spiral inductor which forms part of the tapped-inductor transformer is two to three times larger than the simulated value. However, one cannot determine the actual value of the elements without separate test structures.

Fig. 3-11 shows a typical magnitude spectrum displayed on the spectrum analyzer. This particular spectrum was measured at a higher input power. The log plot reveals an anti-resonance dip which occurs near the resonant peak. As a result, the resonant spectrum appears to be tilted. The anti-resonance could be due to parasitic capacitive coupling between the input and output ports on the PCB substrate. The size of the anti-resonance dip becomes more prominent with higher input power.

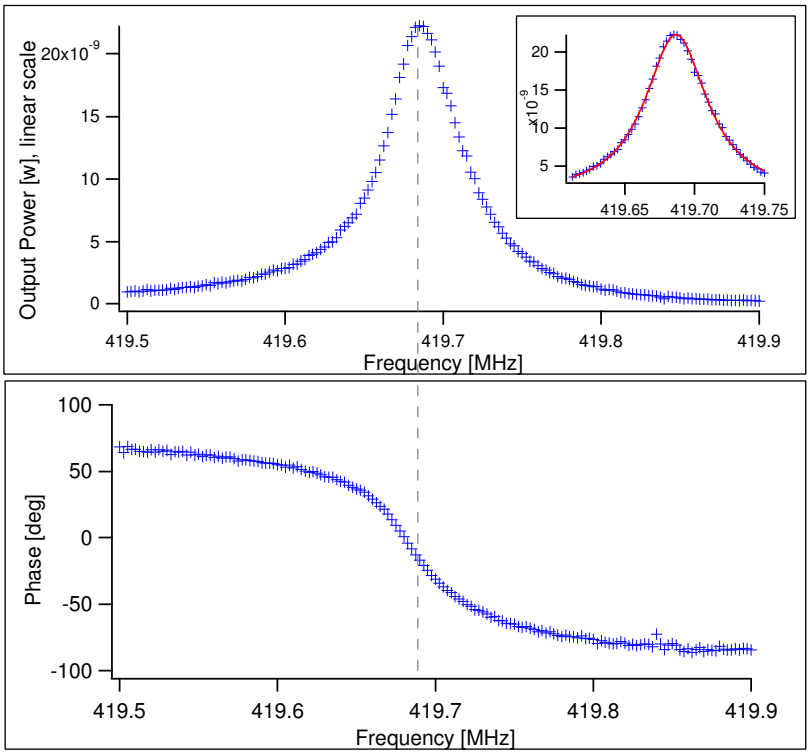

Figure 3-10: Typical magnitude and phase spectra of the readout circuit measured with a network analyzer. The inset shows a Lorentzian fit to the magnitude spectrum near resonance. The resonant frequency for this particular spectrum is extracted to be 419.69 MHz with a quality factor of 7000.

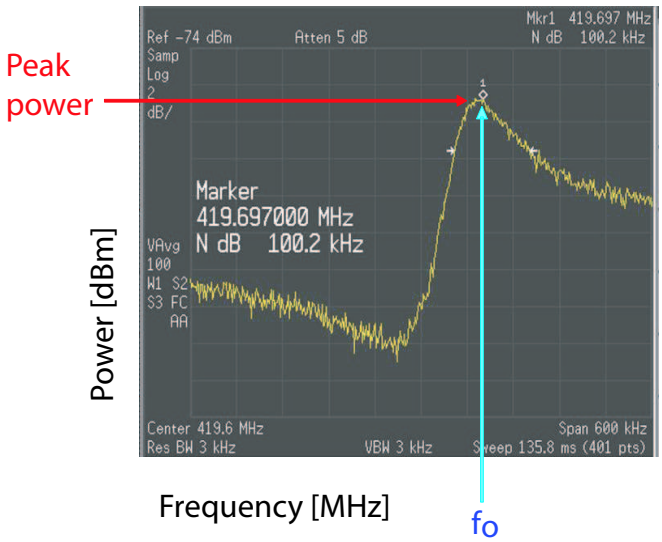

Figure 3-11: A typical magnitude spectrum of the readout circuit as displayed on the spectrum analyzer. An anti-resonance dip was observed near the resonant peak. The size of the anti-resonance dip becomes more prominent with higher input power.

3.3.2 Readout of Qubit states

When an external DC magnetic field was applied through the SQUID, we observed a modulation of the Josephson inductance, which in turn was manifested as a modulation in the resonant frequency of the readout circuit. The resonant frequency shows a periodic dependence with flux, and the periodicity corresponds to Φ_o for the SQUID. The results are shown in fig. 3-12.

At every 1.3 times the SQUID modulation period, a shift in the resonant frequency is observed. These so-called qubit steps represent a qubit transition between oppositely circulating current states, and occur near flux biases of half a flux quantum or $f = 1/2$ for the qubit. As the flux is swept pass $f = 1/2$, it is more energetically favorable for the qubit to change from one circulating current state to another in order to stay in the ground state. The periodicity of the qubit steps (corresponding to a flux quantum for the qubit) and the periodicity of the SQUID lobes (corresponding to a flux quantum for the SQUID) are related by the ratio of their loop areas, which was defined by the fabrication parameters.

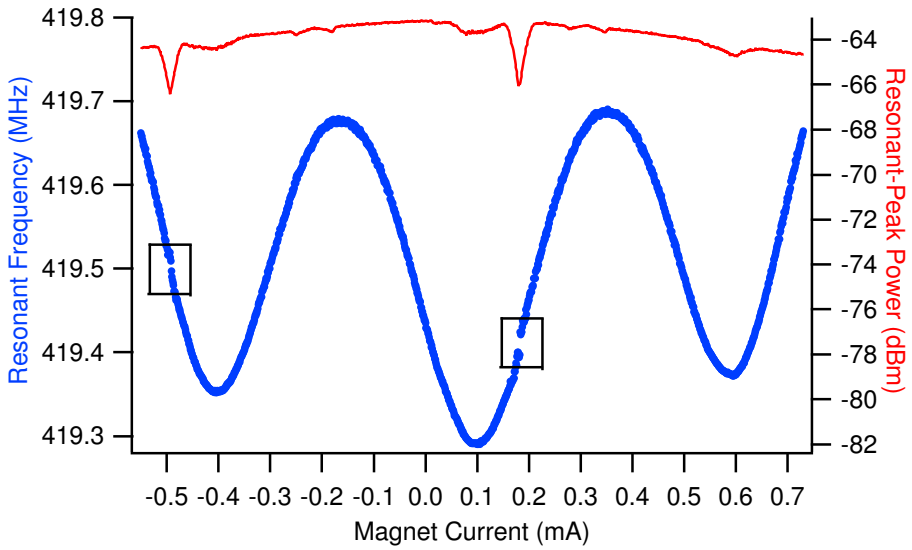

Figure 3-12: The lower plot (left axis) shows the modulation of the resonant frequency with external magnetic field. Qubit steps are found at 0.18 mA and -0.495 mA. The upper plot (right axis) shows the corresponding peak power of the resonant spectrum. The dips in peak power coincide with the qubit steps. The input power was -62dBm. For this particular magnet coil, the magnet current to flux conversion was $0.051\,\mathrm{mA}/\Phi_o$.

Fig. 3-12 also shows that near the qubit step region, the peak power of the resonant spectrum decreases (red plot). The dip in the peak power corresponds to broadening of the resonant spectrum. In fact, the size and the feature of the dip vary with the input power for the readout circuit. This will be re-visited in the next section. It should also be mentioned that the parabolic-like background observed in the frequency modulation curve in fig. 3-12 was due to undesired heating from the magnet current in the soft coax lines. The heating effect causes an increase in the resonant frequency, and is more significant at high magnet current biases.

Zoom-in on qubit steps

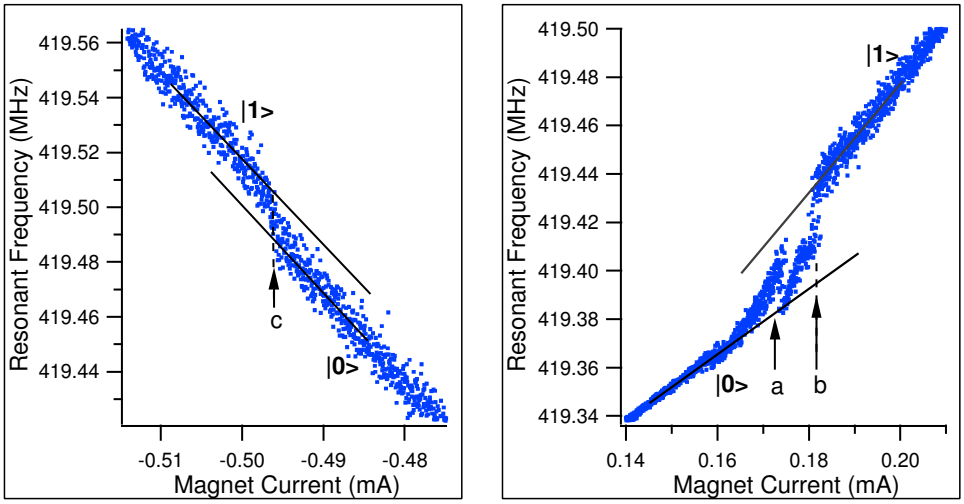

Figure 3-13: Dense scan near the qubit step at -0.495 mA (left) and 0.18 mA (right). The step at 0.18 mA corresponds to a frequency shift of $\Delta f = 40$ kHz at position (b), while the step at -0.495 mA corresponds to a shift of of $\Delta f = 20$ kHz at position (c). The feature at position (a) is reproducible and can only be seen in this particular qubit step.

We performed a dense scan near the qubit steps at -0.495 mA and 0.18 mA with a higher resolution in magnet current. This is shown in fig. 3-13. The step at 0.18 mA corresponds to a frequency shift of $\Delta f = 40$ kHz at position (b), while the step at -0.495 mA falls on a less sensitive region of the SQUID modulation curve and corresponds to a change of $\Delta f = 20$ kHz at position (c). We estimated the coupled flux to the SQUID due to the circulating current of the qubit to be MI_p, where M is the mutual coupling between the SQUID and

the qubit, and I_p is the circulating current estimated by the critical current of the smaller junction. The qubit states will be separated by twice this flux signal, which is estimated to be $0.01\Phi_o$ based on the fabrication parameters. From the experimental data, we extracted the flux signal to be $0.02 \pm 0.005\Phi_o$, which is reasonably close to the expected value. The corresponding change in the Josephson inductance is estimated to be 2 pH (1% change).

Referring to fig. 3-13, the qubit step at 0.18 mA shows some distinct feature at position (a) which was not observed at the other step. While the origin of this feature was not fully characterized and understood, it could be due to inter-well resonant tunneling to the higher energy levels of the qubit as observed in [21].

Comparison with dilution refrigerator data

The data presented so far were measured at 300 mK. We have also performed similar measurements at dilution refrigerator temperatures ~ 10 mK, and the results are shown in fig. 3-14. The purple plot shows the flux-dependence of the *resonant frequency* from the resonant readout using the RF signal lines, while the red plot shows the flux-dependence of the SQUID *switching current* measured with the DC lines. Comparing the results from the two readout methods, we first found that the qubit steps were observed using the resonant readout, but the switching current measurement was not sensitive enough to detect any qubit steps. Second, the periodicity of the switching current modulation is 0.96 times smaller than the periodicity of the frequency modulation. This was accountable for the overall shift between the two plots in the current axis. The reason for this difference in periodicity is not fully understood.

Finally we shall compare the resonant readout data at 10 mK in fig. 3-14 with the 300 mK results in fig. 3-12. The maximum amount of frequency modulation for both sets of data is around 0.4 MHz (419.3 - 419.7 MHz vs. 418.55 - 418.85 MHz). However there is an overall shift of 0.75 MHz in the resonant frequency. This could be due to the difference in the temperatures, or due to the different experimental setup. The parabolic background due to undesired heating in the helium-3 cryostat was no longer evidenced in the dilution refrigerator data.

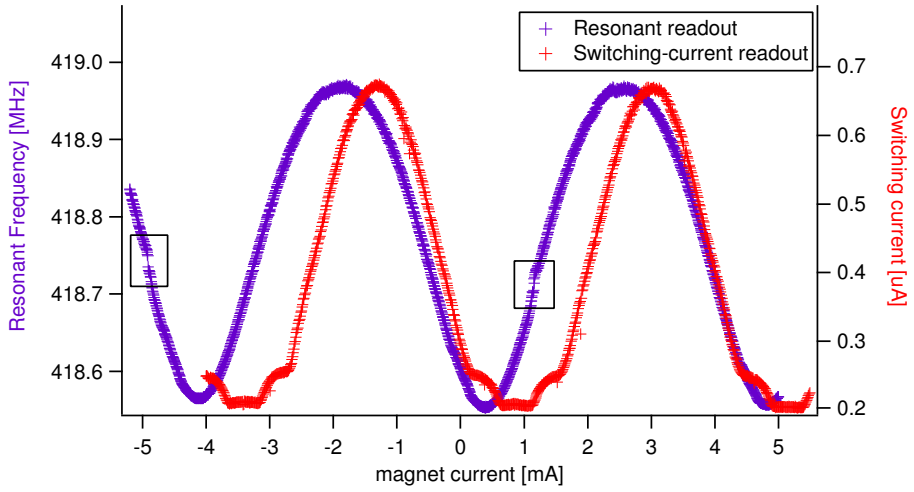

Figure 3-14: Comparison between the two readout methods at 10 mK. The qubit steps were observed using the resonant readout (purple plot) but not the switching current readout (red plot). For this particular magnet coil, the magnet current to flux conversion is 4.51 mA/Φ_o based on the frequency modulation data, and is 4.32 mA/Φ_o based on the switching current modulation data. The periodicity for the latter is 0.96 times smaller.

2d and 3d Frequency modulation graphs with shape of resonant spectrum

So far, we have been focusing on the detection of the qubit state by keeping track of the resonant frequency of the readout circuit. For completeness, we will now show the flux-modulation of the overall resonant spectrum. Figs. 3-15 and 3-16 are from the same set of data as in fig. 3-12. A slice along the frequency axis corresponds to a single resonant spectrum at a certain flux bias. The amplitude of the spectrum is indicated by the color axis. The location of the qubit steps are more clearly indicated by the dip in the peak power or equivalently the broadening of the spectrum. In addition, it can be seen from the plots that the shape of an individual resonant spectrum is similar to the one shown in fig. 3-11, with an anti-resonance dip occurring near the resonant peak. The anti-resonance effect also accounts for the general tilt of the spectrum.

We will return to a more thorough discussion about the shape of the resonant spectrum in chapter 4. It will be shown that as we increased the input power to the resonant circuit, the Josephson inductance of the SQUID became more nonlinear, and had characteristic effects on the shape of the resonant spectrum.

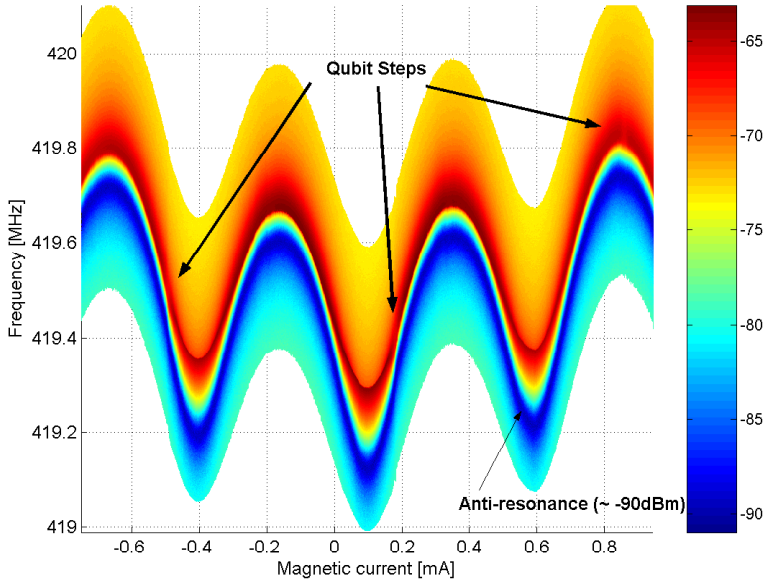

Figure 3-15: 2d frequency modulation graph showing the overall magnitude spectrum of the readout circuit. The amplitude of the spectrum is indicated by the color axis. The qubit steps are indicated by the broadening of the spectrum. The anti-resonant dip can also be seen near the resonant peak.

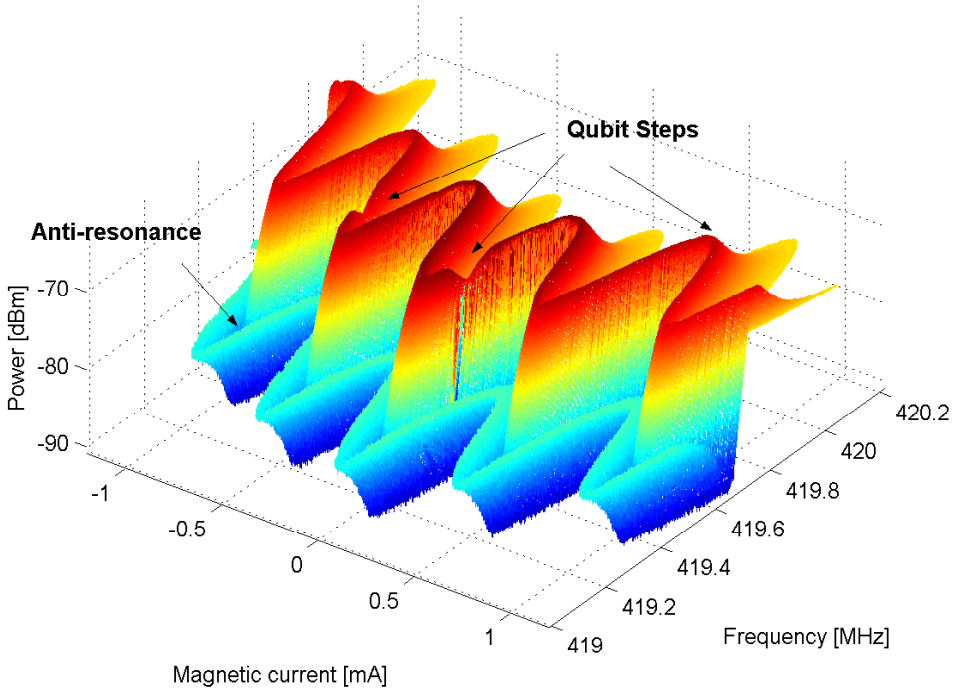

Figure 3-16: 3d frequency modulation graph with the qubit steps indicated by the dips in the peak power.

Readout of Qubit State using Phase measurements

The qubit measurement results presented so far were obtained by measuring the *magnitude spectrum* of the readout circuit with a spectrum analyzer. We have also measured the transmission characteristics of the readout circuit with a network analyzer and obtained the *phase spectrum*, and the qubit steps can also be detected from the phase measurements. Fig. 3-17 shows an example of data taken near the qubit step at 0.1 mA [6]. A vertical slice along the frequency axis corresponds to an individual phase spectrum. With reference to the color axis, the phase of the resonant spectrum changes from 90^o below the resonant frequency (red data points) to -90^o after the resonant frequency (dark blue data points), and the 180^o phase drop occurs near the green region. At the qubit step, the shift in the resonant frequency is about 40 kHz. It can also be seen that between the magnet current bias of 0.05 mA to 0.1 mA, the phase spectrum is broadened. This was also evidenced in the magnitude spectrum and corresponded to the dip in the peak power.

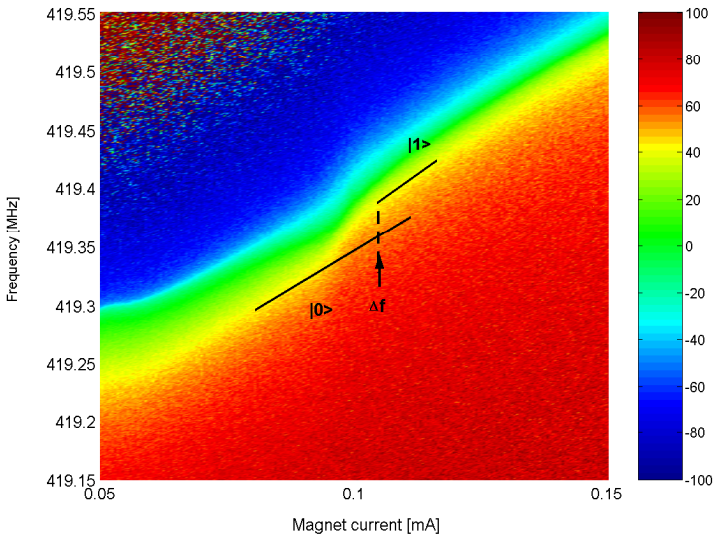

Figure 3-17: Detection of qubit step using the phase measurement. The phase of the readout circuit is given by the color axis. The shift in the resonant frequency is about 40 kHz. The input power for this data set was -62dBm.

[6] This data set was taken in a different cool-down, and the sample was subjected to a slightly different amount of background flux. Thus the location of the qubit step has moved from 0.18 mA as shown in fig. 3-13 to 0.1 mA. The location of the qubit step relative to the SQUID modulation curve was still the same.

3.3.3 Effect of input bias level on readout of qubit state

In this section, we want to characterize how the qubit measurement can be affected by the level of input power to the resonant readout. For instance, we are interested to see how the size of the qubit step (i.e., shift in the resonant frequency), as well as the broadening of the spectrum near the qubit step region (i.e., dip in the peak power) changes with input power.

Power dependence of qubit step

We performed qubit measurements with different input power to the resonant readout, and the corresponding frequency modulation curves are shown in fig. 3-18. The general observation is that when the input power to the readout increases, the amount by which the frequency is modulated over a flux quantum decreases. This turns out to be directly related to the shape of the resonant spectrum which changes with input power due to the nonlinear effects of the SQUID inductance. As the input power increases, the resonant spectrum evolves from being symmetric to being asymmetric, with the tip of the spectrum bending to either the lower or higher frequency side depending on the flux bias. In the case when the flux bias is at integrals of Φ_o , i.e. at the *top* of the frequency modulation curve, the spectrum bends such that the resonant frequency is *lower*. In the opposite case when the flux bias is at half integrals of Φ_o, i.e. at the *bottom* of the frequency modulation curve, the spectrum bends such that the resonant frequency is *higher*. As a result, the overall modulation in the resonant frequency with flux is reduced according to the extent of the bending. This will be made more clear as we focus on the nonlinear effect on the resonant spectrum in chapter 4.

Another interesting observation in fig. 3-18 is that the frequency modulation curves for different input power meet periodically at the inflection points. The inflection points correspond to places where the curvature of the frequency modulation curve changes sign, or equivalently, when the second derivative $d^2 f_o / d\Phi^2$ equals zero. It will later be shown that the asymmetric resonant spectrum changes from bending towards one frequency side to another at the inflection points.

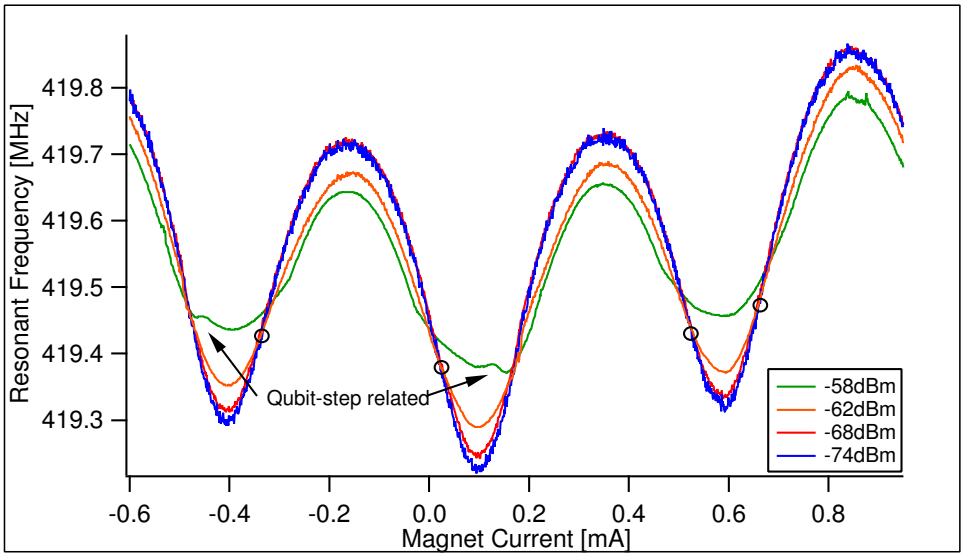

Figure 3-18: Modulation of the resonant frequency of the readout circuit with magnetic flux at various input power. The amount by which the frequency is modulated over a flux quantum is reduced as the resonant circuit enters the nonlinear regime. The polarity of the bending changes at the inflection points which are marked by circles. The hump features for the -58 dBm data are related to the qubit steps at 0.18 and -0.495mA.

Zoom-in on qubit step region

As we zoom in near the qubit step at 0.18 mA in fig. 3-18, the effect of different input power on the size of the qubit step can be observed more clearly. This is shown in fig. 3-19. For power levels below -62 dBm, the shift in the resonant frequency is observed, yet the the size of the shift is slightly scaled down due to the overall reduction in the frequency modulation as mentioned previously.

In the limit of high input power, the qubit step is eventually washed out. This is due to the fact that the nonlinear resonant spectrum changes its bending direction from one frequency side to another, and that this particular qubit step is located near an inflection point and thus is gradually "closed up". However, it will be shown that there is still a range of input power over which one can operate, such that the resonant spectrum has entered the nonlinear regime, but the nonlinear effect is not strong enough to wash out the qubit step. Qubit steps that are located far enough away from an inflection point should not be distorted by the nonlinear effect even at high input power.

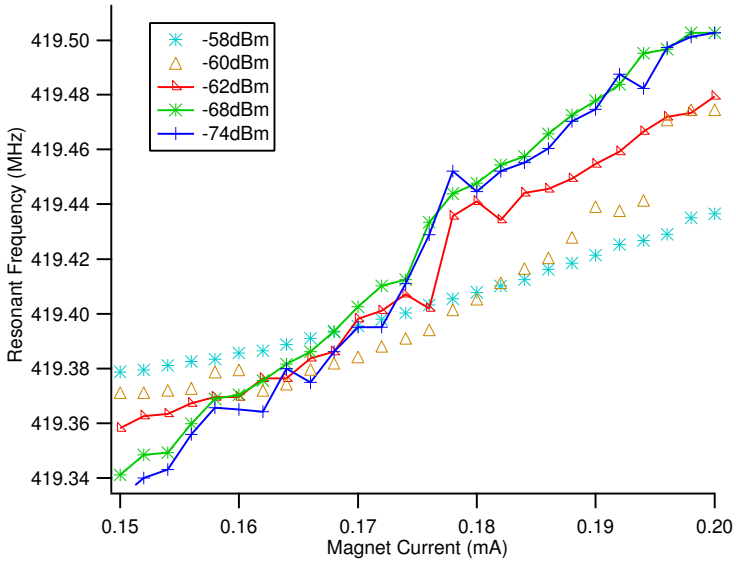

Figure 3-19: A zoom-in of fig. 3-18 near the qubit step at 0.18 mA. For power levels below -62 dBm, the shift in the resonant frequency is observed. In the limit of high input bias, the qubit step is eventually washed out.

Broadening of resonant spectrum near qubit-step region

It was shown earlier that near the qubit step, both the magnitude and the phase spectra of the readout circuit were broadened. This was observed in fig. 3-12 as a "dip" in the peak power of the magnitude spectrum. We further investigated the dependence of the dip with input power, and the results are shown in fig. 3-20. For low input power (below -68 dBm), the resonant peak power remains fairly constant, and there is no dip at the qubit step. As one increases the power, the size of the dip gradually grows and reaches a maximum of -2.6 dB at input power of -61 dBm. In the limit of high power, the dip gradually evolves into a plateau-like feature.

The width of the dip/plateau is plotted as a function of input power in the top plot of fig. 3-21. The data were best fit with a power functional form $y = y_o + Ax^n$ (red line), where the fitting parameters were y_o, A and n. The fitted value of n is 0.467, which means that the width of the dip grows with the square root of the input power, i.e. the input voltage. We re-plotted the data against the input voltage and confirmed a linear fit. This is shown in the bottom plot of fig. 3-21.

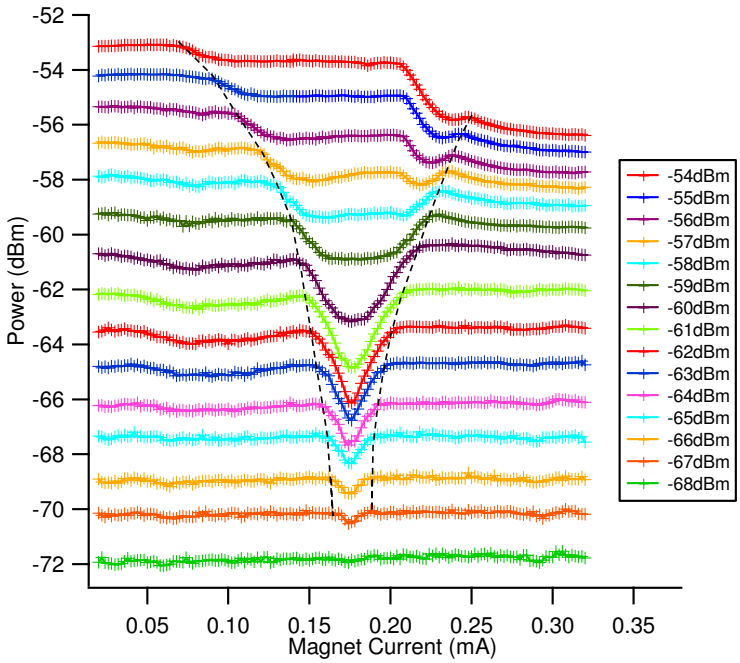

Figure 3-20: The dip feature in the peak power as a function of increasing input power. The dip grows in size and gradually evolves into a plateau-like feature. The dotted lines approximate the overall change of the width.

The broadening of the resonant spectrum could be due to *Landau-Zener transitions* between the ground and excited states of the qubit. The transition is driven by the RF bias to the readout circuit, which in turn could be coupled to the qubit. As a result, the qubit experiences an RF flux bias on top of the DC flux bias. Near $f \sim 1/2$ for the qubit, the RF flux bias drives the qubit back and forth through an avoided crossing. For each sweep, there is a probability for the qubit to be excited to the higher energy state. Since the Landau-Zener tunneling is a non-adiabatic process, the dissipation is manifested as a decrease in the Q or equivalently the broadening of the resonant spectrum. These preliminary results are consistent with the Landau-Zener transition data observed in [37] for the large bias limit.

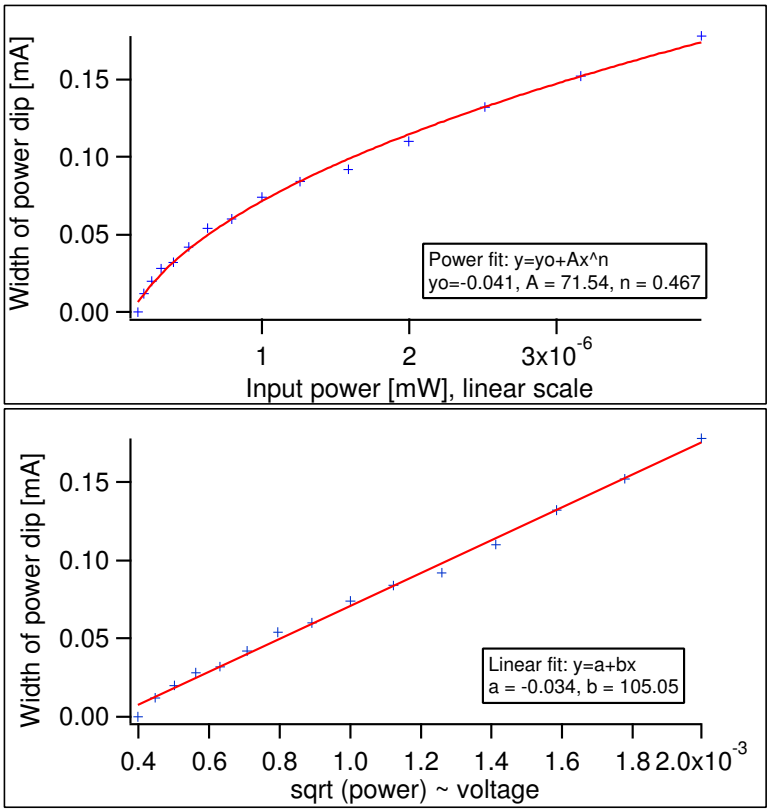

Figure 3-21: Top: The width of the power dip/plateau in fig. 3-20 plotted as a function of input power. The red line corresponds to a power functional fit. Bottom: Re-plot of the data versus the square root of the input power confirms that the width of the power dip has a linear dependence with the input voltage.

3.4 Summary

In this chapter, we have presented the experimental implementation of the resonant scheme for qubit measurement. We have achieved a high quality factor for high readout sensitivity by employing impedance transformation techniques in the resonant circuit design, as well as by fabricating all the circuit elements on-chip. Experimental results at 300 mK confirmed the sensitivity of the readout circuit to distinguish the classical circulating-current states of the qubit. The qubit transition was detected as a shift in the resonant frequency from both magnitude and phase measurements. It will be made more clear in chapter 4 that as a function of input power, one can identify the linear, nonlinear, as well as the hysteretic bias regimes. The results are summarized below:

Power [dBm]	Regime	Qubit step observed
$P \leq -71$	linear	yes
$-70 \leq P \leq -60$	nonlinear	yes
$-59 \leq P \leq -54$	hysteretic	washed out

One could operate the readout circuit in the linear or nonlinear regime, but the qubit step is washed out in the hysteretic regime. Operating the resonant readout circuit in the linear regime has the advantage of keeping the bias current low and reducing the level of decoherence on the qubit. On the other hand, the readout circuit operated in the nonlinear regime can potentially be used as a bifurcation amplifier [48]. The characterization of the readout circuit in the nonlinear regime will be presented in chapter 4.

Chapter 4

Characterization of the Resonant Readout in the Nonlinear Regime

Abstract

The nonlinearity due to the Josephson inductance of the SQUID has characteristic effects on the resonant behavior of the readout circuit. We observed clear manifestation of this nonlinearity given the high quality factor of the resonance. In this chapter, we present the characterization of the readout circuit as the input bias is increased from the linear to the nonlinear regime. The readout circuit biased in the nonlinear regime for qubit readout has the potential use as a bifurcation amplifier.

4.1 Introduction

This chapter is a continuation of the experimental discussions. So far, we have presented data at 300 mK demonstrating that the circulating-current state of the qubit can be detected by a SQUID inductor incorporated in a resonant circuit. By measuring the resonant frequency of the readout circuit, qubit transition between opposite states can be observed as a shift in the resonant frequency. We will now shift our focus to characterizing the resonant behavior of the readout circuit in the nonlinear regime. Recall from section 2.3.1 that the Josephson inductance of a SQUID is nonlinear: the inductance increases with the current bias, and is also a periodic function of the external flux bias. When the input power of the readout circuit is kept low, the SQUID essentially behaves as a linear inductor. As the input power increases, the effective inductance over an oscillation period can either increase or decrease depending on its functional form with the current and flux biases. This nonlinearity in the Josephson inductance have characteristic effects on the resonant spectrum of the readout circuit.

4.2 Resonant behavior in the nonlinear regime

Case when $\Phi = 0$

We will first consider the case when the DC flux bias is zero, at which point the SQUID essentially behaves like a single junction. The critical current of the SQUID, and thus the resonant frequency of the readout circuit are both at the maximum. This corresponds to the top of the frequency modulation curve in fig. 3-12.

The magnitude and phase spectra of the readout circuit are shown in fig. 4-1 as a function of increasing input power. In the low power limit, the resonant response of the readout circuit is linear. The magnitude spectrum has a symmetric Lorentzian shape, while the phase spectrum experiences a 180^o phase drop near the resonant frequency, and the phase shift has a slope limited by the quality factor Q.

As the input power increases, the nonlinearity of the readout circuit also increases. Both the magnitude and phase spectra become asymmetric and have a lower resonant frequency.

The lower resonant frequency indicates that the effective Josephson inductance over an oscillating period is higher. In the limit of high power, the magnitude spectrum exhibits a discontinuity near the resonant frequency, where the system jumps from the lower stable branch to the higher stable branch. The nonlinear phase spectrum also exhibits a discontinuity similar to the magnitude spectrum.

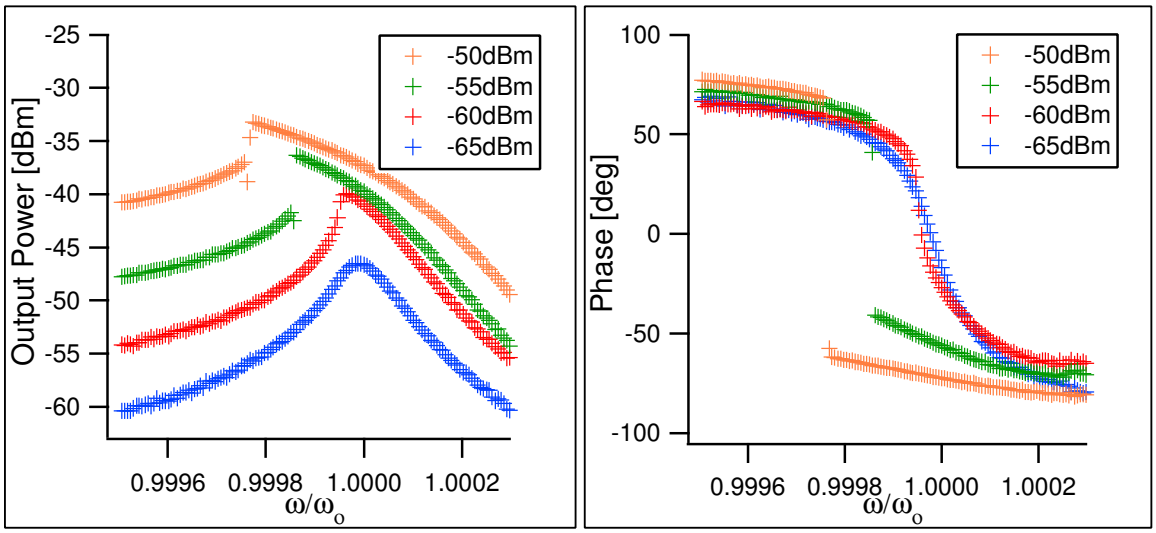

Figure 4-1: Evolution of the magnitude and phase spectra of the resonant readout circuit with increasing input power at $\Phi = 0$. The power ranges over -65 dBm to -50 dBm. The nonlinear resonant peak bends to the *lower* frequency side, indicating that the effective SQUID inductance is *higher* near the resonant frequency.

Case when $\Phi = 0.5\,\Phi_o$ and $0.3\,\Phi_o$

At different flux biases, the shape of the resonant spectrum evolves from the linear to the nonlinear regime in different ways. Fig. 4-2 compares the results at three different flux biases with increasing input power. At $\Phi = 0.5\,\Phi_o$, the resonant response is also linear in the low power limit. As the input power increases, the resonant spectrum becomes increasingly asymmetric. However unlike the case at $\Phi = 0$, the magnitude and phase spectra bend towards the higher frequency side. *The higher resonant frequency indicates that the effective Josephson inductance over an oscillating period is lower.* The spectra corresponding to the highest input power also exhibit a discontinuity near the resonant frequency. However,

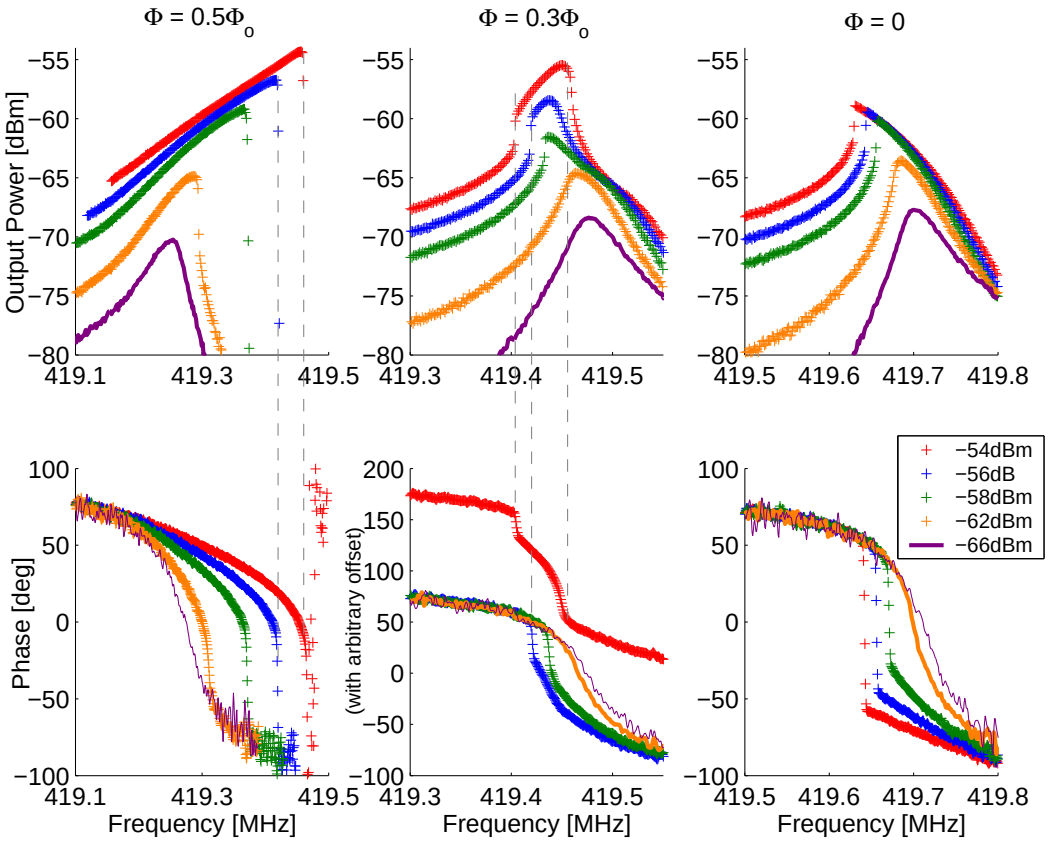

Figure 4-2: Magnitude and phase spectra of the readout circuit at three different flux biases. The magnitude spectra were measured with a the spectrum analyzer, while the phase spectra were measured using a network analyzer. The spectra evolve from being symmetric in the linear regime to being asymmetric in the nonlinear regime. The self-resonance effect which occurs near the resonant frequency accounts for the general tilt in the spectra.

the system now falls from the higher stable branch to the lower stable branch. Another interesting observation is that the magnitude spectrum at $\Phi = 0$ and $0.5\,\Phi_o$ resemble mirror images of each other about a vertical axis. On the other hand, the phase spectra are mirror imaged first about a vertical axis, then about a horizontal axis.

The resonant spectrum evolves continuously with the flux bias. In particular, the asymmetric spectrum changes from bending towards the lower frequency side at $\Phi = 0$, to bending towards the higher frequency side at $\Phi = 0.5\,\Phi_o$. The intermediate behavior is best captured at $\Phi = 0.3\,\Phi_o$ as shown in fig. 4-2. As the input power increases, the nonlinear magnitude spectrum first bends towards the lower frequency side, then gradually evolves into a charac-

teristic shape with two discontinuities near the resonant frequency, once when the magnitude is increasing and once when the magnitude is decreasing. Similarly, the phase spectrum also shows two discontinuities at the same frequency locations, with a partial phase drop at each discontinuity.

It should be mentioned that the magnitude spectra at $\Phi = 0.5\,\Phi_o$ in the high bias limit are interfered by the self-resonant dip which occurs just above the resonant frequency. The transmitted signal at the anti-resonance is very small, and hence the phase experiences a significant amount of noise near that region. The anti-resonance effect also accounts for a general tilt in the spectra at different flux biases.

Finally, we shall summarize two more important observations regarding the nonlinear resonant spectrum based on fig. 4-2.

1. The discontinuity in the nonlinear spectrum where the system jumps from the lower/ higher stable branch to another suggests that multiple solutions occur near that frequency. It will be made clearer from the simulation results that there is in fact a range of frequencies over which the system has two stable solutions (and one unstable solution). The range of frequencies over which multiple solutions occur is referred to as the *bifurcation region*. Depending on the direction of the frequency sweep, hysteretic behavior in the resonant spectrum can be observed. This will be presented in section 4.4. The hysteretic behavior also accounts for the reason why the amount of bending in the resonant spectrum at $\Phi = 0.5\,\Phi_o$ is significantly larger than at $\Phi = 0$.

2. The onset of nonlinearity in the spectrum occurs at a lower input power level for $\Phi = 0.5\,\Phi_o$. This could be due to the fact that the critical current of the SQUID is more suppressed at $\Phi = 0.5\,\Phi_o$, and thus for the same bias current I_{rf}, the ratio of I_{rf}/I_c is higher. As a result, the Josephson inductance has a stronger nonlinear effect.

For completeness, the general evolution of the nonlinear spectrum with magnetic flux is summarized again in fig. 4-3 for a constant input power. The resonant frequency of the readout circuit is modulated periodically with flux, and the spectrum is shown at $0.1\Phi_o$ step between 0 and $0.5\,\Phi_o$.

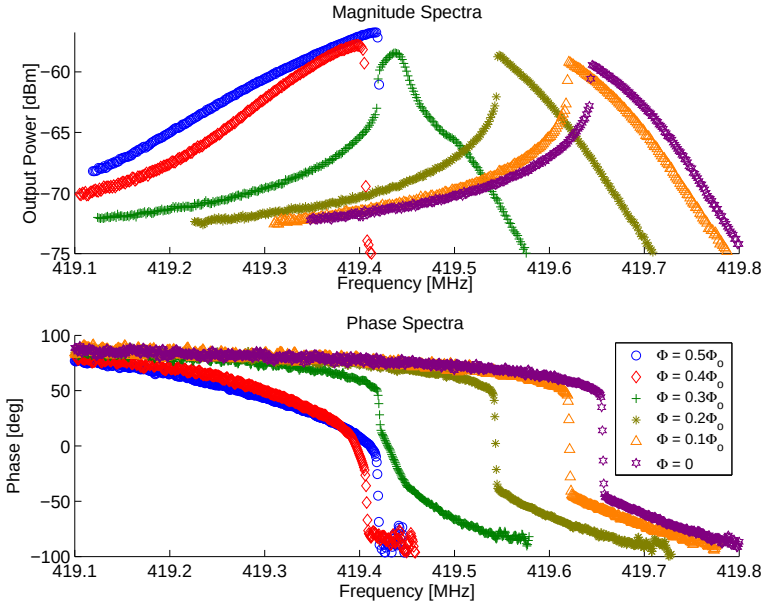

Figure 4-3: As the magnetic flux bias is varied between $\Phi = 0$ to $0.5\,\Phi_o$, the resonant frequency as well as the shape of the resonant spectrum is modulated. The input power for this data set was at -56 dBm, where the resonant circuit was biased in the nonlinear regime.

4.3 Quantifying the amount of nonlinearity in the resonant spectrum

In this section, we want to characterize how the resonant frequency of the nonlinear resonant spectrum changes with increasing input power. In order words, we want to quantify the amount of bending in the nonlinear resonant spectrum. This allows us to compare the experimental data with the simulation results in chapter 5.

In fig. 4-4, the magnitude spectra were measured in 1 dB step in input power to the readout circuit. The results are shown for various flux biases. To determine the resonant frequencies of the spectra, we first performed a polynomial fit (shown as red line) to the data measured at low input power levels, given that those spectra were more affected by noise fluctuation. The resonant frequency was then determined by the location of the resonant peak, which are marked by circles in the figure.

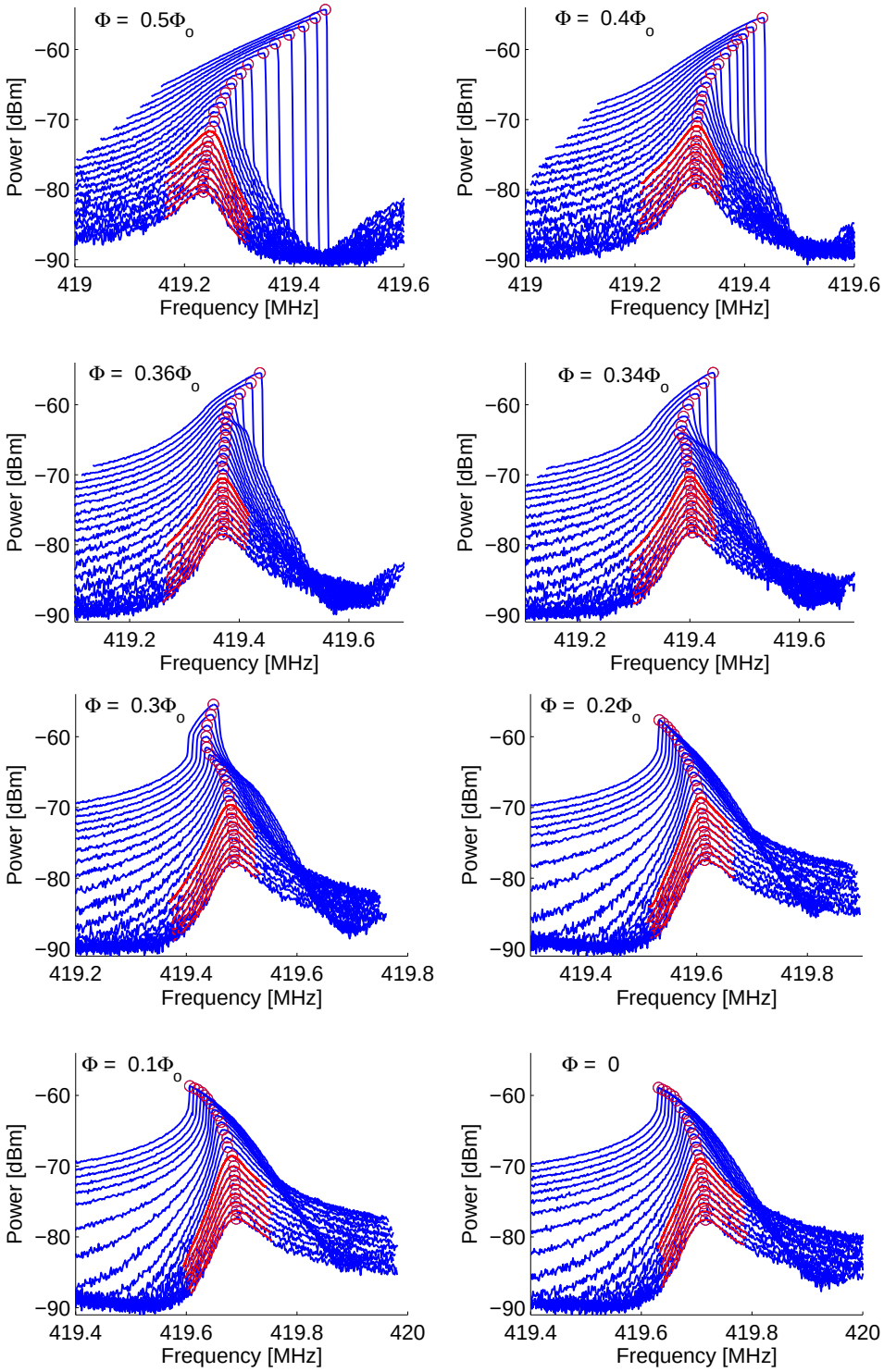

Figure 4-4: Transition of the resonant spectrum from the linear to the nonlinear regime at different flux biases. The characterization was performed in 1dB step between -74 dBm to -54 dBm in input power. The resonant frequency is determined by the location of the resonant peak, and are marked by the circles. The red lines represent the polynomial fits for the spectra measured at low input power.

To quantify the amount of bending, we introduce a parameter which normalizes the resonant frequency of the nonlinear spectrum f_n, relative to the linear spectrum f_o:

$$\delta\omega = \frac{\omega_n - \omega_o}{\omega_o} = \frac{f_n - f_o}{f_o} \tag{4.1}$$

where experimentally, f_o is determined as the resonant frequency of the spectrum measured at the lowest power in fig. 4-4. This corresponds to -74 dBm. Note that the sign of $\delta\omega$ serves as an indication of the polarity of the bending. A *positive* $\delta\omega$ corresponds to the nonlinear spectrum bending to the *higher* frequency side, and a *negative* $\delta\omega$ corresponds to the spectrum bending to the *lower* frequency side.

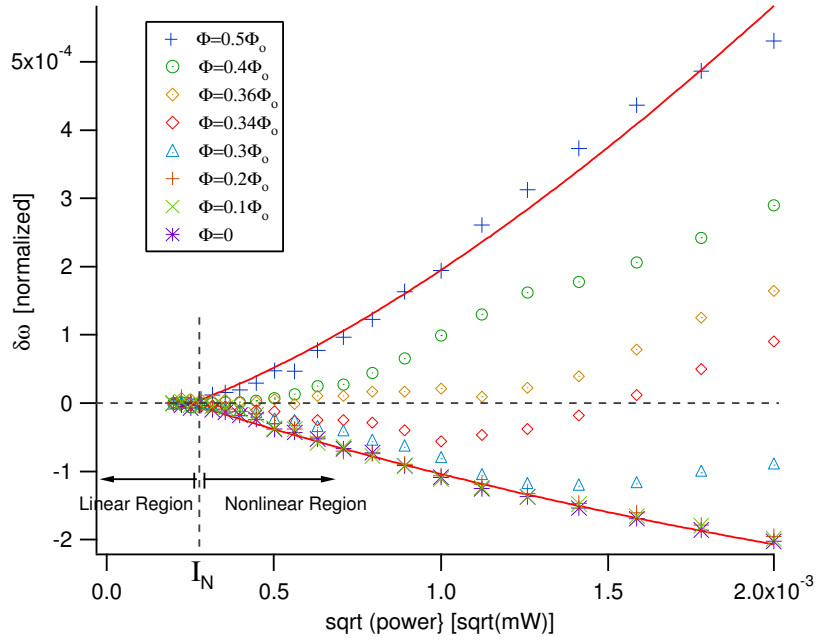

Figure 4-5: Normalized resonant frequency $\delta\omega$ plotted as a function of input voltage/current for different flux biases. A positive/negative $\delta\omega$ corresponds to the nonlinear spectrum bending to the higher/lower frequency side. The transition from the linear to the nonlinear regime occurs at $I_N = 2.8 \times 10^{-4}\sqrt{mW}$, which corresponds to -71 dBm. The red lines are exponential fits but are intended for guiding purposes only.

The normalized frequency $\delta\omega$ is then plotted as a function of input power in fig. 4-5. The x-axis is the square root of the linear input power, which is proportional to the voltage/current bias. The different markers represent the various flux biases. At $\Phi = 0.5\,\Phi_o$

(top plot), $\delta\omega$ is increasingly *positive*, corresponding to the magnitude spectrum bending further to the *higher* frequency side with increasing input bias. On the other hand, at $\Phi = 0$ (bottom plot), $\delta\omega$ becomes increasingly *negative*, corresponding to the magnitude spectrum bending further to the *lower* frequency side with increasing input bias. $\delta\omega$ varies at a slower rate for $\Phi = 0$, indicating that the amount of bending $|\delta\omega|$ is larger at $\Phi = 0.5\,\Phi_o$ than at $\Phi = 0$ for a given input bias. Based on the simulation results shown in fig. 5-15, $\delta\omega$ as a function of input bias does not have a simple functional form. The red lines in the figure are exponential fits and are intended only for guiding purposes. Finally at intermediate flux biases, $\delta\omega$ shows an undulating behavior, corresponding to the magnitude spectrum constantly varying the polarity of its bending.

Referring to fig. 4-5, we have defined the linear region as the range of input bias over which the resonant spectra have the same resonant frequency f_o within experimental uncertainty. On the other hand, the nonlinear region is the input range over which the resonant spectra are asymmetric, and the resonant frequencies are different from f_o. The transition from the linear to the nonlinear region occurs at the bias level of $I_N = 2.8 \times 10^{-4}\sqrt{mW}$, which corresponds to -71 dBm in input power.

4.4 Hysteresis of Resonant Spectrum

Recall that in the limit of high input power, the nonlinear resonant spectrum exhibits a discontinuity near the resonant frequency. The discontinuous edge corresponds to the boundary of a *bifurcation region*, which is the frequency range over which multiple solutions of the system exist. In the experiment, we measured the resonant spectrum by sweeping the driving frequency. Within the bifurcation region, the system settles in the solution branch based upon the previous solution, which in turn is determined by the direction of the frequency sweep. In this section, we will present the hysteretic resonant behavior of the readout circuit which was obtained when we swept the driving frequency in both the forward and backward directions.

Modification of the measurement scheme

Modern spectrum and network analyzers are designed to perform measurements by only sweeping forward in frequency, i.e. from low to high frequency. To perform hysteresis measurements, we introduced an additional RF signal generator[1] which could be controlled independently from the spectrum analyzer. This particular RF generator supports a setting such that the amplitude of the source is not reset upon stepping to a new frequency, which is important in order to obtain the hysteretic behavior. The measurement sequence involved sending a CW input signal to the readout circuit, and then measuring the output signal at the same frequency with a spectrum analyzer. This produces one frequency point on the resonant spectrum. To obtain an overall spectrum, the RF source was programmed to take frequency steps near the resonant frequency in the forward direction from low to high frequency, then backward from high to low frequency. We chose a frequency step of 3 kHz and a span of 0.6 MHz.

Hysteretic resonant behavior

Fig. 4-6 shows the hysteretic magnitude spectra as displayed on the spectrum analyzer for flux biases at $\Phi = 0$ and $0.5\,\Phi_o$. The direction of the frequency sweep is indicated by the white arrow. The yellow and blue branches correspond to the two stable branches, while the white dotted branch (predicted by theory) is unstable and cannot be measured without the implementation of a feedback scheme.

[1] Agilent E8257C PSG Analog Signal Generator, 250 kHz to 20 GHz

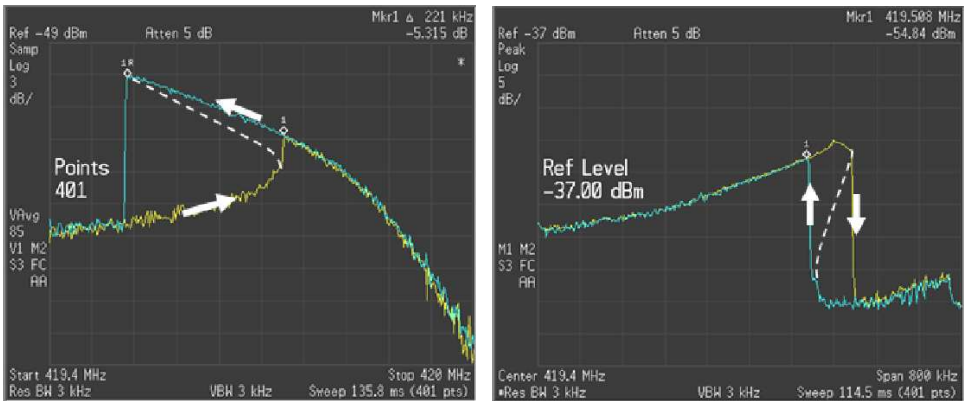

Figure 4-6: Hysteretic behavior of the magnitude spectra at $\Phi = 0$ (left) and $\Phi = 0.5\,\Phi_o$ (right) as displayed on the spectrum analyzer. The yellow trace corresponds to the forward frequency sweep, while the blue trace corresponds to the backward frequency sweep. The unstable branch represented by the white dotted line was not measured experimentally.

For completeness, fig. 4-7 summarizes the hysteretic behavior at six different flux biases at $0.1\Phi_o$ step between $\Phi = 0$ and $0.5\,\Phi_o$. The blue line represents the forward frequency sweep, and the red line represents the backward frequency sweep. As labeled in the figures, we define f_b to be the frequency at which the resonant spectrum jumps from the lower to the higher stable branch, while f_t corresponds to the frequency at which the spectrum falls from the higher to the lower stable branch. According to eqn. 4.1, we can define the normalized frequencies:

$$\delta\omega_t = \frac{\omega_t - \omega_o}{\omega_o} = \frac{f_t - f_o}{f_o} \tag{4.2}$$

$$\delta\omega_b = \frac{\omega_b - \omega_o}{\omega_o} = \frac{f_b - f_o}{f_o} \tag{4.3}$$

The extent of the bifurcation region is given by $|f_t - f_b|$, with the exception of $\Phi = 0.3\,\Phi_o$, in which case the bifurcation regions could be too small to be measured given the chosen frequency sensitivity.

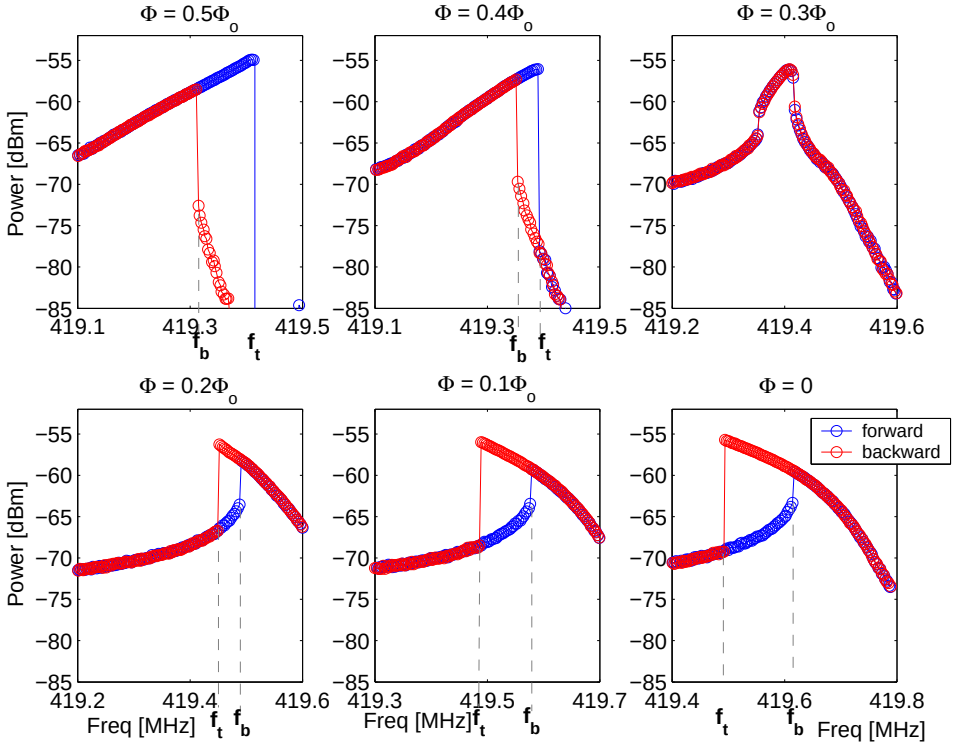

Figure 4-7: Hysteretic behavior at six different flux biases between $\Phi = 0$ and $0.5\,\Phi_o$. The extent of the bifurcation region is given by $|f_t - f_b|$. At $\Phi = 0.3\,\Phi_o$, we expected two bifurcation regions corresponding to the two discontinuous edges. However, the bifurcation regions were too small to be captured with the chosen frequency sensitivity.

The extent of the bifurcation region was then characterized as a function of input power. Fig. 4-8 shows the plots of $\delta\omega_b$ and $\delta\omega_t$ versus the square root of the input power, which is proportional to the voltage/current bias. It can be seen that the hysteretic behavior occurs when the input bias is above a threshold I_H. For $\Phi = 0.5\,\Phi_o$, I_H is about $8.9 \times 10^{-4}\sqrt{mW}$ which corresponds to -61 dBm in power. For the other flux biases, I_H is slightly higher and is about $1.12 \times 10^{-3}\sqrt{mW}$ corresponding to -59 dBm in power. Recall from fig. 4-5 that the onset of nonlinearity actually occurs at -71 dBm. Therefore, hysteretic behavior is not observed until the input bias is high enough to cause a strong nonlinear effect. Comparing the results for different flux biases, we can observe that the extent of the bifurcation region is the largest at $\Phi = 0.5\,\Phi_o$ for a given input bias.

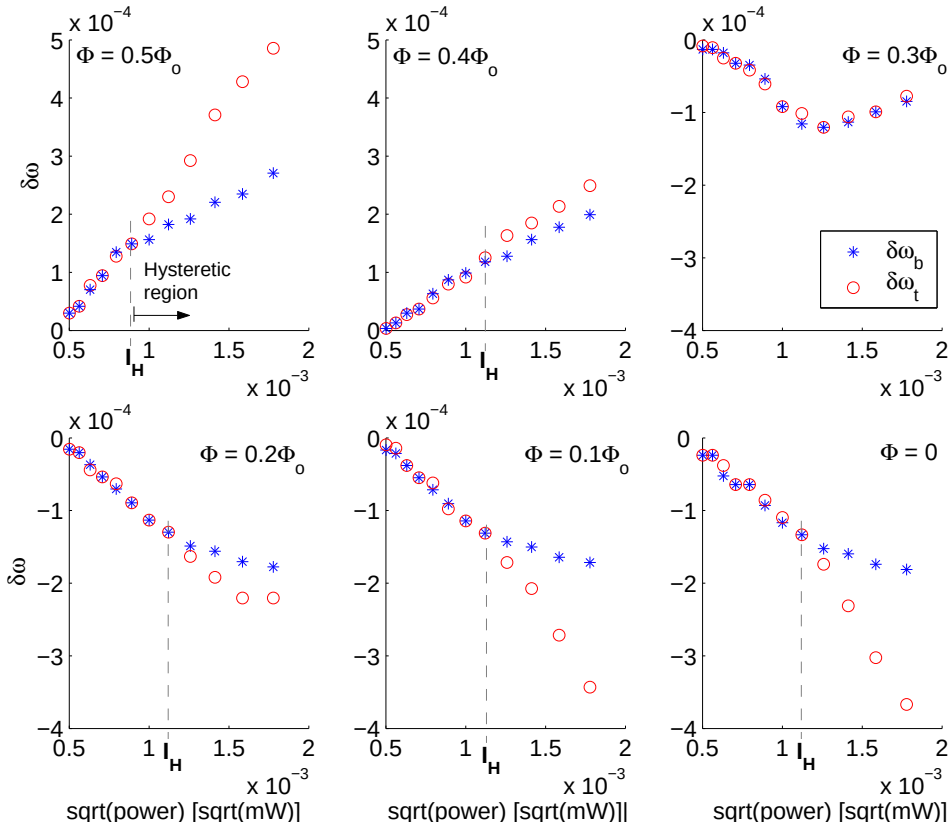

Figure 4-8: A plot of $\delta\omega_t$ and $\delta\omega_b$ as a function of input power for different flux biases. The input power ranges from -66 dBm to -55 dBm in 1 dB step. The extent of the bifurcation region corresponds to $|\delta\omega_t - \delta\omega_b|$. Hysteretic behavior is observed only when the resonant spectrum is highly nonlinear. This occurs when the input bias is above the threshold I_H as labeled in the figures.

4.5 Discussion

In this chapter, we have observed and fully characterized the nonlinear resonant behavior due to the Josephson inductance of the SQUID. The resonant spectrum evolves from being symmetric to asymmetric with increasing level of nonlinearity. The polarity of the asymmetric spectrum is also different depending on the magnetic flux bias. In addition, we performed hysteresis measurements and quantified the extent of the bifurcation region in the spectra. The focus of chapter 5 will be to explain the nonlinear resonant behavior based on results from numerical simulations.

The resonant readout circuit operated in the linear regime has the advantage of keeping the bias current low and reducing the level of decoherence on the qubit. On the other hand, the readout circuit operated in the nonlinear regime can potentially be used as a bifurcation amplifier [48]. This is best illustrated in fig. 4-9, which shows the detection of the qubit signal at a frequency bias f_b. Given the discontinuity of the asymmetric spectrum, one could achieve a better sensitivity when the circuit is biased in the nonlinear regime.

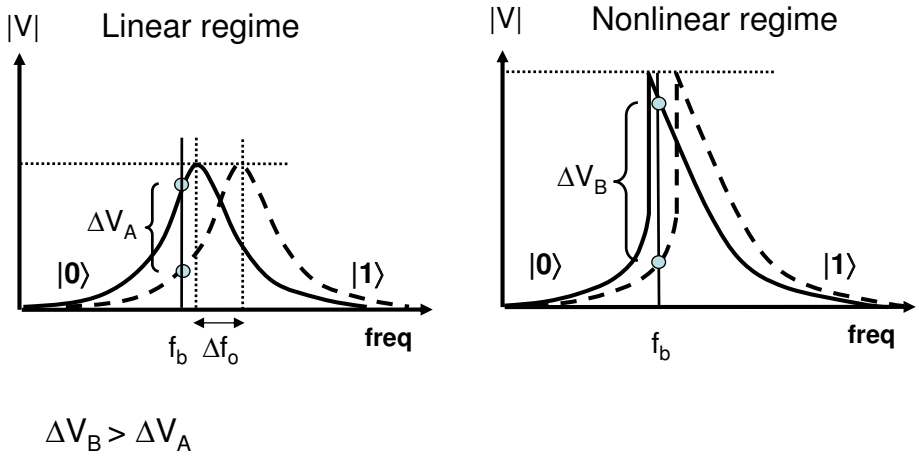

Figure 4-9: Illustration of the nonlinear resonant circuit used as a bifurcation amplifier. The change of voltage signal ΔV_B in the nonlinear case is larger than ΔV_A given the discontinuity of the asymmetric spectrum.

Chapter 5

Simulations of Nonlinear Resonant Behavior in Josephson-junction Circuits

Abstract

The goal of this chapter is to simulate and understand the observed nonlinear resonant behavior of the readout circuit presented in chapter 4. This chapter begins with a discussion of the inductive nature of Josephson elements, followed by an analysis of a single Josephson junction demonstrating the bifurcation phenomenon of the resonant spectrum. To investigate the flux dependence of the resonant behavior, we analyze AC-circuits comprising a SQUID inductor by numerically solving the differential equations. Based on the simulation results, it was suggested that the observed nonlinearity was caused by an oscillating flux that was coupled to the SQUID, rather than the oscillating current bias.

Organization of this chapter

This simulation chapter has been organized in the following way. In section 5.1, a Josephson junction and a SQUID are introduced as nonlinear inductive elements. The purpose is to derive an expression for the Josephson inductance of a SQUID but only in certain biasing limits. Section 5.2 then focuses on the resonant behavior of a single junction; the simplicity allows us to solve the problem analytically and demonstrate the bifurcation phenomenon in the nonlinear resonant spectrum. As we further analyze resonant circuits comprising a SQUID, our approach is to build up a series of resonant circuit models with increasing level of complexity. The results based on three circuit models will be presented in sections 5.4 to 5.6. This approach allows us to gradually include the essential physics to reproduce the nonlinear resonant behavior as observed in the experiment.

5.1 Josephson inductive elements

5.1.1 Josephson inductance of a single junction

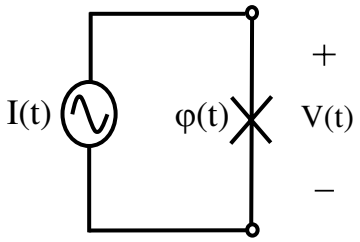

Figure 5-1: Circuit schematic of a Josephson junction.

Josephson junction elements are inductive in nature. This can be derived from the current-phase relation and the voltage-phase relation governing a single junction:

$$I(t) = I_{co} \sin \varphi(t) \tag{5.1}$$

$$V(t) = \frac{\Phi_o}{2\pi} \frac{d\varphi(t)}{dt} \tag{5.2}$$

where I_{co} is the critical current of the junction. Thus, the current of the junction is nonlinear in the gauge-invariant phase φ, while its voltage is proportional to the time derivative of the phase. Recall that the constitutive relation for an inductor is given by

$$V(t) = \frac{d[L(t)i(t)]}{dt} \tag{5.3}$$

where $L \times i$ corresponds to the flux through the inductor. This definition is applicable for the general case when the inductor is nonlinear [1]. If we substitute the current and voltage relations from eqns. 5.1 and 5.2 into eqn. 5.3, we obtain

$$\frac{\Phi_o}{2\pi}\frac{d\varphi}{dt} = \frac{d[L_J(t)I_{co}\sin\varphi]}{dt} \tag{5.4}$$

The Josephson inductance L_J of the junction is extracted to have the following closed-form:

$$L_J = \frac{\Phi_o\varphi}{2\pi I_{co}\sin\varphi} \tag{5.5}$$

where φ is given by $\sin^{-1}(I/I_{co})$. The current-bias dependence of L_J is shown in fig. 5-2. It can be seen that L_J increases with the bias current through the junction as long as the current is below the critical current. Once the current is above I_{co}, the junction is no longer purely inductive [61, 62]. For small bias currents where $I/I_{co} \ll 1$, $\varphi/\sin\varphi$ in eqn. 5.5 is close to unity. In this limit, the junction essentially behaves as a linear inductor with inductance given by $\Phi_o/(2\pi I_{co})$.

5.1.2 Josephson inductance of a SQUID

The above derivation can be extended to extract the Josephson inductance L_J for a SQUID. First, we should note that a SQUID is described by two types of inductances: the Josephson inductance L_J contributed from the Josephson junctions, as well as the loop inductance L_s determined by the geometrical property of the SQUID loop. Unlike the loop inductance, the Josephson inductance is nonlinear and varies with the biasing conditions for the SQUID.

[1] Alternatively, the time-varying inductance can be defined using $V(t) = L(t)(dI(t)/dt)$. The Josephson inductance extracted according to this definition is $L_J = \Phi_o/(2\pi I_{co}\cos\varphi)$ which is also commonly used.

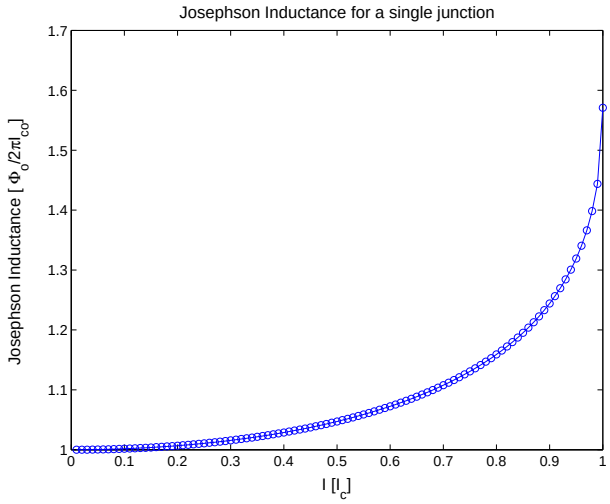

Figure 5-2: Josephson inductance of a single junction as a function of current bias. For $I/I_{co} \ll 1$, the inductance can be approximated by $\Phi_o/(2\pi I_{co})$.

The ratio of the two inductances is usually referred as β_L, and is a useful parameter to gauge the behavior of the SQUID.

$$\beta_L = \frac{L_s}{L_{Jo}} \tag{5.6}$$

$$= \frac{2\pi L_s I_c}{\Phi_o} \tag{5.7}$$

where L_s is equal to $2L$ for the SQUID circuit shown in fig. 5-3, I_c is the critical current of the SQUID given by the sum of the critical currents for both junctions, and L_{Jo} is a constant given by $\Phi_o/(2\pi I_c)$.

For the most general case where the parameters of the SQUID are not restricted by any assumptions, the behavior of the SQUID has to be solved numerically based on the current continuity equation and the fluxiod quantization equation, and the Josephson inductance L_J does not have a closed-form expression. Here, we simplify the problem by assuming the SQUID has *negligible loop inductance* and *symmetric junctions*. The current going through

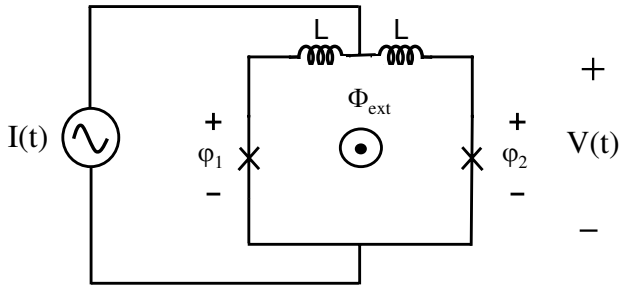

Figure 5-3: Circuit schematic of a SQUID with finite loop inductance

the SQUID is given by

$$I = I_{co} \sin \varphi_1 + I_{co} \sin \varphi_2 \tag{5.8}$$

$$= 2I_{co} \sin \varphi_p \cos \varphi_m \tag{5.9}$$

where we have defined $\varphi_p = (\varphi_1 + \varphi_2)/2$ and $\varphi_m = (\varphi_1 - \varphi_2)/2$. Intuitively, the outer phase variable φ_p is associated with the current bias through the SQUID, while the inner phase variable φ_m is associated with the flux bias through the SQUID loop. The voltage across the SQUID is given by:

$$V = \frac{\Phi_o}{2\pi} \frac{d\varphi_p}{dt} \tag{5.10}$$

Following a similar derivation as eqn. 5.4 for the single junction, we substitute the voltage and current expressions from eqns. 5.9 and 5.10 in eqn. 5.3 to obtain:

$$L_J = \frac{\Phi_o \varphi_p}{4\pi I_{co} \cos \varphi_m \sin \varphi_p} \tag{5.11}$$

Note that φ_p and φ_m are related by the Fluxoid equation:

$$0 = \varphi_m + \frac{2\pi}{\Phi_o} L I_{co} \sin \varphi_m \cos \varphi_p + \frac{\pi \Phi_{ext}}{\Phi_o} \tag{5.12}$$

where Φ_{ext} is the magnetic flux threading the loop, and L corresponds to half the loop

inductance. Since we have assumed the SQUID has negligible loop inductance, φ_m is simply given by $-\pi\Phi_{ext}/\Phi_o$. Thus, eqn. 5.11 can be re-written as:

$$L_J = \frac{\Phi_o \varphi_p}{2\pi I_c(\Phi_{ext}) \sin\varphi_p} \tag{5.13}$$

where $I_c(\Phi_{ext})$ is the *effective critical current* given by $I_c(\Phi_{ext}) = 2I_{co}\cos(\pi\Phi_{ext}/\Phi_o)$, and φ_p is the *effective phase* given by $\varphi_p = \sin^{-1}[I/I_c(\Phi_{ext})]$. Comparing eqn. 5.13 with eqn. 5.5, we see that L_J of a SQUID has the same bias-current dependence as a single junction, but it is also a function of the flux bias. The current and flux dependence is plotted in fig. 5-4. While the Josephson inductance always increases with the bias current, it can increase or decrease with the flux bias due to the periodic dependence.

Finally, in the limit that the current bias is small, $\varphi_p/\sin\varphi_p$ in eqn. 5.13 will be close to unity, and L_J will be dominated by the nonlinearity due to the flux bias:

$$L_J = \frac{\Phi_o}{2\pi I_c(\Phi_{ext})} \tag{5.14}$$

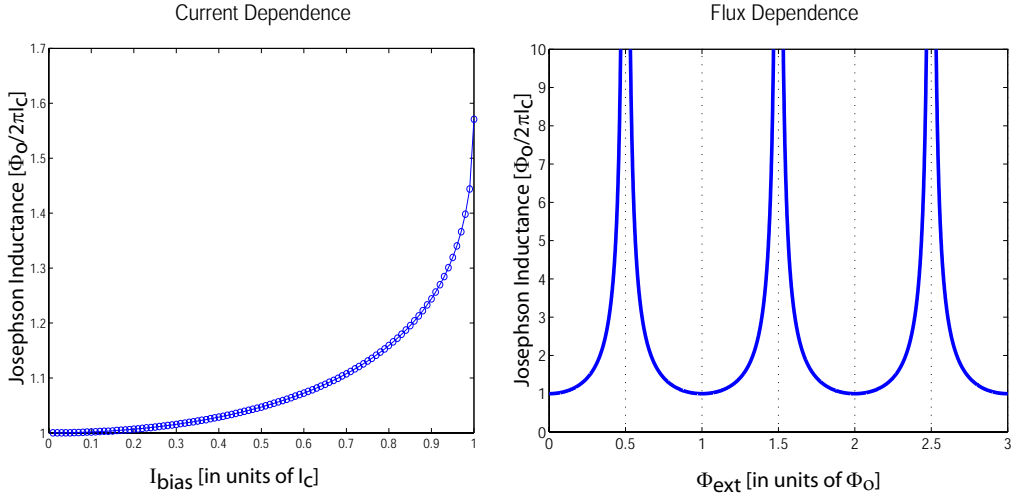

Figure 5-4: The current and flux dependence of the Josephson inductance of a SQUID. The Josephson inductance always increases with the bias current, but it can increase or decrease with the flux bias due to the periodic dependence.

5.2 Analysis of an AC-driven Josephson junction using the Harmonic Balance approach

In this section, we will analyze the behavior of a Josephson junction driven by an AC current source. A single junction described by the RCSJ model exhibits resonant behavior similar to a SQUID shunted by an external capacitor and resistor. The simplicity of a single junction compared to a SQUID allows us to capture the effects of the Josephson inductance, and still be able to express the nonlinear behavior analytically using the harmonic balance approach.

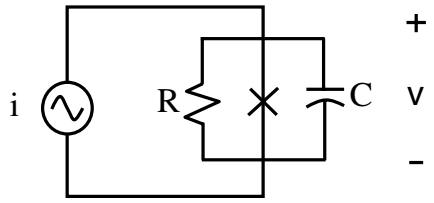

Figure 5-5: RCSJ model of a single junction driven by a sinusoidal current source.

5.2.1 Nonlinear Resonant Behavior

The circuit model of the junction is shown in fig. 5-5. In the case when it is driven by a sinusoidal current source $I(t) = I \sin \omega t$, the system is governed by a second-order nonlinear differential equation:

$$I \sin \omega t = \frac{C\,\Phi_o}{2\pi I_c}\frac{d^2\varphi}{dt^2} + \frac{\Phi_o}{2\pi I_c R}\frac{d\varphi}{dt} + \sin \varphi \tag{5.15}$$

where φ is the gauge invariant phase, and I is the amplitude of the current source normalized with respect to the critical current of the junction I_c. We have used the voltage-phase relation

$$V = \frac{\Phi_o}{2\pi}\frac{d\varphi}{dt} \tag{5.16}$$

The differential equation in 5.15 has the same form as the equation of motion for a driven pendulum with damping. The sine term contributes to the nonlinearity. We want to solve for the magnitude and phase of the junction voltage as a function of the driving frequency. First we assume the trial solution for φ to be in the form:

$$\varphi = A\sin(\omega t + \theta) \tag{5.17}$$

where A is the magnitude and θ the phase shift with respect to the sinusoidal drive. The assumptions we have made with the trial solution are as follows: (1) it does not contain transient components as we are interested only in the steady state solution; (2) the solution is primarily made up of the fundamental frequency. Given the nonlinear nature of the circuit, we expect the true output to contain frequency components other than the driving frequency. Nevertheless, the results from the numerical simulations suggested that the fundamental frequency is the most dominant, followed by the third harmonic which is reasonably small and can be omitted for first approximation. With φ evaluated, the voltage across the junction can be calculated:

$$\begin{aligned} V &= \frac{\Phi_o}{2\pi}\frac{d\varphi}{dt} \\ &= A\omega\frac{\Phi_o}{2\pi}\cos(\omega t + \theta) \end{aligned} \tag{5.18}$$

Using the harmonic balance approach, we substitute the trial solution in 5.17 in the differential equation 5.15. First we evaluate

$$\frac{d^2\varphi}{dt^2} = -A\omega^2\sin(\omega t + \theta) \tag{5.19}$$

$$\frac{d\varphi}{dt} = A\omega\cos(\omega t + \theta) \tag{5.20}$$

$$\begin{aligned} \sin\varphi &= \sin(A\sin(\omega t + \theta)) \\ &= \sum_{n=-\infty}^{\infty} J_n(A)\sin n(\omega t + \theta) \\ &= 2J_1(A)\sin(\omega t + \theta) + 2J_3(A)\sin 3(\omega t + \theta) + \ldots \end{aligned} \tag{5.21}$$

Note that we have expanded the nonlinear term $\sin\varphi$ in a series of Bessel functions. The expansion into Bessel functions conveniently groups the same harmonics together, and thus is advantageous over Taylor series. We shall be keeping only the terms of the fundamental frequency in eqn. 5.21. Substituting expressions 5.19- 5.21 in the differential equation gives:

$$I\sin\omega t = (-aA\omega^2\cos\theta - bA\omega\sin\theta + 2cJ_1(A)\cos\theta)\sin\omega t + (-aA\omega^2\sin\theta + bA\omega\cos\theta + 2cJ_1(A)\sin\theta)\cos\omega t \quad (5.22)$$

where the constants a,b, and c are given by the circuit parameters.

$$a = \frac{C\Phi_o}{2\pi I_c} = \frac{1}{w_o^2} \quad (5.23)$$

$$b = \frac{\Phi_o}{2\pi I_c R} = \tau_{RC} \quad (5.24)$$

$$c = 1 \quad (5.25)$$

Equating the sine and cosine terms on both sides of eqn. 5.22 yields two equations:

$$0 = (2cJ_1(A) - aA\omega^2)\sin\theta + bA\omega\cos\theta \quad (5.26)$$

$$I = (2cJ_1(A) - aA\omega^2)\cos\theta - bA\omega\sin\theta \quad (5.27)$$

Our goal is to solve for the transfer functions A(ω) and $\theta(\omega)$. However, this requires solving for an unknown embedded in the Bessel function. Instead, we could solve for $\omega(A)$ and $\theta(A)$. First, we rearrange eqn. 5.26 and obtain:

$$\frac{\sin\theta}{\cos\theta} = \frac{bA\omega}{aA\omega^2 - 2cJ_1(A)} \quad (5.28)$$

$$or \qquad \sin\theta = \frac{bA\omega}{\sqrt{[aA\omega^2 - 2cJ_1(A)]^2 + (bA\omega)^2}} \quad (5.29)$$

$$\cos\theta = \frac{aA\omega^2 - 2cJ_1(A)}{\sqrt{[aA\omega^2 - 2cJ_1(A)]^2 + (bA\omega)^2}} \quad (5.30)$$

Substituting eqns. 5.29 and 5.30 into eqn. 5.27 gives:

$$-\sqrt{[aA\omega^2 - 2cJ_1(A)]^2 + (bA\omega)^2} = I \tag{5.31}$$

Squaring both sides of the equation,we obtain a *biquadratic equation* in ω.

$$(a^2A^2)\omega^4 + (b^2A^2 - 4aAcJ_1(A))\omega^2 + (4c^2{J_1}^2(A) - I^2) = 0 \tag{5.32}$$

Let

$$\alpha = a^2A^2 \tag{5.33}$$

$$\beta = b^2A^2 - 4aAcJ_1(A) \tag{5.34}$$

$$\gamma = 4c^2{J_1}^2(A) - I^2 \tag{5.35}$$

The roots of the biquadratic equation $(\omega^2)_\pm$ can be evaluated over a range of A:

$$(\omega^2)_\pm = \frac{-\beta \pm \sqrt{\beta^2 - 4\alpha\gamma}}{2\alpha} \tag{5.36}$$

Imaginary roots corresponding to the discriminant in eqn. 5.36 being negative are rejected. $\omega_\pm$ can be further obtained by taking the positive square root of $\omega_\pm^2$

$$\omega_\pm(A) = +\sqrt{(\omega^2)_\pm} \tag{5.37}$$

After we have solved for $\omega_\pm$, we use eqn. 5.30 and eqn. 5.18 to solve for the phase $\theta(\omega)$ and magnitude $|V(\omega)|$ of the junction voltage, respectively.

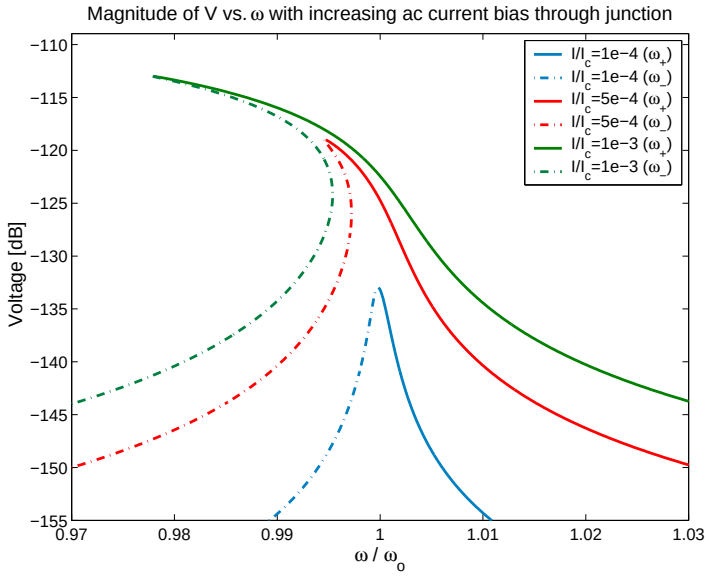

Figure 5-6: A series of magnitude spectra $|V(\omega)|$ with increasing current bias I. For small values of I, the spectrum has a symmetric shape similar to the linear resonant circuit. As the bias current increases, the spectra become more asymmetric with a lower resonant frequency.

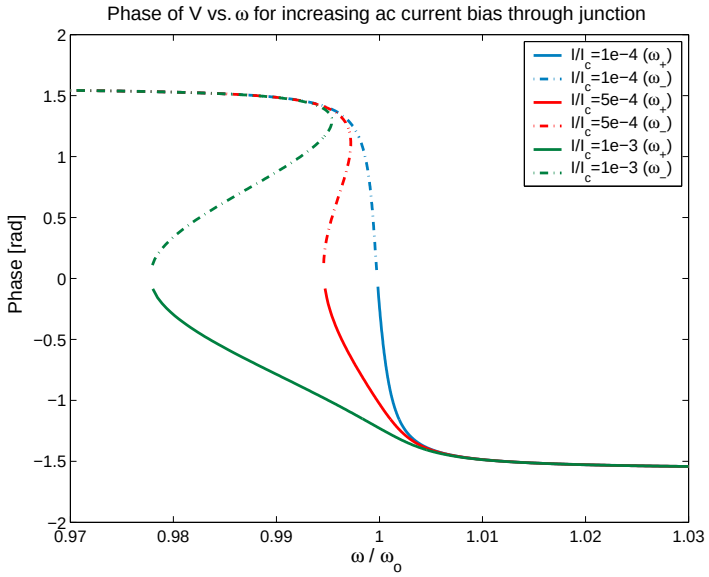

Figure 5-7: Phase spectra $\theta(\omega)$ with increasing current bias.

A series of magnitude and phase spectra of the junction voltage for increasing values of the biasing current I are shown in figs. 5-6 and 5-7. For small values of I with respect to I_c, the magnitude resonant spectrum has a symmetric Lorentzian shape similar to the linear resonant circuit. As the bias current increases, the spectra become more asymmetric with the maxima bending towards the lower frequency side. *This bending towards the lower frequency indicates that the effective inductance over an oscillating period increases.* The phase spectra also evolves as a function of increasing current bias, exhibiting a 180^o shift near the resonant frequency with a slope limited by the quality factor in the linear regime, and becoming multi-valued with increasing bias similar to the magnitude spectra.

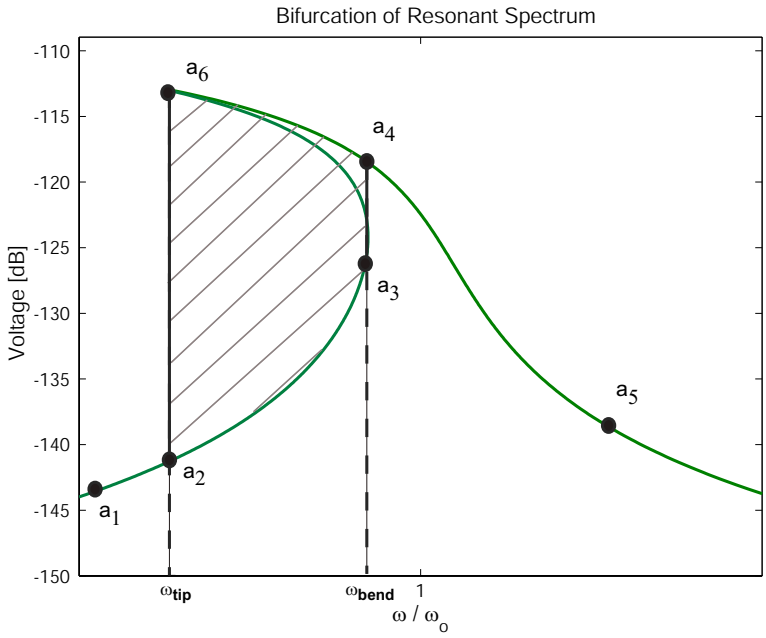

Figure 5-8: Illustration of the bifurcation region in a nonlinear magnitude spectrum. The bifurcation region is bound by ω_{tip} and ω_{bend}, over which there are two stable solution branches marked by [a_2,a_3], [a_4,a_6] and one instable branch marked by [a_3,a_6].

The region over ω/ω_o where multiple solutions occur is referred to as the *bifurcation region.* The bifurcation region for the resonant spectrum is denoted by the shaded region bound by points a_2, a_3, a_4, and a_6 in fig. 5-8. Of the three solution branches within the bifurcation region, the two branches marked by [a_2,a_3] and [a_4,a_6] are stable, while the instable branch is marked by [a_3,a_6]. If the system initially starts at point a_1 and is driven

by increasing frequency, the resulting spectrum will be described by the path a_1-a_2-a_3-a_4-a_5. On the other hand, if the system is then driven by decreasing frequency from a_5, the resulting spectrum will follow a different path a_5-a_4-a_6-a_2-a_1. Thus, hysteretic behavior will be observed, and the amount of hysteresis corresponds to the extent of the bifurcation region.

The nonlinear resonant behavior shown in fig. 5-8 has been demonstrated experimentally in a single junction [63], and in a stripline resonator based on a superconducting NbN granular film with nonlinear inductance due to weak links [64]. Furthermore, the resonant behavior of an LC circuit comprising a varacter diode also demonstrates similar characteristics [2] [65].

5.2.2 Quantifying the Bifurcation Phenomenon

In this section, we want to develop a tool for quantifying the amount of nonlinearity in the resonant circuit by mathematically describing the extent of the bifurcation region in the resonant spectra. In particular, we want to characterize how the positions of a_3 and a_6 in fig. 5-8 change with increasing current bias I to the junction. Considering the hysteresis picture described in the previous section, a_3 corresponds to the discontinuous point at which the *forward* spectrum jumps from the lower to the higher stable branch. Similarly, a_6 corresponds to the point at which the *backward* spectrum falls from the higher to the lower stable branch. Quantifying the nonlinearity in this way allows us to compare the simulation results with experimental data.

High-frequency bound of bifurcation region

To find the high frequency bound ω_{bend} of the bifurcation region, we first recognize that it occurs at the point where the derivative of $\omega_-(A)$ is zero (a_3 in fig. 5-8). From eqns. 5.36 and 5.37, we first obtained a simplified expression for $\omega_-(A)$:

$$\omega_-(A) = \left[\left(\frac{4acJ_1(A) - b^2A}{2a^2A}\right) - \left(\frac{b^4A^2 - 8ab^2cAJ_1(A) + 4a^2I^2}{4a^4A^2}\right)^{\frac{1}{2}}\right]^{\frac{1}{2}} \tag{5.38}$$

[2]The capacitance is nonlinear with the voltage across the diode. The diode capacitance can be approximated by $C_d(v) = C_d(0)/\sqrt{(1 - v/V_\varphi)}$, where $C_d(0)$ is the differential capacitance at v=0, and V_φ is the contact potential of the PN junction.

Let

$$u(A) = \frac{4acJ_1(A) - b^2A}{2a^2A} \tag{5.39}$$

$$v(A) = \frac{b^4A^2 - 8ab^2cAJ_1(A) + 4a^2I^2}{4a^4A^2} \tag{5.40}$$

$\omega_-(A)$ and its derivative can be written as:

$$\omega_-(A) = (u - \sqrt{v})^{\frac{1}{2}} \tag{5.41}$$

$$\omega_-{}'(A) = \frac{1}{2}(u - \sqrt{v})^{-\frac{1}{2}} \left(\frac{du}{dA} - \frac{1}{2\sqrt{v}}\frac{dv}{dA}\right) \tag{5.42}$$

where

$$\frac{du}{dA} = -\frac{2cJ_2(A)}{aA} \tag{5.43}$$

$$\frac{dv}{dA} = \frac{2b^2cA^2J_2(A) - 2aI^2}{a^3A^3} \tag{5.44}$$

and we have used the identity $(J_1(A)/A)' = -J_2(A)/A$. Eqns. 5.41 and 5.42 are shown in fig. 5-9. Setting the derivative in eqn. 5.42 to zero and letting the solution be A_{bend}, or simply A_b:

$$\frac{du}{dA_b} - \frac{1}{2\sqrt{v}}\frac{dv}{dA_b} = 0 \tag{5.45}$$

Squaring both sides of eqn. 5.45 , we obtain a biquadratic equation in I in terms of A_b:

$$\left(\frac{4}{a^4(A_b)^6}\right) I^4 + \left(\frac{-8cJ_2(A_b)[b^2 + 2acJ_2(A_b)]}{a^5(A_b)^4}\right) I^2 + \left(\frac{32b^2c^3J_1(A_b)J_2^2(A_b)}{a^5(A_b)^3}\right) = 0 \tag{5.46}$$

Let

$$D_1 = \frac{4}{a^4(A_b)^6} \tag{5.47}$$

$$D_2 = \frac{-8cJ_2(A_b)[b^2 + 2acJ_2(A_b)]}{a^5(A_b)^4} \tag{5.48}$$

$$D_3 = \frac{32b^2c^3J_1(A_b)J_2^2(A_b)}{a^5(A_b)^3} \tag{5.49}$$

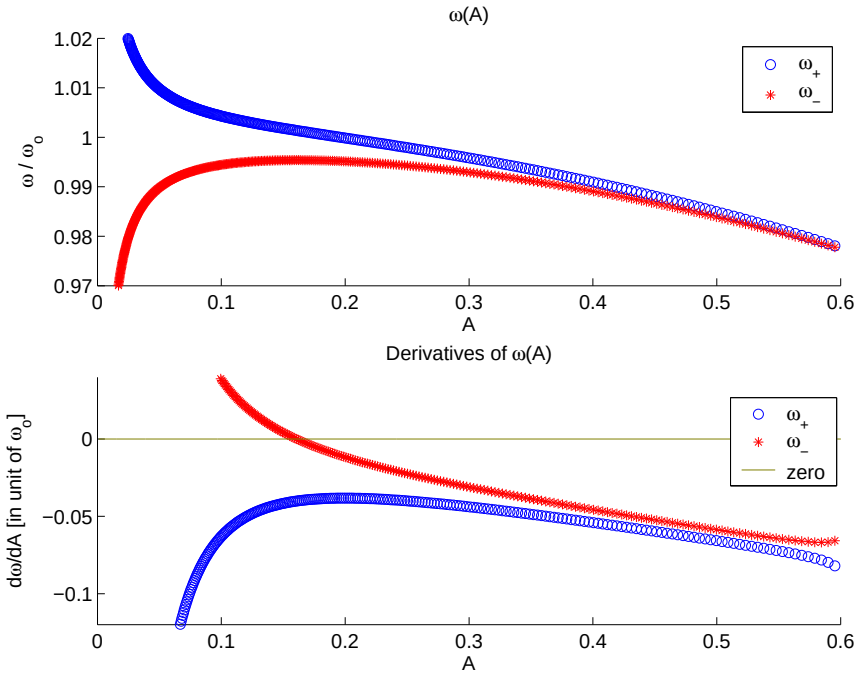

Figure 5-9: $\omega_{-}(A)$ and $\omega_{-}{}'(A)$ in eqns. 5.41 and 5.42 respectively. The point a_3 of the bifurcation region illustrated in fig. 5-8 corresponds to when $\omega_{-}{}'(A)$ is zero.

Our goal is to use eqn 5.46 to solve for $A_b(I)$, which describes how the point at which the derivative of $\omega_{-}(A)$ is zero changes as a function of bias current. However given that A_b is embedded in a Bessel function, it is mathematically easier to solve for $I(A_b)$ instead. This is given by the negative root of the biquadratic equation:

$$I(A_b) = \left(\frac{-D_2 - (D_2^2 - 4D_1D_3)^{\frac{1}{2}}}{2D_1} \right)^{\frac{1}{2}} \tag{5.50}$$

Note that while an analytical expression is obtained for $I(A_b)$, *it is not feasible to extract an analytical expression for* $A_b(I)$ *or* $\omega_b(I)$ *due to the Bessel function dependence.* It will be seen later that this poses a challenge when we try to fit the experimental data. Figs. 5-10 shows the results for $A_b(I)$ and $w_b(I)$ calculated numerically over a range of I. We have introduced a parameter $\delta\omega_b$ which normalizes ω_b relative to the resonant frequency of the linear spectrum ω_o:

$$\delta\omega_b = \frac{\omega_b - \omega_o}{\omega_o} \tag{5.51}$$

where ω_o is given by:

$$w_o = \frac{1}{\sqrt{L_J C}} = \sqrt{\frac{2\pi I_c}{\Phi_o C}} \tag{5.52}$$

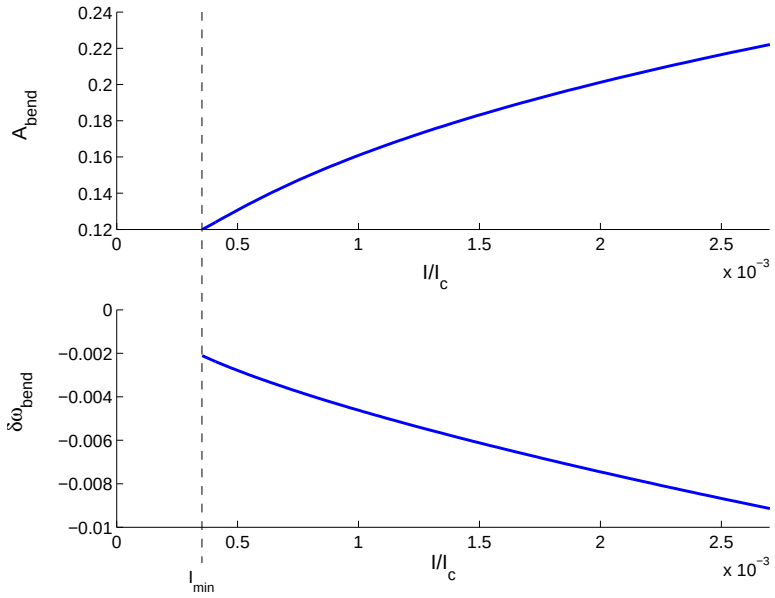

Figure 5-10: Top: A_b calculated as a function of bias current I given by eqn. 5.50. Bottom: $\delta\omega_b$ calculated based on eqns. 5.50 and 5.41. Note that the range of I/I_c for both figures is restricted to be between I_{min} and I_{max}. I_{min} corresponds to the onset of the bending of the spectrum, below which $\omega^{'}(A)$ doesn't have a zero crossing. I_{max} is a constraint imposed by the low frequency bound of the bifurcation region (see fig. 5-11).

Low-frequency bound of bifurcation region

The low-frequency bound of the bifurcation region corresponds to the tip of the resonant spectrum (position a_6 in fig. 5-8). It occurs when the discriminant in eqn. 5.36 is zero. Let the solution be A_{tip} and ω_{tip} (or simply A_t and ω_t), our goal is to solve for their dependence with bias current.

$$\beta^2 - 4\alpha\gamma = b^4 {A_t}^4 - 8ab^2 c {A_t}^3 J_1(A_t) + 4a^2 {A_t}^2 I^2 = 0 \tag{5.53}$$

$$I = \sqrt{\frac{8ab^2 c A_t J_1(A_t) - b^4 {A_t}^2}{4a^2}} \tag{5.54}$$

$A_t(I)$ based on eqn. 5.54 is plotted in fig. 5-11. Referring to the figure, I is restricted to be less than I_{max}. For values of I above I_{max}, the discriminant is always above zero and does not have a zero-crossing. In addition, values of $A_t > A_t(I_{max})$ have to be rejected to keep the function single-valued. The normalized frequency $\delta\omega_t(I) = (\omega_b(I) - \omega_o)/\omega_o$ is also plotted in fig. 5-12.

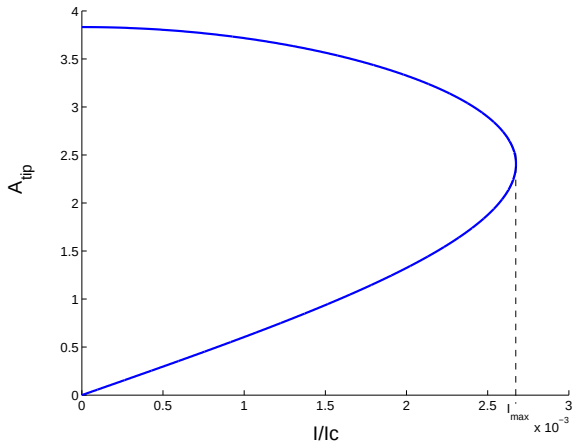

Figure 5-11: A_t as a function of current bias I [eqn. 5.54]. The discriminant has a zero-crossing only for values of I below I_{max}. Values of $A_t > A_t(I_{max})$ have to be rejected to keep the function single-valued.

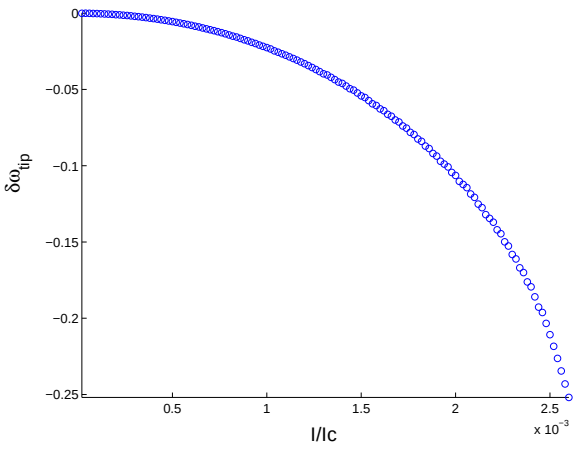

Figure 5-12: $\delta\omega_t$ as a function of current bias I.

Finally, we have combined the results for the high frequency bound $\delta\omega_b$ from fig. 5-10 and the low frequency bound $\delta\omega_t$ from fig. 5-12. This is shown in fig. 5-13. ω_t corresponds to the "tip" of the resonant spectrum, and ω_b corresponds to the "inside bend" where the spectrum is momentarily vertical. The extent of the bifurcation region is defined by $|\omega_b - \omega_t|$. We observe that $\delta\omega_t$ increases faster than $\delta\omega_b$ with input bias. In other words, the extent of the tip of the spectrum grows faster than the inside bend.

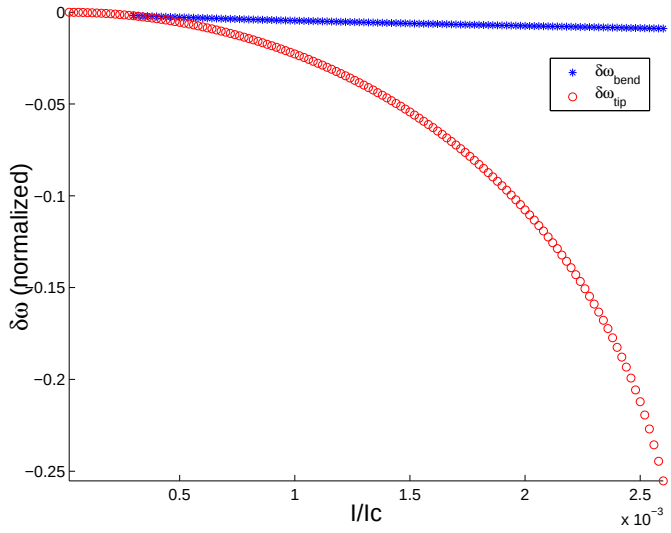

Figure 5-13: A plot of $\delta\omega_t$ and $\delta\omega_b$ as a function of increasing bias current to the junction. The extent of the bifurcation region is defined by $|\omega_b - \omega_t|$. A general observation is that $\delta\omega_t$ increases faster than $\delta\omega_b$ with input bias.

5.2.3 Comparison of Simulations with Experimental Data at $\Phi = 0$

In this section, we compare the nonlinear resonant behavior simulated for a single junction with the experimental data for the SQUID resonant circuit. At zero flux bias, a SQUID essentially behaves like a single junction, thus we shall expect the characteristics of the readout circuit at $\Phi = 0$ to be comparable to the simulations. The basis for comparison will be on (1) the shape of the resonant spectra and (2) the amount of nonlinearity characterized by $\delta\omega$ as a function of input bias.

(1) Comparison based on shapes of resonant spectra

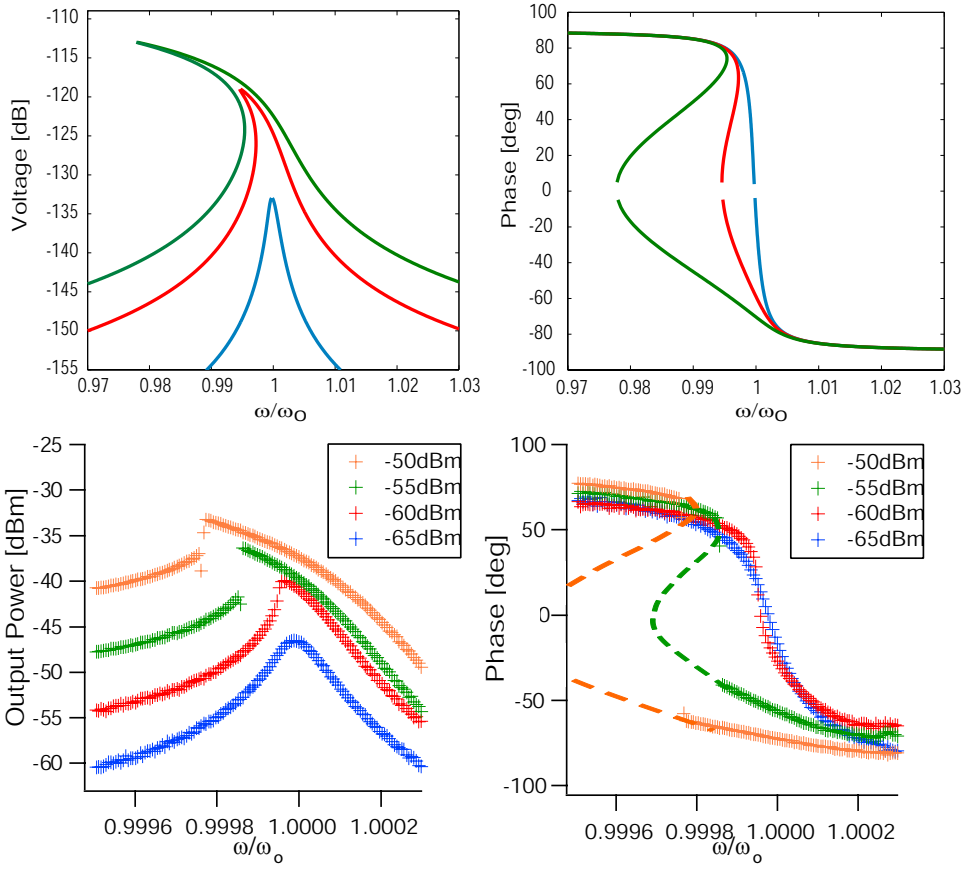

Figure 5-14: A side-by-side comparison between the simulation results for a single junction (top), and the experimental data for the readout circuit at $\Phi = 0$ (bottom). The observed evolution of the spectra from the linear to the nonlinear regime is qualitatively similar to the simulations.

A side-by-side comparison between the simulation results and the experimental data at $\Phi = 0$ is shown in fig. 5-14. The series of resonant spectra correspond to increasing current bias for the simulations, and increasing input power for the data. The observed evolution of the spectra from the linear and the nonlinear regime is qualitatively similar to the simulations. In particular, the nonlinear spectra are asymmetric with a lower resonant frequency, indicating that at $\Phi = 0$, the effective Josephson inductance over an oscillation period increases just like a single junction. The discontinuity observed in the data occurs when the system jumps from the lower stable branch to the higher stable branch over the bifurcation

region. Since the data were obtained by driving the readout circuit with increasing frequency, only the high-frequency bound of the bifurcation region was captured.

(2) Comparison based on the amount of nonlinearity in resonant spectra

Next, we compare the amount of nonlinearity in the resonant circuit as a function of input bias. Fig. 5-15 is a zoom-in of fig. 5-13. We shall define three biasing regions: the *linear*, the *nonlinear*, and the *hysteretic* regions. The definitions are summarized in the following table.

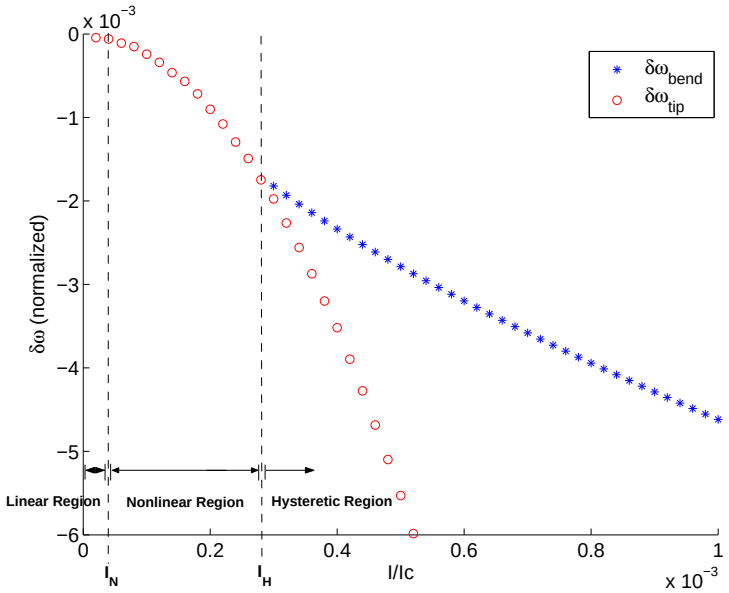

Figure 5-15: Graphical illustration of the linear region, the nonlinear region, and the hysteretic region. I_N labeled in the figure marks the transition from the the linear to the nonlinear region, while I_H marks the transition from the nonlinear to the hysteretic region.

Linear Region ($I < I_N$)	The resonant spectrum is linear and has a symmetric shape, with a resonant frequency of ω_o.
Nonlinear Region ($I_N < I < I_H$)	The resonant spectrum starts to become asymmetric, but remains single-valued and is characterized by a single resonant frequency different from ω_o.
Hysteretic Region ($I > I_H$)	The resonant spectrum is asymmetric with a well-defined bifurcation region where multiple solutions exist. The spectrum is characterized by ω_{tip} and ω_{bend}.

I_N corresponds to the threshold bias where the spectrum makes the transition from the *linear* to the *nonlinear* region, where as I_H marks the transition from the *nonlinear* to the *hysteretic* region.

Fig. 5-16 shows the experimental data of $\delta\omega_t$ and $\delta\omega_b$ at $\Phi = 0$ obtained from the hysteresis measurement discussed in section . Comparing the trend of $\delta\omega$ with the simulations, we find that the transition from the nonlinear to the hysteretic region occurs near the input bias of $I_H \sim 1.12 \times 10^{-3}\sqrt{mW}$, which corresponds to -59 dBm in input power. In fig. 5-17, the data were obtained by sweeping the driving frequency in the forward direction only, so only $\delta\omega_b$ was captured. The measurements extend into the range of low bias, which shows the transition from the linear to the nonlinear regime at $I_N \sim 2.8 \times 10^{-4}\sqrt{mW}$ corresponding to an input power of -71 dBm. The value of I_N was determined based on a more complete set of data at various flux biases presented previously in fig. 4-5.

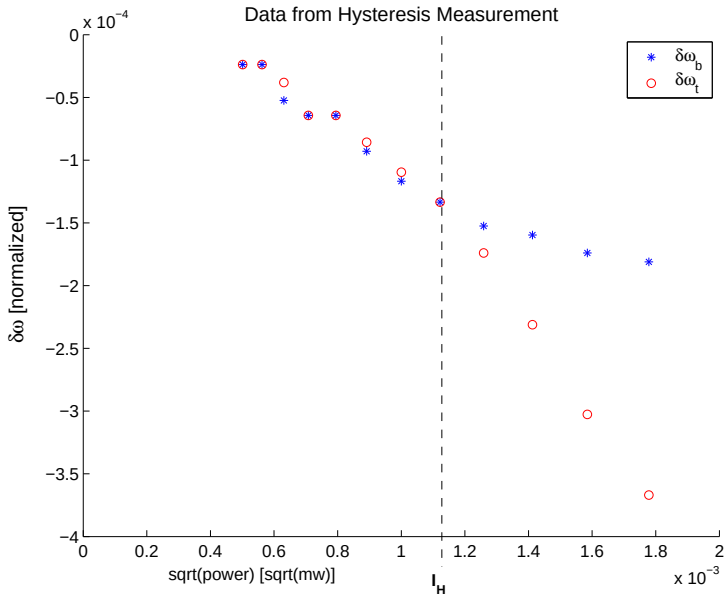

Figure 5-16: Data for $\delta\omega_t$ and $\delta\omega_b$ obtained from both forward and backward frequency sweeps over input power of -66 dBm to -55 dBm. This set of data was previously presented in fig. 4-8.

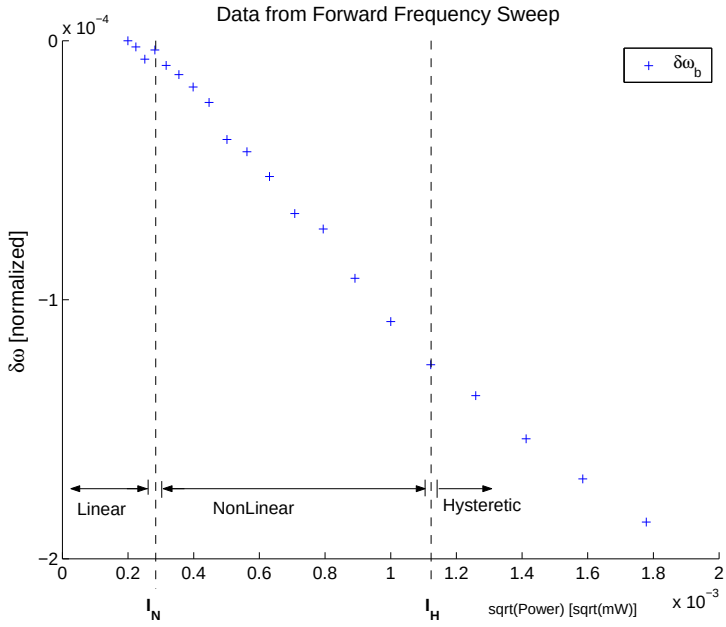

Figure 5-17: Data for $\delta\omega_b$ at $\Phi = 0$ obtained from a forward frequency sweep over input power of -74 dBm to -54 dBm. This set of data was previously presented in fig. 4-5.

5.3 Introduction: Numerical Simulations of Resonant Circuits comprising a SQUID Inductor

In the previous section, the simplicity of a single junction allows us to solve the resonant behavior analytically. To analyze the resonant behavior of an AC-driven circuit comprising a SQUID, one needs to numerically solve the differential equations governing the SQUID consistently with the equations governing the rest of the circuit. The numerical simulations can be difficult due to the complexity of the set of coupled differential equations. This is especially true when the circuit model needs to include the asymmetry of the SQUID junctions, as well as the self inductance and mutual coupling between the circuit loops. Special care has to be taken to ensure that (1) the variables used are the state variables, which correspond to the minimal number of variables necessary to describe the system [66]; (2) the differential equations are normalized, as well as scaled properly with time [appendix]; (3) if possible, the highest derivative of the equations are of the same order. Otherwise, one runs into a set of differential-algebraic equations (DAEs) [70] which are numerically more

challenging to solve.

The approach that we have taken is to develop a series of circuit models which in general has increasing level of complexity. Here, we will present the results based on three circuit models. The first model was developed based on a phenomenological approach. This so-called "toy model" helps us identify the essential physics that is needed to reproduce the nonlinear resonant behavior as observed in the experiment. It is particular useful for us to present the toy model here as a tool to explain things in an intuitive and qualitative manner. The other two models which follow are more detailed and can better represent the actual readout circuit.

In simulating the nonlinear behavior of these resonant circuits, an important idea to keep in mind is that the observed nonlinearity of the SQUID is the result of a competing effect between its two biasing parameters: an oscillating current bias and an oscillating magnetic flux bias. These two parameters can have similar or opposite effects on the nonlinearity depending on the value of the DC flux bias.

5.4 Toy resonant model– a phenomenological approach

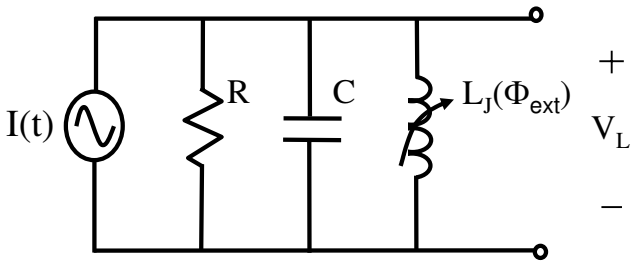

Figure 5-18: Circuit schematic of the toy resonant model driven by a sinusoidal current source. The SQUID is represented by a flux-dependent inductor L_J with inductance given by the functional form in eqn. 5.55. L_J is subjected to an external flux Φ_{ext} which has a DC component as well as an oscillating component.

The circuit schematic of the toy resonant model is shown in 5-18. The SQUID is shown as a nonlinear inductor shunted by an external capacitor and a resistor. The circuit is driven by a sinusoidal current source $I(t) = I \sin \omega t$.

There are two important properties of the toy model:

1. The Josephson inductance of the SQUID is modeled by a flux-dependent nonlinear inductor $L_J(\Phi_{ext})$ which has an analytical form.

2. The external flux Φ_{ext} that is coupled to the inductor has a DC component, as well as an AC component that is proportional to its self-induced flux Φ_L.

5.4.1 Mathematical Analysis

First, we model the Josephson inductance L_J of the SQUID by an analytical form:

$$L_J(\Phi_{ext}) = \frac{\Phi_o}{2\pi I_c(\Phi_{ext})} \tag{5.55}$$

where

$$I_c(\Phi_{ext}) = I_{co}\sqrt{2[(1+\cos\left(\frac{2\pi\Phi_{ext}}{\Phi_o}\right) + (\frac{\Delta_I}{I_c})^2(1-\cos\left(\frac{2\pi\Phi_{ext}}{\Phi_o}\right))]} \tag{5.56}$$

Eqn. 5.56 is a general expression for the critical current of a SQUID with asymmetric junctions of critical currents $I_{co} \pm \Delta_I$ [71]. It has assumed the SQUID has negligible loop inductance. In the limit that $\Delta_I = 0$, then the equation reduces to $I_c(\Phi_{ext}) = 2I_{co}\cos(\pi\Phi_{ext}/\Phi_o)$ used in eqn. 5.13. With reference to eqn. 5.14, eqn. 5.55 gives the Josephson inductance of a SQUID of critical current $I_c(\Phi_{ext})$ in the limit that the current bias is small compared to the critical current. While the assumptions that the SQUID has negligible loop inductance and that the bias current is small may not necessarily be true for the actual circuit, being able to describe the SQUID inductor with an analytical expression provides a good starting point. In addition, the fact that eqn. 5.55 does not include the current dependence allows us to isolate out the nonlinear effect solely due to an oscillating magnetic flux, which turns out to be very useful.

Fig. 5-19 shows the dependence of L_J as a function of magnetic flux for different amount of critical-current asymmetry Δ_I as given by eqns. 5.55 and 5.56. To help our subsequent discussion about the shape of the modulation curve, we keep track of the positions of the inflection points on the curve, i.e. when the curve changes its concavity. The inflection point

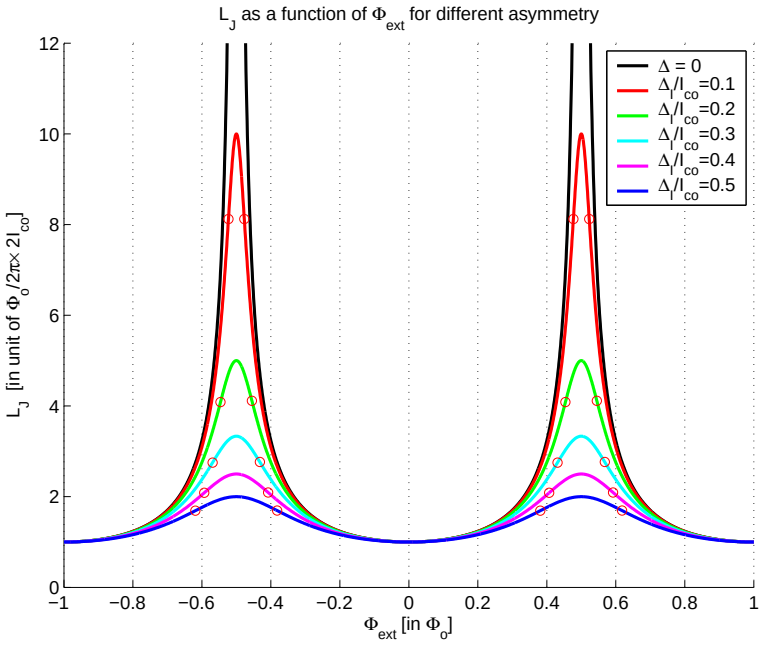

Figure 5-19: Dependence of L_J as a function of magnetic flux for different amount of critical-current asymmetry Δ_I as given by eqns. 5.55 and 5.56. The asymmetry reduces the amount of modulation of L_J with flux, and it also changes the positions of the inflection points denoted by the circular markers.

occurs when the second derivative of $L_J(\Phi_{ext})$ is zero:

$$\frac{d^2 L_J(\Phi)}{d\Phi^2} = 0 \tag{5.57}$$

The inflection points are marked in fig. 5-19. We observed that the inclusion of the asymmetry in the junctions has two effects on the shape of the modulation curve: (1) it reduces the amount of modulation of L_J with flux; (2) it changes the positions of the inflection points.

The resonant frequency of the circuit is given by $1/2\pi\sqrt{L_J C}$ and is plotted in fig. 5-20 for different amount of asymmetry. A side-by-side comparison with the experimental data based on the shape of the modulation curve and the positions of the inflection points suggests that the asymmetry of the junctions are around $\Delta_I = 0.5\, I_c$, and this is the value that we will use for the simulations [3].

[3]In practice, the amount of asymmetry in the fabricated junctions may not be so large, but this value captures the behavior of the data with the toy model.

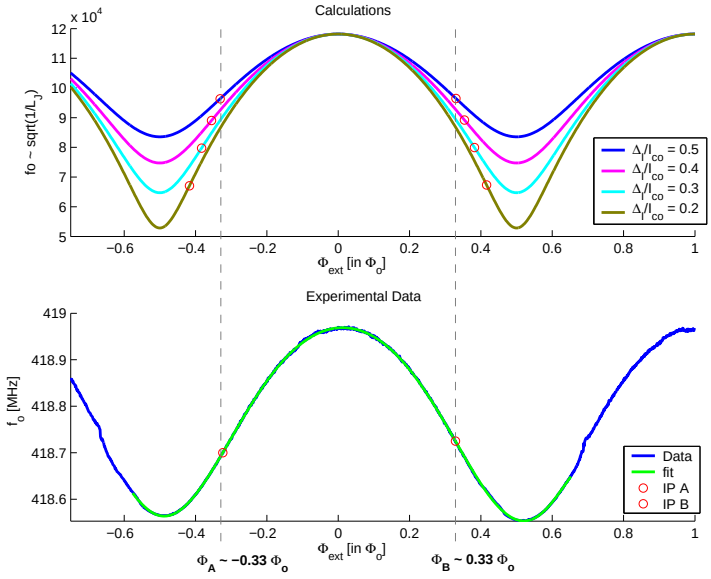

Figure 5-20: Side-by-side comparison of the frequency modulation data with the calculations. The locations of the inflection points suggest that $\Delta_I = 0.5 I_c$.

We now solve the differential equations governing the resonant circuit in fig. 5-18. It is a second-order nonlinear differential equation in the variable Φ_L

$$I \sin \omega t = C \frac{d^2 \Phi_L}{dt^2} + \frac{1}{R} \frac{d\Phi_L}{dt} + \frac{\Phi_L}{L_J(\Phi_{ext})} \tag{5.58}$$

where Φ_L is the flux through the SQUID inductor given by $L_J \times I_L$, and Φ_{ext} is given by

$$\Phi_{ext} = \Phi_{dc} + \Phi_{ac} \tag{5.59}$$

$$\Phi_{ac} = \alpha \Phi_L \tag{5.60}$$

which has a DC component, as well as an AC component that is proportional to Φ_L with proportionality constant α. This brings us to the second property of the toy model: as Φ_L gets large *near the resonant frequency* of the circuit, the amount of external oscillating flux that is coupled to the SQUID also increases, and thus the Josephson inductance becomes more nonlinear. Moreover, the effective inductance over an oscillation period can either increase or decrease depending on the DC flux bias.

5.4.2 Simulation Results

Time-domain results

A typical time signal of the output voltage $V_L(t) = d\Phi_L(t)/dt$ is shown in fig. 5-21. The particular driving frequency was at $\omega_s = 0.9$ GHz, and the flux bias was $\Phi = 0.5\,\Phi_o$. The Fourier transform analysis of the steady state solution reveals that the signal is primarily made up of the fundamental frequency ω_s (at 0.9 GHz), followed by the third harmonic $3\,\omega_s$ (at 2.7 GHz) which is six orders of magnitude smaller.

Similarly, the time signal of the inductance $L_J(t)$ is shown in fig. 5-22. Also referring to the illustration in fig. 5-25, $L_J(t)$ oscillates around the maximum value of 0.1432 nH at $\Phi = 0.5\,\Phi_o$. The dominant frequency component of L_J is twice the driving frequency $2\omega_s$ (1.8 GHz), which is because the functional shape of $L_J(\Phi_{ext})$ is symmetric about $0.5\,\Phi_o$.

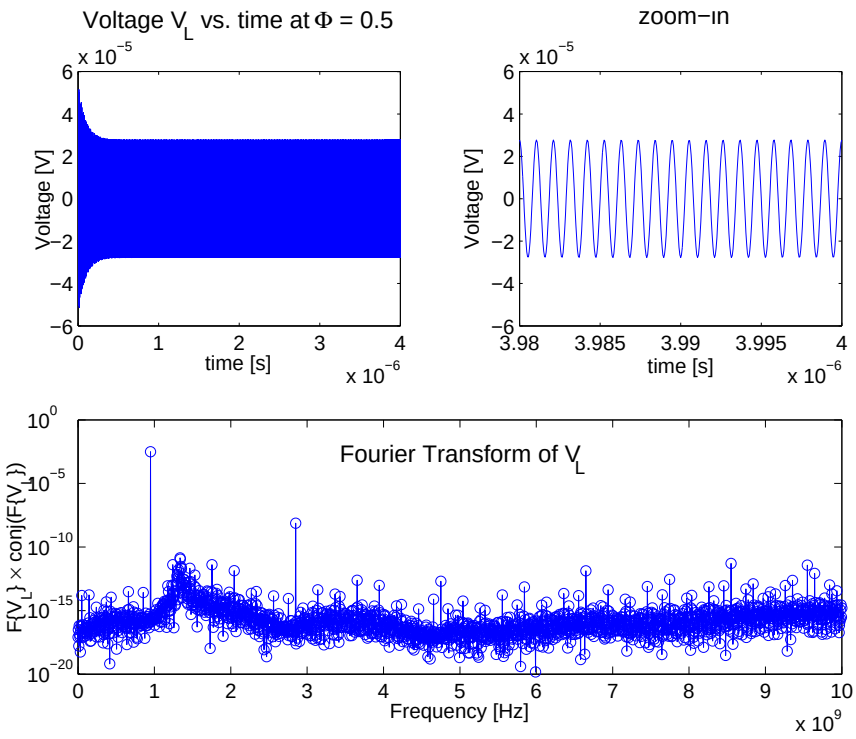

Figure 5-21: Time domain signal and Fourier components of V_L at a driving frequency of 0.9 GHz and $\Phi = 0.5\,\Phi_o$. It is dominated by the odd harmonics.

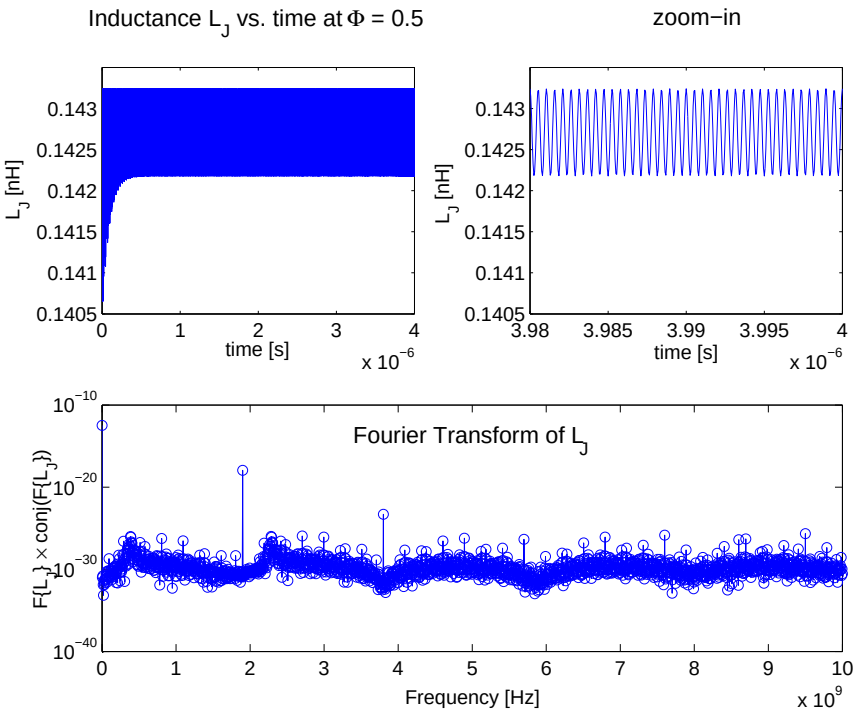

Figure 5-22: Time domain signal and Fourier components of L_J. It is dominated by the DC component and the even harmonics.

Frequency Spectra

By solving the differential equations for V_L at different driving frequency ω_s, we obtain the resonant spectrum of the circuit. In fig. 5-23, the power dependence of the magnitude and phase spectra are shown for three flux biases at $\Phi_{ext} = 0$, $0.3\,\Phi_o$ and $0.5\,\Phi_o$. The simulation results demonstrate qualitative resemblance to the experimental data presented in fig. 4-2 in the following ways:

1. The magnitude and phase spectra evolves from a symmetric shape to an asymmetric shape with increasing bias. The spectra bends towards the lower frequency side at $\Phi = 0$, and towards the higher frequency side at $\Phi = 0.5\,\Phi_o$.

2. The magnitude spectra at $\Phi = 0$ are similar to those at $\Phi = 0.5\,\Phi_o$, only that they are mirror imaged about a vertical axis. On the other hand, the phase spectra at the two flux biases are mirror imaged first about a vertical axis, then about a horizontal axis.

3. At $\Phi = 0.3\,\Phi_o$, the magnitude spectra at the two highest input biases exhibit two discrete jumps, once at a lower frequency when the magnitude is increasing, and another

at a higher frequency when the magnitude is decreasing. Similarly, the phase spectra also show two discontinuities at the same frequency locations. A partial phase drop occurs at the low-frequency discontinuity, while most of the phase drop occurs at the high-frequency discontinuity.

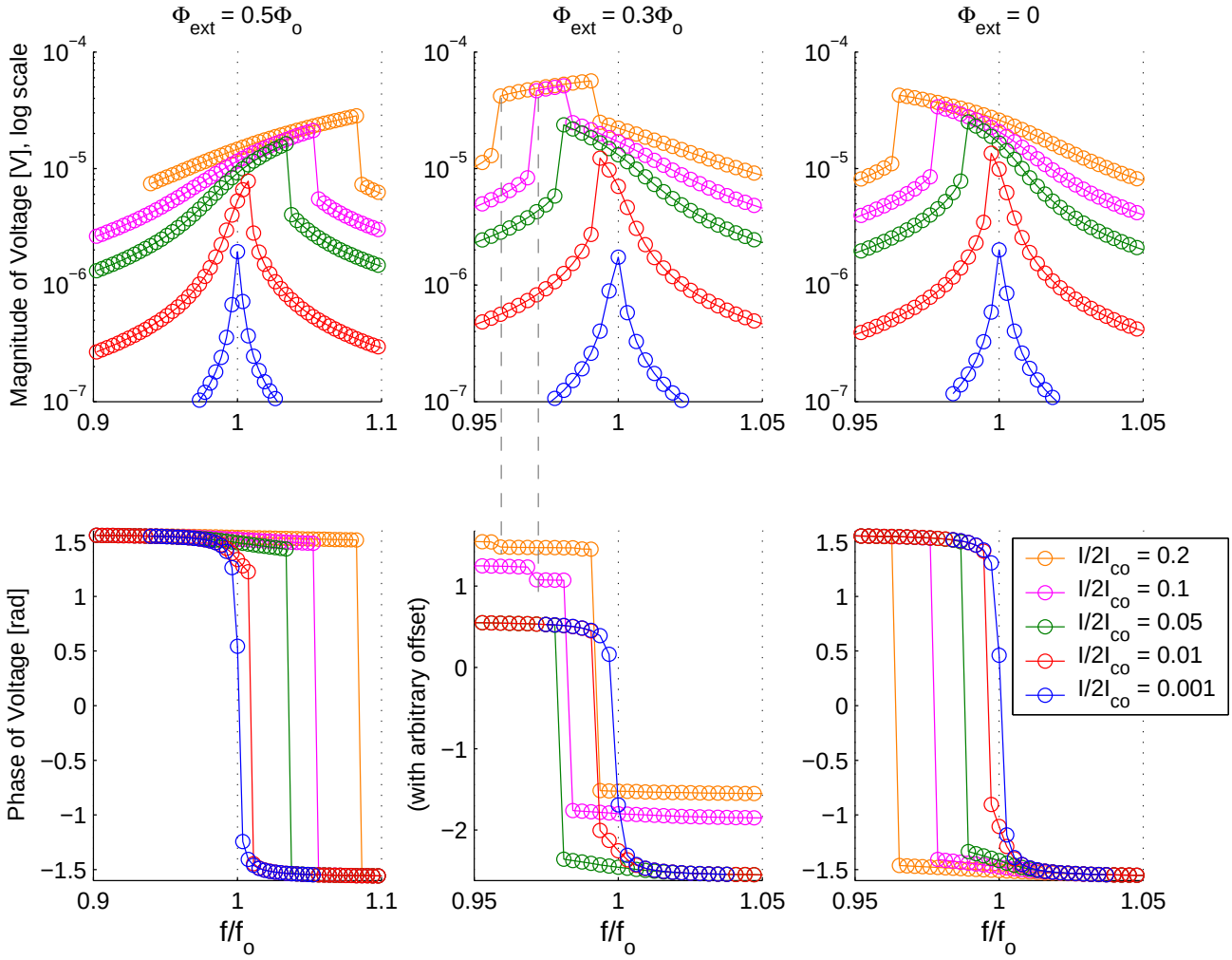

Figure 5-23: Simulation results for the magnitude and phase spectra based on the toy resonant model at three different flux biases. The simulations qualitatively reproduce the experimentally observed behavior presented in fig. 4-2.

The flux dependence of the simulated spectra are shown in fig. 5-24 in steps of $0.1\,\Phi_o$. The results also compare well with the data shown in fig. 4-3.

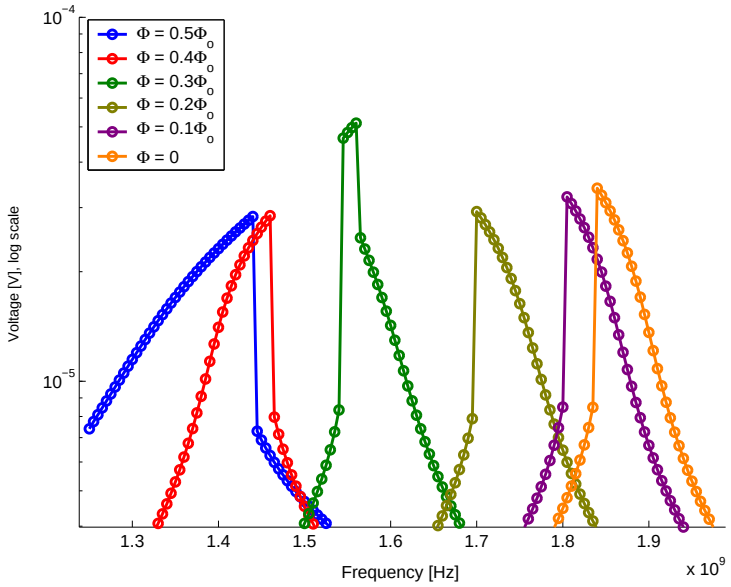

Figure 5-24: Evolution of the nonlinear magnitude spectrum with magnetic flux. The current bias used in the simulations was $I/2I_{co} = 0.1$. The results are comparable with the data in fig. 4-3.

5.4.3 Observations based on the "toy model"

Based on the simulation results from the "toy model", we identify the following factors that are important to explain the resonant behavior of the readout circuit:

1. The dominant nonlinear effect of the SQUID inductance is caused by an oscillating magnetic flux, rather than an oscillating current bias. This is quite an unexpected result given that experimentally, the external flux that was applied to the circuit was strictly DC. One possibility is that this oscillating flux was mutually coupled to the SQUID from a neighboring loop in the actual circuit. In particular, the flux induced in the resonating loop which comprises the SQUID inductor and the capacitor could be quite significant. This is especially true when the driving frequency is near the resonant frequency, at which point the current circulating in the resonating loop is Q times the size of the driving current (Q enhancement effect).

2. The critical-current asymmetry of the SQUID junctions affects the shape of the L_J vs. Φ_{ext} modulation curve, which in turn determines how the resonant spectrum evolves with magnetic flux. A value of $\Delta_I = 0.5\, I_{co}$ was used to reproduce the data with the toy model. As illustrated in fig. 5-25, L_J is minimum at $\Phi = 0$, thus the AC modulation of L_J about this DC bias will result in a *higher* effective inductance. This corresponds to a resonant spectrum which bends towards the *lower* frequency side. On the other hand, L_J is maximum at $\Phi = 0.5\,\Phi_o$, the AC modulation of L_J about this bias results in a *lower* effective inductance. This corresponds to a resonant spectrum bending towards the *higher* frequency side. The locations of the inflection points determine when the resonant spectrum makes the transition from bending towards one frequency side to another.

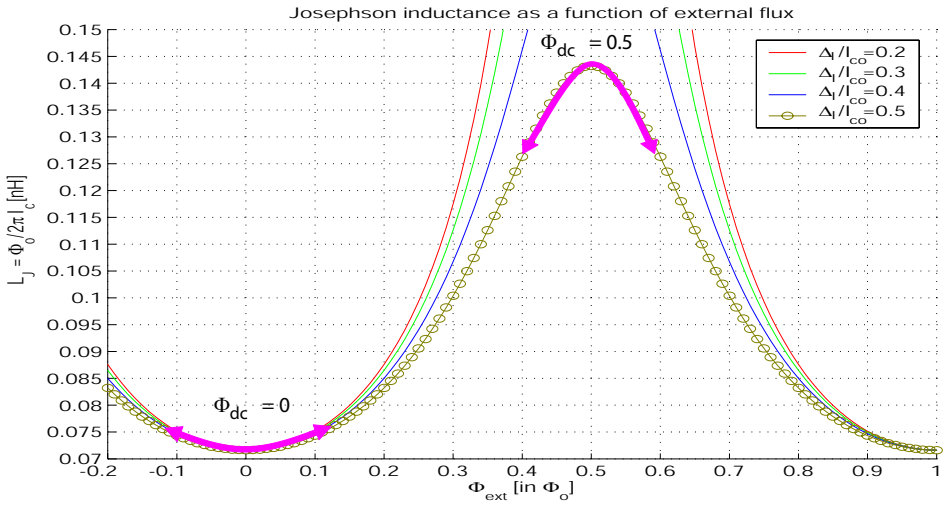

Figure 5-25: Illustration of how the effective inductance can increase or decrease depending on the DC flux bias.

These factors will be incorporated in the real circuit model which will be presented in the next section. It should be commented that the nonlinearity is manifested as a bend in the resonant spectrum because the nonlinear effect is significant only when f is close to the resonant frequency f_o. In the limit that f is far away from f_o, the nonlinear spectrum becomes similar to the linear case.

5.5 Circuit model with internally coupled flux

The circuit model presented in this section attributes the nonlinear resonant behavior to an oscillating flux that is coupled from the resonating loop to the SQUID. The circuit schematic is shown in fig 5-26. The SQUID is represented by the loop on the far right, with the two Josephson junctions each represented by the RCSJ model. The SQUID is shunted by a load capacitor C_L and a load resistor R_L. We take into account the loop inductance of the SQUID which is given by L_a, as well as the loop inductance of the resonating loop L_b. The mutual inductance between the two loops is given by $|M_{ab}| = \kappa\sqrt{L_a L_b}$, where the coefficient of coupling κ is between 0 and 1 based on the fact that the energy stored in the coupled inductors must be non-negative. The SQUID loop is threaded by flux Φ_a while the resonating loop is threaded by Φ_b. The flux through loops c and d are not of interest in this problem.

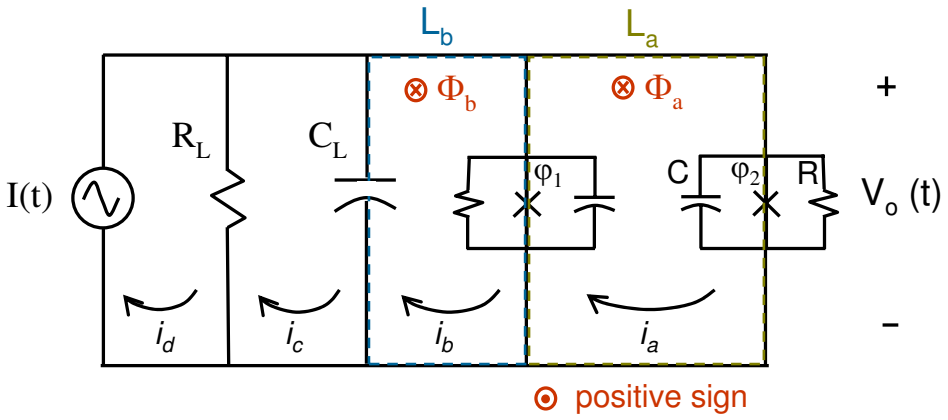

Figure 5-26: Schematic of the circuit model in which the SQUID is coupled to an oscillating flux from the resonating loop. L_a is the loop inductance of the SQUID, while L_b is the loop inductance of the resonating loop.

5.5.1 Mathematical Analysis

The expressions for Φ_a and Φ_b are given by:

$$\Phi_a = L_a i_a + M_{ab} i_b + \Phi_{ext,a} \tag{5.61}$$

$$\Phi_b = L_b i_b + M_{ab} i_a + \Phi_{ext,b} \tag{5.62}$$

where the flux in each loop is given by the sum of the self induced flux, the mutual coupled flux, and the external DC flux bias. We allow the external flux to be different due to difference in the loop areas. In addition, the SQUID is assumed to have asymmetric junctions with parameters defined as:

$$I_{co1} = I_{co} + \Delta_I \qquad I_{co2} = I_{co} - \Delta_I \tag{5.63}$$

$$C_1 = C + \Delta_C \qquad C_2 = C - \Delta_C \tag{5.64}$$

$$R_1 = R + \Delta_R \qquad R_2 = R - \Delta_R \tag{5.65}$$

We will analyze the circuit in terms of loops and mesh currents, rather than branches and nodal voltages. This turns out to be a more natural approach when self-induced flux and mutual-coupled flux are involved. The circuit dynamics are described by a system of nonlinear differential equations governing the SQUID as well as the rest of the resonant circuit. First we write out the constituent relations for the circuit elements in terms of the variables $\{\varphi_1, \varphi_2, V_c\}$, which are the gauge invariant phase across junctions 1 and 2, and the voltage across C_L respectively.

Constituent Relations

$$\begin{array}{lcrcl}
\text{Junction 2} & : & i_a & = & I_{co2}\sin\varphi_2 + \frac{\Phi_o}{2\pi R_2}\frac{d\varphi_2}{dt} + \frac{C_2\Phi_o}{2\pi}\frac{d^2\varphi_2}{dt^2} \\
\text{Junction 1} & : & i_b - i_a & = & I_{co1}\sin\varphi_1 + \frac{\Phi_o}{2\pi R_1}\frac{d\varphi_1}{dt} + \frac{C_1\Phi_o}{2\pi}\frac{d^2\varphi_1}{dt^2} \\
C_L & : & i_c - i_b & = & C_L\frac{dV_c}{dt} \\
R_L & : & i_d - i_c & = & \frac{V_c}{R_L}
\end{array}$$

The relations for junctions 1 and 2 state that the current through each junction is given by the sum of the currents through the Josephson branch, the resistive branch, and the capacitor branch in the RCSJ model.

Equations of Motion

First we perform a change of variables from $\{\varphi_1, \varphi_2, V_c\}$ to $\{\varphi_p, \varphi_m, \varphi_c\}$ so that the variables have the same unit:

$$\varphi_1 = \varphi_p + \varphi_m \tag{5.66}$$

$$\varphi_2 = \varphi_p - \varphi_m \tag{5.67}$$

$$V_c = \frac{\Phi_o}{2\pi}\frac{d\varphi_c}{dt} \tag{5.68}$$

In terms of these variables, one may find it intuitive to think of the circuit as a parallel combination of three Josephson junctions characterized by φ_p, φ_m and φ_c. In this way, R_L and C_L can then be treated as the resistive and capacitive branches of the RCSJ model for junction φ_c (Josephson branch is omitted). The circuit dynamics are governed by a set of three nonlinear differential equations.

1. Current Continuity Equation

$$I\sin\omega t = 2I_{co}\sin\varphi_p\cos\varphi_m + \frac{\Phi_o R}{\pi(R^2-\Delta_R^2)}\frac{d\varphi_p}{dt} + \frac{C\Phi_o}{\pi}\frac{d^2\varphi_p}{dt^2} + \frac{\Phi_o}{2\pi R_L}\frac{d\varphi_c}{dt} + \frac{C_L\Phi_o}{2\pi}\frac{d^2\varphi_c}{dt^2} + f_1 \tag{5.69}$$

2. Fluxoid Quantization Equation (Loop b)

$$0 = \varphi_c - \varphi_p - \varphi_m - \frac{2\pi L_b i_b(\varphi_p,\varphi_m)}{\Phi_o} - \frac{2\pi M_{ab} i_a(\varphi_p,\varphi_m)}{\Phi_o} - \frac{2\pi\Phi_{ext,b}}{\Phi_o} \tag{5.70}$$

3. Fluxoid Quantization Equation for SQUID (Loop a)

$$0 = 2\varphi_m - \frac{2\pi L_a i_a(\varphi_p,\varphi_m)}{\Phi_o} - \frac{2\pi M_{ab} i_b(\varphi_p,\varphi_m)}{\Phi_o} - \frac{2\pi\Phi_{ext,a}}{\Phi_o} \tag{5.71}$$

where f_1 in the current continuity equation includes terms due to the asymmetric junction parameters:

$$f_1 = 2\Delta_I\sin\varphi_m\cos\varphi_p - \frac{\Phi_o\Delta_R}{\pi(R^2-\Delta_R^2)}\frac{d\varphi_m}{dt} + \frac{\Delta_C\Phi_o}{\pi}\frac{d^2\varphi_m}{dt^2} \tag{5.72}$$

and $i_a(\varphi_p, \varphi_m)$, $i_b(\varphi_p, \varphi_m)$ are given by the constituent relations discussed previously.

The fluxoid quantization equations in eqn. 5.70 and 5.71 are in fact integrals of Kirchoff's Voltage Law (KVL) for the corresponding loops, with the constant of integration given by the DC flux Φ_{ext} threading the loop. The integration constants result in a DC offset to the solutions for φ_p, φ_m and φ_c. In particularly, according to eqn. 5.71, $\Phi_{ext,a}$ causes a DC offset in φ_m and to certain extent φ_p due to asymmetry. On the other hand, simulation results show that $\Phi_{ext,b}$ in eqn. 5.70 causes a DC offset only in φ_c without changing φ_m or φ_p.

Therefore, we could have replaced equation 5.70 with its KVL equivalent and still be mathematically correct. This is because the physical parameter of interest V_c is only dependent on the derivative $d\varphi_c/dt$, and will not be affected by a DC offset in φ_c. The resultant set of equations are known as *differential-algebraic equations* (DAEs), given that equations for loop b and loop a will be differed by an order of integration. While certain ode solvers in Matlab such as *ode15s* and *ode23t* can deal with DAEs, they are numerically more challenging to solve. Thus we have adopted the way to write out the differential equations as shown above.

Physical Parameters

(a) Output voltage

$$V_o(t) = \frac{\Phi_o}{2\pi}\frac{d\varphi_2}{dt} = \frac{\Phi_o}{2\pi}\left(\frac{d\varphi_p}{dt} - \frac{d\varphi_m}{dt}\right) \tag{5.73}$$

(b) Capacitor voltage

$$V_c(t) = \frac{\Phi_o}{2\pi}\frac{d\varphi_c}{dt} \tag{5.74}$$

(c) SQUID circulating current (Averaged difference of junction currents)

$$I_{cir} = \frac{I_{JJ1} - I_{JJ2}}{2} \tag{5.75}$$

(d) SQUID bias current (Sum of junction currents)

$$I_{sq} = I_{JJ1} + I_{JJ2} = i_b \tag{5.76}$$

where the junction currents I_{JJ1} and I_{JJ2} are given by the constituent relations.

(e) Flux induced in SQUID

$$\Phi_{induced} = L_a I_{cir} \tag{5.77}$$

(f) Flux coupled to SQUID

$$\Phi_{coupled} = \left(|M_{ab}| - \frac{L_a}{2} \right) i_b = \left(|M_{ab}| - \frac{L_a}{2} \right) I_{sq} \tag{5.78}$$

where M_{ab} is negative, and L_a, L_b are positive. M_{ab} is negative such that the direction of the coupled flux in the SQUID is opposite to the direction of the self-induced flux in the resonating loop, and vice versa. When defining the flux coupled to the SQUID, one needs to subtract the contribution due to the common arm inductance $L_a/2$ from the total mutual coupling M_{ab}. We have assumed the arms of the SQUID to be symmetric.

Comments on competing nonlinear effects:

The nonlinearity of the Josephson inductance is caused by current biases: I_{sq} and I_{cir}, as well as the flux biases: $\Phi_{coupled}$ and $\Phi_{induced}$. The competing effects between the current and the flux biases determine the resultant resonant behavior of the circuit. By varying the relative sizes of the signals, we should be able to control the relative strength of the competing effects. In particular, I_{sq} and $\Phi_{coupled}$ are related by the mutual inductance M_{ab} between the SQUID and the resonating loops. It will be shown that by gradually increasing the size of M_{ab}, the nonlinear effect due to the oscillating flux can be made more prominent.

Numerical Simulations of ODEs

Solving differential equations numerically requires normalizing the equations to be unitless. The time variable also needs to be scaled with respect to the *largest* characteristic time of the circuit to ensure the proper time step was taken by the ode solver to capture the dynamics of the circuit. For a thorough discussion on scaling differential equations for numerical simulations, please refer to appendix B.

The differential equations in 5.69 to 5.71 were coded in Matlab as equivalent system of *first-order* differential equations in the form

$$M\dot{x} = f(x,t) \tag{5.79}$$

where x are the variables of the equations and $\dot{x}$ correspond to its derivatives:

$$x = \begin{bmatrix} \varphi_c \\ \dot{\varphi}_c \\ \varphi_p \\ \dot{\varphi}_p \\ \varphi_m \\ \dot{\varphi}_m \end{bmatrix} \qquad \dot{x} = \begin{bmatrix} \dot{\varphi}_c \\ \ddot{\varphi}_c \\ \dot{\varphi}_p \\ \ddot{\varphi}_p \\ \dot{\varphi_m} \\ \ddot{\varphi_m} \end{bmatrix} \tag{5.80}$$

M is a 6×6 mass matrix. We have added in the terms due to asymmetry of the junctions.

$$M = \begin{bmatrix} \dot{\varphi}_c & \ddot{\varphi}_c & \dot{\varphi}_p & \ddot{\varphi}_p & \dot{\varphi_m} & \ddot{\varphi_m} \\ 1 & 0 & 0 & 0 & 0 & 0 \\ 0 & 0 & 1 & 0 & 0 & 0 \\ 0 & 0 & 0 & 0 & 1 & 0 \\ \frac{\Phi_o}{2\pi R_L I_c} & \frac{\Phi_o C_L}{2\pi I_c} & \frac{a_1\Phi_o}{\pi R I_c} & \frac{C\Phi_o}{\pi I_c} & -\frac{a_1\Phi_o}{\pi\Delta_R I_c} & \frac{\Delta_C\Phi_o}{\pi I_c} \\ 0 & 0 & a_1(d_1 - d_2\frac{\Delta_R}{R}) & d_1C + d_2\Delta_c & a_1(d_2 - d_1\frac{\Delta_R}{R}) & d_1\Delta_c + d_2C \\ 0 & 0 & a_1(b_2 - b_1\frac{\Delta_R}{R}) & b_1\Delta_c + b_2C & a_1(b_1 - b_2\frac{\Delta_R}{R}) & b_1C + b_2\Delta_c \end{bmatrix} \tag{5.81}$$

$f(x,t) =$

$$\begin{bmatrix} \dot{\varphi}_c \\ \dot{\varphi}_p \\ \dot{\varphi}_m \\ \frac{I}{I_c}\sin\omega t - \sin\varphi_p\cos\varphi_m - \frac{2\Delta_I}{I_c}\sin\varphi_m\cos\varphi_p \\ \varphi_p + \varphi_m - \varphi_c - \frac{2\pi d_1}{\Phi_o}(I_{co}\sin\varphi_p\cos\varphi_m + \Delta_I\sin\varphi_m\cos\varphi_p) - \frac{2\pi d_2}{\Phi_o}(I_{co}\sin\varphi_m\cos\varphi_p + \Delta_I\sin\varphi_p\cos\varphi_m) + \frac{2\pi\Phi_b}{\Phi_o} \\ -\varphi_m - \frac{2\pi b_1}{\Phi_o}(I_{co}\sin\varphi_m\cos\varphi_p + \Delta_I\sin\varphi_p\cos\varphi_m) - \frac{2\pi b_2}{\Phi_o}(I_{co}\sin\varphi_p\cos\varphi_m + \Delta_I\sin\varphi_m\cos\varphi_p) + \frac{\pi\Phi_a}{\Phi_o} \end{bmatrix} \tag{5.82}$$

where $I_c = 2I_{co}$, and the constants are given by:

$$a_1 = \frac{1}{1 - \left(\frac{\Delta R}{R}\right)^2} \tag{5.83}$$

$$d_1 = -(2L_b + M_{ab}) \qquad d_2 = M_{ab} \tag{5.84}$$

$$b_1 = \frac{L_a}{2} \qquad b_2 = -\left(\frac{L_a}{2} + M_{ab}\right) \tag{5.85}$$

d_1, d_2, b_1, b_2 have unit of inductance, and a_1 is unitless.

Circuit parameters

Critical current for junction	$I_{co} = 2.3\,\mu A$
Resistor across junction	$R = 500\,\Omega$
Capacitor across junction	$C = 5\,pF$
Load resistor	$R_L = 500\,\Omega$
Load capacitor	$C_L = 100\,pF$
Loop inductance of SQUID	$L_a = 60\,pH$
Loop inductance of resonating loop	$L_b = 800\,pH$
Mutual coupling	$\lvert M_{ab}\rvert = 50\,\text{pH}$ to $150\,\text{pH}$ ($\kappa \approx 0.22$ to 0.68)
Asymmetry of junctions	$\Delta_I / I_{co} = 0.5$

The values were based on the fabrication and design parameters of the actual circuit. The loop inductances and the mutual coupling were estimated based on the FastHenry simulator [54] and were likely to have discrepancies from the actual values.

5.5.2 Simulation Results

The nonlinear magnitude and phase spectra for V_o are shown in fig. 5-27 for different flux biases between $\Phi = 0$ to $0.5\,\Phi_o$. The size of the mutual coupling used was $|M_{ab}|$=50 pH ($\kappa \approx 0.22$). Comparing the shapes of the magnitude spectra with the previous results based on the phenomenological model in fig. 5-24, we can see that the evolution of the spectrum demonstrates a similar trend, varying from bending towards the lower frequency side at $\Phi = 0$ to bending towards the higher frequency side at $\Phi = 0.5\,\Phi_o$. However, the transition of the bending no longer occurs at $\Phi = 0.3\,\Phi_o$, but instead happens only when the flux bias is very near $\Phi = 0.5\,\Phi_o$.

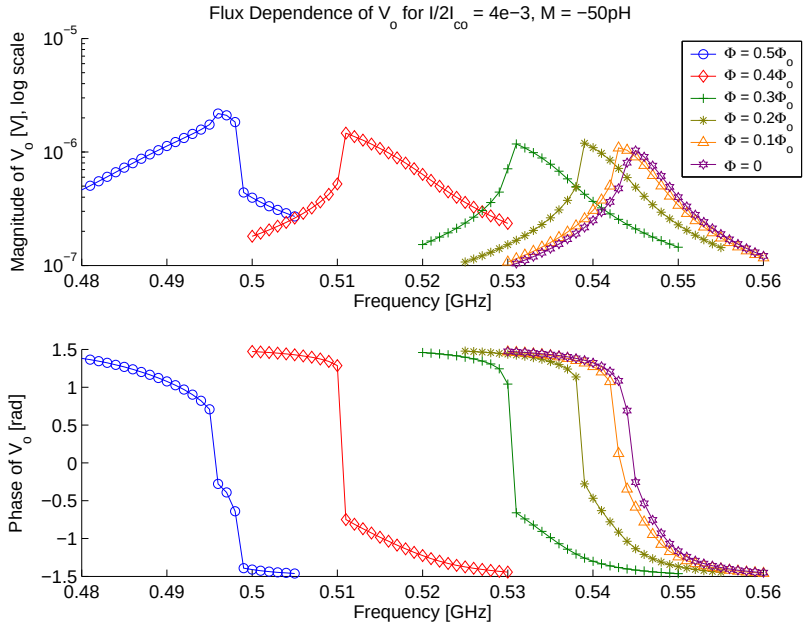

Figure 5-27: The evolution of the nonlinear spectrum with magnetic flux based on the circuit model with internally coupled flux. The mutual coupling between the resonating loop and the SQUID was $|M_{ab}| = 50\,pH$. The transition of the bending occurs very near $\Phi = 0.5\,\Phi_o$.

Subsequent simulation results showed that *by increasing the size of the mutual inductance M_{ab}, and thereby enhancing the nonlinear effect due to the oscillating flux over that due to the bias current*, the resonant behavior became increasingly similar to the results based on the phenomenological model. Fig. 5-28 shows the simulation results when the size of $|M_{ab}|$ was increased from 50 pH to 150 pH. The onset of transition for the bending now occurs at

$\Phi = 0.4\,\Phi_o$.

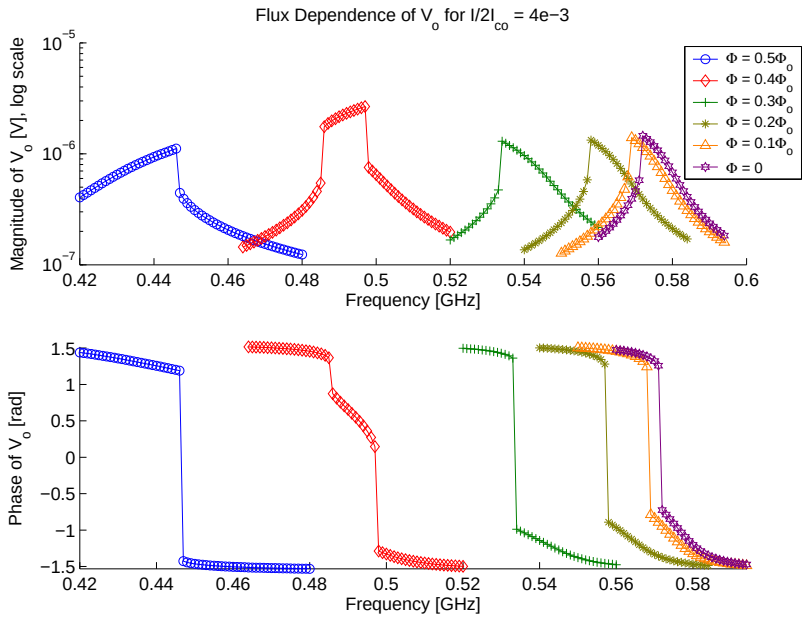

Figure 5-28: Evolution of magnitude spectrum with magnetic flux with the mutual coupling is increased to $|M_{ab}| = 150\,pH$. The onset of transition is now evidenced at $\Phi = 0.4\,\Phi_o$.

While enhancing the effect due to the oscillating flux by increasing the mutual inductance M_{ab} is useful for proof-of-principle purposes, a value of $|M_{ab}| = 150\,\text{pH}$ corresponds to a coupling constant of $\kappa = 0.68$, and is physically unlikely given the geometrical arrangement of the loops in the actual circuit. In the following section, we discuss certain modifications made to the circuit model to allow the possibility that the observed nonlinearity could be due to oscillating flux originated from a different source.

5.6 Circuit model with externally coupled flux

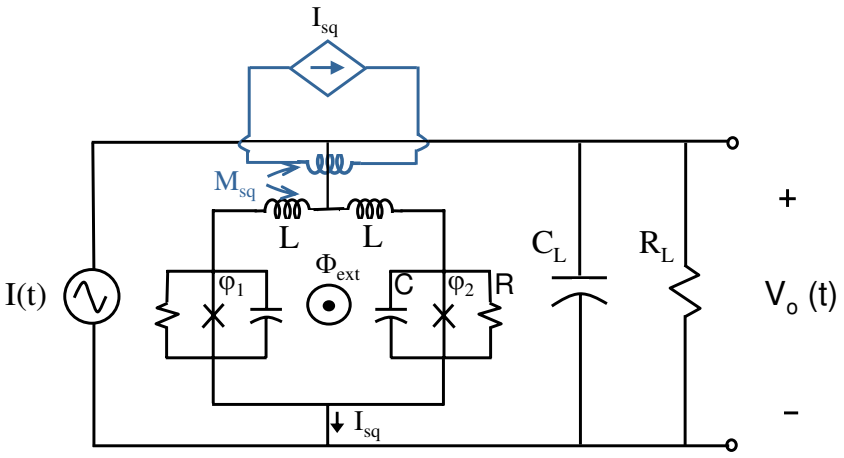

Figure 5-29: Circuit schematic of the resonant model in which the SQUID is coupled to a dependent flux source.

5.6.1 Analysis and Simulation Results

The results from the circuit model with internally coupled flux suggested that with the circuit parameters that we used, the amount of oscillating flux that was being coupled from the resonating loop to the SQUID was not enough to reproduce the observed resonant behavior. In particular, the values for L_a, L_b, and the mutual inductance M_{ab} used were probably not accurate enough to model the actual values. To deal with the uncertainties in the inductance values, we will discuss a circuit model here where the SQUID is coupled *externally* to a dependent flux source. The circuit schematic is shown in fig. 5-29.

For this circuit model, we set the loop inductance of the resonating loop (previously referred as L_b) to be zero. The loop inductance of the SQUID (previously referred as L_a) is given by 2L, where L is the inductance of each arm. The circuit is governed by the current continuity and the fluxoid quantization equations. The mathematical analysis of the circuit is similar to the previous analysis for previous circuit model, and the full analysis can be found in appendix D.

The essence of the model is that the external flux which comes in the fluxoid quantization equation for the SQUID has the form:

$$\Phi_{ext} = \Phi_{dc} + \Phi_{coupled} \tag{5.86}$$

$$\Phi_{coupled} = M_{sq} I_{sq} \tag{5.87}$$

which has the same form as eqn. 5.78 for the previous model. The size of the coupled flux is made to be proportional to the bias current I_{sq} through the SQUID. First, we will use the modified circuit model to reproduce the resonant behavior obtained previously for different values of mutual inductance. To establish a basis for comparison, we recognize that the fluxoid equation for the SQUID will be equivalent for both circuit models (eqns. 5.71 and D.26) if we set

$$M_{sq} = |M_{ab}| - \frac{L_a}{2} \tag{5.88}$$

where M_{sq} is the total mutual coupling $|M_{ab}|$ minus the contribution due to the common arm inductance $L_a/2$. The results are shown in fig. 5-30. As we increase the size of M_{sq}, we observe a similar enhancement of the nonlinear effect due to the oscillating flux coupled to the SQUID. In particular at $M_{sq} = 20\,\text{pH}$, the transition of the peak bending occurs when the flux bias is very near $\Phi = 0.5\,\Phi_o$, and this is comparable to the previous results shown in fig. 5-27. At M_{sq} =120 pH, the transition occurs at $\Phi = 0.4\,\Phi_o$, which is similar to the case shown in fig. 5-28.

As we further increase the size of the mutual coupling M_{sq}, the transition of the peak bending is gradually moved to the flux bias of $\Phi = 0.3\,\Phi_o$. This is shown in fig. D-5. The flux dependence of the resonant spectra now demonstrates qualitative resemblance to the experimental data shown in fig. 4-3. The comparison between this set of simulation results with the data will be presented in the next section.

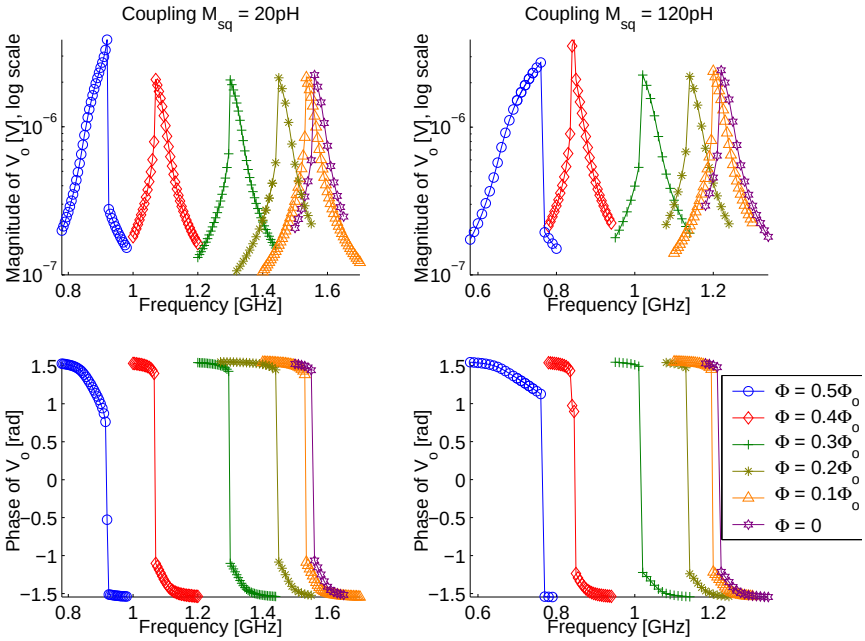

Figure 5-30: Resonant behavior with different magnetic flux biases based on the modified circuit model with externally coupled flux. The simulations are shown for two values of mutual coupling M_{sq}, which should give equivalent results as figs. 5-27 and 5-28.

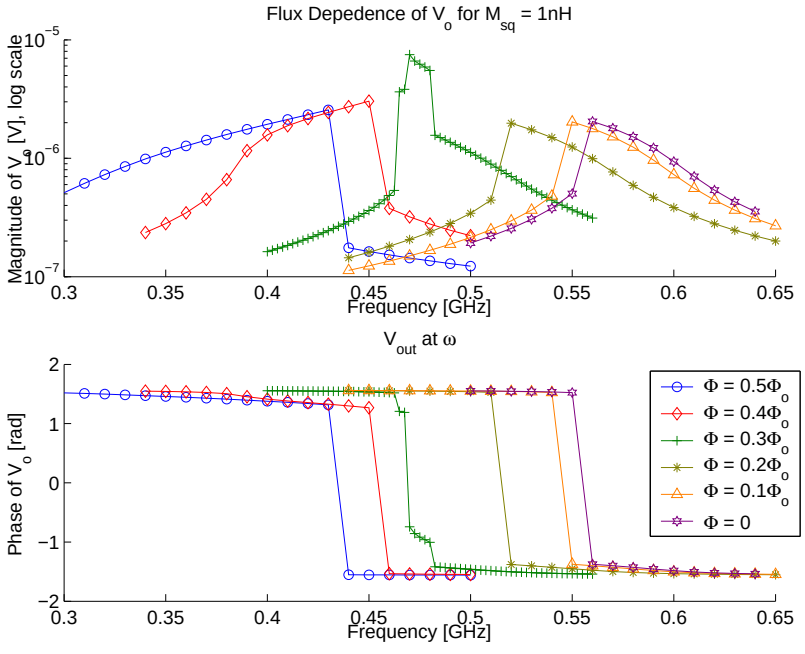

Figure 5-31: Simulation results for $M_{sq} = 1\,\mathrm{nH}$. The onset of transition occurs at $\Phi = 0.3\,\Phi_o$ as observed in the experiment.

5.6.2 Comparison of simulations with experimental data

Comparison based on shapes of resonant spectra

We will compare the experimental data with the simulation results obtained based on the modified circuit model in which the SQUID is externally coupled to a dependent flux source. Fig. 5-32 is a side-by-side comparison between the nonlinear magnitude and phase spectra at various flux biases.

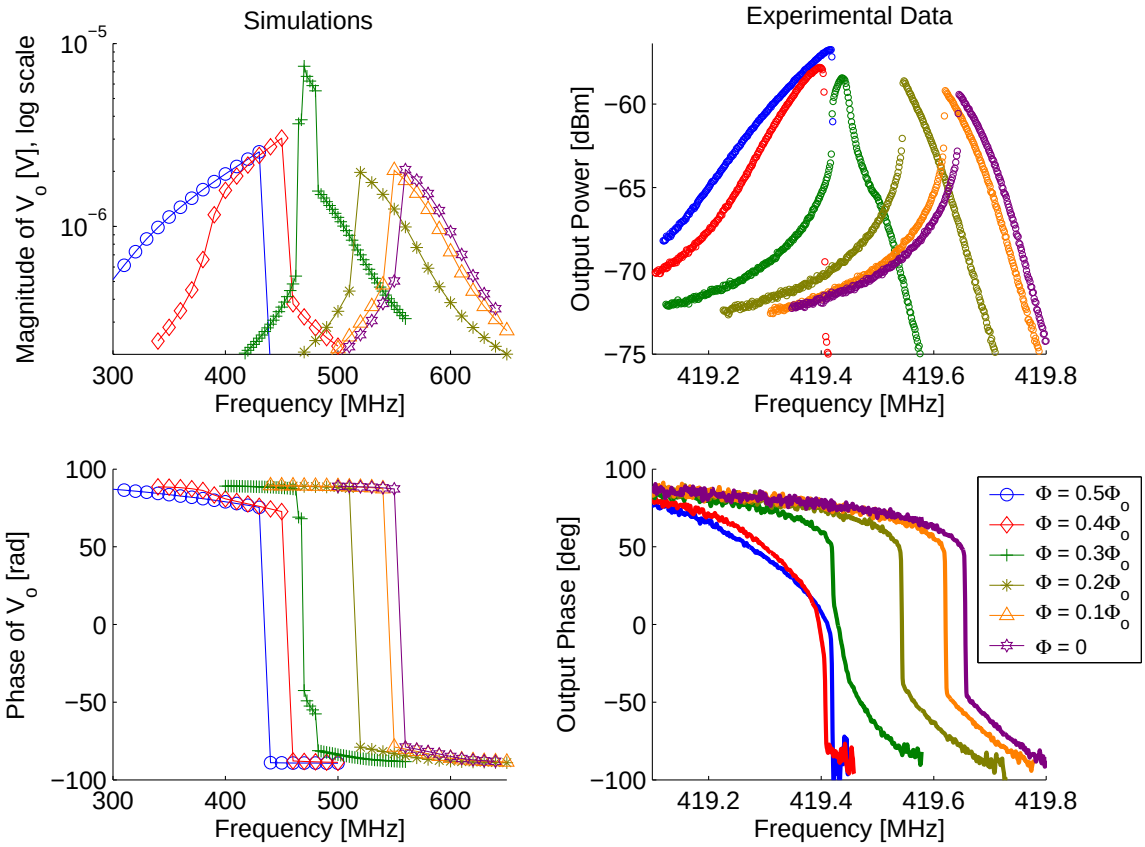

Figure 5-32: Side-by-side comparison between simulations based on the modified circuit model and the experimental data previously shown in fig. 4-3.

The major observations are summarized below:

1. The simulations successfully reproduced the general shape of the spectra as the flux bias was varied from $\Phi = 0$ to $0.5\,\Phi_o$. Both the data and simulations showed that the nonlinear magnitude spectrum gradually evolved from bending towards one frequency side to another, with the transition occurring around $\Phi = 0.3\,\Phi_o$. The phase spectra also showed qualitative resemblance to the data.

2. The quality factor Q of the simulated peaks were on the order of 100, while the Q of the actual circuit was as high as 7000. Due to the Q-enhancement effect, the current going through the SQUID is Q times higher than the driving current at the resonant frequency. Thus the higher the Q, the larger the AC modulation of the SQUID inductance near the resonant frequency, and the more prominent the nonlinear resonant behavior. However with the simulation method that we used, it was numerically challenging to simulate and characterize circuits with extremely high Q, partly because the frequency resolution is limited by the step size of the driving frequency, and also because a large Q circuit would take a long time to reach steady state and make the simulations more computationally intensive.

3. The fractional change in resonant frequency as the flux is varied from 0 to $0.5\,\Phi_o$ is about 200 MHz/475 MHz ($\sim$ 40%) for the simulations, and about 0.4 MHz/419.4 MHz ($\sim$ 0.1%) for the data. This means that in the simulations, the contribution of the Josephson inductance in the overall loop inductance for the resonance is a lot larger than in the actual circuit. This was done on purpose so that the nonlinear effect due to the Josephson inductance can be more easily observed without being limited by the frequency resolution of the simulations.

4. In the measurements, an anti-resonance occurred at proximity to the resonant peak, causing the magnitude spectra to appear tilted. The phase spectra were also affected by a large amount of noise in the anti-resonance region due to the small transmitted signal. The anti-resonance effect was likely due to capacitive parasitics in the experimental configuration and was not modeled in the simulations.

Comparison based on the extent of bifurcation region as a function of input bias

Next, we will characterize the extent of the bifurcation region as a function of input bias. To do that, we simulated the hysteretic behavior of the spectrum by stepping the driving frequency in both the forward and backward directions, and by ensuring that the initial conditions used for the next frequency point were the solutions obtained for the previous frequency point. As illustrated in fig. 5-33, we define the frequency at which the resonant spectrum jumps from the lower to the higher stable branch as ω_{bend}, and the frequency at which the spectrum falls from the higher to the lower stable branch as ω_{tip}.

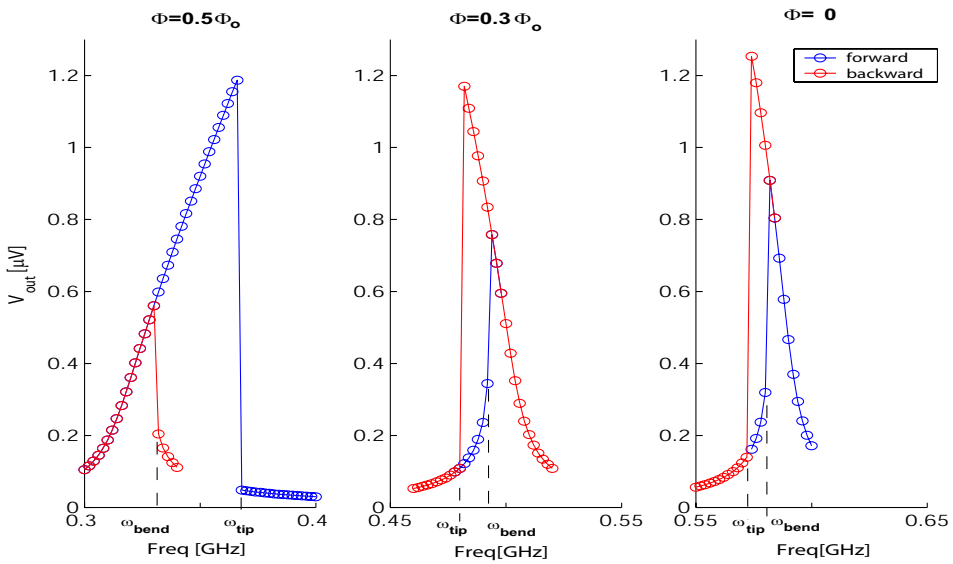

Figure 5-33: Simulations of hysteretic resonant behavior at various flux biases. ω_{bend} is defined as the frequency at which the resonant spectrum jumps from the lower to the higher stable branch, whereas ω_{tip} is the frequency at which the spectrum falls from the higher to the lower stable branch.

Similar to the earlier analysis for a single junction (eqn. 5.51), we normalize ω_{tip} and ω_{bend} with respect to the resonant frequency of the linear spectrum ω_o:

$$\delta\omega_{tip} = \frac{\omega_{tip} - \omega_o}{\omega_o} \tag{5.89}$$

$$\delta\omega_{bend} = \frac{\omega_{bend} - \omega_o}{\omega_o} \tag{5.90}$$

Note that the sign of $\delta\omega$ serves as an indication of the polarity of the bending. A *positive* $\delta\omega$ corresponds to the nonlinear spectrum bending to the *higher* frequency side, and a *negative* $\delta\omega$ corresponds to the spectrum bending to the *lower* frequency side. In addition, the extent of the bifurcation region is given by $|\omega_{tip} - \omega_{bend}|$.

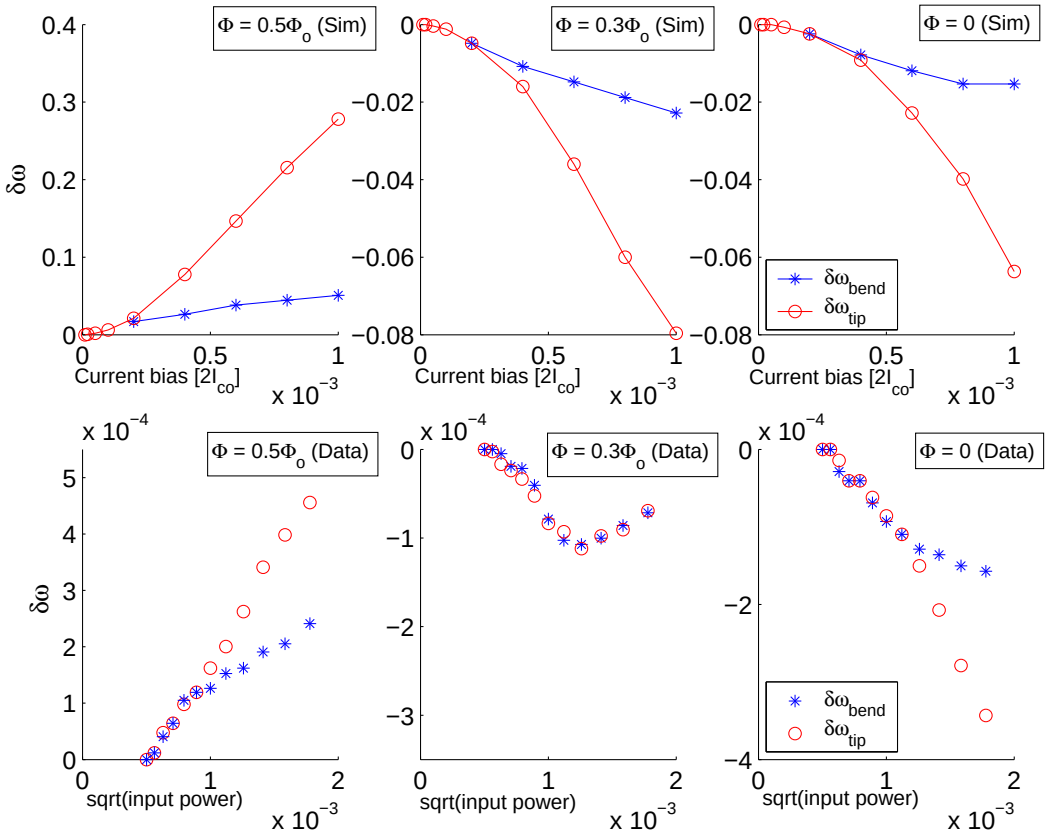

Figure 5-34: Extent of bifurcation region as a function of input bias for the simulations (top) compared with the hysteresis data (bottom). The data were previously presented in fig. 4-8.

In fig. 5-34, $\delta\omega_{tip}$ and $\delta\omega_{bend}$ were plotted as a function of input bias. We shall first focus on the flux biases at $\Phi = 0$ and $\Phi = 0.5\,\Phi_o$. Both the simulations and the data show a similar trend, with ω_{tip} growing at a faster rate than ω_{bend}. When comparing the input-bias dependence, we first locate in the figures the threshold point where ω_{bend} and ω_{tip} deviate, marking the beginning of the hysteretic region. This provides a reference point for us to relate the size of the driving current for the simulations, to the size of the input power for the experimental data. A qualitative comparison seems to suggest that the data corresponds

to a zoom-in of the simulations near the onset of the hysteretic region.

For the case when $\Phi = 0.3\,\Phi_o$, the simulations results are very different from the data. The data capture the fact that the resonant spectrum is constantly flipping from bending towards one frequency side to another as the power is gradually increased (see fig. 4-2). However as for the simulations, the spectrum bends only to the lower frequency side at the intermediate biases. Only at the highest bias that the transition of the peak bending is manifested. It is likely that simulations performed at a nearby flux bias other than $\Phi = 0.3\,\Phi_o$ could better reproduce the data.

5.7 Discussion

In this chapter, we have simulated the resonant behavior of various circuits comprising Josephson junctions. The goal was to reproduce the observed resonant behavior of the readout circuit, and thereby understanding the nonlinear mechanism which governs the circuit behavior.

First, we analyzed the resonant behavior of a Josephson junction using the harmonic balance approach. The simplicity of the single junction allowed us to obtain an analytical solution for the nonlinear resonant behavior, revealing both the stable and the unstable solutions of the bifurcation region (fig. 5-8).

We then proceeded to the simulations of resonant circuits comprising a SQUID. We simulated the circuits from first principles by solving the differential equations governing the SQUID and the rest of the circuit numerically. Our approach was to build up a series of resonant circuit models, three of which have been discussed in detail. The first model, i.e., the toy model, was based on a phenomenological approach where we replaced the SQUID by a nonlinear inductor described by an analytical expression. The nonlinear inductor was a valid approximation for the SQUID inductance within certain biasing and parameter constraints. In the second model, we attribute the nonlinear resonant behavior to the flux coupled from the resonating loop to the SQUID. We were able to demonstrate the competing effects due to the current and flux biases using this model. However, based on the circuit parameters that we used, the amount of nonlinearity due to the coupled flux was not enough to reproduce the data. We then discussed a third model where the SQUID is coupled externally to a dependent flux source. This approach allowed us to increase the size of the coupled flux without being constrained by the uncertainties in the inductance values of the circuit. We were able to qualitatively reproduce the resonant behavior in the data with the simulation results.

The following is a complete list of circuit models that we have analyzed. Circuits 2 and 3 were not discussed in this chapter but can be found in appendix D.

Overview of Circuit Models

Circuit Model	Resonant Behavior	Summary of results
1. Single junction 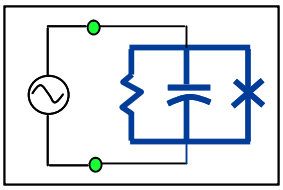	↖	• Nonlinearity of inductance due to current bias
2. R-C-SQUID ($I_{co1} = I_{co2}$) 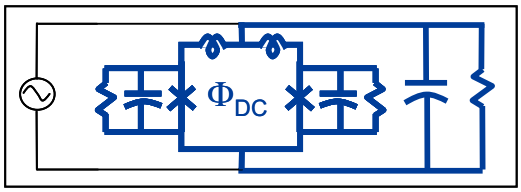	↖↖↖	• SQUID has no asymmetry ($I_{co1} = I_{co2}$) • Nonlinearity of inductance dominated by current bias
3. R-C-SQUID ($I_{co1} \neq I_{co2}$) 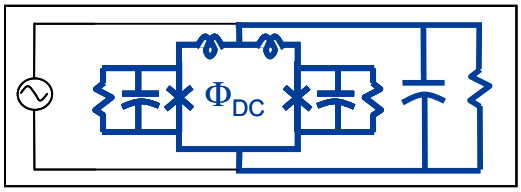	↗↖↖	• AC flux induced by asymmetry becomes significant near $\Phi=0.5\Phi_o$ • Nonlinearity of inductance dominated by current bias except at $\Phi=0.5\Phi_o$ when it is dominated by flux bias.
4. Toy Model ($I_{co1} \neq I_{co2}$) 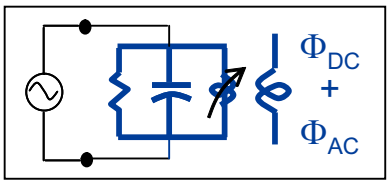	↗↑↖	• AC flux coupled externally • Competing nonlinear effects due to current bias and flux bias • Simulations resemble data when nonlinearity is dominated by flux bias

Circuit Model | Resonant Behavior | Summary of results

5. Circuit Model with ($I_{co1} \neq I_{co2}$) internally coupled flux

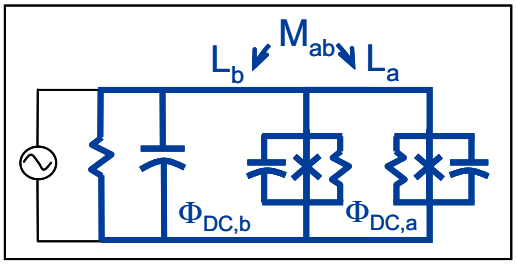

↱↰↰

- AC flux coupled from resonating loop
- Competing nonlinear effects due to current bias and flux bias

6. Circuit Model with ($I_{co1} \neq I_{co2}$) externally coupled flux

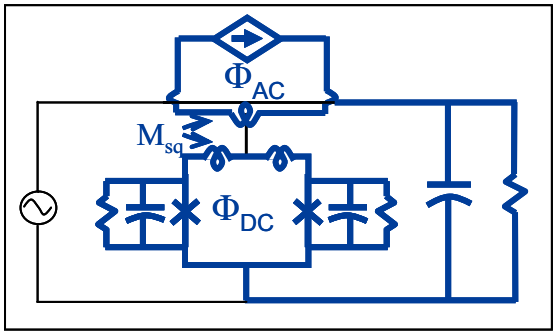

↱↑↰

- AC flux coupled externally
- Competing nonlinear effects due to current bias and flux bias
- Simulations resemble data when nonlinearity is dominated by flux bias

Legend:

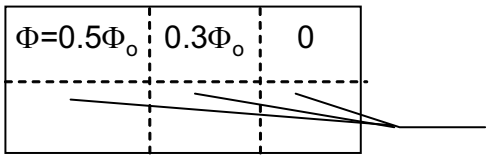

↰ - Nonlinear peak bends to **lower** frequency side

↱ - Nonlinear peak bends to **higher** frequency side

↑ - Transition of peak bending occurs

Observations based on the simulation results

The simulation results lead to the following suggestions about the actual circuit:

1. The nonlinear resonant behavior was due to an oscillating flux that was being coupled to the readout SQUID. We showed that the AC modulation from this oscillating flux can result in a higher or lower effective Josephson inductance depending on the DC flux bias, hence causing the flux-dependent resonant behavior that was observed experimentally. The size of this oscillating flux is proportional to the bias current through the SQUID, and is estimated to be on the order of $0.1\,\Phi_o$ near the resonant frequency. The source of this oscillating flux likely originates from the resonating loop. However, due to uncertainties in the actual on-chip values for the capacitances and inductances, as well as numerical limitation to simulate circuits with very high Q-factor, we were only able to reproduce the experimental results with an unexpectedly large mutual coupling.

2. The simulations also suggested that the junctions of the readout SQUID have asymmetric critical currents. Junction asymmetry was one of the possible explanations given the shape of the frequency modulation curve with magnetic flux. We showed that the amount of asymmetry has an effect on the curvature as well as the position of the inflection points on the frequency modulation curve. The amount of asymmetry was estimated to be $\Delta_I = 0.5\,I_{co}$, and is likely to be too large to be practical. Given that the SQUID junctions were designed to be $1.5 \times 1.5\,\mu m^2$, the maximum asymmetry was estimated to be at most 20 % based on process testing results.

Recommended future work:

The following experiments are recommended to address some of the issues raised by the simulations:

1. Design new resonant readout samples where the readout SQUID has known junction asymmetry. One can perform a systematic characterization of how the resonant behavior changes with different amount of asymmetry. The fabrication process at Lincoln Lab can now make junctions with sub-micron resolution, and should provide the required junction resolution for this experiment.

2. To eliminate undesired flux being coupled from the resonating loop to the readout SQUID, we have designed a new circuit where the resonating capacitor is split and placed on both sides of the SQUID. Thus, the resonating loop is also split symmetrically, and any induced flux on one side will be canceled out by a similar amount of flux on the other side. This design has been fabricated at Lincoln Lab and is awaiting to be tested. This will be further discussed in section 6.2.3.

3. Test structures for on-chip capacitors and spiral inductors are important to characterize the actual value of the circuit elements. Given the complexity of the readout circuit design, this will help explain the resultant resonant frequency as well as the quality factor of the circuit. Knowing the values of the lumped elements will also help estimating the loop inductances and mutual inductances between the loops.

Chapter 6

Conclusions and Future work

6.1 Conclusions

In this thesis, I have developed a resonant readout scheme for a niobium persistent current qubit. This dispersive readout approach is expected to be an improvement over the conventional readout scheme in reducing the level of decoherence on the qubit. Minimizing readout-induced decoherence is an important step towards improving the *measured* coherence times for superconducting qubits, and thereby demonstrating the feasibility of using macroscopic solid-state systems as building blocks for a quantum computer.

The first part of this thesis focused on the experimental implementation of the resonant readout scheme. This involved designing a high-Q resonant circuit to be coupled to the qubit, developing an experimental procedure for RF testing at cryogenic temperatures, and characterizing the behavior of the resonant circuit at different biases for qubit readout. The major experimental results were:

- We have confirmed the high sensitivity of the resonant readout at 300 mK by distinguishing the circulating current states of the qubit as a shift in the resonant frequency of the readout circuit.

- We have demonstrated the possibility of implementing a high-Q readout circuit using impedance transformation techniques, and by fabricating all the circuit elements on-chip. The capability to incorporate the necessary circuitry on-chip with available

fabrication technology is an important advantage for niobium-based qubits.

- We have observed novel manifestation of the nonlinearity due to the Josephson inductance of the SQUID. Not only that the resonant spectrum of the readout circuit became asymmetric in the nonlinear regime, the polarity of the asymmetry evolved periodically as a function of DC magnetic flux bias to the SQUID.

In the second part of the thesis, I focused on the numerical simulations of the resonant behavior of circuits comprising a SQUID inductor. I simulated the circuits from first principles by solving the differential equations governing the SQUID and the rest of the circuit. Our approach was to build up a series of resonant circuit models with increasing level of complexity, and gradually include the essential physics to reproduce the nonlinear resonant behavior as observed in the experiment. The major results were:

- Based on the simulations, the experimentally observed nonlinearity was due to an oscillating flux that was coupled to the readout SQUID. The source of this oscillating flux was likely originated from the resonating loop.

- The simulations also suggested a significant amount of asymmetry in the critical currents of the SQUID junctions. The suggested level of asymmetry was needed to explain the data within the circuit models, but is likely to be too large for the actual sample based on process testing results.

- The simulation techniques developed for solving differential equations of resonant circuits comprising a SQUID inductor could be applied in the future for circuits with different configurations.

To further advance the thesis project to the next level, future experiments will involve probing the quantum dynamics of the qubit with the resonant readout technique at dilution refrigerator temperatures. The coherence times of the qubit can then be compared with previous results using the switching current readout. Some preliminary experimental work has been carried out and will be presented in the following section.

6.2 Future Work

One of the future goals is to employ the resonant readout scheme for probing the quantum dynamics of the qubit at dilution refrigerator temperatures. The main objective would be to perform similar qubit experiments discussed in section 2.2.4, and to compare the coherence times of the qubit with previous results from the switching current readout. The following sections discuss the preliminary work which has been carried out to achieve this goal. This mainly involves (1) the development of a time-resolved measurement scheme, and (2) an improved electronic setup designed for the low temperature stages of the dilution refrigerator.

6.2.1 Time-resolved Resonant Readout

In the time-resolved scheme, the resonant readout is biased at a single frequency near the resonant frequency. The qubit signal is detected as a difference in the magnitude or phase of the output voltage, rather than a shift in the resonant frequency. The following discussion focuses on the implementation of the fast readout scheme, and is not intended to be specific for a certain experiment. The generic pulse sequence for the rapid measurement scheme is shown in fig. 6-1. The readout is to be performed on a μs timescale.

The qubit dynamics are controlled by microwave pulses, with a frequency typically between 1-40 GHz. The readout pulse is of frequency ~ 500 MHz near the resonant frequency of the resonant circuit. Depending on the state of the qubit, the voltage response of the readout circuit will be different. The response time τ_{ss} of the resonant circuit depends on the quality factor Q, and is estimated to be $0.6\,\mu s$ for a Q on the order of 1000.

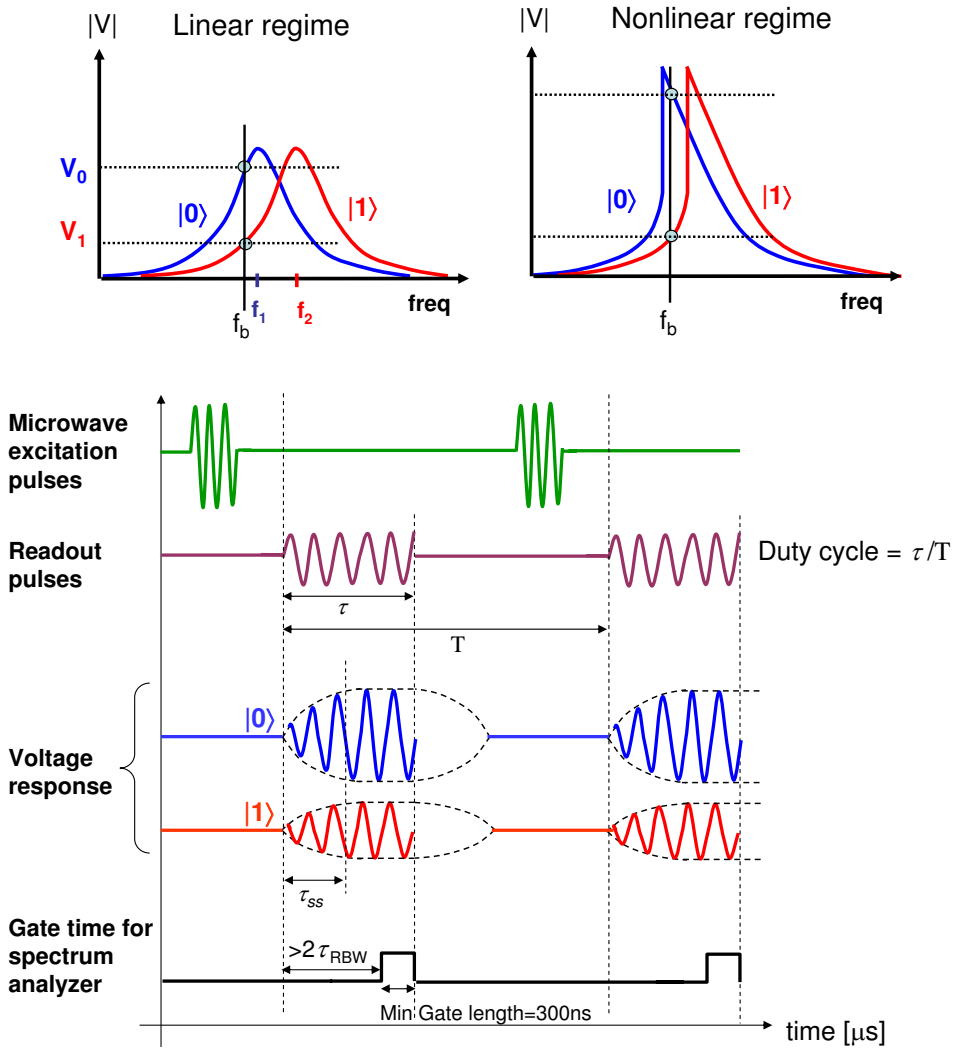

Figure 6-1: Pulse sequence of the time-resolved resonant readout. The spectrum analyzer is shown operated with the gated-time measurement. The fast measurement scheme is to be performed on a μs timescale.

Pulse spectrum measurement vs. Gated time measurement

To measure the voltage response, the spectrum analyzer is first put in zero span about the frequency of interest. Then there are two choices with the detection modes of the spectrum analyzer: pulse spectrum measurement [77] and gated time measurement [78]. The first way is to have the spectrum analyzer detecting for a period of N × T, where N is the number of repeating pulses, and T is the period of the pulse train (see fig. 6-1). The amplitude of the voltage measured at the analyzer will be reduced by the duty cycle of the pulse train:

$$V_{SA} = \frac{A\tau}{T} \tag{6.1}$$

where A is the original amplitude of the voltage response, and τ/T is the duty cycle of the pulse train. This option may be less desirable if the waiting time between subsequent measurements is relatively long, and thus the signal will be reduced significantly by the low duty cycle.

An alternative option is to perform gated time measurements with the spectrum analyzer, where one can control the window of time when the spectrum analyzer is detecting. This is illustrated in the pulse sequence in fig. 6-1. The minimum gate length for our spectrum analyzer model is 300 ns [1], which should be reasonably fast enough as a start. However, one should be aware that there is a charging time for the filter associated with the resolution bandwidth (RBW) given by $\tau_{RBW} = 1/RBW$. As illustrated in fig. 6-1, the time elapse between the beginning of the signal of interest and the start of the gate time should be longer than the setup time (SUT), where $SUT = 2 \times \tau_{RBW}$.

6.2.2 Low-temperature electronic setup for dilution refrigerator

The proposed electronic scheme for the dilution refrigerator experiments is shown in fig. 6-2. This is similar to the 300 mK setup in fig. 3-8. The main improvement to the electronic setup will be the addition of a low-noise cryogenic amplifier [2] at the 4 K stage. The amplifier design is based on HEMT transistors. It has a gain of 36 dB with noise temperature of 1.0 K at

[1] Gated time option for Agilent E4407B ESA series Spectrum Analyzer, 9 kHz to 26.5 GHz
[2] QCA-U-430-2Z01 Cryogenic Amplifier, 340 MHz to 520 MHz

430 MHz when tested at 15 K. The improved noise performance allows signals to be detected with fewer numbers of averaging in a spectrum analyzer. It may even allow the possibility of detection using a fast oscilloscope [3] in the time domain. The fast oscilloscope does not have as narrow a resolution bandwidth as the spectrum analyzer, and thus is less sensitive in detecting small signals.

To reduce the noise introduced by the cryogenic amplifier back on the sample, a standard technique is to include an isolator [4] between the amplifier and the device. The isolator is a passive, non-reciprocal microwave device which allows signal to flow in one direction only. Typical isolators work at frequencies higher than at least 100 MHz.

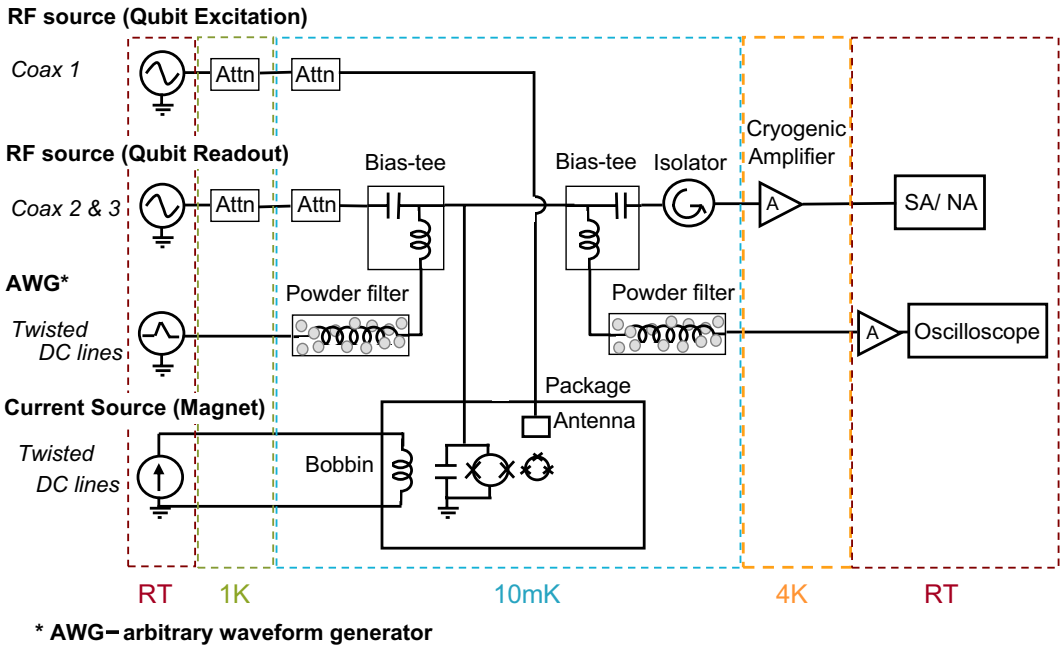

Figure 6-2: The proposed electronic scheme for experiments in the dilution refrigerator. The main improvement is the low-noise cryogenic amplifier at the 4 K stage, and the isolator which prevents noise to be fed from the amplifier to the device.

[3] Tektronix TDS 7104 Digital Phosphor Oscilloscope, 1 GHz bandwidth
[4] Nova Microwave Inc., 0042IAS Isolator, 350 MHz to 500 MHz

6.2.3 Testing of new symmetric circuit design

With the goal to minimize oscillating flux coupled from the resonating loop to the readout SQUID, we have designed new resonant circuits with a symmetric configuration. One of such symmetric designs is shown in fig. 6-3. With a comparison to the earlier QC4 design in fig. 3-3, the resonating capacitor is split and realized by C_2 on both sides of the SQUID. Thus, the resonating loop is also split symmetrically, and any induced flux on one side will be canceled out by a similar amount of flux on the other side. In addition, the new circuit schematic employs an L-match impedance network on both the input and the output sides, while the tapped-inductor transformer is eliminated.

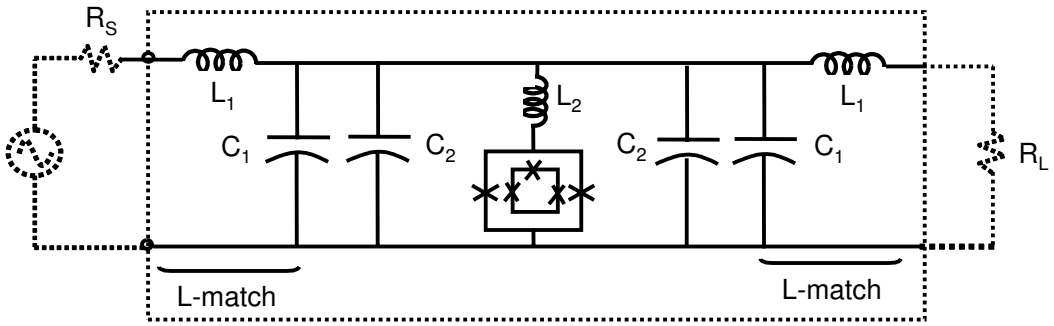

Figure 6-3: Circuit schematic of the symmetric resonant circuit design. The resonating capacitance is provided by C_2 on both sides of the SQUID. L-match impedance network are employed on the input and output sides. The component values are $L_J = 0.2\,\text{nH}$, $L_1 = 69\,\text{nH}$, $L_2 = 0.78\,\text{nH}$, $C_1 = 1.4\,\text{pF}$, and $C_2 = 50\,\text{pF}$. The junctions of the SQUID are each shunted by a 5 pF capacitor (not shown). The components within the dotted box were fabricated on-chip.

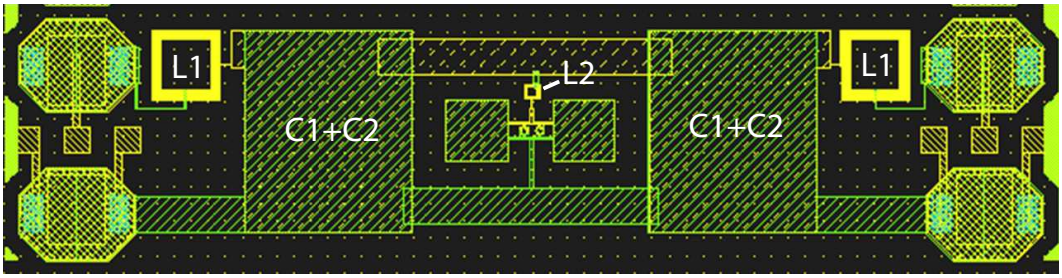

Figure 6-4: Layout of the symmetric circuit as shown in the XIC design tool.

The layout of the circuit design is shown in figure 6-4. Devices have been fabricated in the DSM fabrication run at Lincoln Laboratory and are awaiting to be tested. In addition, test structures for on-chip capacitors and spiral inductors were also incorporated on-chip (fig. 6-5). Being able to determine the actual values of the on-chip circuit elements will be important to understand the resultant resonant behavior of the readout circuit.

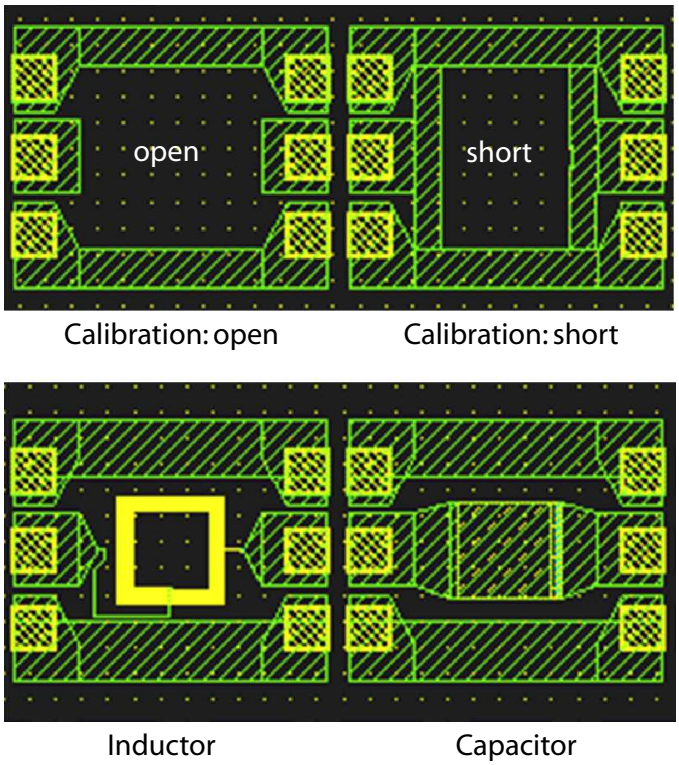

Figure 6-5: Examples of test structures for a spiral inductor and a capacitor. The top structures are to be used as calibration standards for open and short circuits.

Appendix A

Analysis of Tapped-inductor Impedance Transformation

Abstract

The circuit design of the resonant readout in fig. 3-4 has employed the tapped-inductor transformation technique to achieve a high quality factor. This appendix provides a derivation of the design equations in 3.2 and 3.3.

The tapped-inductor transformation is shown in fig. A-1 with a resonating capacitor. The transformer is usually used to raise R_2 to a higher resistance R_T at the resonant frequency, and thus raising the Q of the resonator. We want to derive the equations relating R_T to R_2, given the design parameters L_1 and L_2. The design equations can be obtained by converting the tapped configuration to its equivalent RL shunt using series-parallel transformations of impedances.

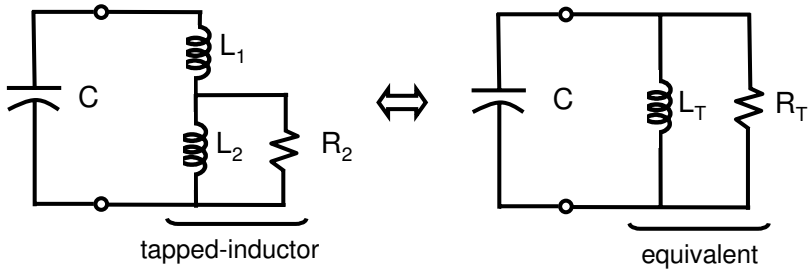

Figure A-1: [left]: Configuration of a tapped-inductor transformation shunted by a resonant capacitor; [right]: Equivalent circuit

We begin by establishing some formula required for series to parallel transformation and vice versa:

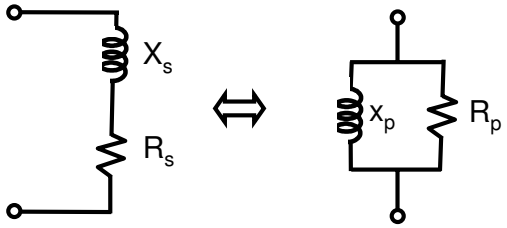

Figure A-2: Series to parallel transformation. The reactive element could be either an inductor or capacitor, with $X = \omega L$ for an inductor and $X = -1/\omega C$ for a capacitor

The reactive element is shown here as an inductor, but in reality can either be an inductor ($X = \omega L$) or a capacitor ($X = -1/\omega C$). First, we note that the Qs of the series and parallel network are given by:

$$Q_s = \frac{|X_s|}{R_s} \qquad Q_p = \frac{R_p}{|X_p|} \tag{A.1}$$

$$= \frac{\omega L_s}{R_s} \qquad = \frac{R_p}{\omega L_p} \tag{A.2}$$

We can assign a Q to the network as one can imagine connecting a capacitor to the ports as in fig. A-1. In that case, ω will be set to ω_o, and the formula will be consistent with those for a series and parallel RLC circuit. Note that at resonance, the reactance of the capacitor and the inductor are equal, i.e. $w_oL = 1/w_oC$.

If we claim that the series and the parallel networks are equivalent, the Qs of the two networks must also be equal. Therefore, we obtain the following Q-invariance relation which will be used later for the conversion:

$$Q_s = Q_p \tag{A.3}$$
$$\frac{\omega L_s}{R_s} = \frac{R_p}{\omega L_p}$$

We then write out the impedances of both the series and parallel networks:

$$Z_p = \frac{j\omega L_p R_p}{j\omega L_p + R_p}$$
$$= R_p(\frac{\omega^2 L_p^2}{R_p^2 + \omega^2 L_p^2}) + j\omega L_p(\frac{R_p^2}{R_p^2 + \omega^2 L_p^2}) \tag{A.4}$$

$$Z_s = R_s + j\omega L_s \tag{A.5}$$

By equating Z_p with Z_s, we can convert from a parallel to a series network according to the equations:

$$R_s = R_p(\frac{\omega^2 L_p^2}{R_p^2 + \omega^2 L_p^2}) = R_p(\frac{1}{{Q_p}^2 + 1}) \tag{A.6}$$

$$L_s = L_p(\frac{R_p^2}{R_p^2 + \omega^2 L_p^2}) = L_p(\frac{{Q_p}^2}{{Q_p}^2 + 1}) \tag{A.7}$$

We have used the fact that $R_p/\omega L_p$ is simply Q_p. From the Q-invariance principle in

eqn. A.3, the same equations can also be used when converting from a series to parallel configuration. We can conveniently interchange Q_s and Q_p depending on the conversion we are performing. The formula are summarized below:

$$\boxed{\begin{aligned} &parallel \rightarrow series : R_s = R_p(\frac{1}{Q^2+1}), \quad X_s = X_p(\frac{Q^2}{Q^2+1}) \\ &series \rightarrow parallel : R_p = R_s(Q^2+1), \quad X_p = X_s(\frac{Q^2+1}{Q^2}) \end{aligned}}$$

For a high Q circuit where $(Q^2+1) \approx Q^2$, we can make the following useful approximations:

$$\boxed{\begin{aligned} R_s &\approx \frac{R_p}{Q^2} \\ X_s &\approx X_p \end{aligned}}$$

Now we will proceed to analyze the tapped-inductor transformation. Our goal is to obtain the transformation relation by relating R_4 to R_2 in terms of L_1 and L_2. The steps of conversion are shown in fig. A-3.

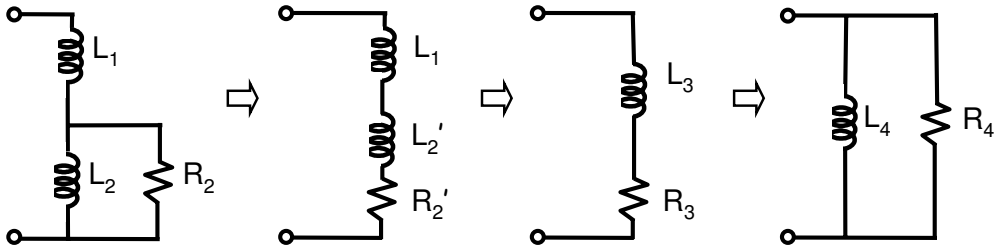

Figure A-3: Converting a tapped-inductor configuration to a simple inductor-resistor shunt

From step 1 to 2: (parallel to series)

$$L_2{}' = L_2(\frac{{Q_2}^2}{{Q_2}^2+1}) = L_2(\frac{R_2^2}{R_2^2+\omega^2 L_2^2}) \tag{A.8}$$

$$R_2{}' = R_2(\frac{1}{{Q_2}^2+1}) = R_2(\frac{\omega^2 {L_2}^2}{{R_2}^2+\omega^2 {L_2}^2}) \tag{A.9}$$

Step 2 to 3:

$$L_3 = L_1 + {L_2}' \tag{A.10}$$

$$R_3 = {R_2}' \tag{A.11}$$

Step 3 to 4: (series to parallel)

$$L_4 = L_3(\frac{{Q_3}^2 + 1}{{Q_3}^2}) = \frac{{R_3}^2}{\omega^2 L_3}(\frac{\omega^2 {L_3}^2}{{R_3}^2} + 1) \tag{A.12}$$

$$R_4 = R_3({Q_3}^2 + 1) = R_3(\frac{\omega^2 {L_3}^2}{{R_3}^2} + 1) \tag{A.13}$$

If we assume the Q of the circuit is high, we can make the approximation that $(Q^2+1) \approx Q^2$. In this case, we can make some significant simplifications:

$$L_4 \approx L_1 + L_2 \tag{A.14}$$

$$R_4 \approx R_2 \left(\frac{L_1 + L_2}{L_2}\right)^2 \tag{A.15}$$

So the transformation factor in the case of $Q^2 >> 1$ is given below. Note that the expression does not depend on the operating frequency.

$$\boxed{\frac{R_4}{R_2} = (\frac{L_1+L_2}{L_2})^2} \tag{A.16}$$

Without the high-Q approximation, the transformed resistance and inductance are related to the original parameters by:

$$L_4 = \frac{{R_2}^2(\frac{\omega^2 {L_2}^2}{{R_2}^2+\omega^2 {L_2}^2})^2}{\omega^2(L_1 + L_2(\frac{R_2^2}{R_2^2+\omega^2 L_2^2}))} \left[\frac{\omega^2(L_1 + L_2(\frac{R_2^2}{R_2^2+\omega^2 L_2^2}))^2}{{R_2}^2(\frac{\omega^2 {L_2}^2}{{R_2}^2+\omega^2 {L_2}^2})^2} + 1\right] \tag{A.17}$$

$$R_4 = R_2(\frac{\omega^2 {L_2}^2}{{R_2}^2 + \omega^2 {L_2}^2}) \left[\frac{\omega^2(L_1 + L_2(\frac{R_2^2}{R_2^2+\omega^2 L_2^2}))^2}{{R_2}^2(\frac{\omega^2 {L_2}^2}{{R_2}^2+\omega^2 {L_2}^2})^2} + 1\right] \tag{A.18}$$

Appendix B

Scaling ODEs for Numerical Simulations

Abstract

When solving a set of differential equations numerically, it is oftentimes necessary to scale the time variable with respect to the largest characteristic time of the circuit. This ensures that the ode solver takes the appropriate time step to capture the dynamics of the system. This appendix illustrates the techniques to scale differential equations with two simple examples: a linear RLC circuit, and a single Josephson junction represented by the RCSJ model. It then discusses the scaling for the differential equations governing the resonant readout circuit presented in section 5.5.

Simple parallel RLC circuit

For a simple parallel RLC circuit driven by a current source, the differential equation is given by:

$$I = i_L + \frac{L}{R}\frac{di_L}{dt} + LC\frac{d^2 i_L}{dt^2} \tag{B.1}$$

The coefficient of the first derivative has unit of time, and is the characteristic time for the inductor and resistor:

$$\tau_L = \frac{L}{R} \tag{B.2}$$

The coefficient of the second derivative has unit of $(time)^2$, and is the product of the characteristic times for L-R and R-C:

$$\tau_L \tau_{RC} = \frac{L}{R}(RC) = LC \tag{B.3}$$

Thus equation B.1 can be rewritten as:

$$I = i_L + \tau_L \frac{di_L}{dt} + \tau_L \tau_{RC}\frac{d^2 i_L}{dt^2} \tag{B.4}$$

To scale the equations for numerical simulations, we first write the equation in terms of normalized quantity:

$$1 = \tilde{i_L} + \tau_L \frac{d\tilde{i_L}}{dt} + \tau_L \tau_{RC}\frac{d^2\tilde{i_L}}{dt^2} \tag{B.5}$$

where $\tilde{i_L} = i_L/I$

Then we need to scale the time variable according to the characteristic times of the equation. Our goal is to scale time t to a dimensionless quantity τ such that:

$$t = A\tau \tag{B.6}$$

$$\frac{dx}{d\tau} = A\frac{dx}{d\tau} \tag{B.7}$$

where x is the dependent variable (in this case $x = \tilde{i_L}$) of the differential equation, and A is

a scaling parameter which has the unit of time. The independent variable of the differential equation will be scaled from t to τ as follows:

$$1 = \tilde{i_L} + \frac{\tau_L}{A}\frac{d\tilde{i_L}}{d\tau} + \frac{\tau_L \tau_{RC}}{A^2}\frac{d^2\tilde{i_L}}{dt^2} \tag{B.8}$$

There are two choices of A given the equation has two characteristic times. First we choose A to be the characteristic time τ_L, then the coefficient of the first derivative term will be unity after the scaling:

$$A = \tau_L \tag{B.9}$$

$$1 = \tilde{i_L} + \frac{d\tilde{i_L}}{d\tau} + \frac{\tau_{RC}}{\tau_L}\frac{d^2\tilde{i_L}}{d\tau^2} \tag{B.10}$$

This will be useful for the case when the coefficient of the last term $\tau_{RC}/\tau_L \ll 1$, which means the dynamics of the system is governed by the combination of L and R.

The other choice of A is such that the coefficient of the second derivative term is unity:

$$A = \sqrt{\tau_L \tau_{RC}} \tag{B.11}$$

$$1 = \tilde{i_L} + \frac{\tau_L}{\sqrt{\tau_L \tau_{RC}}}\frac{d\tilde{i_L}}{d\tau} + \frac{d^2\tilde{i_L}}{d\tau^2} \tag{B.12}$$

$$1 = \tilde{i_L} + \frac{1}{Q}\frac{d\tilde{i_L}}{d\tau} + \frac{d^2\tilde{i_L}}{d\tau^2} \tag{B.13}$$

where $Q = R\sqrt{C/L}$ which is the quality factor for a parallel circuit. This way of scaling the equation is useful when $\tau_{RC}/\tau_L \gg 1$ or in other words, when the Q of the circuit is high. The dynamics of the system is governed by the combination of R and C.

Single Josephson Junction

The differential equation of a Josephson junction represented by the RCSJ model driven by a current source I is given by:

$$I = I_c \sin\varphi + \frac{\Phi_o}{2\pi R}\frac{d\varphi}{dt} + \frac{C\Phi_o}{2\pi}\frac{d^2\varphi}{dt^2} \tag{B.14}$$

where φ is the gauge-invariant phase of the junction. We first normalize the equation by I_c:

$$\frac{I}{I_c} = \sin\varphi + \frac{\Phi_o}{2\pi I_c R}\frac{d\varphi}{dt} + \frac{C\Phi_o}{2\pi I_c}\frac{d^2\varphi}{dt^2} \tag{B.15}$$

if one linearizes the equation so that $\sin\varphi \sim \varphi$ with the assumption that φ is small, then equation B.15 has the same form as eqn. B.5. The linearization of the equation is not necessary for the discussion here. We recognize that $\Phi_o/2\pi I_c$ is the Josephson inductance of the junction. Thus the equation can be further rewritten in terms of the characteristic times:

$$\frac{I}{I_c} = \sin\varphi + \tau_{L_J}\frac{d\varphi}{dt} + \tau_{L_J}\tau_{RC}\frac{d^2\varphi}{dt^2} \tag{B.16}$$

Similar to the regular RLC resonant circuit, we can scale the time variable of the equation into a dimenionless quantity by a choice of A so that $t = A\tau$. Again, A has the unit of time, and there are two ways to scale the equation depending on the choice of A.

$$A = \tau_{L_J} \tag{B.17}$$

$$\frac{I}{I_c} = \sin\varphi + \frac{d\varphi}{d\tau} + \frac{\tau_{RC}}{\tau_{L_J}}\frac{d^2\varphi}{d\tau^2} \tag{B.18}$$

where the coefficient of the first derivative is unity, and the coefficient of the second derivative gives the ratio of the time constants. This ratio τ_{RC}/τ_{L_J} is a measure of the importance of the capacitance, and is also known as the Stewart-McCumber parameter, β_c. This way of scaling the equation is useful when $\beta_c \ll 1$ and that the dynamics of the system is governed by the combination of L and R.

The other choice of A is:

$$A = \sqrt{\tau_{L_J}\tau_{RC}} \tag{B.19}$$

$$\frac{I}{I_c} = \sin\varphi + \sqrt{\frac{\tau_{L_J}}{\tau_{RC}}}\frac{d\varphi}{d\tau} + \frac{d^2\varphi}{d\tau^2} \tag{B.20}$$

$$\tag{B.21}$$

which is useful when $\beta_c \gg 1$ and that the dynamics of the system is governed by the combination of R and C.

Resonant Resonant Circuit

The differential equations governing the resonant readout circuit presented in section 5.5 are given in eqns. 5.69 to 5.71. They are reviewed below (assuming no asymmetry):

KCL

$$I \sin \omega t = I_c \sin \varphi_p \cos \varphi_m + \frac{V_c}{R_L} + C_L \frac{dV_c}{dt} + \frac{\Phi_o}{\pi R} \frac{d\varphi_p}{dt} + \frac{C\Phi_o}{\pi} \frac{d^2\varphi_p}{dt^2} \tag{B.22}$$

where $I_c = 2I_{co}$. Normalize the equation by I_c:

$$\tilde{I} \sin \omega t = \sin \varphi_p \cos \varphi_m + \frac{\Phi_o}{2\pi I_c R_L} \frac{d\varphi_c}{dt} + \frac{\Phi_o C_L}{2\pi I_c} \frac{d^2\varphi_c}{dt^2} + \frac{\Phi_o}{\pi I_c R} \frac{d\varphi_p}{dt} + \frac{C\Phi_o}{\pi I_c} \frac{d^2\varphi_p}{dt^2} \tag{B.23}$$

where $\tilde{I} = I/I_c$ and $V_c = \frac{\Phi_o}{2\pi} \frac{d\varphi_c}{dt}$. From the coefficient of the derivative terms, we recognize four characteristic times:

$$\begin{aligned} (1) \quad & \tau_{L_J,R/2} && = \tfrac{\Phi_o}{\pi I_c R} \\ (2) \quad & \sqrt{\tau_{L_J,R} \tau_{R,2C}} && = \sqrt{\tfrac{C\Phi_o}{\pi I_c}} \\ (3) \quad & \tau_{L_J,R_L} && = \tfrac{\Phi_o}{2\pi I_c R_L} \\ (4) \quad & \sqrt{\tau_{L_J,R} \tau_{R,C_L}} && = \sqrt{\tfrac{C_L \Phi_o}{2\pi I_c}} \end{aligned} \tag{B.24}$$

KVL

$$-f(\varphi_p, \varphi_m) = -V_c + \frac{\Phi_o}{2\pi} \frac{d\varphi_p}{dt} + \frac{b_{1p}\Phi_o}{2\pi R} \frac{d^2\varphi_p}{dt^2} + \frac{b_{1p} C\Phi_o}{2\pi} \frac{d^3\varphi_p}{dt^3} + \frac{b_2 \Phi_o}{2\pi R} \frac{d^2\varphi_m}{dt^2} + \frac{b_2 C\Phi_o}{2\pi} \frac{d^3\varphi_m}{dt^3} \tag{B.25}$$

where b_{1p} and b_{1m} and b_2 have unit of inductance, and

$$\begin{aligned} f(\varphi_p, \varphi_m) = b_{1p} I_{co} (\cos \varphi_p \cos \varphi_m \frac{d\varphi_p}{dt} - \sin \varphi_p \sin \varphi_m \frac{d\varphi_m}{dt}) \\ + b_2 I_{co} (\cos \varphi_p \cos \varphi_m \frac{d\varphi_m}{dt} - \sin \varphi_p \sin \varphi_m \frac{d\varphi_p}{dt}) \end{aligned} \tag{B.26}$$

Normalize the equation by I_cR:

$$-\tilde{f}(\varphi_p,\varphi_m) = -\frac{\Phi_o}{2\pi I_cR}\frac{d\varphi_c}{dt} + \frac{\Phi_o}{2\pi I_cR}\frac{d\varphi_p}{dt} + \frac{\Phi_o b_{1p}}{2\pi I_cR^2}\frac{d^2\varphi_p}{dt^2} + \frac{\Phi_o b_{1p}C}{2\pi I_cR}\frac{d^3\varphi_p}{dt^3} + \frac{\Phi_o b_2}{2\pi I_cR^2}\frac{d^2\varphi_m}{dt^2} + \frac{\Phi_o b_2 C}{2\pi I_cR}\frac{d^3\varphi_m}{dt^3} \quad \text{(B.27)}$$

where $\tilde{V}_c = (2\pi/\Phi_o)V_c$ and $\tilde{f}(\varphi_p,\varphi_m) = f(\varphi_p,\varphi_m)/I_cR$. There are five characteristic times

$$\begin{array}{lll} (1) & \tau_{L_J,R} & = \frac{\Phi_o}{2\pi I_cR} \\ (2) & \sqrt{\tau_{L_J,R}\tau_{L_1,R}} & = \sqrt{\frac{\Phi_o b_{1p}}{2\pi I_cR^2}} \\ (3) & (\tau_{L_J,R}\tau_{L_1,R}\tau_{R,C})^{1/3} & = (\frac{\Phi_o b_{1p}C}{2\pi I_cR})(1/3) \\ (4) & \sqrt{\tau_{L_J,R}\tau_{L_2,R}} & = \sqrt{\frac{\Phi_o b_2}{2\pi I_cR^2}} \\ (5) & (\tau_{L_J,R}\tau_{L_2,R}\tau_{R,C})^{1/3} & = (\frac{\Phi_o b_2 C}{2\pi I_cR})(1/3) \end{array} \quad \text{(B.28)}$$

Fluxoid Equation

$$0 = \varphi_m + \frac{\pi I_c}{\Phi_o}(b_2\sin\varphi_p\cos\varphi_m + b_{1m}\cos\varphi_p\sin\varphi_m) + \frac{b_2}{R}\frac{d\varphi_p}{dt} + b_2C\frac{d^2\varphi_p}{dt^2} + \frac{b_{1m}}{R}\frac{d\varphi_m}{dt} + b_{1m}C\frac{d^2\varphi_m}{dt^2} - \frac{\pi\Phi_{ext}}{\Phi_o} \quad \text{(B.29)}$$

Characteristic times are:

$$\begin{array}{lll} (1) & \tau_{L_2,R} & = \frac{b_2}{R} \\ (2) & \sqrt{\tau_{L_2,R}\tau_{R,C}} & = \sqrt{b_2C} \\ (3) & \tau_{L_{1m},R} & = \frac{b_{1m}}{R} \\ (4) & \sqrt{\tau_{L_{1m},R}\tau_{R,C}} & = \sqrt{b_{1m}C} \end{array} \quad \text{(B.30)}$$

In our simulations, we normalized the time variable with respect to the largest characteristic time.

Appendix C

Summary of Equations governing a SQUID

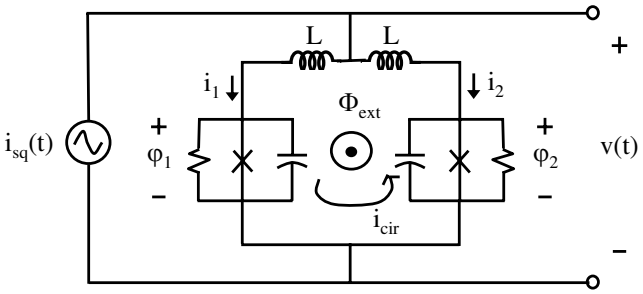

Figure C-1: Circuit schematic of a SQUID circuit driven by an AC current source.

Assumptions

The SQUID has *symmetric* arms each of inductance L, thus $L_{loop} = 2L$.

The SQUID has *symmetric* junctions each with critical current of I_{co}

Conventions

$$\varphi_p = \frac{\varphi_1 + \varphi_2}{2} \tag{C.1}$$

$$\varphi_m = \frac{\varphi_1 - \varphi_2}{2} \tag{C.2}$$

$$I_{cir} = \Phi_{induced}/L_{loop} \tag{C.3}$$

Current in each arm:

$$i_1 = I_{co}\sin\varphi_1 + \frac{\Phi_o}{2\pi R}\frac{d\varphi_1}{dt} + \frac{C\Phi_o}{2\pi}\frac{d^2\varphi_1}{dt^2} \tag{C.4}$$

$$i_2 = I_{co}\sin\varphi_2 + \frac{\Phi_o}{2\pi R}\frac{d\varphi_2}{dt} + \frac{C\Phi_o}{2\pi}\frac{d^2\varphi_2}{dt^2} \tag{C.5}$$

Sum and Difference of Currents:

$$\frac{i_1+i_2}{2} = \frac{I_{co}}{2}(\sin\varphi_1+\sin\varphi_2) + \frac{\Phi_o}{2\pi R}\frac{d}{dt}\left(\frac{\varphi_1+\varphi_2}{2}\right) + \frac{C\Phi_o}{2\pi}\frac{d^2}{dt^2}\left(\frac{\varphi_1+\varphi_2}{2}\right) \tag{C.6}$$

$$= I_{co}\cos\varphi_m\sin\varphi_p + \frac{\Phi_o}{2\pi R}\frac{d\varphi_p}{dt} + \frac{C\Phi_o}{2\pi}\frac{d^2\varphi_p}{dt^2} \tag{C.7}$$

$$\frac{i_1-i_2}{2} = \frac{I_{co}}{2}(\sin\varphi_1-\sin\varphi_2) + \frac{\Phi_o}{2\pi R}\frac{d}{dt}\left(\frac{\varphi_1-\varphi_2}{2}\right) + \frac{C\Phi_o}{2\pi}\frac{d^2}{dt^2}\left(\frac{\varphi_1-\varphi_2}{2}\right) \tag{C.8}$$

$$= I_{co}\sin\varphi_m\cos\varphi_p + \frac{\Phi_o}{2\pi R}\frac{d\varphi_m}{dt} + \frac{C\Phi_o}{2\pi}\frac{d^2\varphi_m}{dt^2} \tag{C.9}$$

Note: $I_{cir} \equiv (i_1 - i_2)/2$ for the case of equal arm inductances.

Current Continuity Equation with AC drive

$$i_{sq}(t) = 2\left(\frac{i_1+i_2}{2}\right) \tag{C.10}$$

$$= 2I_{co}\cos\varphi_m\sin\varphi_p + \frac{2}{R}\frac{\Phi_o}{2\pi}\frac{d\varphi_p}{dt} + 2C\frac{\Phi_o}{2\pi}\frac{d^2\varphi_p}{dt^2} \tag{C.11}$$

Fluxoid Quantization Equation for an AC drive

$$0 = -\varphi_1 + \varphi_2 - \frac{2\pi}{\Phi_o}Li_1 + \frac{2\pi}{\Phi_o}Li_2 - \frac{2\pi}{\Phi_o}\Phi_{ext} \tag{C.12}$$

$$0 = -\left(\frac{\varphi_1-\varphi_2}{2}\right) - \frac{2\pi}{\Phi_o}L\left(\frac{i_1-i_2}{2}\right) - \frac{\pi}{\Phi_o}\Phi_{ext} \tag{C.13}$$

$$0 = \varphi_m + L\left(\frac{2\pi}{\Phi_o}I_{co}\sin\varphi_m\cos\varphi_p + \frac{1}{R}\frac{d\varphi_m}{dt} + C\frac{d^2\varphi_m}{dt^2}\right) + \frac{\pi\Phi_{ext}}{\Phi_o} \tag{C.14}$$

Definition of Voltage across a SQUID

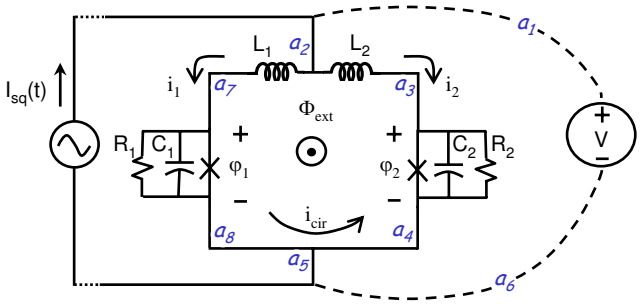

Figure C-2: Circuit diagram of a DC SQUID driven by an AC source. The SQUID has arm inductances L_1 and L_2, and junctions represented by the RCSJ model. The voltage across the SQUID is represented by the voltmeter reading.

Our objective is to find the voltage across a DC SQUID, which is represented here by the voltmeter reading. Our approach to find the voltage is to go around a closed loop. In this case, the two possible loops are a1-2-3-4-5-6 or a1-2-7-8-5-6, and both should give the same result. When going around the loop, we take into account any voltage across a lumped element, as well as the induced EMF due to any time-varying flux that is enclosed in the voltmeter loop according to Faraday's Law.

Note that in the circuit model for the DC SQUID, L_1 and L_2 are loop inductances that are used to model flux generated in the SQUID loop (and possibly in nearby loops). Physically, these inductors are traces and do not have any internal winding. Thus there is no localized flux associated with the inductors, and the voltage (i.e. induced EMF) across the inductors themselves are zero. Nevertheless, the induced EMF due to the time-varying flux contributed by these inductors *in the SQUID loop* needs to be taken into account. The difference between the cases when the inductors represent loop inductance or actual windings is illustrated in fig. C-3. The SQUID circuit under consideration belongs to the case shown on the left of fig. C-3.

For this discussion, we restrict the external flux Φ_{ext} in the circuit diagram be DC only. Therefore the only AC flux will be due to the induced flux caused by the AC driving current. Referring to fig. C-2, we express the voltmeter reading by going around a closed loop.

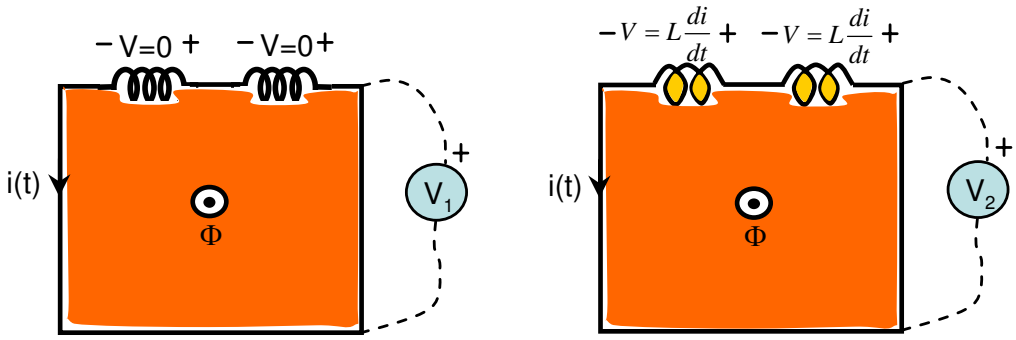

Figure C-3: [Left]: Inductors represent loop inductance and contributes flux only in the loop. V_1 is given by $\frac{d\Phi}{dt}$, where $\Phi = 2Li$. [Right]: Inductors are made up of physical windings, and generate flux both locally and also mutually coupled to the loop. V_2 is given by $\frac{d\Phi}{dt} + 2L\frac{di}{dt}$, where $\Phi = 2Mi$, and M is the mutual coupling between the windings and the loop.

Loop a1-2-3-4-5-6: let $V = V_a$

$$V_a - \frac{\Phi_o}{2\pi}\dot{\varphi}_2 = 0 \tag{C.15}$$

$$V_a = \frac{\Phi_o}{2\pi}\dot{\varphi}_2 \tag{C.16}$$

Note that this path does not enclose the SQUID loop, so there is no time-varying flux, and V_a is simply equal to the junction-2 voltage. For this discussion, we have ignored any flux contribution of L1 and L2 outside of the SQUID loop.

Loop a1-2-7-8-5-6: let $V = V_b$

$$V_b - \frac{\Phi_o}{2\pi}\dot{\varphi}_1 - \frac{d\Phi}{dt} = 0 \tag{C.17}$$

$$V_b = \frac{\Phi_o}{2\pi}\dot{\varphi}_1 + 2L\frac{d}{dt}\left(\frac{i_1 - i_2}{2}\right) \tag{C.18}$$

Note that V_b is equal to the junction-1 voltage, as well as the induced emf due to the time-varying flux in the SQUID loop.

Summary:

$$\boxed{\begin{aligned} V &= \frac{\Phi_o}{2\pi}\dot{\varphi}_2 \\ or\ \ V &= \frac{\Phi_o}{2\pi}\dot{\varphi}_1 + 2L\frac{d}{dt}\left(\frac{i_1 - i_2}{2}\right) \end{aligned}}$$

It is always good to check that the derivative of the fluxoid quantization equation is consistent with the voltage equation:

Fluxoid Equation:

$$0 = -\varphi_1 + \varphi_2 - \frac{2\pi}{\Phi_o}L_1 i_1 + \frac{2\pi}{\Phi_o}L_2 i_2 - \frac{2\pi\Phi_{ext}}{\Phi_o} \tag{C.19}$$

Voltage Equation

$$V_a = V_b \tag{C.20}$$

$$0 = \frac{\Phi_o}{2\pi}\dot{\varphi}_2 - \frac{\Phi_o}{2\pi}\dot{\varphi}_1 - L\frac{di_1}{dt} + L\frac{di_2}{dt} \tag{C.21}$$

Finally, note that:

$$V_a \neq \frac{\Phi_o}{2\pi}\dot{\varphi}_2 + L\frac{di_2}{dt} \tag{C.22}$$

$$V_b \neq \frac{\Phi_o}{2\pi}\dot{\varphi}_1 + L\frac{di_1}{dt} \tag{C.23}$$

Appendix D

Analysis of Resonant Circuit Model with Externally Coupled Flux

Abstract

In this appendix, we present the mathematical analysis for the circuit model presented in section 5.6. The analysis for circuit models 2 and 3 in section 5.7 will also be discussed.

D.1 Resonant circuit with Asymmetric SQUID

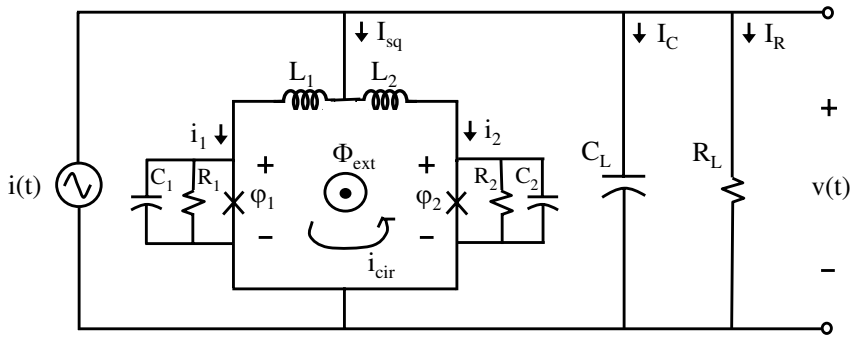

Figure D-1: Resonant circuit comprising an asymmetric SQUID. The external flux bias Φ_{ext} is assumed to be strictly DC.

In this section, we will present the analysis for circuit models 2 and 3 in section 5.7. The resonant circuit in D-1 corresponds to circuit model 2 when the SQUID has symmetric junctions, and corresponds to circuit model 3 when we assume the SQUID to have asymmetric junctions. The analysis below has included the terms due to the asymmetry, which can be set to zero for the symmetric case. The SQUID parameters due to the asymmetry are defined as follows:

$$I_{c1} = I_{co} + \Delta_I \qquad I_{c2} = I_{co} - \Delta_I \tag{D.1}$$

$$C_1 = C + \Delta_C \qquad C_2 = C - \Delta_C \tag{D.2}$$

$$R_1 = R + \Delta_R \qquad R_2 = R - \Delta_R \tag{D.3}$$

In addition, we have allowed the possibility that the loop inductance of the two arms are asymmetric. However, inductance asymmetry was not needed to explain the nonlinearity in the resonant behavior observed experimentally. In the simulations, we always set Δ_L to be zero.

$$L_1 = L + \Delta_L \qquad L_2 = L - \Delta_L \tag{D.4}$$

Variables

$$\varphi_p = \frac{\varphi_1 + \varphi_2}{2} \qquad \varphi_1 = \varphi_p + \varphi_m \tag{D.5}$$

$$\varphi_m = \frac{\varphi_1 - \varphi_2}{2} \qquad \varphi_2 = \varphi_p - \varphi_m \tag{D.6}$$

Current in each arm

$$i_1 = I_{c1}\sin\varphi_1 + \frac{\Phi_o}{2\pi R_1}\frac{d\varphi_1}{dt} + \frac{C_1\Phi_o}{2\pi}\frac{d^2\varphi_1}{dt^2} \tag{D.7}$$

$$= (I_{co} + \Delta_I)\sin\varphi_1 + \frac{\Phi_o}{2\pi(R + \Delta_R)}\frac{d\varphi_1}{dt} + (C + \Delta_c)\frac{\Phi_o}{2\pi}\frac{d^2\varphi_1}{dt^2} \tag{D.8}$$

$$i_2 = I_{c2}\sin\varphi_2 + \frac{\Phi_o}{2\pi R_2}\frac{d\varphi_2}{dt} + \frac{C_2\Phi_o}{2\pi}\frac{d^2\varphi_2}{dt^2} \tag{D.9}$$

$$= (I_{co} - \Delta_I)\sin\varphi_2 + \frac{\Phi_o}{2\pi(R - \Delta_R)}\frac{d\varphi_2}{dt} + (C - \Delta_c)\frac{\Phi_o}{2\pi}\frac{d^2\varphi_2}{dt^2} \tag{D.10}$$

Sum and difference of junction currents

$$\frac{i_1 + i_2}{2} = I_{co}\sin\varphi_p\cos\varphi_m + \frac{\Phi_o R}{2\pi(R^2 - {\Delta_R}^2)}\frac{d\varphi_p}{dt} + \frac{C\Phi_o}{2\pi}\frac{d^2\varphi_p}{dt^2} + \Delta_I\sin\varphi_m\cos\varphi_p - \frac{\Phi_o\Delta_R}{2\pi(R^2 - {\Delta_R}^2)}\frac{d\varphi_m}{dt} + \frac{\Delta_C\Phi_o}{2\pi}\frac{d^2\varphi_m}{dt^2} \tag{D.11}$$

$$\frac{i_1 - i_2}{2} = I_{co}\sin\varphi_m\cos\varphi_p + \frac{\Phi_o R}{2\pi(R^2 - {\Delta_R}^2)}\frac{d\varphi_m}{dt} + \frac{C\Phi_o}{2\pi}\frac{d^2\varphi_m}{dt^2} + \Delta_I\sin\varphi_p\cos\varphi_m - \frac{\Phi_o\Delta_R}{2\pi(R^2 - {\Delta_R}^2)}\frac{d\varphi_p}{dt} + \frac{\Delta_C\Phi_o}{2\pi}\frac{d^2\varphi_p}{dt^2} \tag{D.12}$$

SQUID Current

$$I_{sq} = i_1 + i_2 = 2I_{co}\sin\varphi_p\cos\varphi_m + 2\Delta_I\sin\varphi_m\cos\varphi_p + \frac{2\Phi_o R}{2\pi(R^2 - {\Delta_R}^2)}\frac{d\varphi_p}{dt} + \frac{2C\Phi_o}{2\pi}\frac{d^2\varphi_p}{dt^2} - \frac{2\Phi_o\Delta_R}{2\pi(R^2 - {\Delta_R}^2)}\frac{d\varphi_m}{dt} + \frac{2\Delta_c\Phi_o}{2\pi}\frac{d^2\varphi_m}{dt^2} \tag{D.13}$$

We will now analyze the resonant circuit shown in fig. D-1. The current continuity equation and the fluxoid equations are given below:

Current Continuity Equation

$$I \sin \omega t = I_{sq} + I_c + I_R \tag{D.14}$$

where I_{sq} is given by eqn. D.13, I_c and I_R are expressed in terms of the SQUID voltage:

$$I_R = \frac{V_{sq}}{R_L} = \frac{\Phi_o}{2\pi R_L}\left(\frac{d\varphi_p}{dt} - \frac{d\varphi_m}{dt}\right) \tag{D.15}$$

$$I_c = C_L \frac{dV_{sq}}{dt} = \frac{C_L \Phi_o}{2\pi}\left(\frac{d^2\varphi_p}{dt^2} - \frac{d^2\varphi_m}{dt^2}\right) \tag{D.16}$$

where

$$V_{sq} = \frac{\Phi_o}{2\pi}\left(\frac{d\varphi_p}{dt} - \frac{d\varphi_m}{dt}\right) \tag{D.17}$$

Eqn. D.14 becomes:

$$\begin{aligned} I \sin \omega t - 2I_{co} \sin \varphi_p \cos \varphi_m - 2\Delta_I \sin \varphi_m \cos \varphi_p = \\ + \left(\frac{\Phi_o R}{\pi({R^2} - {\Delta_R}^2)} + \frac{\Phi_o}{2\pi R_L}\right)\frac{d\varphi_p}{dt} + \left(\frac{C\Phi_o}{\pi} + \frac{C_L\Phi_o}{2\pi}\right)\frac{d^2\varphi_p}{dt^2} \\ - \left(\frac{\Phi_o \Delta_R}{\pi({R^2} - {\Delta_R}^2)} + \frac{\Phi_o}{2\pi R_L}\right)\frac{d\varphi_m}{dt} + \left(\frac{\Delta_C\Phi_o}{\pi} - \frac{C_L\Phi_o}{2\pi}\right)\frac{d^2\varphi_m}{dt^2} \end{aligned} \tag{D.18}$$

Fluxoid Quantization Equation

$$0 = \varphi_m + \frac{2\pi L}{\Phi_o}\left(\frac{i_1 - i_2}{2}\right) + \frac{2\pi\Delta_L}{\Phi_o}\left(\frac{i_1 + i_2}{2}\right) + \frac{\pi\Phi_{ext}}{\Phi_o} \tag{D.19}$$

$$\begin{aligned} \varphi_m + \frac{\pi\Phi_{ext}}{\Phi_o} + \left(\frac{2\pi L I_{co}}{\Phi_o} + \frac{2\pi\Delta_L\Delta_I}{\Phi_o}\right)\sin\varphi_m \cos\varphi_p + \left(\frac{2\pi L\Delta_I}{\Phi_o} + \frac{2\pi\Delta_L I_{co}}{\Phi_o}\right)\sin\varphi_p\cos\varphi_m \\ = \left(\frac{L\Delta_R}{{R^2} - {\Delta_R}^2} - \frac{\Delta_L R}{{R^2} - {\Delta_R}^2}\right)\frac{d\varphi_p}{dt} - (L\Delta_c + \Delta_L C)\frac{d^2\varphi_p}{dt^2} \\ - \left(\frac{LR}{{R^2} - {\Delta_R}^2} - \frac{\Delta_L\Delta_R}{{R^2} - {\Delta_R}^2}\right)\frac{d\varphi_m}{dt} - (LC + \Delta_L\Delta_c)\frac{d^2\varphi_m}{dt^2} \end{aligned} \tag{D.20}$$

Coding in Matlab

We will code the differential equations in eqns. D.18 and D.20 in the form:

$$Mx' = f(t, x) \tag{D.21}$$

where x is the vector of dependent variables, and x' is the vector of corresponding derivatives:

$$x = \begin{bmatrix} \varphi_p \\ \frac{d\varphi_p}{dt} \\ \varphi_m \\ \frac{d\varphi_m}{dt} \end{bmatrix} \qquad x' = \begin{bmatrix} \frac{d\varphi_p}{dt} \\ \frac{d^2\varphi_p}{dt^2} \\ \frac{d\varphi_m}{dt} \\ \frac{d^2\varphi_m}{dt^2} \end{bmatrix} \tag{D.22}$$

M is the mass matrix defined as:

$$\begin{bmatrix} 1 & 0 & 0 & 0 \\ 0 & 0 & 1 & 0 \\ \frac{\Phi_o R}{\pi(R^2-{\Delta_R}^2)} + \frac{\Phi_o}{2\pi R_L} & \frac{2C\Phi_o + C_L\Phi_o}{2\pi} & -\left(\frac{\Phi_o\Delta_R}{\pi(R^2-{\Delta_R}^2)} + \frac{\Phi_o}{2\pi R_L}\right) & \frac{\Delta_C\Phi_o}{\pi} - \frac{C_L\Phi_o}{2\pi} \\ \frac{L\Delta_R - \Delta_L R}{R^2-{\Delta_R}^2} & -(L\Delta_c + \Delta_L C) & \frac{\Delta_L\Delta_R - LR}{R^2-{\Delta_R}^2} & -(LC + \Delta_L\Delta_c) \end{bmatrix} \tag{D.23}$$

where the 3^{rd} row corresponds to the current continuity equation, and the 4^{th} row corresponds to the fluxoid quantization equation.

In addition, f(t,x) is given by:

$$f = \begin{bmatrix} \frac{d\varphi_p}{dt} \\ \frac{d\varphi_m}{dt} \\ I\sin\omega t - 2I_{co}\sin\varphi_p\cos\varphi_m - 2\Delta_I\sin\varphi_m\cos\varphi_p \\ \varphi_m + \frac{\pi\Phi_{ext}}{\Phi_o} + \left(\frac{2\pi L I_{co}}{\Phi_o} + \frac{2\pi\Delta_L\Delta_I}{\Phi_o}\right)\sin\varphi_m\cos\varphi_p + \left(\frac{2\pi L\Delta_I}{\Phi_o} + \frac{2\pi\Delta_L I_{co}}{\Phi_o}\right)\sin\varphi_p\cos\varphi_m \end{bmatrix} \tag{D.24}$$

Simulation Results

When we set the junction asymmetry to zero, the results for the nonlinear resonant spectrum of the circuit at various flux biases are shown in fig. D-2. The spectra bend to the lower frequency side, indicating that the effective inductance is always higher. This occurs because the nonlinear effect is due to the oscillating current bias through the SQUID, rather than an oscillating flux bias.

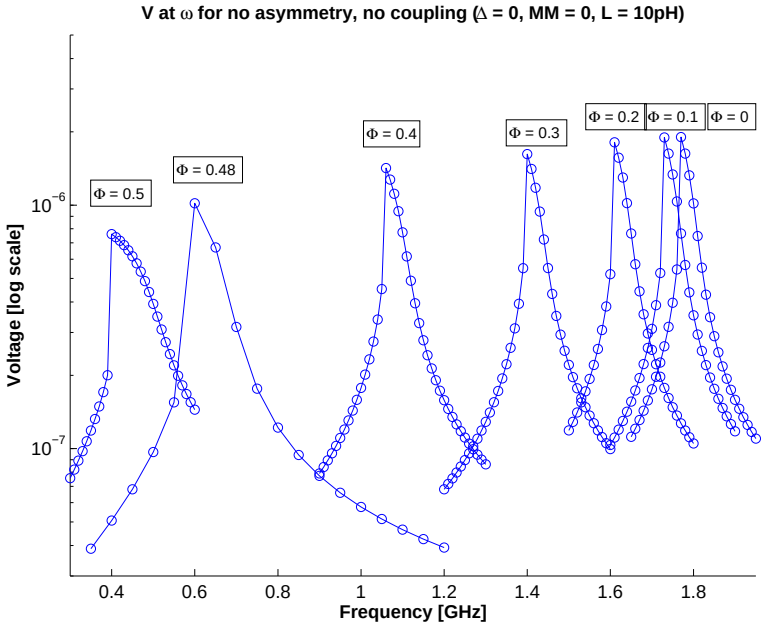

Figure D-2: Simulation results for circuit model 2 in section 5.7. Nonlinear resonant spectra at different flux biases bend only to the lower frequency side. The nonlinear effect is due to the oscillating current bias through the SQUID.

As we introduced asymmetry to the critical currents of the SQUID junctions, the amount of induced flux in the SQUID loop increases due to the asymmetry. However, this effect is significant only when the flux is near $\Phi = 0.5\,\Phi_o$. The resonant spectrum bends towards the higher frequency side near $\Phi = 0.5\,\Phi_o$, when the nonlinear effect due to the induced flux dominates over that due to the current bias. This is shown in fig. D-3.

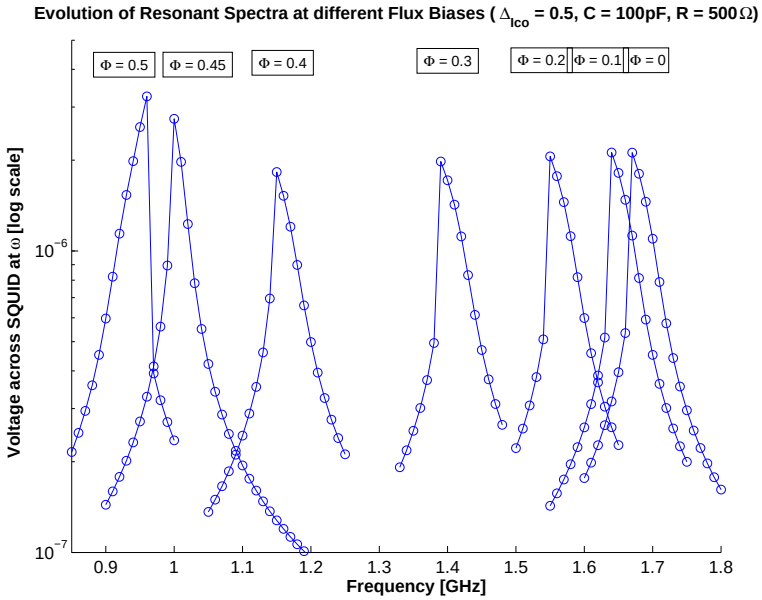

Figure D-3: Simulation results for circuit model 3 in section 5.7. The SQUID junctions are assumed an asymmetry of $\Delta_I = 0.5\, I_{co}$. The induced flux due to the asymmetric junctions becomes significant only near $\Phi = 0.5\, \Phi_o$, and causes the resonant spectrum to bend towards the higher frequency side.

D.2 Resonant circuit with externally coupled flux

To increase the nonlinear effect due to an oscillating flux, the SQUID is coupled to an external flux source as shown in fig. D-4. The externally coupled flux is given by

$$\Phi_{coupled} = M_{sq} I_{sq} \tag{D.25}$$

where M_{sq} models the mutual coupling between the SQUID and the dependent flux source, and I_{sq} is given by eqn. D.13. The current continuity equation in eqn. D.18 remains the same, while we need to modify the fluxoid equation in D.20. This is given in eqn. D.26.

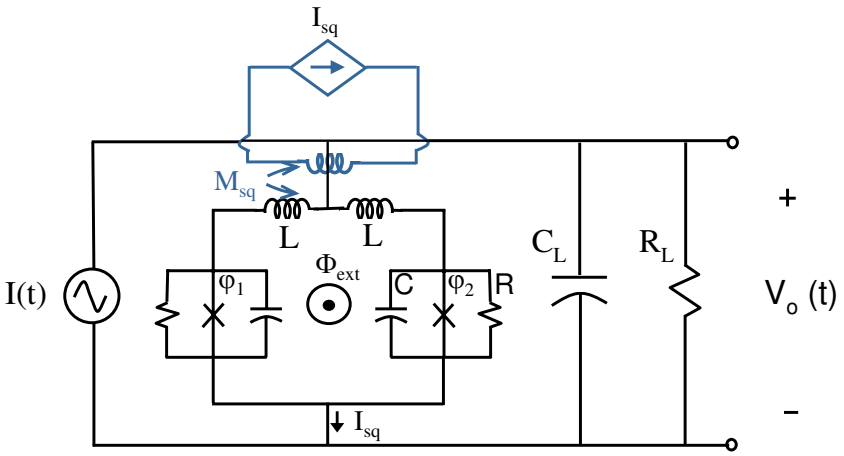

Figure D-4: Circuit schematic of the resonant model in which the SQUID is coupled to a dependent flux source.

Fluxoid Quantization Equation with Mutual Coupling to Resonating Loop

$$0 = \varphi_m + \frac{2\pi L}{\Phi_o}\left(\frac{i_1 - i_2}{2}\right) + \frac{2\pi \Delta_L}{\Phi_o}\left(\frac{i_1 + i_2}{2}\right) + \frac{\pi \Phi_{ext}}{\Phi_o} + \frac{\pi M I_{sq}}{\Phi_o} \tag{D.26}$$

Again, it should be noted that in the simulations, Δ_L is set to zero. Eqn. D.26 can be expanded into:

$$\begin{aligned}
&\varphi_m + \frac{\pi \Phi_{ext}}{\Phi_o} + \left(\frac{2\pi L I_{co}}{\Phi_o} + \frac{2\pi \Delta_L \Delta_I}{\Phi_o}\right)\sin\varphi_m \cos\varphi_p + \left(\frac{2\pi L \Delta_I}{\Phi_o} + \frac{2\pi \Delta_L I_{co}}{\Phi_o}\right)\sin\varphi_p \cos\varphi_m \\
&\quad + \frac{2\pi M I_{co}}{\Phi_o}\sin\varphi_p \cos\varphi_m + \frac{2\pi M \Delta_I}{\Phi_o}\sin\varphi_m \cos\varphi_p = \\
&\left(\frac{L\Delta_R}{R^2 - {\Delta_R}^2} - \frac{\Delta_L R}{R^2 - {\Delta_R}^2} - \frac{MR}{R^2 - {\Delta_R}^2}\right)\frac{d\varphi_p}{dt} - (L\Delta_c + \Delta_L C + MC)\frac{d^2\varphi_p}{dt^2} \\
&- \left(\frac{LR}{R^2 - {\Delta_R}^2} - \frac{\Delta_L \Delta_R}{R^2 - {\Delta_R}^2} - \frac{M\Delta_R}{R^2 - {\Delta_R}^2}\right)\frac{d\varphi_m}{dt} - (LC + \Delta_L \Delta_c + M\Delta_c)\frac{d^2\varphi_m}{dt^2}
\end{aligned} \tag{D.27}$$

The last row of the mass matrix in eqn. D.23 needs to be modified:

$$\left[\begin{array}{cccc} \frac{L\Delta_R - \Delta_L R - MR}{R^2 - {\Delta_R}^2} & -(L\Delta_c + \Delta_L C + MC) & \frac{M\Delta_R + \Delta_L \Delta_R - LR}{R^2 - {\Delta_R}^2} & -(LC + \Delta_L \Delta_c + M\Delta_c) \end{array}\right] \tag{D.28}$$

In addition, the last row of f(x,t) in eqn. D.24 now becomes:

$$\varphi_m + \frac{\pi\Phi_{ext}}{\Phi_o} + \left(\frac{2\pi L I_{co}}{\Phi_o} + \frac{2\pi\Delta_L\Delta_I}{\Phi_o}\right)\sin\varphi_m\cos\varphi_p + \left(\frac{2\pi L\Delta_I}{\Phi_o} + \frac{2\pi\Delta_L I_{co}}{\Phi_o}\right)\sin\varphi_p\cos\varphi_m + \frac{2\pi M I_{co}}{\Phi_o}\sin\varphi_p\cos\varphi_m + \frac{2\pi M\Delta_I}{\Phi_o}\sin\varphi_m\cos\varphi_p \tag{D.29}$$

The resultant resonant spectra are shown in fig. D-5 for an asymmetry of $\Delta_I = 0.5\, I_{co}$, and a mutual coupling of $M_{sq} = 1\,\mathrm{nH}$. The nonlinear effect due to the coupled flux dominates, and the nonlinear spectrum now evolves from bending towards one frequency side to another. This is consistent with the observations from the experiment.

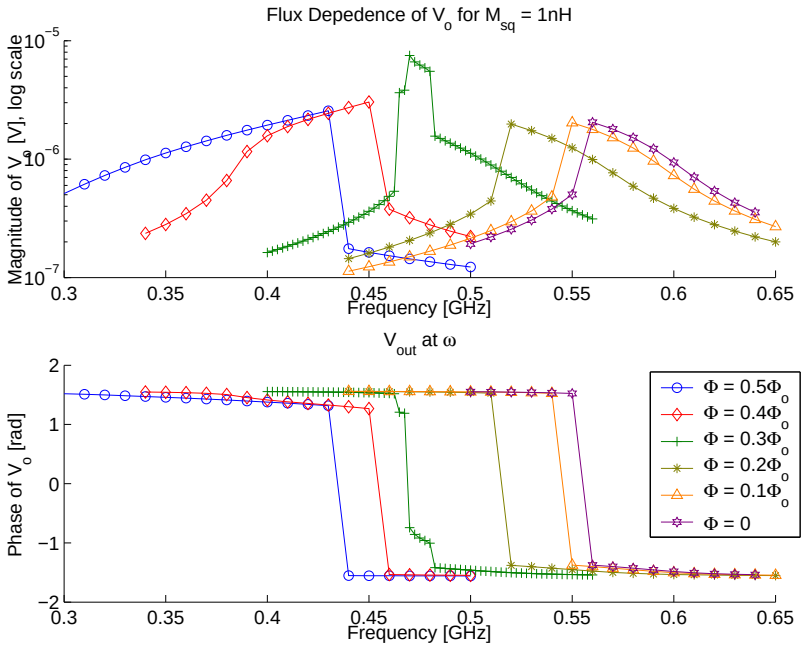

Figure D-5: Simulation results for $M_{sq} = 1\,\mathrm{nH}$. The onset of transition occurs at $\Phi = 0.3\,\Phi_o$ as observed in the experiment.

Appendix E

Selected Reprints

Resonant Readout of a Persistent Current Qubit

Janice C. Lee, William D. Oliver, Terry P. Orlando, and Karl K. Berggren

***Abstract*—We have implemented a resonant circuit that uses a SQUID as a flux-sensitive Josephson inductor for qubit readout. In contrast to the conventional switching current measurement that generates undesired quasiparticles when the SQUID switches to the voltage state, our approach keeps the readout SQUID biased along the supercurrent branch during the measurement. By incorporating the SQUID inductor in a high-Q resonant circuit, we can distinguish the two flux states of a niobium persistent-current (PC) qubit by observing a shift in the resonant frequency of both the magnitude and the phase spectra. The readout circuit was also characterized in the nonlinear regime to investigate its potential use as a nonlinear amplifier.**

***Index Terms*—Nonlinear oscillators, persistent-current qubits, resonant circuits, SQUIDs.**

I. Introduction

QUANTUM computation with superconducting flux qubits commonly relies on DC SQUID magnetometers for qubit readout. While the coherent control of quantum dynamics has been demonstrated in several flux-qubit systems [1]–[3], a major challenge has been to reduce the level of decoherence of the qubit state caused by the readout circuit. In the case of persistent-current qubits, the conventional SQUID switching-current readout has several drawbacks. To distinguish the flux state of the qubit, one typically ramps the current bias through the SQUID and records the presence or absence of a switching event. Decoherence due to this readout process occurs mainly in three ways: (1) nonzero SQUID currents result in SQUID-potential asymmetries, which remove the first-order current-noise isolation and are thereby associated with higher levels of decoherence (e.g. through the mutual coupling of broadband noise from the SQUID bias lines to the qubit loop) [4]; (2) the generation of quasiparticles from the SQUID switching events limits the repetition rate of the readout; and (3) the undesired excitation of the qubit into higher energy states during the ramping or switching of the SQUID.

Manuscript received October 5, 2004. This work was supported in part by the Air Force Office of Scientific Research (AFOSR) under Grant F49620-01-1-0457 under the DoD University Research Initiative on Nanotechnology (DURINT) Program, in part by a National Science Foundation (NSF) graduate fellowship, and MIT Lincoln Laboratory by Department of the Air Force under Air Force Contract F19628-00-C-0002. The opinions, interpretations, conclusions, and recommendations are those of the author(s) and are not necessarily endorsed by the United States government.

J. C. Lee and T. P. Orlando are with the Department of Electrical Engineering and Computer Science, Massachusetts Institute of Technology, Cambridge, MA 02139 USA (e-mail: janlee@mit.edu).

W. D. Oliver is with the MIT Lincoln Laboratory, Lexington, MA 02420 USA (e-mail: oliver@ll.mit.edu).

K. K. Berggren was with the MIT Lincoln Laboratory, Lexington, MA 02420, USA. He is now with the Department of Electrical and Computer Engineering, Massachusetts Institute of Technology, Cambridge, MA 02139 USA (e-mail: berggren@mit.edu).

Digital Object Identifier 10.1109/TASC.2005.850077

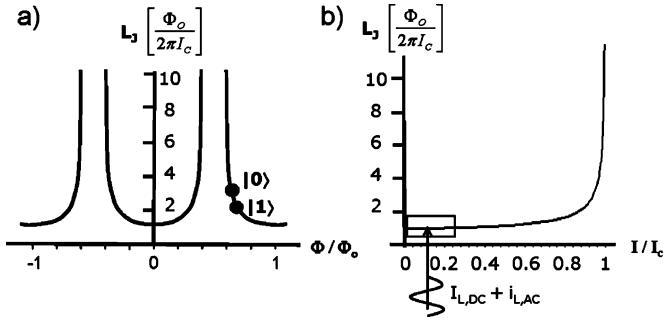

Fig. 1. a) The SQUID Josephson inductance is a periodic function of the external magnetic flux. The figure shows the qubit-mediated Josephson inductance for the two flux states ($|0\rangle$ and $|1\rangle$) at a flux bias near 0.7 Φ_o. b) Dependence of the Josephson inductance on the bias current. A small current bias corresponds to a linear inductance, i.e., independent of current (boxed region). Increasing current bias causes the SQUID inductor to behave nonlinearly, which has observable effects on the resonant spectrum.

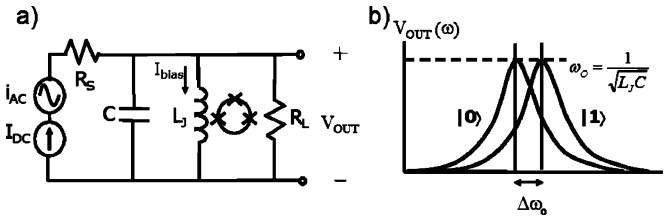

Fig. 2. a) A generic parallel RLC circuit, in which the inductor is realized by a SQUID, with its Josephson inductance being mediated by the qubit. b) The transition between qubit states is detected as a shift in the resonant frequency.

To address in part these sources of readout-induced decoherence, we have experimentally implemented a resonant readout technique that only requires the readout SQUID to be biased at low currents along the supercurrent branch. The low current bias tends to maintain the first-order noise isolation, helping to minimize the level of decoherence of the qubit. Since the SQUID does not switch to the voltage state, the number of quasiparticles is also drastically reduced. In addition, the resonant readout approach utilizes a narrow-band filter that shields the qubit from broadband noise. Similar resonant readout approaches have been demonstrated in [5] and [6], and the implementation has been extended to the nonlinear regime in [7].

The principle of the resonant readout technique for the persistent-current qubit is to determine the flux state of the qubit by measuring the Josephson inductance of the readout SQUID. As illustrated in Fig. 1, the SQUID Josephson inductance is nonlinear: it is a nonlinear and periodic function of the external magnetic flux (used here to detect the qubit state), as well as a nonlinear function of the bias current (used here to control the degree of nonlinearity in the resonant circuit). To measure the Josephson inductance with high sensitivity, we incorporate the SQUID inductor in a high-Q resonant circuit. The change in Josephson inductance corresponding to a transition between qubit states is detected as a shift in the resonant frequency (Fig. 2).

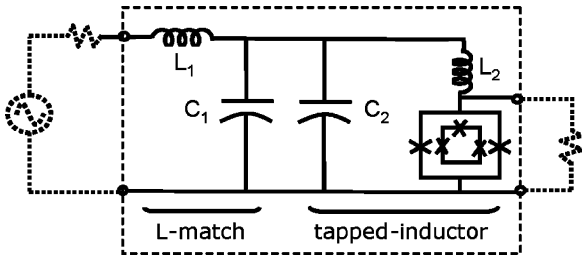

Fig. 3. Circuit schematic of the resonant readout circuit. Tapped-inductor and L-match impedance transformations were employed to achieve a high quality factor. The component values are $L_1 = 69\,\mathrm{nH}$, $C_1 = 1.4\,\mathrm{pF}$, $C_2 = 100\,\mathrm{pF}$, $L_2 = 0.78\,\mathrm{nH}$. The junctions of the SQUID are each shunted by a 5 pF capacitor (not shown). The components within the dotted box were fabricated on-chip.

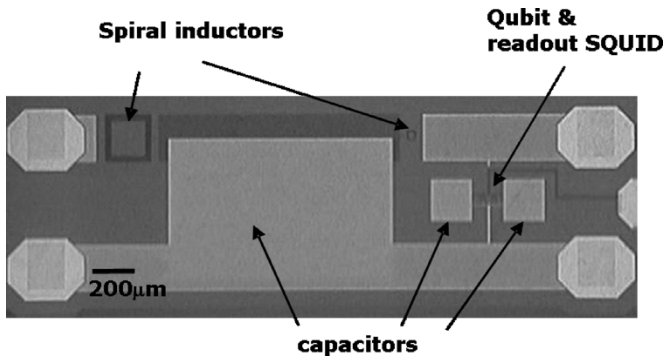

Fig. 4. Optical micrograph of the actual device fabricated at MIT Lincoln Laboratory.

II. Resonant Circuit Design and Fabrication

A. On-Chip Resonant Circuit Design

The circuit design of the resonant readout circuit is shown in Fig. 3. The components within the dotted box were implemented on-chip. The qubit is inductively coupled to the readout SQUID inductor, which in turn is incorporated in a parallel resonant circuit. To achieve a high quality factor, a tapped-inductor impedance transformation was employed to step-up the output impedance seen by the oscillator at its resonant frequency. The SQUID inductor is part of this tapped-inductor configuration. An L-match network was also used on the input side to match the input impedance to the transformed output impedance. The transformations were designed to yield a resonant frequency $f_0 \sim 500\,\mathrm{MHz}$ and a quality factor $Q \sim 150$ [8].

B. Device Fabrication

The device was fabricated with a planarized Nb trilayer process at MIT Lincoln Laboratory [9]. The PC qubit is a superconducting loop interrupted by three Josephson junctions. Two of the junctions have the same size with nominal dimensions of $1.0 \times 1.0\ \mu\mathrm{m}^2$. The third junction is smaller with nominal dimensions of $0.9 \times 0.9\ \mu\mathrm{m}^2$. The junctions of the readout SQUID are $1.5 \times 1.5\ \mu\mathrm{m}^2$. Based on the results of the process tests, the current density was approximately $120\ \mathrm{A/cm}^2$. The dimensions of the qubit loop and the SQUID loop are $18.0 \times 18.0\ \mu\mathrm{m}^2$ and $20.8 \times 20.8\ \mu\mathrm{m}^2$ respectively, with an estimated mutual inductance of 30 pH. The inductors were square spirals with a linewidth and spacing of 1 μm. The capacitors were made out of Nb electrodes, with the dielectric layers being 50 nm of NbO_x and 200 nm of SiO_2. A device micrograph is shown in Fig. 4.

III. Measurement Techniques

The device was measured in a ^{3}He refrigerator at MIT Lincoln Laboratory. The DC lines were made from shielded soft-coaxes and were filtered at the ^{3}He pot sample stage with copper powder filters. The RF lines were attenuated at both the 1 K and ^{3}He stages. A bias-tee was mounted on the sample stage to combine the DC and RF signals. While the RF lines were used for the resonant readout, the DC lines were used to characterize the I-V properties of the SQUID junctions and to provide the option of additional DC bias to the SQUID. The chip was mounted on a PCB substrate with coplanar-waveguide

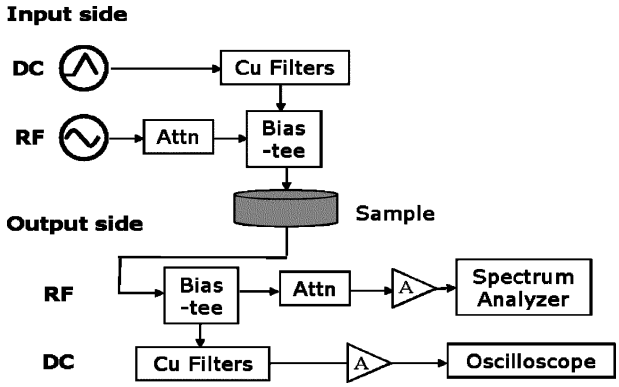

Fig. 5. Circuit schematic of the experimental setup.

structures and was housed inside an RF package. A superconducting coil was wrapped around the outside of the RF package to provide the external flux bias. An additional thermometer was mounted directly on the package to monitor the sample temperature.

A schematic of the experimental implementation is shown in Fig. 5. The frequency spectra of the readout circuit were measured with a network analyzer and/or a spectrum analyzer as a function of the input power from a tracking generator. The signal frequencies were centered about the resonant frequency and within a span of 0.6 MHz. Each spectrum was acquired with a RBW of 3 kHz and then averaged 100 times. The signal from the resonant circuit was amplified at room temperature with a 50 dB LNA before being measured.

IV. Experimental Results

A. Readout of Qubit States

The resonant frequency of the readout circuit was measured to be about 420 MHz while the quality factor Q is on the order of a thousand. The observed Q is higher than the designed value; the discrepancy was likely due to the higher inductances of the spiral inductors. The resonant spectra were modulated with an external magnetic field. The periodic modulation of the resonant frequency and the corresponding peak amplitude are shown in Fig. 6. A discontinuity in the frequency is evidenced at every 1.3 periods of the SQUID lobe (lower trace, Fig. 6). These steps correspond to transitions of the qubit between opposite flux states, while the periodicity is determined by the ratio of the SQUID to

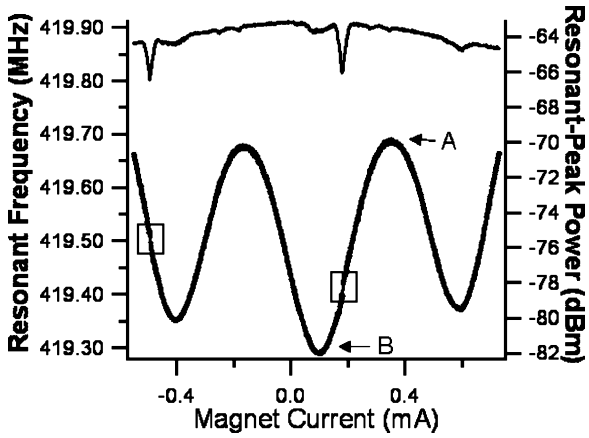

Fig. 6. The lower plot (left axis) shows the modulation of the resonant frequency with external magnetic field. Qubit steps corresponding to transitions between opposite flux states were observed at every 1.3 periods of the SQUID lobe. The upper plot (right axis) shows the corresponding peak amplitude of the resonant spectrum. The dip in peak power coincides with the qubit step.

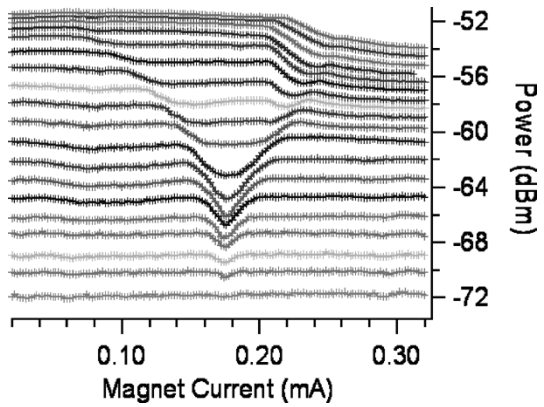

Fig. 7. Observation of the resonant peak power with increasing input power near a qubit step. The source power ranges from −68 dBm to −50 dBm in 1 dB step. A dip starts to develop at the flux value corresponding to the position of the qubit step, and is gradually washed out with increasing power.

qubit loop areas. The shift in the resonant frequency was about 40 kHz, corresponding to a change in Josephson inductance of 2 pH. While the data shown in Fig. 6 were obtained by measuring the magnitude of the resonant spectra, we have also detected the state of the qubit by measuring the phase of the resonant readout circuit with comparable sensitivity.

A dip in resonant peak power was also observed to coincide with the qubit steps (upper trace, Fig. 6). This dip corresponds to a broadening of the resonant spectrum (not shown). To further understand the nature of the dip in the resonant peak power, we performed the measurements over a range of input power near one of the qubit steps (Fig. 7). For low current amplitudes, the resonant peak power remains fairly constant, and there is no dip at the qubit step. As one increases the current amplitude, the size of the dip grows and is eventually washed out at the highest biases. For all values of current amplitudes, the qubit step in the resonant frequency was still clearly observed. These preliminary results are consistent with the Landau-Zener transition data observed in [10] in the large bias limit. The temperature dependence of the results is to be further explored at dilution refrigerator temperatures.

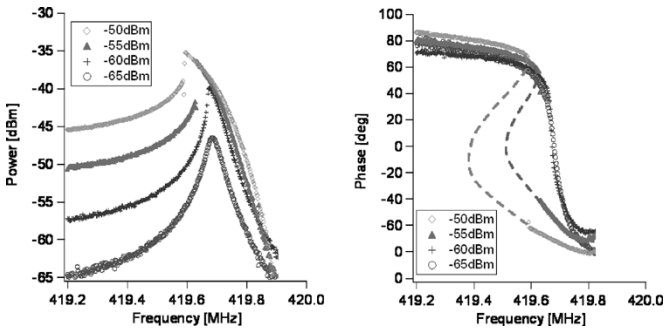

Fig. 8. Magnitude and phase measurements of the resonant readout circuit in the linear and nonlinear regimes at the top of the SQUID lobe. In the linear case, the magnitude spectrum has a symmetric Lorenzian shape, while the phase at resonance is continuous with a slope limited by the quality factor Q. In the nonlinear case, the magnitude and phase spectra have two stable branches, resulting in a discontinuity. The theoretical predictions are shown in dotted line for the phase spectra.

B. Nonlinearity of Resonant Readout Circuit

As the bias current through the SQUID is increased along the supercurrent branch, the Josephson inductance becomes increasingly nonlinear and has observable effects on the resonant circuit spectra. Fig. 8 shows the behavior of the magnitude and phase spectra with increasing input power at the top of the SQUID lobe (position [A], Fig. 6). The magnitude spectrum evolves from a symmetric Lorenzian shape (linear oscillator) to an asymmetric shape with a discontinuity (nonlinear oscillator). The resonant spectrum leans toward lower frequencies, indicating that the effective inductance over an oscillation period is higher with increasing current bias. On the other hand, the phase experiences a 180° shift at the resonant frequency. At low current biases and thus in the linear regime, the phase shift is continuous with frequency and has a finite slope at resonance that is limited by the quality factor. In the nonlinear case, the phase spectra exhibit a discontinuity similar to the magnitude spectra. The discontinuity corresponds to a bifurcation point at which the nonlinear resonant circuit has two stable solutions. Since the data shown in Fig. 8 were only measured with a forward frequency sweep (i.e., from low to high frequencies), the spectra exhibit only one of the two stable branches.

Fig. 9 shows the hysteretic magnitude spectra with both stable branches measured using forward and backward frequency sweeps. The third branch (displayed as a white dotted line) is unstable and inaccessible without the implementation of a feedback scheme. The behavior of the spectra at two different magnetic field biases is also shown in Fig. 9. The spectrum evolves from leaning toward the lower frequencies to leaning toward the higher frequencies as the flux bias changes from the top to the bottom of the SQUID lobe.

The characterization of the readout scheme presented here involved measuring the magnitude or phase spectra and, subsequently, identifying the qubit transition as a shift in the resonant frequency. While this approach was beneficial for characterizing the resonant readout circuit, its implementation as a qubit readout scheme will likely involve pulsing the resonant circuit at a single frequency near the resonant frequency. Pulsing allows for a temporal resolution of the qubit state measurement, and the qubit state would be determined as a change in either the output amplitude or phase within the pulse. The circuit quality

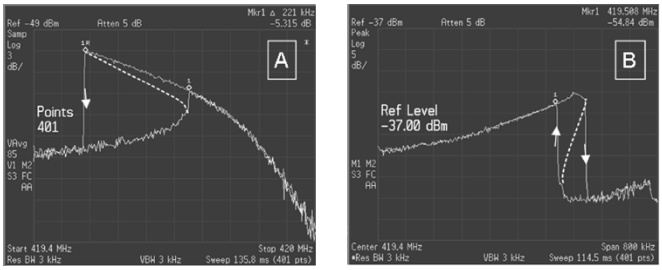

Fig. 9. Hysteretic behavior of the resonant spectrum was observed when the readout circuit was operated in the nonlinear regime. The results are shown for two magnetic flux biases: top [A] and bottom [B] of the SQUID lobe. The two stable branches were measured directly. The unstable branch was not measured, but is illustrated with a white dotted line.

factor will determine the rate at which this information can be obtained. From this perspective, the readout circuit operated in the nonlinear regime has the potential to be used as a nonlinear amplifier. One can choose to bias near the discontinuity point and benefit from the high sensitivity [7].

V. Conclusion

We have implemented a resonant readout scheme for the persistent-current qubit by using the readout SQUID as a flux-sensitive inductor. This approach only requires low current biases through the SQUID and reduces the level of decoherence of the qubit as induced by the readout process. The results presented were measured from an on-chip niobium device at 300 mK, and the readout scheme was confirmed to have the sensitivity to distinguish the two qubit states. The readout circuit was also characterized in both the linear and nonlinear regime. Future experiments involving the spectroscopy of the qubit states using the resonant approach will be performed at dilution refrigerator temperatures.

Acknowledgment

The authors would like to acknowledge D. E. Oates, K. Segall, D. S. Crankshaw, and Y. Yu for useful discussions. Thanks also go to T. J. Weir for technical assistance.

References

[1] I. Chiorescu, Y. Nakamura, C. J. P. M. Harmans, and J. E. Mooij, "Coherent quantum dynamics of a superconducting flux qubit," *Science*, vol. 299, p. 1869, 2003.

[2] Y. Yu, S. Han, X. Chu, S.-I. Chu, and Z. Wang, "Coherent temporal oscillations of macroscopic quantum states in a Josephson junction," *Science*, vol. 296, p. 889, 2002.

[3] J. M. Martinis, S. Nam, and J. Aumentado, "Rabi oscillations in a large Josephson-junction qubit," *Physical Review Letters*, vol. 89, p. 1 179 011, 2002.

[4] L. Tian, S. Lloyd, and T. P. Orlando, "Decoherence and relaxation of a superconducting quantum bit during measurement," *Physical Review B*, vol. 65, p. 144 516, 2002.

[5] A. Lupascu, C. J. M. Verwijs, R. N. Schouten, C. J. P. M. Harmans, and J. E. Mooij, "Nondestructive Readout for a Superconducting Flux Qubit," cond-mat/0311510.

[6] E. Il'ichev, N. Oukhanski, A. Izmalkov, T. Wagner, M. Grajcar, H.-G. Meyer, A. Y. Smirnov, A. Maassen van den Bring, M. H. S. Amin, and A. M. Zagoskin, *Physical Review Letters*, vol. 91, p. 097 906, 2003.

[7] I. Siddiqi, R. Vijay, F. Pierre, C. M. Wilson, M. Metcalfe, C. Rigetti, L. Frunzio, and M. H. Devoret, "An RF-Driven Josephson Bifurcation Amplifier for Quantum Measurements," cond-mat/0312623.

[8] J. C. Lee, "Magnetic Flux Measurement of Superconducting Qubits With Josephson Inductors," MS thesis, MIT, 2002.

[9] D. Nakada, K. K. Berggren, E. Macedo, V. Liberman, and T. P. Orlando, "Improved critical-current density uniformity by using anodization," *IEEE Transactions on Applied Superconductivity*, vol. 13, no. 2, Jun. 2003.

[10] A. Izmalkov, M. Grajcar, E. Il'ichev, M. Oukhanski, T. Wagner, H.-G. Meyer, W. Krech, M. H. S. Amin, A. Maassen van den Brink, and A. M. Zagoskin, "Observation of macroscopic Landau-Zener transitions in a superconducting device," *Europhysics Letters*, vol. 65, no. 6, pp. 844–849, 2004.

antagonized when added in combination (Fig. 4E). The TNF+EGF and TNF+insulin treatments were distinctly separated from one another: EGF appeared to antagonize TNF-induced apoptosis by specifically reducing the projection along the stress-apoptosis axis 1 without any change along axis 2 (Fig. 4E); in contrast, insulin actively promoted prosurvival signaling along axis 2 while also inhibiting stress-apoptosis signaling along axis 1. Therefore, analyzing the multi-input stimuli through these model-derived biological "basis axes" (Fig. 4D) helped to reveal the different network strategies used by EGF and insulin to antagonize TNF-induced apoptosis.

Finally, to determine the contributions of TNF-induced autocrine circuits in the model, we mapped the TNF+C225 and TNF+IL-1ra treatments (Fig. 4F). The projection of TNF along the stress-apoptosis axis (Fig. 4F) was enforced by the autocrine circuits, which increased the contribution along axis 1 and decreased the contribution along axis 2. This is consistent with the notion that regulated autocrine circuits provide microenvironment-dependent feedback to cells during phenotypic decision processes, such as death-survival (*11*, *32*). Furthermore, it illustrated directly that effects of complex environmental stimuli were entirely contained within the two canonical basis axes distilled from the original 660-dimensional signaling metric space by the PLS model (Fig. 4D).

In summary, by using a systems approach that combines quantitative experiments with data-driven modeling, we identified two canonical axes—a stress-apoptosis axis and a survival axis—that together constitute a molecular basis set for the signaling network that controls apoptosis. These axes capture the dynamic intracellular signal processing of diverse stimuli, including autocrine-feedback circuits. Our work illustrates how a complex signaling network can be reduced empirically to a much simpler computational model that is directly tied to biological mechanism.

References and Notes

1. J. Downward, *Nature* **411**, 759 (2001).
2. J. E. Dumont, S. Dremier, I. Pirson, C. Maenhaut, *Am. J. Physiol. Cell Physiol.* **283**, C2 (2002).
3. M. J. Bissell, D. Radisky, *Nat. Rev. Cancer* **1**, 46 (2001).
4. T. Bouwmeester *et al.*, *Nat. Cell Biol.* **6**, 97 (2004).
5. X. Zhu *et al.*, *J. Immunol.* **173**, 7141 (2004).
6. K. Lei, R. J. Davis, *Proc. Natl. Acad. Sci. U.S.A.* **100**, 2432 (2003).
7. J. A. Lamb, J. J. Ventura, P. Hess, R. A. Flavell, R. J. Davis, *Mol. Cell* **11**, 1479 (2003).
8. M. T. Abreu-Martin *et al.*, *Am. J. Physiol.* **276**, G599 (1999).
9. Materials and methods are available as supporting material on *Science* Online.
10. K. A. Janes *et al.*, *Mol. Cell. Proteomics* **2**, 463 (2003).
11. K. A. Janes *et al.*, in preparation.
12. S. Gaudet *et al.*, *Mol. Cell Proteomics* **4**, 1569 (2005).
13. M. T. Abreu-Martin, A. Vidrich, D. H. Lynch, S. R. Targan, *J. Immunol.* **155**, 4147 (1995).
14. M. M. Remacle-Bonnet *et al.*, *Cancer Res.* **60**, 2007 (2000).
15. G. Del Bino *et al.*, *Cell Prolif.* **32**, 25 (1999).
16. Z. Darzynkiewicz *et al.*, *Cytometry* **27**, 1 (1997).
17. T. Vanden Berghe *et al.*, *Methods Mol. Med.* **98**, 101 (2004).
18. V. A. Fadok, D. L. Bratton, S. C. Frasch, M. L. Warner, P. M. Henson, *Cell Death Differ.* **5**, 551 (1998).
19. J. J. Ventura, P. Cogswell, R. A. Flavell, A. S. Baldwin Jr., R. J. Davis, *Genes Dev.* **18**, 2905 (2004).
20. H. Kamata *et al.*, *Cell* **120**, 649 (2005).
21. F. H. Cruzalegui, G. E. Hardingham, H. Bading, *EMBO J.* **18**, 1335 (1999).
22. K. A. Janes *et al.*, *J. Comput. Biol.* **11**, 544 (2004).
23. P. Geladi, B. R. Kowalski, *Anal. Chim. Acta* **185**, 1 (1986).
24. O. Alter, P. O. Brown, D. Botstein, *Proc. Natl. Acad. Sci. U.S.A.* **97**, 10101 (2000).
25. K. A. Janes, J. G. Albeck, S. Gaudet, data not shown.
26. D. W. Nicholson, N. A. Thornberry, *Trends Biochem. Sci.* **22**, 299 (1997).
27. Y. Yarden, M. X. Sliwkowski, *Nat. Rev. Mol. Cell Biol.* **2**, 127 (2001).
28. J. Rouse *et al.*, *Cell* **78**, 1027 (1994).
29. J. C. Lee *et al.*, *Nature* **372**, 739 (1994).
30. D. Yadav, N. Sarvetnick, *Curr. Opin. Immunol.* **15**, 697 (2003).
31. K. Ozaki, W. J. Leonard, *J. Biol. Chem.* **277**, 29355 (2002).
32. H. S. Wiley, S. Y. Shvartsman, D. A. Lauffenburger, *Trends Cell Biol.* **13**, 43 (2003).
33. U. B. Nielsen, M. H. Cardone, A. J. Sinskey, G. MacBeath, P. K. Sorger, *Proc. Natl. Acad. Sci. U.S.A.* **100**, 9330 (2003).

34. We thank J. Kelly for programming the metric extraction algorithms. This work was supported by the NIH grant P50-GM68762 (M.B.Y., D.A.L, and P.K.S.) and the Whitaker Foundation (K.A.J.). M.B.Y. was supported by NIH grant GM059281.

Supporting Online Material

www.sciencemag.org/cgi/content/full/310/5754/1646/DC1
Materials and Methods
Figs. S1 to S4
Tables S1 to S4
Database S1
References

27 June 2005; accepted 3 November 2005
10.1126/science.1116598

REPORTS

Mach-Zehnder Interferometry in a Strongly Driven Superconducting Qubit

William D. Oliver,[1]* Yang Yu,[2] Janice C. Lee,[2] Karl K. Berggren,[2] Leonid S. Levitov,[3] Terry P. Orlando[2]

We demonstrate Mach-Zehnder–type interferometry in a superconducting flux qubit. The qubit is a tunable artificial atom, the ground and excited states of which exhibit an avoided crossing. Strongly driving the qubit with harmonic excitation sweeps it through the avoided crossing two times per period. Because the induced Landau-Zener transitions act as coherent beamsplitters, the accumulated phase between transitions, which varies with microwave amplitude, results in quantum interference fringes for $n = 1$ to 20 photon transitions. The generalization of optical Mach-Zehnder interferometry, performed in qubit phase space, provides an alternative means to manipulate and characterize the qubit in the strongly driven regime.

The development of artificial atoms with lithographically defined superconducting circuits presents a new paradigm of quantum solid-state physics (*1*), allowing the realization and exploration of new macroscopic quantum phenomena (*2*–*9*), and also holding promise for applications in quantum computing (*10*). Of the various effects demonstrated with qubits, the most important are time-dependent coherent phenomena. Those include the observation of Rabi oscillations in charge, flux, and phase qubits (*2*, *5*–*9*), entanglement of two qubits (*11*), coherent oscillation (*12*) and bifurcation (*13*) in multilevel systems, and the demonstration of basic elements of coherent control (*14*–*16*). Artificial atoms strongly coupled to photons have opened the arena of "circuit quantum electrodynamics" (c-QED) (*17*, *18*).

Here, we demonstrate an application of superconducting qubits to quantum physics, realized in a strongly driven flux qubit and described in terms of a Mach-Zehnder (MZ) interferometer. The conventional MZ setup

[1]MIT Lincoln Laboratory, 244 Wood Street, Lexington, MA 02420, USA. [2]Department of Electrical Engineering and Computer Science, [3]Department of Physics, Massachusetts Institute of Technology (MIT), Cambridge, MA 02139, USA.

*To whom correspondence should be addressed. E-mail: oliver@ll.mit.edu

uses two beamsplitters: The first divides an optical signal into two coherent waves that travel along paths with different effective lengths, and the second recombines and superposes these waves, leading to quantum interference fringes in the measured output signal. In a driven qubit, according to an idea discussed by Shytov *et al.* (*19*), the beamsplitters can be realized by Landau-Zener (LZ) transitions at a level avoided crossing. Over one oscillation period of the driving field, the qubit is swept through the avoided crossing twice (Fig. 1A). Starting from the marker, at the first LZ transition (time t_1), the ground state $|0\rangle$ is split into a coherent superposition of the ground and excited states, $|1\rangle$ and $|0\rangle$, which, after evolving independently and accumulating a relative phase $\Delta\theta_{12}$, interfere at the second LZ transition (time t_2). The corresponding qubit-state energy evolution (first period, Fig. 1B) between the recurrent LZ transitions (shaded region) provides a phase-space analog to the two arms and the beamsplitters of an optical MZ interferometer (top left, Fig. 1B). The interference phase

$$\Delta\theta_{12} = \frac{1}{\hbar}\int_{t_1}^{t_2}\varepsilon(t)dt,\ \ \varepsilon(t) = \varepsilon_{|0\rangle}(t) - \varepsilon_{|1\rangle}(t) \quad (1)$$

where $\hbar = h/2\pi$, h is the Planck constant, and ε is the energy difference between states $|0\rangle$ and $|1\rangle$, depends on the magnitude of the qubit energy detuning excursion for times $t_1 < t < t_2$. The interference fringes in the occupation probability correspond to integer and half-integer values of $\Delta\theta_{12}/2\pi$. Known as Stückelberg oscillations with Rydberg atoms (*20*, *21*), this mechanism can be applied to quantum control (*22*).

The qubit MZ interferometer differs in a number of ways from an optical interferometer. First, instead of a photon, the interferometry is performed with the use of the quantum state of a qubit. Second, in the qubit, we have the interference of paths in phase space rather than in coordinate space; the phase $\Delta\theta_{12}$ (Eq. 1) is determined by the qubit level splitting, which plays the role of the optical path length. Finally, because they are more fragile than photons and easier to decohere, qubit states can be manipulated in a coherent fashion only at relatively short time scales.

We used a periodic driving signal, a harmonic variation of the qubit detuning $\varepsilon(t)$

$$\mathcal{H} = -\frac{1}{2}(\Delta\sigma^x + \varepsilon(t)\sigma^z),$$
$$\varepsilon(t) = \varepsilon_0 + A_{\mathrm{rf}}\cos\omega t \quad (2)$$

where Δ is the tunnel splitting, σ^x and σ^z are Pauli matrices, ε_0 is the detuning proportional to dc flux bias, and A_{rf} is the radio frequency (rf) field amplitude proportional to the rf flux bias (*23*). In this case (Fig. 1B), we have cascaded LZ transitions which occur when the driving amplitude exceeds detuning, giving rise to the interference fringes at $A_{\mathrm{rf}} > |\varepsilon_0|$ (Fig. 1C). Although the phase $\Delta\theta_{12}$ equals the shaded area in Fig. 1B and is dependent on A_{rf}, the total phase gained over one period, $\theta = [1/\hbar]\int\varepsilon(t)dt = 2\pi\varepsilon_0/\hbar\omega$, equals the difference of the shaded and unshaded areas and is independent of A_{rf}. As consecutive pairs of LZ transitions (consecutive MZ interferometers) interfere constructively when $\theta = 2\pi n$, the fringes will appear around the resonance detuning values

$$\varepsilon_{0,n} = nh\nu \quad (3)$$

where $n = 0, 1, 2, \ldots$ and $\nu = \omega/2\pi$. Another interpretation of this condition is that the sequential LZ transitions excite multiphoton resonances.

Although coherent multiphoton resonances between discrete states of an rf-driven charge qubit have been reported (*5*, *24*) and multiphoton transitions used to drive Rabi oscillations in a flux qubit (*25*, *26*), in these works as well as in the earlier work on quantum dot systems (*27*, *28*), only a few photon transitions could be observed, with coherence quickly weakening as rf amplitude increased (*29*). In contrast, we were able to observe coherent resonances of very high order, up to $n = 20$, which requires driving the system at a high rf amplitude. The fringes for high n are as clear as those for $n \cong 1$, indicating that the qubit preserves a substantial amount of coherence even in the strongly driven regime.

We realized a tunable artificial atom with a niobium persistent-current qubit (Fig. 2A), a superconducting loop interrupted by three Josephson junctions (*30*). When the qubit loop is threaded with a magnetic flux $f_q \approx \Phi_0/2$, the system exhibits a double-well potential-energy landscape (fig. S1). The classical states of the wells are persistent currents I_q with opposing circulation, described by energy bands $\pm\varepsilon_0/2 = \pm I_q\Phi_0\delta f_q$ linear in the flux detuning $\delta f_q \equiv f_q - \Phi_0/2$. The double-well barrier allows quantum tunneling of strength Δ, opening the avoided

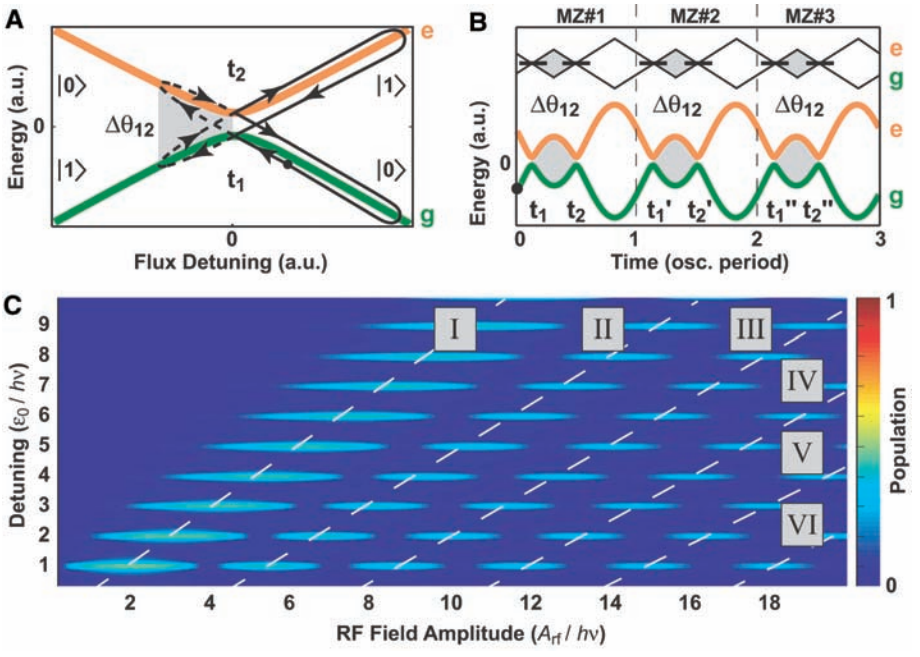

Fig. 1. MZ interference in a strongly driven qubit. (**A**) Starting at the dot marker, the qubit state is swept by an rf field. After an LZ transition at the first avoided crossing (time t_1), the resulting superposition state of $|0\rangle$ and $|1\rangle$ (dashed lines) accumulates a phase $\Delta\theta_{12}$ (shaded region) and interferes at the return LZ transition (time t_2). The qubit state is subsequently driven away from the avoided crossing and then returns to the starting flux position. This single period of qubit evolution is a single MZ interferometer. Depending on the interference phase $\Delta\theta_{12}$, amplitude may build in the excited state. a.u., arbitrary units. (**B**) The corresponding qubit energy variation induced by a periodic rf field, Eq. 2, results in an equivalent optical cascade of MZ interferometers (MZ#1 to #3, top) with resonance condition Eq. 3. (**C**) The population of the qubit excited state, Eq. 6, as a function of rf amplitude A_{rf} and detuning ε_0. Note the interference fringes (I to VI) at $A_{\mathrm{rf}} > \varepsilon_0$ and the multiphoton resonances at $\varepsilon_0 = nh\nu$.

crossing near $\delta f_q = 0$ (Fig. 1A). Detuning the flux tilts the double well and, thereby, modifies its eigenenergies and eigenstates. The qubit states are read out with a dc superconducting quantum interference device (DC-SQUID), a sensitive magnetometer that distinguishes the flux generated by the circulating currents. The device was fabricated at MIT Lincoln Laboratory (*23*).

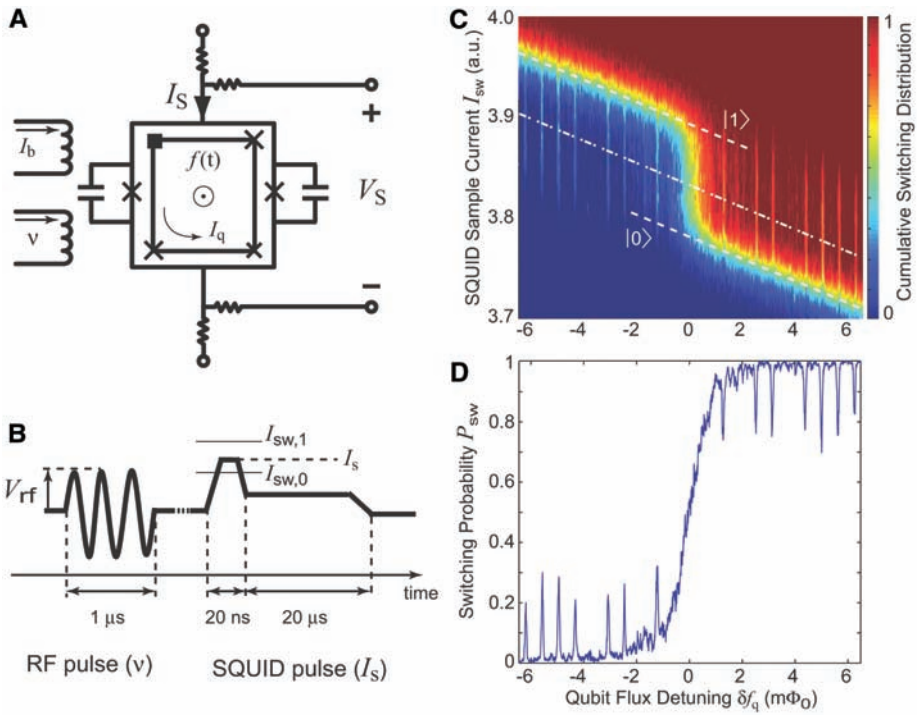

Fig. 2. Multiple resonances in a strongly driven flux qubit. (**A**) Circuit schematic of the three-junction flux qubit (inner loop) with circulating current I_q and the DC SQUID readout (outer loop); Josephson junctions are indicated with an ×. A time-dependent flux $f(t) \propto \varepsilon(t)$ threading the qubit is a sum of the flux bias due to the dc current I_b and a pulsed ac current at frequency ν irradiating the qubit and driving transitions between its quantum states. The SQUID is shunted by two 1-pF capacitors to lower its resonance frequency. Resistors mark the environmental impedance isolating the SQUID. (**B**) The time sequence for the rf pulse (duration 1 μs and rf-source voltage V_{rf}) and SQUID sample current I_s. A repetition period of 5 ms allows for equilibration between trials. (**C**) A cumulative switching-probability distribution of the qubit as a function of I_s and the qubit flux detuning δf_q under rf excitation at $V_{rf} \approx 0.12$ V_{rms} and ν = 1.2 GHz. Multiphoton transitions are observed between the qubit states |0⟩ and |1⟩ and are symmetric about the qubit step ($\delta f_q = 0$ mΦ$_0$). a.u., arbitrary units. (**D**) The 1D switching probability P_{sw} extracted from (C) (dash-dotted line scan).

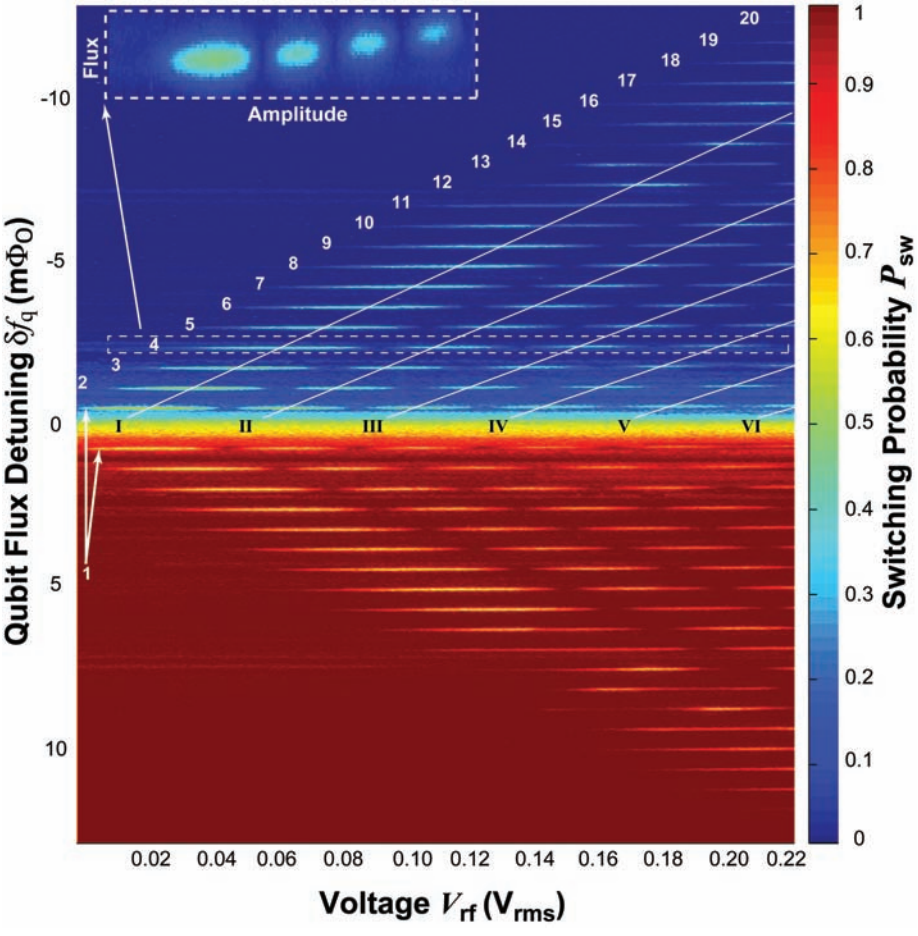

Fig. 3. Multiphoton interference fringes show a Bessel staircase. Switching probability P_{sw} is plotted as a function of qubit flux detuning δf_q and voltage V_{rf} at frequency ν = 1.2 GHz. *n*-photon resonances are labeled 1 to 20. Each *n*-photon resonance exhibits oscillations in P_{sw} resulting from a MZ-type quantum interference that results in a Bessel dependence $J_n(\lambda)$, where λ is the rf amplitude scaled by $h\nu$ (Eq. 4). Roman numerals mark the interference fringes of $J_n(\lambda)$ (solid white lines). The *n*-photon resonances are symmetric about the qubit step (0 mΦ$_0$). (Inset) Close-up of the $n = 4$ photon resonance.

We drove transitions between the qubit states by applying a 1-μs rf pulse (Fig. 2B) at frequency ν and rf-source voltage V_{rf} (*31*). After a short (≈10-ns) delay, we read out the qubit state by driving the DC-SQUID with a 20-ns "sample" current I_s followed by a 20-μs "hold" current. The SQUID will switch to its normal state voltage V_s if $I_s > I_{sw,0}$ ($I_s > I_{sw,1}$), corresponding to qubit states $|0\rangle$ and $|1\rangle$. By sweeping the sample current and flux detuning while monitoring the presence of a SQUID voltage over many trials, a cumulative switching-distribution function was generated, revealing the "qubit step" (Fig. 2C). At specific values of flux detuning, the rf field at ν = 1.2 GHz becomes resonant with the energy level separation, allowing *n*-photon absorption, Eq. 3; this results in a partial population transfer between the qubits states, manifest as regularly spaced "spikes" in Fig. 2C. We obtained one-dimensional (1D) scans of the "switching probability" P_{sw} (the population of state $|0\rangle$) shown in Fig. 2D by following a flux-dependent sample current $I_{sw,0} < I_s < I_{sw,1}$ (dash-dotted line in Fig. 2C). Such 1D scans were then accumulated as a function of the rf source parameters V_{rf} (Fig. 3) and ν (fig. S2).

The switching probability P_{sw} (color scale in Fig. 3) versus qubit flux detuning δf_q and voltage V_{rf} at frequency ν = 1.2 GHz is shown in Fig. 3 (*23*). The *n*-photon resonances, labeled by *n* = 1 to 20, exhibit MZ interference fringes (I to VI) as a function of V_{rf}. The fringes exhibit a Bessel-function dependence, $J_n(\lambda)$, so we call the steplike pattern in Fig. 3 a "Bessel staircase." For each of the *n*-photon resonances, we took a higher resolution scan (e.g., Fig. 3 inset) and fitted the resonance areas and widths in Fig. 4 (*23*).

Multiphoton transitions at the resonances (Eq. 3) in the strong driving regime, $|A_{rf}|, h\nu \gg \Delta$, occur by means of fast LZ transitions. The notion of quasi-stationary qubit levels $\pm[1/2](\varepsilon_0^2+\Delta^2)^{1/2}$ is inadequate in this regime and, instead, we use a different approach, transforming the Hamiltonian (Eq. 2) to a nonuniformly rotating frame, $\mathcal{H}' = e^{-(i/2)\phi(t)\sigma^z}\mathcal{H}'e^{(i/2)\phi(t)\sigma^z}$, where $\phi(t) = \lambda\sin\omega t$ with dimensionless rf-field amplitude

$$\lambda = A_{rf}/h\nu \qquad (4)$$

The rf field disappears from the detuning term, reappearing as a phase factor of the off-diagonal term: $\mathcal{H}' = -[1/2](\varepsilon_0\sigma^z + \Delta e^{-i\phi(t)}\sigma^+ + \text{h.c.})$, where h.c. is hermitian conjugate. Given that $\Delta \ll h\nu$, near the *n*th resonance $nh\nu \cong \varepsilon_0$ we can replace the phase factor $e^{-i\phi(t)}$ by its *n*th Fourier har-

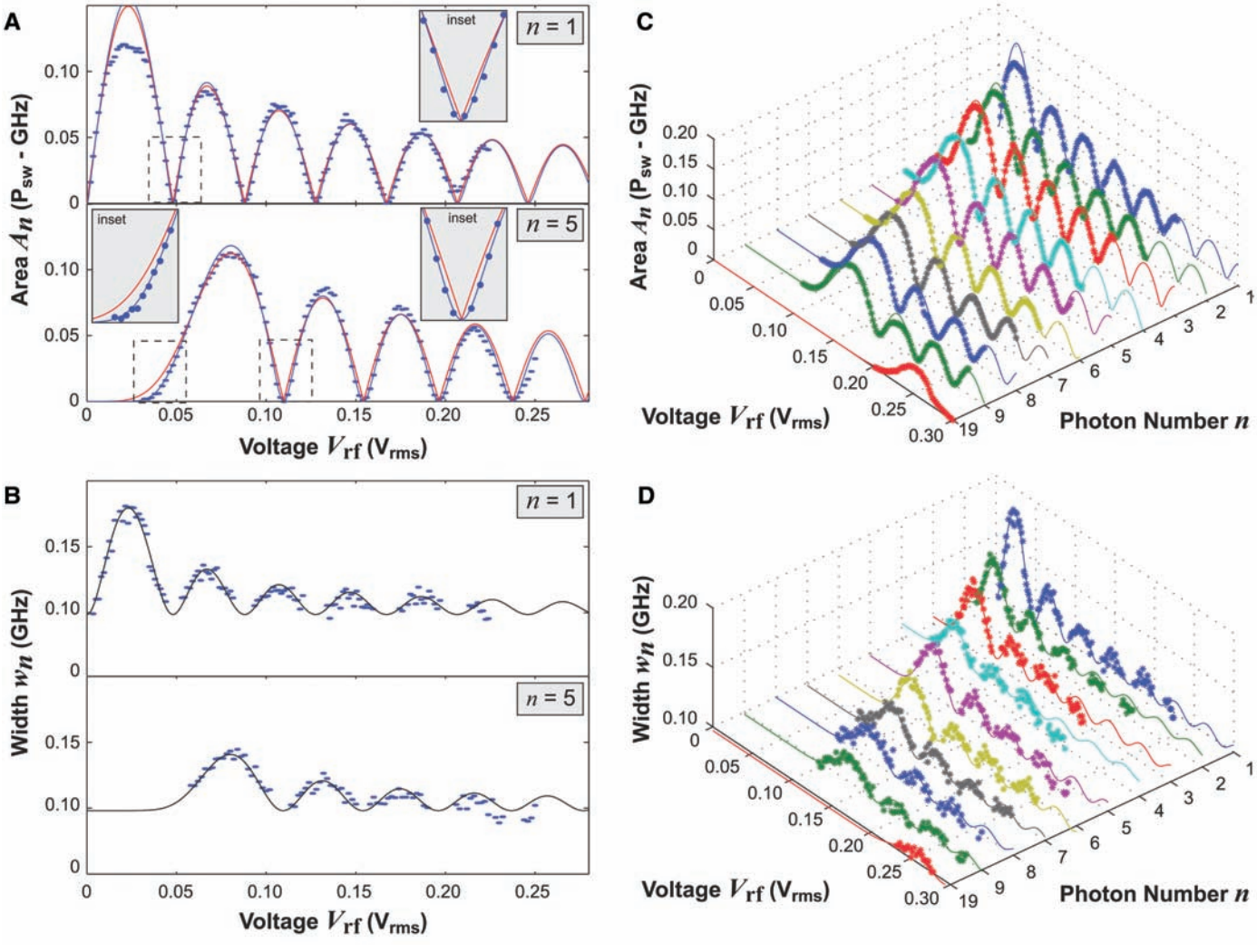

Fig. 4. Analysis of the resonance area and width. (**A**) Resonance area A_n versus voltage V_{rf} for the *n* = 1 and *n* = 5 photon transitions. The Bessel dependence $J_n(\lambda)$ is observed over several lobes. The data are best fit by functions that include decoherence (blue line) rather than omit it (red line). (Insets) Decoherence becomes more pronounced as photon number increases. (**B**) The resonance width w_n versus voltage V_{rf} for *n* = 1 and *n* = 5 also exhibits a Bessel dependence. (**C** and **D**) The area (C) and the width (D) plotted for resonances *n* = 1 to 9 and *n* = 19.

monic, $J_n(\lambda)e^{-in\omega t}$, where J_n is the Bessel function. The resulting effective Hamiltonian $\mathcal{H}' \approx \mathcal{H}_n$ is of a "rotating-field" form

$$\mathcal{H}_n = -\frac{1}{2}\begin{pmatrix} \varepsilon_0 & e^{-in\omega t}\Delta_n \\ e^{in\omega t}\Delta_n^* & -\varepsilon_0 \end{pmatrix} \quad (5)$$

where $\Delta_n = \Delta J_n(\lambda)$. The resonance approximation (Eq. 5) describes transitions at an arbitrary ratio $A_{\mathrm{rf}}/h\nu$. Standard Rabi dynamics analysis of the Hamiltonian (Eq. 5) with the initial state $|0\rangle$ gives the time-averaged occupation probability of the excited state $P_{\mathrm{sw}}^{(n)} = [1/2]\,|\Delta_n|^2/((\varepsilon_0 - nh\nu)^2 + |\Delta_n|^2)$. This expression predicts Lorentz-shaped resonances of width $\delta\varepsilon = |\Delta_n|$. The result, a sum of independent contributions with different n,

$$P_{\mathrm{SW}} = \frac{1}{2}\sum_n \frac{|\Delta_n|^2}{(\varepsilon_0 - nh\nu)^2 + |\Delta_n|^2} \quad (6)$$

is displayed in Fig. 1C. The agreement with the observed resonances is notable: The oscillations in rf power, described by $J_n(\lambda)$, accurately predict both the overall profile of the fringes (Fig. 3) and the fine details, such as positions of the nodes (Fig. 4).

In the frequency dependence of P_{sw} for voltages $V_{\mathrm{rf}} = 71\ \mathrm{mV_{rms}}$ and $V_{\mathrm{rf}} = 7.1\ \mathrm{mV_{rms}}$ (fig. S2), the resonances approach the qubit step as frequency decreases, in accordance with the linear energy versus flux-detuning dependence. MZ interference fringes are again visible. The number of resonances increases at low frequencies, due primarily to the frequency dependence of λ and in lesser part, a frequency-dependent mutual coupling.

Our analysis of peak profile accounts for the relaxation and dephasing, as well as for the inhomogeneous broadening due to low-frequency noise. These effects can be separated from one another by considering the peak areas A_n, which, in contrast with the widths of the resonances w_n, are not affected by inhomogeneous broadening. The standard Bloch approach yields

$$A_n = \frac{T_1\Delta_n^2}{4\sqrt{T_1T_2\Delta_n^2 + 1}},$$
$$w_n = \frac{1}{\pi T_2^*} + \frac{\sqrt{T_1T_2\Delta_n^2 + 1}}{\pi T_2} \quad (7)$$

where $T_{1,2}$ represents the longitudinal and transverse relaxation times, and T_2^* describes the inhomogeneous broadening. These are aggregate relaxation times averaged over the periodic qubit detuning, which, in the operating limit $\varepsilon_0 \gg \Delta$, tends to overestimate T_1 and underestimate T_2 compared with their values at the avoided crossing.

Figure 4A shows the Bessel dependence of the $n = 1$ and $n = 5$ resonance areas fit by Eq. 7 including (blue) and omitting (red) times $T_{1,2}$. The corresponding resonance widths and their fittings are shown in Fig. 4B. Figure 4, C and D, show the resonance area and width, respectively, for 10 resonances, including $n = 19$. Fitting the areas and widths yields self-consistent estimates: $T_1 \approx 20\ \mu\mathrm{s}$, $T_2 \approx 15$ to 25 ns, $T_2^* \approx 5$ to 10 ns, and $\Delta/\hbar \approx (2\pi)4$ MHz. The T_1, T_2, and Δ estimates are similar to those reported by Yu *et al*. (*26*). The nearly linear behavior at the nodes of J_n (Fig. 4A) indicates that the decoherence is small compared with the splitting: $T_1T_2(\Delta/\hbar)^2 \approx 250$ for $n = 1$ and decreases slightly for $n = 5$. The fit/data discrepancy for the first fringe for $n = 1$, which disappears as n increases, is traced to ~20% thermal population of the excited state because of its proximity to the qubit step (supporting online material text).

This MZ interferometry technique can be applied to qubit characterization and model validation, two increasingly important research areas in quantum information science. In addition to coherence times, which can be obtained by multiple means, MZ interferometry allows the direct calibration of the microwave amplitude driving the qubit through the Bessel argument λ; we found the rf mutual coupling (±SD) to be $M_q = 100 \pm 2$ fH over all 20 resonances. The agreement between the two-level Hamiltonian in Eq. 2 and the observed resonances $n = 1$ to 10 in Fig. 3 is notable. The MZ technique also reveals shortcomings of the two-level model at strong driving. For example, the influence of a second MZ interferometer at the avoided crossing between the first and second excited states results in the moiré-like pattern observed for resonances $n > 12$. Also notable is an observed (~0.1 GHz) shift in the resonance positions at strong driving [Fig. 3 inset]. Both effects require the presence of higher excited states modeled by the full qubit Hamiltonian (*26*, *30*). The high stability and coherence of the strongly driven qubit, even at $n = 20$ photon transitions, illustrates not only the potential for nonadiabatic control methods (*22*), but also indicates the high potential of niobium devices fabricated in a fully planarized, scalable process for superconductive quantum computation.

References and Notes

1. Y. Makhlin, G. Schön, A. Shnirman, *Rev. Mod. Phys.* **73**, 357 (2001).
2. Y. Nakamura, Y. A. Pashkin, J. S. Tsai, *Nature* **398**, 786 (1999).
3. J. R. Friedman, V. Patel, W. Chen, S. K. Tolpygo, J. E. Lukens, *Nature* **406**, 43 (2000).
4. C. H. van der Wal *et al.*, *Science* **290**, 773 (2000).
5. Y. Nakamura, Y. A. Pashkin, J. S. Tsai, *Phys. Rev. Lett.* **87**, 246601 (2001).
6. D. Vion *et al.*, *Science* **296**, 886 (2002).
7. Y. Yu, S. Han, X. Chu, S.-I. Chu, Z. Wang, *Science* **296**, 889 (2002).
8. J. M. Martinis, S. Nam, J. Aumentado, C. Urbina, *Phys. Rev. Lett.* **89**, 117901 (2002).
9. I. Chiorescu, Y. Nakamura, C. J. P. M. Harmans, J. E. Mooij, *Science* **299**, 1869 (2003).
10. M. A. Nielsen, I. L. Chuang, *Quantum Computation and Quantum Information* (Cambridge Univ. Press, Cambridge, 2000).
11. A. J. Berkley *et al.*, *Science* **300**, 1548 (2003).
12. J. Claudon, F. Balestro, F. W. J. Hekking, O. Buisson, *Phys. Rev. Lett.* **93**, 187003 (2004).
13. I. Siddiqi *et al.*, *Phys. Rev. Lett.* **93**, 207002 (2004).
14. Y. A. Pashkin *et al.*, *Nature* **421**, 823 (2003).
15. T. Yamamoto, Y. A. Pashkin, O. Astafiev, Y. Nakamura, J. S. Tsai, *Nature* **425**, 941 (2003).
16. R. McDermott *et al.*, *Science* **307**, 1299 (2005).
17. I. Chiorescu *et al.*, *Nature* **431**, 159 (2004).
18. A. Wallraff *et al.*, *Nature* **431**, 162 (2004).
19. A. V. Shytov, D. A. Ivanov, M. V. Feigel'man, *Eur. Phys. J. B* **36**, 263 (2003); This article discusses the adiabatic Landau-Zener regime, corresponding to driving the system at low frequency $\hbar\omega \ll \Delta$. In contrast, we operate at high frequencies, $\hbar\omega \gg \Delta$, which leads to a number of differences, notably the multiphoton resonances.
20. M. C. Baruch, T. F. Gallagher, *Phys. Rev. Lett.* **68**, 3515 (1992).
21. S. Yoakum, L. Sirko, P. M. Koch, *Phys. Rev. Lett.* **69**, 1919 (1992).
22. H. Nakamura, *Nonadiabatic Transition* (World Scientific, London, 2001).
23. Materials and methods are available as supporting material on *Science* Online.
24. Y. Nakamura, J. S. Tsai, *J. Supercond.* **12**, 799 (1999).
25. S. Saito *et al.* (preprint available at http://arxiv.org/abs/cond-mat/0508448).
26. Y. Yu *et al.* (preprint available at http://arxiv.org/abs/cond-mat/0508587).
27. L. P. Kouwenhoven *et al.*, *Phys. Rev. Lett.* **73**, 3443 (1994).
28. T. Fujisawa, S. Tarucha, *Jpn. J. Appl. Phys.* **36**, 4000 (1997).
29. S. Saito *et al.*, *Phys. Rev. Lett.* **93**, 037001 (2004).
30. T. P. Orlando *et al.*, *Phys. Rev. B* **60**, 15398 (1999).
31. V_{rf} is the rf voltage at the source generator. The rf-field amplitude A_{rf}, which drives the qubit, is parameterized in units of energy, and it is proportional to V_{rf}. The proportionality constant can be inferred from the interference fringe spacing and the Bessel argument λ.

32. We thank V. Bolkhovsky, G. Fitch, D. Landers, E. Macedo, R. Slattery, and T. Weir at MIT Lincoln Laboratory; D. Berns, J. Habif, and D. Nakada at the MIT campus for technical assistance; and D. Cory, S. E. Harris, A. J. Kerman, and S. Lloyd for helpful discussions. This work was supported by the Air Force Office of Scientific Research (F49620-01-1-0457) under the Defense University Research Initiative in Nanotechnology program. The work at Lincoln Laboratory was sponsored by the U.S. Department of Defense under Air Force Contract no. FA8721-05-C-0002.

Supporting Online Material

www.sciencemag.org/cgi/content/full/1119678/DC1
Materials and Methods
SOM Text
Figs. S1 and S2
References and Notes

2 September 2005; accepted 1 November 2005
Published online 10 November 2005;
10.1126/science.1119678
Include this information when citing this paper.

Energy Relaxation Time between Macroscopic Quantum Levels in a Superconducting Persistent-Current Qubit

Yang Yu, D. Nakada, Janice C. Lee, Bhuwan Singh, D. S. Crankshaw, T. P. Orlando, and Karl K. Berggren
Massachusetts Institute of Technology, Cambridge, Massachusetts 02139, USA

William D. Oliver
MIT Lincoln Laboratory, Lexington, Massachusetts 02420, USA
(Received 28 October 2003; published 18 March 2004)

We measured the intrawell energy relaxation time $\tau_d \simeq 24$ μs between macroscopic quantum levels in the double well potential of a Nb persistent-current qubit. Interwell population transitions were generated by irradiating the qubit with microwaves. Zero population in the initial well was then observed due to a multilevel decay process in which the initial population relaxed to lower energy levels during the driven transitions. The decoherence time, estimated from τ_d within the spin-boson model, is about 20 μs for this configuration with a Nb superconducting qubit.

DOI: 10.1103/PhysRevLett.92.117904 PACS numbers: 03.67.Pp, 03.65.Yz, 85.25.Cp, 85.25.Dq

Recent successes with superconducting qubits (SQs) have enhanced the feasibility of implementing quantum computing (QC) with Josephson devices [1–9]. Rabi oscillations, which are a preliminary requirement of QC, have been reported in charge, phase, and flux qubits [3–8]. However, the systematic experimental investigation of decoherence, which is a key issue for SQs, is sparse so far due to the challenge of the time resolution of the measurement. Although long decoherence times have been demonstrated in some special configurations [4,5,8,10], the limiting source of decoherence in the SQs remains unidentified. On the other hand, the decoherence time for SQs, including energy and phase relaxation times, is predicted to be proportional to the level of dissipation, which results from the coupling between the qubits and the environment [11,12]. Therefore, quantifying the dissipation is extremely useful in the design of qubits from various new materials, because it indicates whether the dissipation is at least low enough to make error-tolerant QC feasible. Previous methods to determine the dissipation of devices are either applicable at relatively high temperatures [10] or rely on indirect measurements of switching probabilities [13]. In addition, all long decoherence times (~ 1 μs) reported have been obtained in NbN and Al SQs [4,5,8,10]. It is important to know whether a promising decoherence time can be achieved in Nb-based SQs, which has a more mature fabrication capability. In this Letter, we present time-resolved measurements of the intrawell relaxation time τ_d in a Nb persistent-current (PC) qubit. We found that $\tau_d \simeq 24$ μs. The corresponding phase-decoherence time within a spin-boson model (SBM) is inferred to be longer than 20 μs. These long decoherence times indicate a strong potential for QC employing Nb-based SQs.

A PC qubit is a superconducting loop broken by three underdamped Josephson junctions (JJs) [Fig. 1(a)]. Two JJs are designed to have the same critical current, and the third one is designed to be α times smaller. For $0.5 < \alpha < 1$ and with an externally applied magnetic field close to a half-flux quantum $\Phi_0/2$, the system is analogous to a particle in a two-dimensional potential well with eigenenergies calculated in Ref. [14]. However, the lowest relevant states effectively reflect a particle in a one-dimensional double-well potential with quantized energy levels shown in Fig. 1(b), and whose classical states in each well correspond to macroscopic persistent currents of opposite sign [15]. The potential shown in Fig. 1(b) can be tilted by changing the frustration f_q, the magnetic flux threading the loop in units of Φ_0. The two classical states are coupled via quantum tunneling through the barrier between the wells. In addition, the system can interact with a monochromatic electromagnetic (microwave) field, and microwaves with frequency matching the energy level spacing can generate transitions between the two macroscopic quantum states, namely, photon-induced transitions (PITs) [2,8].

The samples used in this study were fabricated at MIT Lincoln Laboratory in a Nb trilayer process [16]. The critical current density is $J_c \sim 370$ A/cm^2. The critical currents of the large and small JJs in the qubit, determined from thermal activation studies [17], are $I_c \simeq 1.2$ and 0.75 μA, respectively ($\alpha \simeq 0.63$). The qubit energy

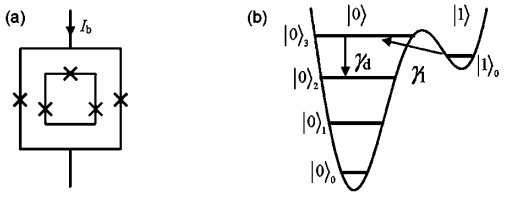

FIG. 1. (a) Schematic of the PC qubit surrounded by a readout dc SQUID. (b) Schematic of the qubit's double-well potential with energy levels for an applied frustration close to $0.485\Phi_0$. Microwaves pump the qubit from the lowest level of $|1\rangle$ ($|1\rangle_0$) to the third excited level of $|0\rangle$ ($|0\rangle_3$), then decay to the second excited level of $|0\rangle$ ($|0\rangle_2$) with a rate γ_d.

level structure calculated using qubit parameters is shown in Fig. 2 of Ref. [14]. The persistent current in the qubit loop can be read out by a dc SQUID which surrounds the qubit. For our device parameters [14,17], the persistent current will generate an additional magnetic flux of ~ 3 mΦ_0 in the SQUID, resulting in a 0.3 μA change in the switching current I_{sw} of the SQUID that can be easily detected at $T < 50$ mK. The sample was mounted on a chip carrier that was enclosed in an oxygen-free-copper sample cell and thermally anchored to the mixing chamber (MC) of a dilution refrigerator. The devices were magnetically shielded by four cryoperm-10 cylinders surrounding the inner vacuum can. All electrical leads that connected the SQUID to room temperature electronics were carefully filtered by electromagnetic interference filters (at 300 K), RC filters (at 1.6 K), and copper powder filters (at 15 mK). Microwaves were injected to the qubit via a separate semirigid cryogenic coaxial cable with 20 dB attenuators at the 1 K pot and the MC. Battery-powered low-noise preamplifiers were used for all measurements. The diagnostic tests performed on JJs indicated that there was no significant extrinsic noise in our system.

Spectroscopy of the qubit energy levels was achieved using microwave pulses to produce PITs. For each measurement trial (Fig. 2), we first prepared the qubit in state $|1\rangle$ by tilting the potential (i.e., applying frustration) to a regime where the system has a single well and then waiting a sufficiently long time. After the qubit had relaxed to its ground state, the potential was tilted back to the frustration where it was to be measured. At low temperatures, the qubit will have a finite probability of remaining in $|1\rangle$, which is effectively metastable on the time scales considered in this Letter. We then applied microwaves with duration time t_{pul}, inducing transitions between states $|1\rangle$ and $|0\rangle$. After the microwaves were shut off, the bias current of the SQUID was ramped through values slightly higher than its critical current I_{c0}. The qubit state ($|0\rangle$ or $|1\rangle$) was then read out from the current at which the SQUID switched to a finite voltage state [**0** or **1** in Fig. 2(d)]. For a fixed frustration, this procedure was repeated more than 10^3 times to minimize the statistical error. A histogram of I_{sw} clearly shows the probability distribution of the qubit state occupation. Shown in Fig. 3 are contour plots of the switching-current histograms obtained by scanning the frustration at $T = 15$ mK. Each vertical slice is a histogram of I_{sw}, and the color represents the number of switching events (proportional to the switching probability). A bimodal structure in the switching-current distribution, caused by the opposite persistent current of the qubit, was observed at $f_q \sim 0.485\Phi_0$. The lower branch represents the qubit in the $|0\rangle$ state, and the upper branch represents the qubit in the $|1\rangle$ state. The substantial population in state $|1\rangle$ demonstrates that we had successfully prepared the qubit in $|1\rangle$, because, near $f_q \sim 0.485\Phi_0$, the qubit had a much higher single-well ground-state energy in $|1\rangle$ than that in $|0\rangle$.

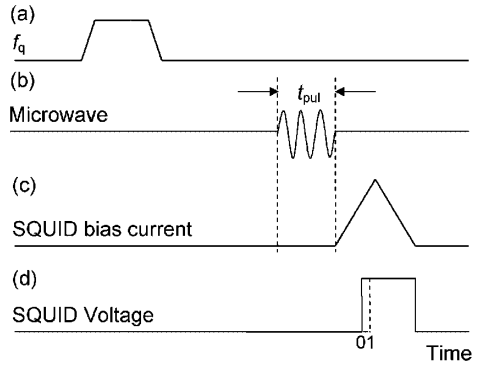

FIG. 2. Time profiles of (a) bias frustration, (b) microwave amplitude, (c) SQUID bias current, and (d) SQUID voltage for one measurement trial. **0** and **1** indicate that the qubit states ($|0\rangle$ or $|1\rangle$) result in different I_{sw}.

However, the energy barrier height and width relative to the lowest energy level of state $|1\rangle$, denoted as $|1\rangle_0$, were small enough so that the qubit had a large probability of tunneling to $|0\rangle$. The leftmost tip of the higher branch marked a fixed frustration point $f_q \approx 0.484\Phi_0$, below which it was impossible for the qubit to stay in $|1\rangle$, because the potential becomes essentially a single-well $|0\rangle$ state. Microwaves, with frequencies matching the energy difference between $|1\rangle_0$ and one of the levels of $|0\rangle$, were used to generate transitions between states $|1\rangle$

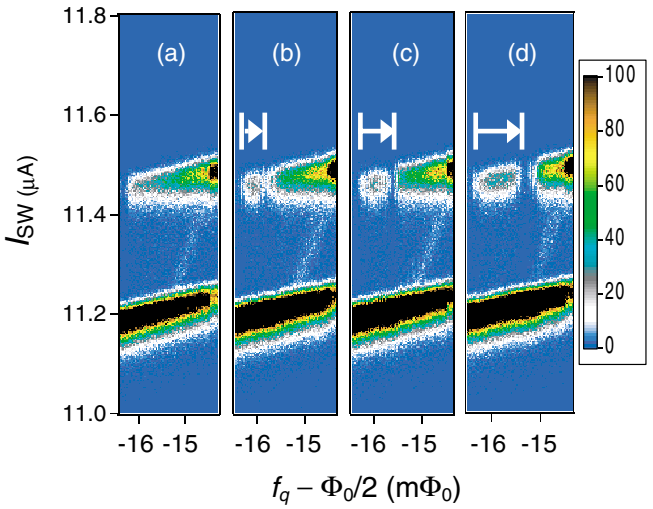

FIG. 3 (color). Contour plots of the switching current distribution (a) without microwaves and with microwaves at (b) $\nu = 6.77$, (c) 7.9, and (d) 9.66 GHz. In each plot, the leftmost tip of the upper branch corresponds to a fixed frustration point $f_q \approx 0.484\Phi_0$. Without microwave irradiation, the population in the upper branch (state $|1\rangle$) decreased continuously to zero as the frustration decreased from $\Phi_0/2$. Microwaves pumped the population from state $|1\rangle$ to state $|0\rangle$ at the resonant frustration, the bias point at which the microwave frequency matched the energy level spacing between two states. The white arrows indicate that the resonant frustration moves toward $\Phi_0/2$ with increasing microwave frequency, in agreement with the qubit energy structure [Ref. [14]].

and $|0\rangle$. The most striking feature of the contour plots is that a population "gap" (i.e., zero population region) in the $|1\rangle$ branch was created by the microwaves [Figs. 3(b)–3(d)]. With increasing microwave frequency, the gap moved away from the tip, as expected from the energy level structure [Ref. [14]]. The quantitative agreement between the gap position and the energy level structure confirmed that the gap resulted from the microwave PIT between the two macroscopic quantum states $|1\rangle_0$ and $|0\rangle_3$ (the third excited energy level of the state $|0\rangle$). We believe that the PIT here was an incoherent process, because the microwave pulse duration was 600 μs, much longer than the estimated decoherence time (0.1–100 μs) [2,8,15]. Additionally, no periodic variation of population with varying pulse duration (for long pulses) was observed. In a simple two-level system, observing such a gap would be unexpected for an incoherent transition, since the population in the lower level ($|1\rangle_0$) should always be larger than 0.5 in that case [18]. In order to address this gap phenomenon in our multilevel system, a multilevel pump-decaying model is introduced.

For simplicity we considered only three levels, the initial state $|1\rangle_0$, the $|0\rangle_3$ state to which radiation induces a transition, and the state $|0\rangle_2$ to which the population of $|0\rangle_3$ decays. More accurately, the state $|0\rangle_3$ decays to $|0\rangle_2$, $|0\rangle_1$, and $|0\rangle_0$, but, for ease of calculation, we collectively label these states as $|0\rangle_2$ with an overall effective intrawell decay rate $\gamma_d \equiv 1/\tau_d$. The temporal evolution of the three-level system under microwave irradiation is thereby described by the following three coupled rate equations:

$$\frac{dP_{10}}{dt} = -\gamma_1 P_{10} + (\gamma_1 + \gamma_2) P_{03}, \tag{1}$$

$$\frac{dP_{03}}{dt} = \gamma_1 P_{10} - (\gamma_1 + \gamma_2) P_{03} - \gamma_d P_{03}, \tag{2}$$

$$\frac{dP_{02}}{dt} = \gamma_d P_{03}, \tag{3}$$

in which P_{10}, P_{03}, and P_{02} are the occupation probabilities of levels $|1\rangle_0$, $|0\rangle_3$, and $|0\rangle_2$, respectively. γ_1 is the stimulated transition rate between $|1\rangle_0$ and $|0\rangle_3$, and γ_2 is the spontaneous relaxation rate from $|0\rangle_3$ to $|1\rangle_0$. Generally, for a given system, γ_1 is proportional to the microwave power P_{rf}, and γ_2 can be considered to be a constant [18]. For the initial condition $P_{10}(0) = 1$, with $P_{03}(0) = P_{02}(0) = 0$, Eqs. (1)–(3) can be solved analytically. For $\gamma_1 \gtrsim \gamma_d$, which is satisfied in our experiment, the probability of finding the qubit remaining in the state $|1\rangle_0$ at $t > 1/(2\gamma_1 + \gamma_2 + \gamma_d)$ is given by

$$P_{10}(t) \approx a_1 e^{-t/\tau'}, \tag{4}$$

where a_1 depends weakly on the microwave power and can be considered as a constant in the relevant time scale,

$$\tau' \simeq (2 + \gamma_2/\gamma_1)\tau_d = (2 + \gamma_2/A P_{\mathrm{rf}})\tau_d, \tag{5}$$

and A is the coupling constant between the microwave source and the qubit. The physical picture of the three-level pump-decaying process is that microwaves populate the highest level with a population $P_{03} \propto 1/(2 + \gamma_2/\gamma_1)$, which decays to the lowest level with a rate γ_d. Therefore, the effective decay rate of the population of the initial state is given by Eq. (5), and with t sufficiently long, $P_{10}(t) \to 0$; this agrees with the experimental observations.

A significant impact of Eqs. (4) and (5) is that τ_d can be determined by measuring $P_{10}(t)$. Because I_{sw} of $|0\rangle$ is smaller than that of $|1\rangle$, pumping the system from state $|1\rangle$ to state $|0\rangle$ will generate a dip in the I_{sw} average as a function of frustration, and the dip amplitude is proportional to $1 - P_{10}$. Figure 4 shows the dip amplitude as a function of the microwave irradiation time t_{pul}. The nominal power of the microwave source was $P_{\mathrm{rf}} = 31.3$ μW. The time constant τ', obtained from a best fit, is 130 ± 20 μs. We emphasize that τ' is not equal to τ_d, but, rather, it depends on γ_2/γ_1. For large P_{rf} (i.e., $\gamma_1 \gg \gamma_2$), τ' will saturate to $2\tau_d$. For $\gamma_1 \sim \gamma_2$, we are able to determine τ_d by measuring the P_{rf} dependence of τ'. Shown in Fig. 5 is τ' measured at various P_{rf}. τ' saturates at about 50 μs for $P_{\mathrm{rf}} > 0.2$ mW. By adjusting γ_2/A and τ_d as fitting parameters, we obtained $\tau_d \simeq 24.3 \pm 2.7$ μs from a best fit to Eq. (5), which is consistent with dc tunneling spectroscopy measurements [14]. This long intrawell energy relaxation time is of the same order of magnitude as the reported energy relaxation times in NbN and Al-based qubits [4,5,8,10]. Note that γ_2 is another important parameter which determines interwell energy relaxation. Unfortunately, we could not directly extract γ_2 from the fitting, because we do not know the coupling constant A. Future experiments in which microwave coupling is independently characterized should allow the extraction of γ_2.

The primary effect of the environmental dissipation on the intrawell dynamics of the PC qubits is that, at low temperature ($k_B T \ll$ level spacing), the width of an excited level with energy E_n is given approximately by $\gamma_d \simeq E_n/Q$, where Q is the quality factor of the classical small

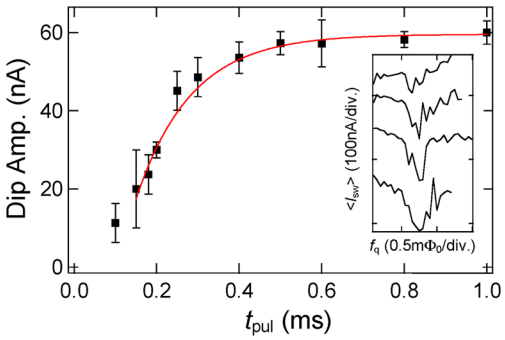

FIG. 4 (color online). The amplitude of the microwave resonant dip as a function of microwave duration t_{pul}. The microwave frequency $\nu = 9.66$ GHz and nominal power $P_{\mathrm{rf}} = 31.3$ μW. The solid squares are experimental data and the line is a best fit to an exponential decay. The inset shows the resonant dips at $t_{\mathrm{pul}} = 0.2$, 0.5, 0.8, and 1 ms, from top to bottom.

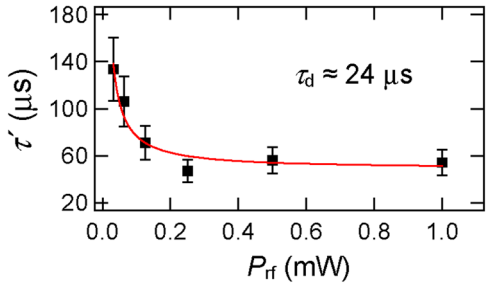

FIG. 5 (color online). τ' vs microwave power for $\nu = 9.66$ GHz. The solid line is a best fit to Eq. (5).

oscillation in the potential well [19]. From τ_d we determined $Q \sim 5 \times 10^5$, close to the value obtained from thermal activation measurements at intermediate temperatures 0.3–1.2 K [17]. Note that Q is proportional to the subgap resistance, which ideally depends on the temperature as $\sim e^{\Delta_s/k_B T}$ [20], where Δ_s is the superconducting gap voltage. The temperature independence of Q suggests the presence of additional environmental sources of dissipation [15].

This long intrawell relaxation time is important for experiments in QC in two ways. First, the lower two energy levels in the left well, $|0\rangle_0$ and $|0\rangle_1$, could themselves be used as the two qubits states, with a third state $|0\rangle_3$ used as the readout state. Because our PC qubit had no leads directly connected to it and the magnetic coupling circuit is optimally designed to lessen the effects of the electromagnetic environment, the PC qubit is much less influenced by this environment than are other similar single-junction schemes [5,6,9]. Second, if we assume that the environment can be modeled as an Ohmic bath, as in the SBM, then we can estimate the decoherence times of a PC qubit in which the qubit states are those of opposite circulating current [2,8,15]. The energy relaxation and phase-decoherence times are given in the SBM for an Ohmic environment by [11]

$$\tau_{\rm relax}^{-1} \simeq \pi \alpha_L \sin^2 \eta \Delta E/\hbar, \tag{6}$$

$$\tau_\varphi^{-1} = \tau_{\rm relax}^{-1}/2 + 2\pi \alpha_L k_B T \cos^2 \eta/\hbar, \tag{7}$$

where ΔE is the energy difference between levels in opposite wells, $\eta \approx {\rm tg}^{-1}(\Delta/\Delta E)$ is the mixing angle, Δ is the tunneling amplitude between the wells, and $\alpha_L \sim 1/Q$ is the quantum damping parameter [19] which we estimate using our measured Q value. For our Nb PC qubit operating with opposite circulating currents states (for instance, biased near $f_q \approx 0.485\Phi_0$, where $\Delta \approx 2$ GHz and $\Delta E \approx 4$ GHz), a conservative estimate gives $\tau_{\rm relax} \gtrsim 30$ μs and $\tau_\varphi \gtrsim 20$ μs at 15 mK. We emphasize that an Ohmic environment model may not adequately describe all sources of decoherence; these times must be viewed as estimates pending experimental verification. Nonetheless, for a typical Rabi frequency $\Omega = 1$ GHz, we obtained a quantum quality factor $> 10^4$, larger than the oft-quoted basic requirement for error-tolerant QC. Considering the attractiveness of Nb-based SQs from the point of view of robust and well-developed fabrication methods, these times indicate that they are a promising candidate for realizing a scalable quantum computer.

In summary, we directly measured the intrawell relaxation time of a Nb-based PC qubit by generating PITs between macroscopically distinct quantum states. A multilevel decay process was observed with an intrawell relaxation time of about 24 μs and a Q factor of greater than 10^5, indicating that these intrawell levels are well isolated from the environment and are themselves a good qubit candidate. Likewise, these measurements suggest that the flux qubits operating between wells could also have sufficient decoherence times, demonstrating good prospects for well-fabricated Nb junctions, with their more mature technology, to be used as SQs.

We thank K. Segall, B. Cord, D. Berns, and A. Clough for technical assistance and S. Valenzuela, M. Tinkham, L. Levitov, and M. Vavilov for helpful discussions. This work was supported by AFOSR Grant No. F49620-01-1-0457 under the DURINT program and by ARDA. The work at Lincoln Laboratory was sponsored by the U.S. DOD under the Air Force, Contract No. F19628-00-C-0002.

[1] J. R. Friedman *et al.*, Nature (London) **406**, 43 (2000).
[2] C. H. van der Wal *et al.*, Science **290**, 773 (2000).
[3] Y. Nakamura, Y. A. Pushkin, and J. S. Tsai, Nature (London) **398**, 786 (1999).
[4] D. Vion *et al.*, Science **296**, 886 (2002).
[5] Y. Yu *et al.*, Science **296**, 889 (2002).
[6] J. M. Martinis *et al.*, Phys. Rev. Lett. **89**, 117901 (2002).
[7] Y. A. Pashkin *et al.*, Nature (London) **421**, 823 (2003).
[8] I. Chiorescu *et al.*, Science **299**, 1869 (2003).
[9] A. J. Berkley *et al.*, Science **300**, 1548 (2003).
[10] S. Han *et al.*, Science **293**, 1457 (2001).
[11] A. J. Leggett *et al.*, Rev. Mod. Phys. **59**, 1 (1987); Y. Makhlin, G. Schön, and A. Shnirman, Rev. Mod. Phys. **73**, 357 (2001).
[12] W. H. Zurek, Phys. Today **44**, No. 10, 36 (1991).
[13] C. Cosmelli *et al.*, Phys. Rev. Lett. **82**, 5357 (1999); S. Han and R. Rouse, Phys. Rev. Lett. **86**, 4191 (2001).
[14] D. S. Crankshaw *et al.*, Phys. Rev. B (to be published).
[15] T. P. Orlando *et al.*, Phys. Rev. B **60**, 15 398 (1999).
[16] K. K. Berggren *et al.*, IEEE Trans. Appl. Supercond. **9**, 3271 (1999).
[17] K. Segall *et al.*, Phys. Rev. B **67**, 220506 (2003).
[18] D. J. Griffiths, *Introduction to Quantum Mechanics* (Prentice-Hall, Englewood Cliffs, NJ, 1995), p. 311.
[19] J. M. Schmidt, A. N. Cleland, and J. Clarke, Phys. Rev. B **43**, 229 (1991); W. Bialek, S. Chakravarty, and S. Kivelson, Phys. Rev. B **35**, 120 (1987).
[20] P. Silvestrini *et al.*, Phys. Rev. Lett. **60**, 844 (1988).

Bibliography

[1] A. O. Caldeira, and A. J. Leggett, "Quantum tunnelling in a dissipative system," *Annals of Physics*, v 149, n 2, p 374-456, 1983.

[2] A. J. Leggett, S. Chakravarty, A. T. Dorsey, M. P. A. Fisher, A. Garg, and W. Zwerger, "Dynamics of the Dissipative Two-State System," *Rev. Mod. Phys.*, **59**, 1, 1987.

[3] A. J. Leggett, "Schrodinger's cat and her laboratory cousins," *Contemporary Physics*, vol. 25, p. 583-598, 1984.

[4] R. P. Feynman, "Simulating Physics with Computers," *International Journal of Theoretical Physics*, 21: 467488, 1982.

[5] P. Shor, "Algorithms for Quantum Computation: Discrete Log and Factoring," *Proceedings of the 35th annual symposium on foundations of computer science*, S. Goldwasser, Ed., IEEE Computer Society, Los Alamitos, CA, 124-34, 1994.

[6] D. P. DiVincenzo, "The Physical Implementation of Quantum Computation," *Fortschritte der Physik*, 48, 771, 2000.

[7] Experimental Aspects of Quantum Computing, *Quantum Information Processing*, Vol 3, Issue 1-5, 2004.

[8] A Quantum Information Science and Technology Roadmap, http://qist.lanl.gov, 2004

[9] C. Ramanathan, N. Boulant, Z. Chen, D. G. Cory, I. Chuang, M. Steffen, "NMR Quantum Information Processing," *Quantum Information Processing*, Vol 3, Issue 1 - 5, p. 15, 2004.

[10] M. H. Devoret, and J. M. Martinis, "Implementing Qubits with Superconducting Integrated Circuits," Quantum Information Processing, Vol 3, Issue 1 - 5, p. 163, 2004.

[11] M. H. Devoret, and R. J. Schoelkopf, "Amplifying quantum signals with the single-electron transistor," *Nature*, **406**, 1039, p 1039-46, 2002.

[12] Y. Nakamura, Yu. A. Pashkin and J. S. Tsai, "Coherent control of macroscopic quantum states in a single-Cooper-pair box," *Nature*, **398**,p. 786-788, 1999.

[13] Yu. A. Pashkin, T. Yamamoto, O. Astafiev, Y. Nakamura, D. V. Averin, and J. S. Tsai, "Quantum oscillations in two coupled charge qubits," *Nature*, **421**, p. 823-826, 2003.

[14] A. J. Berkley, H. Xu, R. C. Ramos, M. A. Gubrud, F. W. Strauch, P. R. Johnson, J. R. Anderson, A. J. Dragt, C. J. Lobb, and F. C. Wellstood, "Entangled Macroscopic Quantum States in Two Superconducting Qubits," *Science*, **300**, p. 1548-1550, 2003.

[15] T. Yamamoto, Yu. A. Pashkin, O. Astafiev, Y. Nakamura, J. S. Tsai, "Demonstration of conditional gate operation using superconducting charge qubits," Nature, **425**, p.941-4, 2003.

[16] C.H. van der Wal, A.C.J. ter Haar, F.K. Wilhelm, R.N. Schouten, C.J.P.M. Harmans, T.P. Orlando, S. Lloyd, and J.E. Mooij, "Quantum Superposition of Macroscopic Persistent-Current States," *Science,* **290**, p.773-7, 2000.

[17] I. Chiorescu, Y. Nakamura, C. J. P. M. Harmans and J. E. Mooij, "Coherent Quantum Dynamics of a Superconducting Flux Qubit", *Science*, **299**, 1869-71, 2003.

[18] J. R. Friedman, V. Patel, W. Chen, S. K. Tolpygo, and J. E. Lukens, "Quantum Superposition of Distinct Macroscopic States," *Nature*, **406**, 43, 2000.

[19] T. Kutsuzawa, H. Tanaka, S. Saito, H. Nakano, K. Semba, H. Takayanagi, "Coherent control of a flux qubit by phase-shifted resonant microwave pulses," *Applied Physics Letters*, v 87, n 7, p 73501-1-3, 2005.

[20] B.L.T. Plourde, T.L. Robertson, P.A. Reichardt, T. Hime, S. Linzen, C.-E. Wu, John Clarke, "Flux Qubits and Readout Device with Two Independent Flux Lines," *Physical Review B*, v 72, n 6, p 60506-1-4, 2005.

[21] Y. Yu, S. Han, X. Chu, S. Chu, and Z. Wang, "Coherent Temporal Oscillations of Macroscopic Quantum States in a Josephson Junction", *Science,* **296**, 889-92, 2002.

[22] J. M. Martinis, S. Nam, J. Aumentado, and C. Urbina, "Rabi Oscillations in a Large Josephson-Junction Qubit", *Phys. Rev. Lett.*, **89**, 117901-1-4, 2002.

[23] D. Vion, A. Aassime, A. Cottet, P. Joyez, H. Pothier, C. Urbina, D . Esteve, and M.H. Devoret, "Manipulating the Quantum State of an Electrical Circuit", *Science*, **296**, 886-9, 2002.

[24] A. Lupascu, E. F. C. Driessen, L. Roschier, C. J. P. M. Harmans, J. E. Mooij, "High-contrast dispersive readout of a superconducting flux qubit using a nonlinear resonator," *Physical Review Letters*, v 96, n 12, 2006.

[25] M. Grajcar, A. Izmalkov, E. Il'ichev, Th. Wagner, N. Oukhanski, U. Hbner, T. May, I. Zhilyaev, H. E. Hoenig, Ya. S. Greenberg, V. I. Shnyrkov, D. Born, W. Krech, H.-G. Meyer, Alec Maassen van den Brink, and M. H. S. Amin, "Low-frequency measurement of the tunneling amplitude in a flux qubit," *Phys. Rev. B*, **69**, 060501, 2004.

[26] E. Il'ichev, N. Oukhanski, A. Izmalkov, Th. Wagner, M. Grajcar, H.-G. Meyer, A.Yu. Smirnov, A. Maassen van den Bring, M.H.S. Amin, and A.M. Zagoskin, "Continuous monitoring of Rabi oscillations in a Josephson flux qubit", *Phys. Rev. Lett.*, **91**, 097906, 2003.

[27] I. Siddiqi, R. Vijay, M. Metcalfe, E. Boaknin, L. Frunzio, R.J. Schoelkopf, M.H. Devoret, "Dispersive measurements of superconducting qubit coherence with a fast, latching readout," *Physical Review B*, v 73, n 5, 2006.

[28] A. Wallraff, D. I. Schuster, A. Blais, L. Frunzio, J. Majer, M. H. Devoret, S. M. Girvin, and R. J. Schoelkopf, "Approaching Unit Visibility for Control of a Superconducting Qubit with Dispersive Readout," *Phys. Rev. Lett.*, **95**, 060501, 2005.

[29] A. J. Leggett, "Superconducting Qubits–a Major Roadblock Dissolved?" *Science*, Vol. 296. no. 5569, pp. 861 - 862, 2002.

[30] J. E. Mooij, T. P. Orlando, L. Levitov, L. Tian, C. van der Wal, and S. Lloyd, "Josephson Persistent-Current Qubit," *Science,* **285**, 1036-9, 1999.

[31] T. P. Orlando, J.E. Mooij, L. Tian, C.H. van der Wal, L.S. Levitov, S. Lloyd, and J.J. Mazo, "Superconducting Persistent-Current Qubit," *Phys. Rev. B,* **60**, 15398, 1999.

[32] L. Tian, S. Lloyd, and T.P. Orlando, "Decoherence and relaxation of a superconducting quantum bit during measurement," *Phys. Rev. B,* **65**, 144516, 2002.

[33] K. M. Lang, S. Nam, J. Aumentado, C. Urbina, and J. M. Martinis, "Banishing Quasiparticles From Josephson-Junction Qubits: Why and How to do it," *IEEE Transactions On Applied Superconductivity*, **13**, 989-993, 2003.

[34] D. Nakada, K.K. Berggren, E. Macedo, V. Liberman, and T.P. Orlando, "Improved Critical-Current-Density Uniformity by Using Anodization," *IEEE Trans. Appl. Superconductivity*, **13**, 111-4, 2003.

[35] J. C. Lee, "Magnetic Flux Measurement of Superconducting Qubits with Josephson Inductors," S.M. Thesis, MIT, 2002.

[36] J. C. Lee, W. D. Oliver, T. P. Orlando, K. K. Berggren, "Resonant readout of a persistent current qubit," *IEEE Transactions on Applied Superconductivity*, v 15, n 2, p 841-4, June 2005.

[37] A. Izmalkov, M. Grajcar, E. Il'ichev, M. Oukhanski, Th. Wagner, H. -G. Meyer, W. Krech, M. H. S. Amin, Alec Maassen van den Brink and A. M. Zagoskin, "Observation of macroscopic Landau-Zener transitions in a superconducting device," *Europhysics Letters*, 65 (6), 844-849, 2004.

[38] P. L. Hagelstein, S. D. Senturia, T. P. Orlando, *Introductory Applied Quantum and Statistical Mechanics.* John Wiley & Sons Inc., 2004.

[39] T. P. Orlando, "Quantum Circuits and Quantum Computing," 6.975 Lecture notes, 2003.

[40] M. H. Levitt, *Spin Dynamics: Basics of Nuclear Magnetic Resonance*. John Wiley & Sons, Ltd., 2001.

[41] T. A. Fulton and L. N. Dunkleberger, " Lifetime of the zero-voltage state in Josephson tunnel junctions," *Phys. Rev. B*, **9**, 4760-7, 1974.

[42] M. H. Devoret, J. M. Martinis, and John Clarke, "Measurements of Macroscopic Quantum Tunneling out of the Zero-Voltage State of a Current-Biased Josephson Junction," *Phys. Rev. Lett.*, **55**, 19081911, 1985.

[43] M. Büttiker, E. P. Harris, and R. Landauer, "Thermal activation in extremely underdamped Josephson-junction circuits," *Phys. Rev. B*, **28**, 12681275, 1983.

[44] K. Segall, D. S. Crankshaw, D. Nakada, B. Singh, J. Lee, T. P. Orlando, K. K. Berggren, N. Markovic, S. O. Valenzuela, M. Tinkham, "Experimental characterization of the two current states in a Nb persistent-current qubit," *IEEE Transactions on Applied Superconductivity,* **v 13**, n 2, June 2003, p 1009-12.

[45] Y. Yu, W. D. Oliver, J. C. Lee, K. K. Berggren, L. S. Levitov, T. P. Orlando, "Multi-Photon, Multi-Level Dynamics in a Superconducting Persistent-Current Qubit," cond-mat/0508587.

[46] W. D. Oliver, Y. Yu, J. C. Lee, K. K. Berggren, L. S. Levitov, T. P. Orlando, "Mach-Zehnder Interferometry in a Strongly Driven Superconducint Qubit," *Science*, **310**, 1653, 2005.

[47] Y. Yu, W. D. Oliver, D. Nakada, J. C. Lee, K. K. Berggren, T. P. Orlando, "Energy Relaxation Times in a Nb Persistent Current Qubit," IEEE Transactions on Applied Superconductivity, vol. 15, no.2., June 2005.

[48] I. Siddiqi, R. Vijay, F. Pierre, C. M. Wilson, M. Metcalfe, C. Rigetti, L. Frunzio, and M. H. Devoret, "RF-Driven Josephson Bifurcation Amplifier for Quantum Measurement," *Phys. Rev. Lett.*, **93**, 207002, 2004.

[49] J. W. Nilsson, *Electric Circuits*, Addison-Wesley Publishing Company, Inc., 1990.

[50] W. H. Hayt, J. E. Kemmerly, *Engineering Circuit Analysis*, McGraw-Hill, Inc., 1986.

[51] C. Bowick, *RF Circuit Design*. Newnes Press, 1982.

[52] T. H. Lee, *The Design of CMOS Radio-Frequency Integrated Circuits*. Cambridge University Press, 2003.

[53] K. Berggren, E. Macedo, D. Feld, and J. Sage, "Low Tc Superconductive Circuits Fabricated on 150mm-Diameter Wafers Using a Doubly Planarized Nb/AlOx/Nb Process," *IEEE Trans. Appl. Superconductivity*, **9**, 3271-4, 1999.

[54] M. Kamon, M. J. Tsyk, and J. White, "FASTHENRY: A Multipole-Accelerated 3-D Inductance Extraction Program," IEEE Trans. on Microwave Theory and Tech., 1994.

[55] S. S. Mohan, M. del Mar Hershenson, S. P. Boyd, and T. H. Lee, "Simple accurate expressions for planar spiral inductances," *IEEE Journal of Solid-state circuits*, 34(10), 1999.

[56] C. Patrick Yue, and S. Simon Wong, "Design strategy of on-chip inductors for highly integrated rf systems," *IEEE 36th Design Automation Conference Proceedings*, pg. 982, 1999.

[57] W. D. Oliver and V. Bolkhovsky, DSM2 Design Rules, MIT Lincoln Laboratory, 2005.

[58] J. M. Martinis, M. H. Devoret, and J. Clarke, "Experimental tests for the quantum behavior of a macroscopic degree of freedom: The phase difference across a josephson junction," *Physical Review B*, 35 (10), 1987.

[59] A. Fukushima, A. Sato, A. Iwasa, Y. Nakamura, T. Komatsuzaki, and Y. Sakamoto, "Attenuation of microwave filters for single-electron tunneling experiments," IEEE Transaction on Instrumentation and Measurement, 46(2), 1997.

[60] Y. Yu, D. Nakada, J. C. Lee, B. Singh, D. S. Crankshaw, T. P. Orlando, K. K. Berggren, W. D. Oliver, "Energy relaxation time between macroscopic quantum levels in a superconducting persistent-current qubit," *Phys. Rev. Lett.*, **92**, 117904, 2004.

[61] F. Auracher, and T. Van Duzer, "RF impedance of supercondcuting weak links," *J. Appl. Phys.*, Vol. 44, No. 2, 1973.

[62] M. Perpeet, M. A. Hein, H. Piel, S. Beuven, M. Siegel, E. Sodtke, "Microwave impedance of $YBa_2Cu_3O_7$ step-edge junctions," *Proceedings of EUCAS 1995, the Second European Conference on Applied Superconductivity*, pt. 2, p 1255-8, vol.2, 1995.

[63] T. Holst, J. Bindslev Hansen, "The plasma resonance in microwave-driven small Josephson tunnel junctions," *Physica B*, v 165-166, p. 1649-50, 1990,

[64] C. C. Chin, D. E. Oates, G. Dresselhaus, and M. S. Dresselhaus, "Nonlinear electrodynamics of superconducting NbN and Nb thin films at microwave frequencies," *Physical Review B*, v 45, n 9, p 4788, 1992.

[65] F. Kouril, and K. Vrba, *Non-linear and parametric circuits, Principles, theory and applications*. John Wiley & sons, 1988.

[66] E. S. Kuh, and R. A. Rohrer, "The State-Variable Approach to Network Analysis," *Proceedings of the IEEE*, v 53, n 7, p 672-686, 1965.

[67] L. O. Chua, and D. N. Green, "Graph-Theoretic Properties of Dynamic Nonlinear Networks," *IEEE Transactions on Circuits and Systems*, vol. CAS-23, No. 5, 1976.

[68] G. M. Bernstein, and M. A. Lieberman, "A Method for Obtaining a Canonical Hamiltonian for Nonlinear LC Circuits," *IEEE Transactions on Circuits and Systems*, vol. 36, no. 3, 1989.

[69] C. A. Desoer, E. S. Kuh, *Basic Circuit Theory*. McGraw-Hill, Inc., 1969.

[70] U. M. Ascher, L. R. Petzold, *Computer Methods for Ordinary Differential Equations and Differential-Algebraic Equations*. Society for Industrial and Applied Mathematics, 1998.

[71] A. Barone, and G. Paterno, *Physics and applications of the Josephson effect*. John Wiley & sons, 1982.

[72] T. P. Orlando and K. A. Delin, *Foundations of Applied Superconductivity.* Addison-Wesley Co., Massachusetts, 1991.

[73] T. van Duzer, C. W. Turner, *Superconductive Devices and Circuits.* Prentice Hall, Inc., New Jersey, 1999.

[74] S. H. Strogatz, *Nonlinear Dynamics and Chaos.* Addison Wesley Publishing Company, 1994.

[75] D. S. Crankshaw, *Measurement and On-chip Control of a Niobium Persistent Current Qubit*, Doctoral Thesis, MIT, 2003.

[76] D. Y. Nakada, *Fabrication and Measurement of a Niobium Persistent Current Qubit*, Doctoral Thesis, MIT, 2004.

[77] Pulsed RF Spectrum Analysis. Spectrum Analyzer Series Application Note 150-2, Agilent Technologies.

[78] Time-gated Spectrum Analysis: New Measurment Fundamentals Product Note, PN 8590-2, Agilent Technologies.